Assen Zlatarov University
Burgas, Bulgaria

ANNUAL

1

VOLUME XLVII, BOOK 1, 2018

TECHNICAL AND NATURAL SCIENCES

ASSEN ZLATAROV UNIVERSITY
BURGAS, BULGARIA

ANNUAL

Vol. XLVII, BOOK 1, 2018

TECHNICAL AND NATURAL SCIENCES

Assen Zlatarov University

Assen Zlatarov University
Annual, Vol. XLVII, Book 1, 2018
Burgas 8010, Bulgaria
ISSN 2603-3968

ASSEN ZLATAROV UNIVERSITY
BURGAS, BULGARIA

ANNUAL

Vol. XLVII, BOOK 1, 2018

TECHNICAL AND NATURAL SCIENCES

BURGAS ● 2018

VOLUME XLVII (1). CONTENTS

ANNUAL OF ASSEN ZLATAROV UNIVERSITY, BURGAS
BULGARIA, 2018, v. XLVII (I)

UNIFORM M^2-COMPUTABILITY OF THE GENERALISED MEAN

Ivan Georgiev
E-mail: ivandg@yahoo.com

ABSTRACT

We have studied the subrecursive complexity of the generalised mean of a fixed finite set of positive real numbers. We have proved that if all these real numbers have M^2*-computable approximations, then the generalised mean with exponent p, considered as a real function of p, can be realised by* M^2*-substitutional operators, acting on approximations of p.*

Key words: *the subrecursive class* M^2*, computable real function, generalised mean, one-point extension*

INTRODUCTION

This paper is in the field of computable analysis, which can be seen as a theoretical framework for exact real computation. The study of the applications of the subrecursive class M^2 in computable analysis originated in paper [3]. The results proven there imply that the set of all real numbers which have M^2-computable approximations is a field which is closed under applications of the elementary functions of calculus. More concretely, it is shown that all elementary functions of calculus restricted to compact subsets of their domains are uniformly M^2-computable. This means there exists a uniform way of transforming approximations of the argument of a real function into an approximation of its value. Moreover, this transformation can be realised by M^2-substitutional operators, which are a simple kind of Type-2 operators, defined explicitly by terms involving functions from M^2. One of the next goals of the research was to study the complexity of real functions, which are extensions of elementary functions by finitely many points in the domain, where these functions are continuous. Results in [1] show that under natural assumptions, the uniformly M^2-computable real functions are closed under such kind of extensions. The aim of the present paper is to apply these results to the generalised mean with exponent *p*, which is an example of such real function. In order to do this we will consider a more general scenario in which the real function behaves smoothly around the points of the extension.

COMPUTING REAL NUMBERS AND REAL FUNCTIONS

We denote the set of all natural numbers (positive integers and zero) by N and the set of all real numbers by R. A *name* of a real number is a triple (f, g, h) of unary total functions in N, such that the inequality $\left|\frac{f(n)-g(n)}{h(n)+1}\right| < \frac{1}{n+1}$ is true for any $n \in \mathrm{N}$. Let F be a class of total functions in N. A real number ξ is F-*computable* if there exists a name (f, g, h) of ξ, such that *f*, *g* and *h* belong to F. A real function $\theta : D \to \mathrm{R}$, where $D \subseteq \mathrm{R}^k$ for $k \in \mathrm{N}$, is *uniformly* F-*computable* if there exists a triple (*F*, *G*, *H*) of F-substitutional operators, such that for all $(\xi_1, \ldots, \xi_k) \in D$ and all triples $(f_1, g_1, h_1), \ldots, (f_k, g_k, h_k)$, which are names of $\xi_1, \ldots, \xi_k$, respectively, the triple

$$(F(f_1, g_1, h_1, \ldots, f_k, g_k, h_k),\ G(f_1, g_1, h_1, \ldots, f_k, g_k, h_k),\ H(f_1, g_1, h_1, \ldots, f_k, g_k, h_k))$$

is a name of the real number $\theta(\xi_1, \ldots, \xi_k)$. For a precise definition of the class of F-substitutional operators and their properties, see Section 2.2 in [3]. If F is the class of all recursive functions, we obtain notions of computability for real numbers and real functions, which turn out to be equivalent to the ones in [2]. In this paper we shall consider the case F = M^2, where M^2 is the class of all total functions in N, which are polynomially

bounded and have Δ_0 definable graphs. All basic elementary functions of calculus (sum, product, difference, *n*-th root, sin, cos, arcsin, etc.) are uniformly M^2-computable on their whole domains. The only exceptions are the reciprocal, the logarithmic and the exponential real functions, since any uniformly M^2-computable real function is bounded by some polynomial. Nevertheless, the following real functions, related to them are uniformly M^2-computable:

the real function $\theta_r : D \to \mathrm{R}$, defined by

$$\theta_r(\xi,\eta) = 1/\xi, \qquad (1)$$

where $D = \{(\xi,\eta) \in \mathrm{R}^2 \mid |\xi\eta| \geq 1\}$,

the real function $\theta_l : \tilde{D} \to \mathrm{R}$, defined by

$$\theta_l(\xi,\eta) = \ln \xi, \qquad (2)$$

where $\tilde{D} = \{(\xi,\eta) \in \mathrm{R}^2 \mid \xi > 0, \xi\eta \geq 1\}$,

the real function $\theta_e : \mathrm{R}^2 \to \mathrm{R}$, defined by

$$\theta_e(\xi,\eta) = \min(e^{\xi},\eta). \qquad (3)$$

For proofs, confer Example 14, Theorem 6 and Theorem 7 in [3].

It is easy to see that the substitution operation on real functions preserves uniform M^2-computability. It follows that all elementary functions of calculus are uniformly M^2-computable on the compact subsets of their domains and thus they preserve M^2-computability of real numbers.

ONE-POINT EXTENSIONS OF REAL FUNCTIONS

Our main result is based on a particular kind of smooth one-point extension of a real function.

Theorem 1. Let *D* be a subset of R, such that 0 is an interior point of *D*. Let $\rho : D \to \mathrm{R}$ be a differentiable real function, which is uniformly M^2-computable and satisfies $\rho(0) = 0$. Let there exist a neighbourhood *U* of 0, $U \subseteq D$ and positive real numbers A, α, such that $|\rho'(\xi)| \leq A|\xi|^{\alpha}$ for all $\xi \in U$. Then the real function $\theta : D \to \mathrm{R}$, defined by

$$\theta(\xi) = \begin{cases} \dfrac{\rho(\xi)}{\xi} & \text{if } \xi \in D \setminus \{0\}, \\ 0 & \text{if } \xi = 0, \end{cases}$$

is uniformly M^2-computable.

Proof. For any $\xi \in U, \xi \neq 0$ by the mean value theorem, there exists $\eta \in U$ between 0 and ξ, such that

$$\frac{\rho(\xi)}{\xi} = \frac{\rho(\xi)-\rho(0)}{\xi-0} = \rho'(\eta).$$

Thus $\left|\dfrac{\rho(\xi)}{\xi}\right| = |\rho'(\eta)| \leq A|\eta|^{\alpha} \leq A|\xi|^{\alpha}$. It follows that $|\theta(\xi)| \leq A|\xi|^{\alpha}$ for any $\xi \in U$. Thus by Example 5.4 in [1] we can choose a unary function $r \in \mathrm{M}^2$, such that for all $t \in \mathrm{N}$, $\xi \in D$ the inequality $|\xi| < \dfrac{1}{r(t)+1}$ implies the inequality $|\theta(\xi)| \leq \dfrac{1}{t+1}$. Moreover, $\theta(\xi) = \rho(\xi)\theta_r(\xi,\eta)$ for all $(\xi,\eta) \in \mathrm{R}^2$, such that $\xi \in D$ and $|\xi\eta| \geq 1$, where θ_r is defined in (1). Thus θ is uniformly M^2-computable for such ξ, η. It remains to apply Theorem 5.2 in [1]. End of proof.

We note that the assumption $\rho(0) = 0$ is necessary. Otherwise θ would be unbounded around 0 and thus it would not be uniformly M^2-computable (it would not even be computable, since computability of real functions implies their continuity).

PROPERTIES OF THE GENERALISED MEAN

For a natural number $n \geq 2$ and positive real numbers $x_1, x_2, ..., x_n$, which we denote shortly by $\underset{\sim}{x}$, the *generalised mean with exponent p* is defined by

$$GM_p(\underset{\sim}{x}) = \begin{cases} \left(\dfrac{x_1^p + x_2^p + ... + x_n^p}{n}\right)^{\frac{1}{p}} & \text{if } p \neq 0, \\ \sqrt[n]{x_1 x_2 ... x_n} & \text{if } p = 0. \end{cases}$$

We consider $GM_p(\underset{\sim}{x})$ as a real function of *p* for fixed positive $x_1, x_2, ..., x_n$. The following facts are well-known:

- GM_p is continuous in 0;
- if $x_1 = x_2 = ... = x_n$, then $GM_p(\underset{\sim}{x})$ is a constant real function;
- if not all of $x_1, x_2, ..., x_n$ are equal, then $GM_p(\underset{\sim}{x})$ is a strictly increasing real function;
- $\lim\limits_{p \to -\infty} GM_p(\underset{\sim}{x}) = \min(x_1, x_2, ..., x_n) = m$;

- $\lim_{p\to+\infty} GM_p(\overset{\mathrm{r}}{x}) = \max(x_1, x_2, ..., x_n) = M$;
- $m \le GM_p(\overset{\mathrm{r}}{x}) \le M$;
- $GM_{-p}(\overset{\mathrm{r}}{x}) = 1/GM_p(\frac{1}{x_1}, \frac{1}{x_2}, ..., \frac{1}{x_n})$. (4)

MAIN RESULT

Theorem 2. Let $x_1, x_2, ..., x_n$ be fixed positive M^2-computable real numbers. Then the real function GM_p is uniformly M^2-computable.

Proof. Let us denote $r = \sqrt[n]{x_1 x_2 \mathrm{K}\ x_n}$. Then r and $\ln r$ are M^2-computable real numbers and we have $\ln r = \frac{\ln x_1 + \ln x_2 + \mathrm{K}\ \ln x_n}{n}$. For simplicity we will omit the arguments $x_1, x_2, ..., x_n$. Let us define $L(p) = \ln GM_p - \ln r$ and

$u(p) = x_1^p + x_2^p + \mathrm{K} + x_n^p$. Then we have

$$L(p) = \begin{cases} \dfrac{\ln \dfrac{u(p)}{n} - p.\ln r}{p}, & \text{if } p \neq 0, \\ 0, & \text{if } p = 0. \end{cases}$$

Assuming the denotation from Theorem 1, we have

$$\rho(p) = \ln \frac{u(p)}{n} - p.\ln r = \ln u(p) - \ln n - p.\ln r,$$

$$\rho'(p) = \frac{u'(p)}{u(p)} - \ln r,$$

$$\rho''(p) = \frac{u''(p)u(p) - u'(p)^2}{u(p)^2},$$

where

$u'(p) = \ln x_1.x_1^p + \ln x_2.x_2^p + \mathrm{K} + \ln x_n.x_n^p$,

$u''(p) = \ln^2 x_1.x_1^p + \ln^2 x_2.x_2^p + \mathrm{K} + \ln^2 x_n.x_n^p$.

Clearly, $u(0) = n$, $u'(0) = \ln x_1 + \ln x_2 + \mathrm{K} + \ln x_n$.

Therefore $\rho(0) = \rho'(0) = 0$ and $\rho''(p)$ is continuous everywhere. In particular, its continuity in 0 implies that there exists an open neighbourhood U of 0, such that $\rho''(p)$ is bounded in U. Let us choose a positive real number A, such that $|\rho''(p)| \le A$ for all $p \in U$. For any $\xi \in U$ by the mean value theorem, there exists $\eta \in U$ between 0 and ξ , such that

$\rho'(\xi) = \rho'(\xi) - \rho'(0) = \rho''(\eta).\xi$.

Hence $|\rho'(\xi)| \le |\rho''(\eta)|.|\xi| \le A|\xi|^{\alpha}$ for $\alpha = 1$. To apply Theorem 1 for the real function L it remains to prove that ρ is uniformly M^2-computable. To this end we consider the equality

$$\ln(x_1^p + x_2^p + \mathrm{K} + x_n^p) = p.\ln M + \ln\left(\left(\frac{x_1}{M}\right)^p + \left(\frac{x_2}{M}\right)^p + \mathrm{K} + \left(\frac{x_n}{M}\right)^p\right),$$

where as above $M = \max(x_1, x_2, ..., x_n)$. For any M^2-computable real number $\alpha \le 1$ we have that α^p is uniformly M^2-computable for $p \in (-1, \infty)$, because we have the equalities

$$\alpha^p = e^{p.\ln\alpha} = \min(e^{p.\ln\alpha}, \frac{1}{\alpha}) = \theta_e(p.\ln\alpha, \frac{1}{\alpha}),$$

where θ_e is the real function defined in (3). Therefore the sum

$$\left(\frac{x_1}{M}\right)^p + \left(\frac{x_2}{M}\right)^p + \mathrm{K} + \left(\frac{x_n}{M}\right)^p \quad (5)$$

is a uniformly M^2-computable real function for $p \in (-1, \infty)$. Moreover, at least one of the summands in (5) has value 1 for all values of p. Thus employing the real function θ_l from (2) with $\eta = 1$ we obtain that the natural logarithm of the sum (5) is uniformly M^2-computable for $p \in (-1, \infty)$. From this we easily obtain that $\rho(p)$ is uniformly M^2-computable for $p \in (-1, \infty)$ and by Theorem 1 the same is true for L (p). We also have $GM_p = e^{L(p)+\ln r} =$ $= \min(e^{L(p)+\ln r}, M) = \theta_e(L(p) + \ln r, M)$, so we conclude that GM_p is uniformly M^2-computable for $p \in (-1, \infty)$. Now we apply what we have just proven, but for the reciprocal numbers $\frac{1}{x_1}, \frac{1}{x_2}, ..., \frac{1}{x_n}$. We obtain that the real function $GM_p(\frac{1}{x_1}, \frac{1}{x_2}, ..., \frac{1}{x_n})$ is uniformly M^2-computable for $p \in (-1, \infty)$. Using equality (4) and the fact that $1/GM_p(\frac{1}{x_1}, \frac{1}{x_2}, ..., \frac{1}{x_n})$ is equal to $\theta_r(GM_p(\frac{1}{x_1}, \frac{1}{x_2}, ..., \frac{1}{x_n}), M)$, we conclude that GM_p is uniformly M^2-computable for $p \in (-\infty, 1)$. Finally, we have two uniformly M^2-

computable restrictions of GM_p to $(-1,\infty)$ and to $(-\infty,1)$. To combine them into one real function we utilise the following equality: $GM_p = GM_{\frac{p+|p|}{2}} + GM_{\frac{p-|p|}{2}} - GM_0$, valid for all $p \in (-\infty,+\infty)$. The right-hand side is uniformly M^2-computable for all $p \in (-\infty,+\infty)$ and thus the same is true for GM_p. End of proof.

CONCLUSION

The obtained results can be immediately generalised to any class F of total functions in N which contains M^2 and is closed under substitution - for example, the class L^2 of the lower elementary functions or the levels E^n of the Grzegorczyk's hierarchy of the primitive recursive functions for $n \geq 2$.

An interesting question for further investigation is the following: is the real function $GM_p(\overset{\mathrm{r}}{x})$ uniformly M^2-computable not just as a function of p, but also as a function of $x_1, x_2, ..., x_n$ for fixed $n \geq 2$?

REFERENCES

1. Georgiev, I., Uniform and conditional M^2-computability of some nonelementary real functions. (to be published)

2. Grzegorczyk, A., Computable functionals. *Fund. Math.*, **42**, (1955), pp. 168-202.

3. Skordev, D., Weiermann, A., Georgiev, I., M^2-computable real numbers. *J. Logic and Computation*, **22** (issue 4), (2012), pp. 899-925.

ANNUAL OF ASSEN ZLATAROV UNIVERSITY, BURGAS
BULGARIA, 2018, v. XLVII (I)

HIRSHFELD SURFACE ANALYSIS OF BIS(2-AMINOTHIAZOLE)DICHLOROZINC(II)

Rumyana Yankova
E-mail: r_iankova@yahoo.com

ABSTRACT

The title molecule, bis(2-aminothiazole)dichlorozinc(II) ([Zn(2-aminothiazole)$_2$Cl$_2$]) was characterized by means of Hirshfeld surface analysis. A detailed analysis of the intermolecular interactions via Hirshfeld surface analysis and fingerprint plots revealed that the [Zn(2-aminothiazole)$_2$Cl$_2$ structure is stabilized mainly by the formation of Cl···H/H···Cl hydrogen bonds. However, contributions from H···H and C···C contacts were also observed. The enrichment ratio was obtained by comparing the actual contacts in the crystal with those computed as if all types of contacts had the same probability to form.

Key words: *bis(2-aminothiazole)dichlorozinc(II), Hirshfeld surface, Fingerprint plot*

INTRODUCTION

Heterocyclic compounds (pyridine, imidazole, thiazole) are better ligands because they contain nitrogen and sulphur as donor atoms. Schiff base ligands are widely studied in the field of coordination chemistry due to their facile syntheses and good solubility in common solvents. The coordination compounds with these ligands exhibit a wide spectrum of biological activities [1, 2]. Thiazole metal complexes are becoming important as biochemical and antimicrobial reagents [3, 4].

Hirshfeld surface is becoming a valuable tool for analyzing intermolecular interactions [5, 6]. Hirshfeld surface is defined by that region around a molecule where the weight function is $w(r) \geq 0.5$, that is, the region where the promolecule contribution to the procrystal electron density exceeds that from all other molecules in the crystal. A weight function following Hirshfeld is the sum of spherical atom electron densities from the molecule (promolecule) of interest divided by the same sum for the crystal (procrystal) [7, 8]:

$$w(r) = \frac{\rho_{\text{promolecule}}(r)}{\rho_{\text{procrystal}}(r)} = \frac{\sum_{A \in \text{molecule}} \rho_A(r)}{\sum_{A \in \text{crysal}} \rho_A(r)}, \qquad (1)$$

where $\rho_A(r)$ is a sp herically-averaged atomic electron density centred on nucleus A, and the promolecule and procrystal are sums over the atoms belonging to the molecule and to the crystal, respectively.

A three-dimensional picture of intermolecular close contacts in a crystal is obtained by mapping the distances d_e (distances from points on the surface to the nearest atoms outside the surface) and d_i (distances from points on the surface to the nearest atoms inside the surface) on the Hirshfeld surface. The normalized contact distance – d_{norm} is defined in terms of d_e, d_i and the van der Waals radii of the atoms (r^{vdw}) – equation 2. They are also used to generate a fingerprint plot [9], a concise two-dimensional summary of intermolecular interactions in the crystal.

$$d_{\text{norm}} = \frac{d_i - r_i^{\text{vdw}}}{r_i^{\text{vdw}}} + \frac{d_e - r_e^{\text{vdw}}}{r_e^{\text{vdw}}}, \qquad (2)$$

The crystal structure of the titled compound is presented in the work of Macíček and Davarski [10] for the first time. The molecule structure and electronic properties is discussed on the basis of the Density Functional Theory [11].

Hirshfeld surface analysis for analyzing intermolecular interactions in [Zn(2-aminothiazole)$_2$Cl$_2$], and their related fingerprint plots were carried out using the program Crystal Explorer [12].

The crystallographic information file (.cif) was retrieved from the Cambridge Crystallographic Data Center as supplementary publication no. CCDC 1289048.

RESULTS AND DISCUSSION

The interactions in the crystal structure of bis(2-aminothiazole)dichlorozinc(II) were examine with the Hirshfeld surface and associated 2-D fingerprint plots [13, 14].

The Hirshfeld surfaces are defined within the crystal [13]. Consequently, Hirshfeld surfaces reflect the interplay between different atomic sizes and intermolecular contacts in the crystal [15]. The crystal structure, Hirshfeld surface of the title compound mapped with d_{norm}, shape index and curvedness are shown in Figure 1. It was established that d_{norm} values vary from –0.4057 to +1.1478 Å, the shape index ranges from –0.9953 to +0.9978 Å, the curvedness from –3.3734 to +0.4632 Å.

The d_{norm} mapping showed the existence of a bright red area in the Hirshfeld surface due to a strong interaction between a chlorine atom (Cl^2) in the structure on the inside of the Hirshfeld surface and a hydrogen atom (H^3) in the structure on the outside of the Hirshfeld surface via $Cl^2 \cdots H^3$ hydrogen bond (Figure 1B). The presence of an identical hydrogen bond ($H^3 \cdots Cl^2$) between a chlorine atom (Cl^2) in the structure on the outside of the Hirshfeld surface and a hydrogen atom (H^3) in the structure on the inside of the Hirshfeld surface was detected. A value of 2.282 Å was observed as the length of the aforementioned hydrogen bonds. It was established that a hydrogen bond appeared between molecule on the inside surface and two molecules outside expressed by $Cl^1 \cdots H^4$ and $H^4 \cdots Cl^1$ interactions. A value of 2.387 Å was observed as the length of the hydrogen bonds.

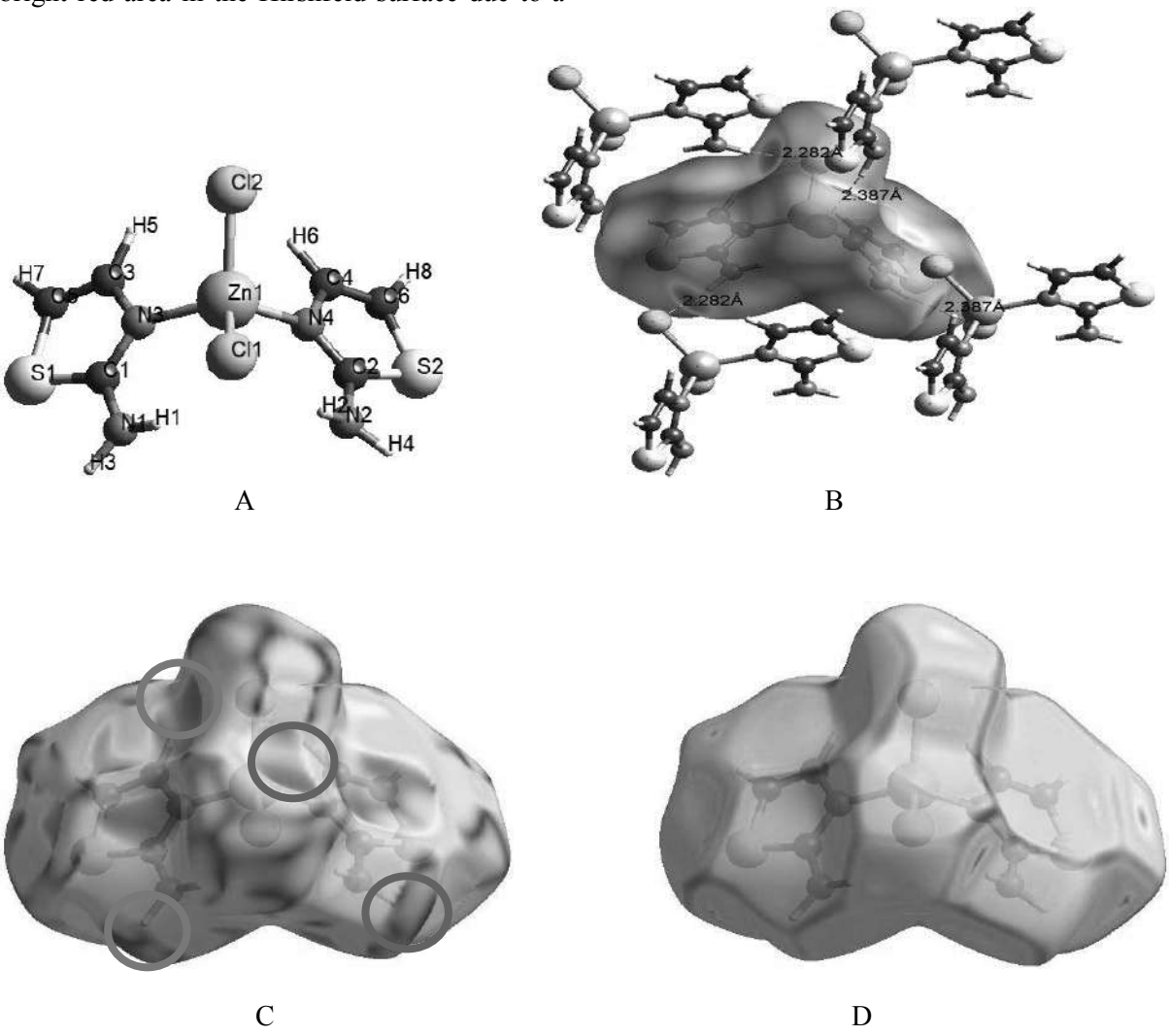

Fig. 1. Crystal structure and numbering of atoms for [Zn(2-aminothiazole)$_2$Cl$_2$] (A); Hirshfeld surface mapped with d_{norm} (B), shape index with areas of complementarity identified (paired circles) (C) and curvedness (D).

For the identification of complementarity between molecules in the crystal packing structure shape index was used [16]. Features on the shape index surface that had an identical pattern but opposite colours indicated areas of intermolecular complementarity. These areas are presented in Figure 1C. The red patches represent regions related to atoms of the π-stacked molecule above them. The blue patches represent regions which are an indication for ring atoms of the molecule inside the surfaces. The red region marked with a red circle on the shape index mapping refers to $Cl^{2}\cdots H^{3}$–π interaction, the red region marked with a blue circle characterizes the $Cl^{1}\cdots H^{4}$–π interaction. These interactions have a contribution of 18.9%. The blue regions marked with red and blue circles depict an area of complementarity where the hydrogen atoms from amino groups (H^3 and H^4, respectively) are positioned under chlorine atoms and have a contribution of 14.2%.

A measure of the shape of the surface area of the molecule is the curvedness [17]. The curvedness for bis(2-aminothiazole)dichlorozinc(II) is presented on Figure 1D. The low values of curvedness correspond to flat areas of the surface. Sharp curvature areas correspond to high values of curvedness and usually tend to divide the surface into patches, indicating interactions between neighbouring molecules. The large flat region which is delineated by a blue outline refers to the π···π stacking interactions.

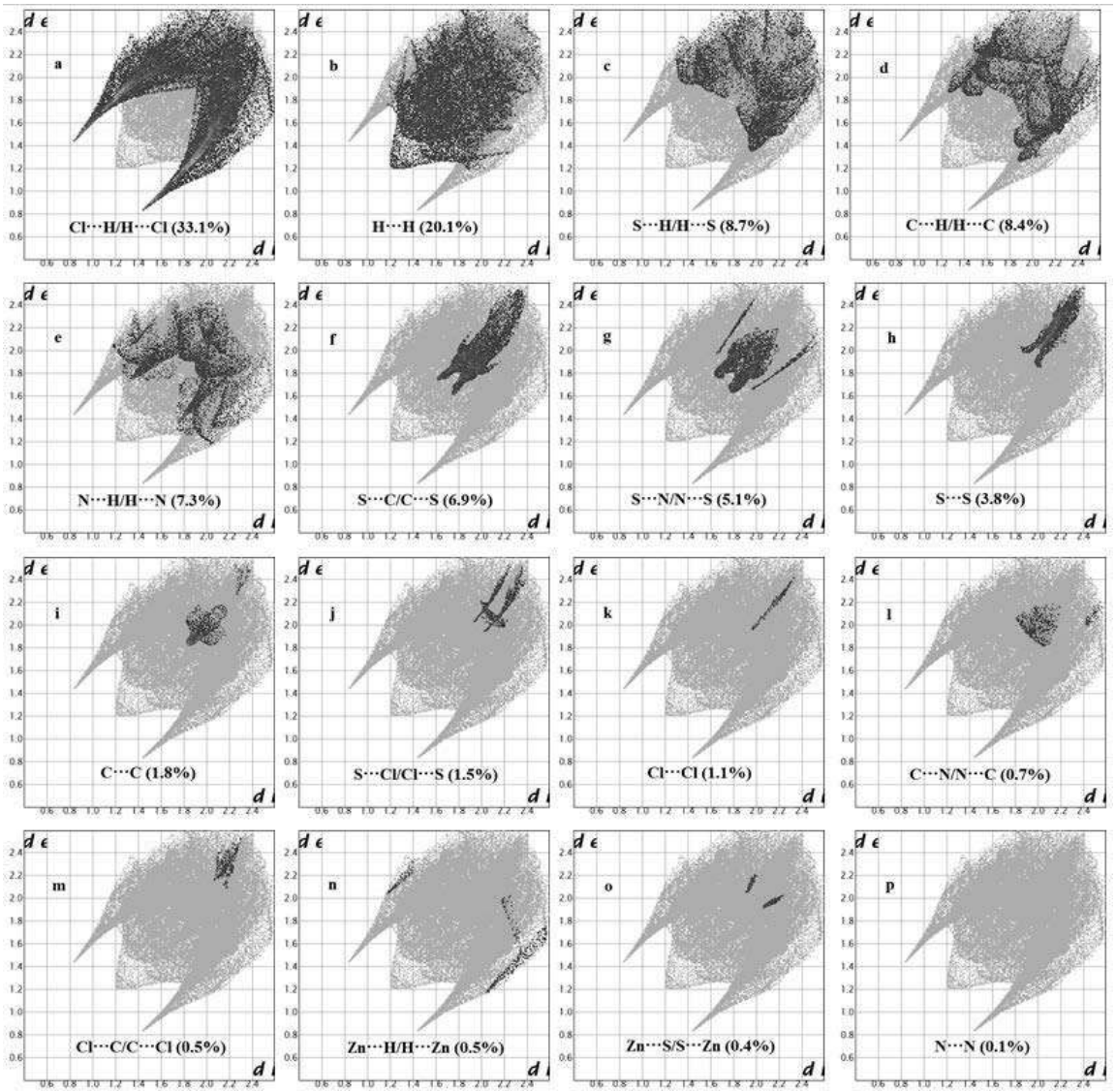

Fig. 2. The 2-D fingerprint plot with percentages of the different contributions for [Zn(2-aminothiazole)$_2$Cl$_2$]

The expanded two dimensional fingerprint plots, which are in the range 0.6 – 2.4 Å with the closest external (d_e) and the closest internal (d_i) distance scales displayed on the graph axes, not only clearly identify each type of intermolecular contact, but also enable the analysis of very small differences in these patterns and as such represent an entirely new way of summarizing the major intermolecular contacts of an entire crystal structure [18]. The fingerprint plots can be decomposed to highlight particularly close contacts between the elements. Figure 2 shows the associated fingerprint plots of bis(2-aminothiazole) dichlorozinc(II) showing the significant contributions of different intermolecular interactions on the Hirshfeld surface.

It can be seen that the highest contribution of total Hirshfeld surface is attributed to Cl···H/H···Cl interactions with 33.1%; they are attributed to the N–H···Cl hydrogen-bonding interactions, and appear as two sharp symmetric spikes in two-dimensional fingerprint plots around a sum of $d_i + d_e \sim 2.2$ Å (Fig. 2a). The bottom right spike characterized the Cl···H interactions with a contribution of 18.9%. The calculated distances between the nearest atoms present inside and outside the surface were approximately equal to 1.4 and 0.8 Å, respectively. The H···Cl interactions with a slightly lower contribution (14.2%) of the total surface were detected in the form of a top left spike. In that case, values of 0.8 and 1.4 Å were obtained as d_i and d_e, respectively. The contacts H···H with 20.1% contribution of total Hirshfeld surface appear in the middle of the scattered points in the two-dimensional fingerprint maps with a single broad peak at $d_i = d_e = 1.2$ Å (Fig. 2b). Pairs of blunted spikes corresponding to S···H/H···S (8.7%) contacts at $d_i + d_e \sim 3.4$ Å; C···H/H···C (8.4%) contacts at $d_i + d_e \sim 3.2$ Å and N···H /H···N (7.3%) contacts at $d_i + d_e \sim 3.1$ Å are evident in the overall fingerprint plots (Fig. 2c, d, e). The fingerprint plots corresponding to the contacts C···C (Fig. 2i) show the presence of a triangle at $d_i = d_e = 1.8$ Å, because there is the π–π interactions in our crystalline stacking [19].

The percentage of contacts between one or two chemical elements can be used to calculate the enrichment ratios (E_{XY}). The enrichment ratio of a pair of elements is defined as the ratio between the proportion of actual contacts in the crystal and the theoretical proportion of random contacts [20]:

$$E_{XY} = \frac{C_{XY}}{R_{XY}}, \qquad (3)$$

The enrichment ratios of the various intermolecular contacts in [Zn(2-aminothiazole)$_2$ Cl$_2$] are recorded in Table 1.

Table 1. Enrichment ratio of different inter-contact and percentage of each atom on the surface Hirshfeld in [Zn(2-aminothiazole)$_2$Cl$_2$]

Atoms	H	N	Cl	C	S	Zn
H	0.83	1.12	1.81	0.85	0.59	1.13
N	–	0.23	0	0.52	2.54	0
Cl	–	–	0.32	0.13	0.27	0
C	–	–	–	1.78	2.27	0
S	–	–	–	–	1.67	2.94
Zn	–	–	–	–	–	0
Surf., %	49.1	6.65	18.65	10.05	15.1	0.45

For a pair of elements with a higher propensity to form contacts, the E value is larger than one. In contrary, pairs which tend to avoid contacts yield an E value lower than one [20]. Calculations showed that 49.10% of the molecular surface is generated by H atoms, followed by the Cl ones with surface contribution of 18.65%. A value of 15.10% was attributed to the S atoms, 10.05% was attributed to the C atoms, 6.65% was attributed to the N atoms, while Zn atoms complement the total molecular surface with a contribution of 0.45% (Table 1). Taking into account the 2-D fingerprint plots analysis (Fig. 2), it was clear that the surface data depicted in Table 1 are in accordance with the statement that hydrogen bonds containing chlorine atoms were mainly involved in the [Zn(2-aminothiazole)$_2$Cl$_2$] structure. This result was further confirmed by means of the calculated enrichment ratio values (Table 1). For instance, the Cl···H contacts are considerably favoured ($E_{Cl\cdots H} = 1.81$) in the title compound, which corresponds to a contribution of 33.1% of the total Hirshfeld surface (Fig. 2a). The high value enrichment ratio of the contact C···C ($E_{C\cdots C} = 1.78$) due to extensive π–π interactions in the crystal packings of compound. The absence of C–H··· π is reflected in a low enrichment ratio ($E_{C\cdots H} = 0.85$). The heterocyclic group of [Zn(2-aminothiazole)$_2$Cl$_2$] displays high $E_{S\cdots C}$ and $E_{S\cdots S}$ values. This is explained by the sulphur, which becomes more abundant on t he Hirshfeld surface ($S_S = 15.1$). The H···H contacts, expressed as interactions with a c ontribu-

tion of 20.1% of the total Hirshfeld surface (Fig. 2b), were notably under-represented with an enrichment ratio of 0.83 (Table 1). On the contrary, a higher value enrichment ratio of the contact Zn···S ($E_{Zn\cdots S}$ = 2.94) was detected in the case of Zn·· · S contacts, in spite of their significantly lower contribution (0.4%) in the total Hirshfeld surface (Fig. 2o) in comparison with that of H·· ·H contacts.

A study of Hirshfeld surface carried out on the title compound gives the following measurement: molecular volume – 307.15 Å^3, surface area – 282.95 Å^2, globularity – 0.778 as well as asphericity – 0.047.

CONCLUSIONS

The present paper is a theoretical investigation of the intermolecular interactions in bis(2-aminothiazole)dichlorozinc(II). The intermolecular interactions were examined via Hirshfeld surface, mapped with d_{norm}, shape index and curvedness, and associated 2-D fingerprint plots. It was establishes that d_{norm} values varied from –0.4057 to +1.1478 Å, the shape index ranges from –0.9953 to +0.9978 Å, the curvedness from –3.3734 to +0.4632 Å. 2-D fingerprint plots analysis showed that 33.1% of the total Hirshfeld surface was attributed to Cl·· ·H/H·· · Cl interactions. A value of 20.1% characterized the H·· ·H interactions. The first type of interactions expressed N–H···C l bonds between molecules on the inside and molecules outside of the Hirshfeld surface. These interactions play a c onsiderable role in stabilizing the self-assembly process.

REFERENCES

1. Garnovskii, A.D., O.A. Osipov, L.I. Kuznetsova, N.N. Bogdashev. *Russ. Chem. Rev.*, **42**, (1973), p. 177.
2. Shepherd, R.E. S. Zhang. *Trans. Metal Chem.*, **19**, (1994), p. 146.
3. Neelakantan, M.A., S.S. Marriappan, J. Dharmaraja, T. Jeyakumar, K. Muthukumaran. *Spectrochim. Acta Mol. Biomol. Spectrosc.*, **71**, (2008), p. 628.
4. Raman, N., R.S. Johnson., J. Joseph, R.J. Dhaveethu. *J. Chil. Chem. Soc.*, **52**, (2007), p. 1138.
5. Spackman, M.A., P.G. Byrom. *Chemical physics letters*, **267,** (1997), p. 215.
6. McKinnon, J.J., A. S. Mitchell, M.A. Spackman. *Chemistry–A European Journal*, **4**, (1998), p. 2136.
7. Hirshfeld, F.L. *Theoretica chimica acta*, **44**, (1977), p. 129.
8. McKinnon, J.J., D. Jayatilaka, M.A. Spackman. *Chemical Communications*, **37**, (2007), p. 3814.
9. Spackman, M.A., J.J. McKinnon. *CrystEngComm*, **4**, (2002), p. 378.
10. Macíček, J., K. Davarski, *Acta Crystallographica Section C: Crystal Structure Communications*, **49**, (1993), p. 592.
11. Yankova, R. *Open Access Library Journal*, **2**, (2015), p. 1.
12. Turner, M.J., J.J. McKinnon, S.K. Wolff, D.J. Grimwood, P.R. Spackman, D. Jayatilaka, M.A. Spackman, CrystalExplorer17 (2017) University of Western Australia.
13. Shit, S., C. Marschner, S. Mitra, *Acta Chim. Slov.*, **63**, (2016), p. 129.
14. Fezai, R., M. Rzaigui. *J. Fluoresc*., **28**, (2018), p. 183.
15. Safin, D.A., K. Robeyns, Y. Garcia. *Cryst. Eng. Comm.* **18**, (2016), p. 7284.
16. Shukla, R., T.P. Mohan, B. Vishalakshi, D. Chopra. *Cryst. Eng. Comm.*, **16**, (2014), p. 1702.
17. Wang, W., Y. Ling, L.-J. Yang, Q.-L. Liu, Y.-H. Luo, B.-W. Sun, *Res. Chem. Intermed.*, **42**, (2016), p. 3157.
18. S. Karthik Kumara, L.D. Naveen, Mahadevaswamy, A.K. Kariyappa, N.K. Lokanath. *Chem. Data Coll*., **9**, (2017), p. 251.
19. Wardell, J.L., M.M. Jotani, E.R. Tiekink. *Acta Crystallographica Section E: Crystallographic Communications*, **72**, (2016), p. 1691.
20. Jelsch, C., K. Ejsmont, L. Huder. *IUCrJ*, **1**, (2014), p. 119.

ANNUAL OF ASSEN ZLATAROV UNIVERSITY, BURGAS
BULGARIA, 2018, v. XLVII (1)

REGRESSION METHODS FOR DETERMINATION OF THERMODYNAMIC PROPERTIES OF SELENITES OF RARE EARTH ELEMENTS

Ginka Baikusheva-Dimitrova, Svetlana Genieva, Rumyana Yankova
E-mail: g_baikusheva@abv.bg

ABSTRACT

The paper suggests two regression methods for determination of the standard entropies of the selenites of rare earth elements: the interpolation formulae of Newton for non-equidistant values of the argument from the numerical methods of mathematical analysis and development of a regression equation of 6th order. The two methods were compared and their precision estimated.

Key words: *rare-earth selenites, thermodynamic data, entropy, thermodynamic methods, regression analysis, coefficient of determination, F-statistics.*

INTRODUCTION

The selenites of rare earth elements are materials which are not thoroughly studied regarding their structure, properties and thermal stability. Their thermodynamic values like standard enthalpy ΔH^{o}_{298}, standard entropy ΔS^{o}_{298} and free energy of Gibbs ΔG^{o}_{298} [1-3] of these compounds are little known which has determined the interest towards them recently.

The standard entropy of formation of compounds is an important thermodynamic characteristic which is used for thermodynamic calculations in inorganic and analytical chemistry and physical chemistry to study and develop various processes. [4, 5].

The aim of the present work is to determine the values of the standard entropies of the selenites of rare earth elements synthesized by four suggested numerical methods which give the best results. The dependence of the standard entropies of formation ΔS^{o}_{298} on their molecular masses is shown graphically. The value of the relative error of the calculations was small, which the precision and adequacy of the numerical methods used. To calculate the standard entropies of the selenites studied, two regression methods were used: interpolation formulae of Newton for non-equidistant values of the argument from the numerical methods of mathematical analysis and creation of a regression equation of 6th order. The two methods were compared.

MATERIALS AND METHODS

Four methods for determination of the standard entropy ΔS^{0}_{298} of the selenites of the type $Me_2(SeO_3)_3$ (where Me = La, Ce, Pr, Nd, Sm, Eu, Gd, Tb, Dy, Ho, Er, Tm, Yb) studied were suggested. The methods used are [6,7]:

1. Method of Kumok (determination of ΔS^{o}_{298} of crystalline substances is reduced to the sum of the entropies of the corresponding ionic components);
2. Method of Kelly (the standard entropy of crystalline substances equals the sum of the entropies of the oxides contained in them);
3. Method of Vineru (the standard entropy of the solid inorganic substances is linearly dependent on the logarithm of the corresponding molecular masses);
4. Method of Latimer (determination of ΔS^{0}_{298} of crystalline substances is reduced to the sum of the entropies of the corresponding ionic increments which are positive for the positive ions while for negative ions the increments depend on cation nature).

The standard entropy of the substances studied was determined as the average of the four methods. The precision was also estimated [8].

Two methods for calculation of the standard entropies of the selenites studied are suggested: the interpolation formulae of Newton [9] for non-equidistant values of the argument from the numerical methods of mathematical analysis and development of a regression equation of 6th order.

Let the interval $[x_o, x_n]$ contains $n + 1$ points $x_o, x_1, \ldots, x_n$, which are the interpolation angles. In our case, $n + 1 = 11$. The interpolation formula of Newton for non-equidistant values of the argument is generally expressed as:

$$P(x) = y_o + [x_o, x_1].(x - x_o) + \\ + [x_o, x_1, x_2].(x - x_o).(x - x_1) + ... + \\ + [x_o, x_1, ..., x_n].(x - x_o).(x - x_1) \\ ...(x - x_{n-1}) \quad (1)$$

where:

y_o – the initial value of the function;

$[x_o, x_1]$ – divided differences of first order:

$$[x_o, x_1] = \frac{y_1 - y_o}{x_1 - x_o};$$

$[x_o, x_1, x_2]$ - divided differences of second order:

$$[x_o, x_1, x_2] = \frac{[x_1, x_2] - [x_o, x_1]}{x_2 - x_o};$$

... $[x_o, x_1, ..., x_n]$ – divided differences of n^{th} order:

$$[x_o, x_1, ..., x_n] = \frac{[x_1, ..., x_n] - [x_o, ..., x_{n-1}]}{x_n - x_o}.$$

The polynomial is expressed as follows:

$$P(x) = y_o + \sum_{i=1}^{10} A_i, \quad (2)$$

where:

$A_i = [x_o, x_1, ..., x_i].x(x - x_1)(x - x_2)...(x - x_{i-1})$.

The values of A_i for the selected interpolation angles x_o, x_1,…, x_{10} were calculated. The standard entropies of formation calculated by the Newton polynomial for the interpolation angles coincided with the measured ones, as expected.

With the Newton interpolation polynomial derived (1), the value of the function cam be calculated at points different from the interpolation angles.

A simplified method for determination of the standard entropies of the selenites studied is suggested, which describes the dependence between the entropy ΔS^o_{298} and the molecular mass M. The regression model has the following form:

$$\Delta S^o_{298} = b + a_1.M + a_2.M^2 + a_3.M^3 + \\ a_4.M^4 + a_5.M^5 + a_6.M^6, \quad (3)$$

where: b, a_1, a_2, ..., a_6 – regression coefficients.

For estimation of the quality of the regression models, the coefficient of determination R^2 is used which determines the degree of the linear dependence between the regressors taking part in the model and the predicted value of the initial quantity [10-13]**.** An essential condition in this case is to check the significance of R^2 which is performed using the Fisher criterion

$$F = \frac{R^2}{(1 - R^2)} \cdot \frac{(N_1 - k)}{(k - 1)}, \quad (4)$$

Where: k – number of estimated parameters of the model; N_1 – volume of the subset of the experimental data. The higher the calculated value of R^2, the more reliable is the regression model derived.

RESULTS AND DISCUSSION

The standard entropy of the compounds studied was determined as the arithmetic average of the results obtained by the four methods (Koumok, Kelly, Vineru amd Latimer). The values of

obtained are shown in Table 1. The standard deviation and the relative error were also calculated.

It can be seen from Table 1 that the relative error ε% calculated was less than 5% which is a very good result indicating that the methods used are suitable for analysis and prediction of compounds of the same type.

To calculate the standard values of the entropy of the lanthanide selenites using their molecular masses, the interpolation formulae of Newton for non-equidistant values of the argument was employed.

The interpolation polynomial of Newton was composed for 11 angles of interpolation for which the value of the polynomial coincides with the arithmetic averages of the entropies calculated by the four methods. To facilitate the computation of the polynomial, the molecular mass of $La_2(TeO_3)_3$ is assumed to null ($x_o = 0$). The molecular masses of the selenites, the assumed interpolation angles X and the corresponding values of the entropy Y are presented in Table 2.

The values of the divided differences A_i were calculated for the interpolation angles selected x_o, x_1,…, x_{11}. The standard entropy ΔS^0_{298} obtained for the interpolation angles coincides with the arithmetic average values measured by the four methods, as it should be according to the interpolation methods of analysis.

The calculated divided differences A_i are shown in Table 3.

The values of the divided differences A_i were calculated for the interpolation angles selected x_o,

$x_1,\ldots, x_{11}$. The standard entropy ΔS^{0}_{298} obtained for the interpolation angles coincides with the arithmetic average values measured by the four methods, as it should be according to the interpolation methods of analysis.

Table 1. Arithmetic average of the value ΔS^{o}_{298} of selenites, standard deviation σ, relative error ε%.

Compound	M		σ	ε%
$La_2(SeO_3)_3$	658.34	326.38	11.6	3.38
$Ce_2(SeO_3)_3$	660.76	336.11	13.2	3.74
$Pr_2(SeO_3)_3$	662.34	341.14	13.1	3.67
$Nd_2(SeO_3)_3$	669.00	338.79	14.5	4.08
$Sm_2(SeO_3)_3$	681.24	338.76	12.5	3.51
$Eu_2(SeO_3)_3$	684.46	337.42	11.7	3.31
$Gd_2(SeO_3)_3$	695.02	343.07	12.6	3.52
$Tb_2(SeO_3)_3$	698.38	345.86	12.0	3.33
$Dy_2(SeO_3)_3$	705.52	344.54	10.7	2.96
$Ho_2(SeO_3)_3$	710.38	347.64	11.9	3.28
$Er_2(SeO_3)_3$	715.04	346.18	11.4	3.15
$Tm_2(SeO_3)_3$	718.38	340.93	9.4	2.62
$Yb_2(SeO_3)_3$	726.60	340.93	9.6	2.69

Table 2. Molecular masses of the selenites M, interpolation angles (X) and corresponding values of entropy (Y)

Compound	*M*		*X*	*Y*
$La_2(SeO_3)_3$	658.34	x_o	0	326.38
$Ce_2(SeO_3)_3$	660.76	x_1	2.42	336.11
$Pr_2(SeO_3)_3$	662.34	x_2	4	341.14
$Nd_2(SeO_3)_3$	669	x_3	10.66	338.79
$Eu_2(SeO_3)_3$	684.46	x_4	26.12	337.42
$Gd_2(SeO_3)_3$	695.02	x_5	36.68	343.07
$Tb_2(SeO_3)_3$	698.38	x_6	40.04	345.86
$Ho_2(SeO_3)_3$	710.38	x_7	52.04	347.64
$Er_2(SeO_3)_3$	715.04	x_8	56.7	346.18
$Tm_2(SeO_3)_3$	718.38	x_9	60.04	340.93
$Yb_2(SeO_3)_3$	726.6	x_{10}	68.26	340.94

The calculated divided differences A_i are shown in Table 3.

Table 3 shows the standard entropies $\overline{\Delta S}^{0}_{298}$ (arithmetic averages obtained from the four

methods) and the values of ΔS^{0}_{298} calculated by the Newton polynomial. For the selected interpolation angles, the values calculated by the polynomial coincide with the arithmetic average values obtained by the four methods, as expected. For compounds outside the interpolation angles, ($Sm_2(SeO_3)_3$ and $Dy_2(SeO_3)_3$), the entropies were calculated by the Newton polynomial. It can be seen that there was good accordance with the corresponding arithmetic average values of these substances.

A simplified method for determination of the standard entropies of the selenites studied (eq.3) which describes the dependence between the entropy ΔS^{o}_{298} and the molecular mass *M*. The values of the entropies obtained are presented in Table 4.

For the estimation of the qualities of the two regression methods, the Fisher criterion and the coefficient of determination R^2 were used. The values obtained for the F-test and R^2 are shown in Table5.

Table 3. Divided differences calculated at the interpolation angles

X	Y	I row	II row	III row	IV row
0	326.38	4.02066	-0.2093	-0.02063	0.0015
2.42	336.11	3.18354	-0.4292	0.018613	-0.0005
4	341.14	-0.35285	0.01195	0.000368	-1E-05
10.66	338.79	-0.08862	0.02397	-9.4E-05	-6E-05
26.12	337.42	0.53504	0.02122	-0.00253	0.00011
36.68	343.07	0.83036	-0.0444	0.000834	-0.0003
40.04	345.86	0.14833	-0.0277	-0.00648	0.00087
52.04	347.64	-0.31330	-0.1573	0.018089	
56.7	346.18	-1.57186	0.13608		
60.04	340.93	0.00122			
68.26	340.94				

V row	VI row	VII row	VIII row	IX row	X row
-5.5E-05	1.73055E-06	-3.9E-08	8.127E-10	-2E-11	4.3E-13
1.4E-05	-2.97764E-07	7.1E-09	-2.52E-10	1.2E-11	
-1E-06	8.78508E-08	-7.4E-09	5.238E-10		
3.7E-06	-3.26961E-07	2.63E-08			
-1E-05	1.18555E-06				
3.7E-05					

Table 4. Arithmetic average values of $\Delta\overline{S}^{0}_{298}$ (by the four methods) and polynomial) and regression

Compound	M	$\Delta\overline{S}^{0}_{298}$	ΔS^{0}_{298} (polynomial)	ΔS^{0}_{298} (regression)
$La_2(SeO_3)_3$	658.34	326.38	326.38	328.4381
$Ce_2(SeO_3)_3$	660.76	336.11	336.11	335.1064
$Pr_2(SeO_3)_3$	662.34	341.14	341.14	337.9552
$Nd_2(SeO_3)_3$	669	338.79	338.79	341.6048
$Sm_2(SeO_3)_3$	681.24	338.76	336.1	338.0407
$Eu_2(SeO_3)_3$	684.46	337.42	337.42	338.0333
$Gd_2(SeO_3)_3$	695.02	343.07	343.07	342.2238
$Tb_2(SeO_3)_3$	698.38	345.86	345.86	344.1567
$Dy_2(SeO_3)_3$	705.52	344.54	348.4	347.2122
$Ho_2(SeO_3)_3$	710.38	347.64	345.86	347.6335
$Er_2(SeO_3)_3$	715.04	345.86	347.64	346.7059
$Tm_2(SeO_3)_3$	718.38	347.64	346.18	345.6552
$Yb_2(SeO_3)_3$	726.6	346.18	340.93	346.6242

Table 5. Estimation of the two regression methods

Method	Equation	F – test	R^2
Interpolation equation of Newton	$P(x) = y_o + \sum_{i=1}^{10} A_i$	80.46	0.8797
Simplified regression equation	$\Delta S^{o}_{298} = b + a_1.M + a_2.M^2 + a_3.M^3 + a_4.M^4 + a_5.M^5 + a_6.M^6$	103.94	0.9088

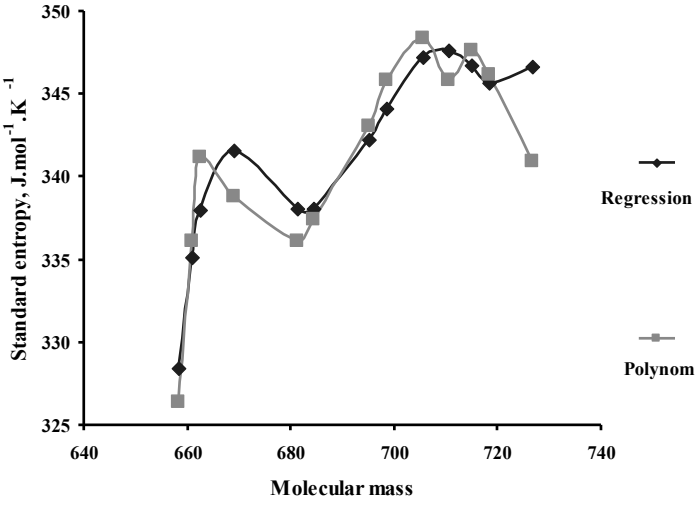

Fig. 1. Standard entropies calculated by the two mathematical methods (polynomial and regression)

It can be seen from Table 5 that the coefficients of determination for the two methods had values close to unity. The simplified regression equation gave value higher than that of the Newton interpolation method. This illustrates the very good coincidence with the prediction.

In Fig. 1, the standard entropies obtained by the two mathematical methods: Newton polynomial and simplified regression equation are plotted and compared.

For compounds for which no data can be found in the literature, the interpolation method and the regression model can successfully determine the standard entropies of compounds of the same type. This is the way the standard entropy of the radioactive $Pm_2(SeO_3)_3$ was determined: (336.614 $J.mol^{-1}.K^{-1}$ (the Newton interpolation method) and (341.330 $J.mol^{-1}.K^{-1}$ (the regression equation).

The difference is negligible. Both methods can successfully be used for analysis and prediction but the simplified regression equation is easier to compute and has higher coefficient of determination.

CONCLUSIONS

1. The present paper suggests two mathematical methods for calculating the standard values of the entropy of the lanthanide selenites studied from their molecular masses: the interpolation formulae of Newton for non-equidistant values of the argument and development of regression equation of 6^{th} order.

2. With the Newton interpolation polynomial derived, the function can be calculated at points other than the interpolation angles. These are the compounds $Sm_2(SeO_3)_3$ and $Dy_2(SeO_3)_3$.

3. A simplified method for determination of the standard entropies of the selenites studied was suggested, which describes the dependence between the entropy and the molecular mass.

4. Using the interpolation method and the regression model, the standard entropies of substances for which there are no data in the literature can successfully be determined on the basis of their molecular masses. This was the way by which the standard entropy of radio-active $Pm_2(SeO_3)_3$ was determined: (336.614 $J.mol^{-1}.K^{-1}$ (the Newton interpolation method) and (341.330 $J.mol^{-1}.K^{-1}$ (regression equation).

5. Both methods can successfully be used for analysis and prediction but the simplified regression equation is easier for calculating and has a higher coefficient of determination.

REFERENCES

1. Serway, J. Beicher and J. Jewett, Physics for Scientists and Engineers, *North Carolina State University and California State Polyte-chnic University*, *Pomona*, (2000), p. 579.
2. Atanasova, L., G. Baikusheva-Dimitrova, G. Gospodinov. Specific Heat Capacity and Thermodynamic Properties of Li_4TeO_4, K_2TeO_3 and $K_2Te_4O_9$, *Journal Oxidation Communications*, (2018), **41** (3), p. 353.
3. Baikusheva-Dimitrova, G., S. Genieva, R. Yankova. Synthesis, thermal behavior and thermodynamic data of hafnium selenite tetraaqaa complex. *International Journal of Scientific Engineering and Applied Science (IJSEAS)*, March (2017), **III** (3), p. 137.
4. Volostchina, A. L. And V. A. Obolontschik, *Ukrainskii Chem. Journal*, (1998), **48**, p. 1028.
5. Barin, I.,. Thermochemical data of pure substances, VCH Verlag gesellschaft, D-6940 *Weinheim*, (2003), **1** and **2**, p. 777, 972, 1406.
6. Kasenov, B., A. Pashynkin, at all. Thermodynamic Methods in nonorganic Chemistry, *Karagandinsky University*, (1999).
7. Baikusheva-Dimitrova, G. Calculation and Prognosis of the Thermodynamic Properties of Rare Earth Tellurites of the $Ln_2Te_4O_{11}$ Type, *Journal Oxidation Communications*, (2012), **35** (3), p. 776.
8. Mustafa, Y., G. Baikusheva-Dimitrova, S. Genieva, R. Jankova. Determination of the Standard Entropies of Rare-earths Selenites. *Journal Science & Technologies*, (2017), **VII** (3), *Publishing House Union of Scientists*, *Stara Zagora*, *Bulgaria*, p. 66.
9. Baikusheva-Dimitrova, G., S. Genieva, R. Jankova.Interpolation Method for Calculation of the Entropy of Selenites of the Rare-earths. *Journal Science & Technologies*, (2017), **VII** (3), *Publishing House Union of Scientists*, *Stara Zagora*, *Bulgaria*, p. 66.
10. Markov, S. Mathematical Modeling. *Science*, *Sofia*, (1997).
11. Nikolaeva Z.. Imitation Model of Solar Radiation and Concentrations of Ozone and Nitrogen Dioxide in the Atmosphere. *Journal Oxidation Communications*, (2018), **41** (2), p. 231.
12. Nikolaeva Z.. Analisis of the Ground Level Concentrations of Ozone in Atmospheric Air. *Journal Oxidation Communications*, (2017), **40** (1-II), p. 469.
13. Kolchakova, G., N. Enev, S. Koruderlieva, M. Ivanova. Study on the Possibility to U tilize Ashes from Thermal Power Stations for the

Production of Construction Ceramic Ma-terials. *Annual Assen Zlatarov University*, *Burgas*, (2017), **XLVI** (1), p. 28.

14. Nikolaeva Z., G. Baikusheva – Dimitrova, G. Visokov. Investigation of the energy processes in the Greenhouse effect. *Journal Oxidation Communications*, (2012), **35** (2), p. 516.

ANNUAL OF ASSEN ZLATAROV UNIVERSITY, BURGAS
BULGARIA, 2018, v. XLVII (1)

QUANTUM-CHEMICAL CALCULATION OF COMPLEXES OF GLUTATHIONE WITH IONS OF TRANSITION METALS

Viktoriya Trifonova, Anife Ahmedova, Krasimir Vassilev
E-mail: viki_trend@abv.bg

ABSTRACT

The geometric optimization of complexes of glutathione weas carried out by the semi-empirical quantum chemical method ZINDO/1 from HyperChem 5.1 software package. The valence angles in coordination structures were calculated. The full energy of complexes of GSH varies from -463.13615 for Fe^{2+} to -493.76894 a.u. for Cu^{2+} complexes. The study of the complexes provides reasons to suggest the probable stereostructure of complexes of glutathione.

Key words: *metal complexes, glutathione, quantum- chemical calculation, structure, oxidation*

INTRODUCTION

Glutathione (GSH) is a tripeptide built from glutamine acid residue, cysteine and glycine:

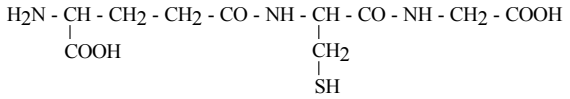

The amino acids and peptides are capable of forming chelate complexes with many metal ions. Usually, the metal ion bonds to the amino and carboxyl groups of the amino acid. Much more stable complexes can be obtained with amino acids containing functional side groups, e.g. histidine, containing imidazole; tyrosine, containing phenol ring; cysteine, containing sulfhydryl group or serine, containing hydroxyl group.

The physicochemical properties of glutathione with some divalent 3d metals like Ni^{2+}, Co^{2+}, Zn^{2+} were studied [1]. In these complexes, glutathione takes part as hexadentate ligand coordinated to the central metal ion by oxygen, nitrogen and sulfur atoms. The complexes of glutathione with Cu^{2+} and Co^{2+} were tested for antifungal activity. The complexes with Co^{2+} are highly toxic to *Alternaria alternata* at concentration 500 ppm, and at 250 ppm the complex is toxic to *Alternaria tenuissima*. The complexes of glutathione with Cu^{2+} are toxic to *Alternaria carthami, Alternaria alternata and F usarium Sp.* [Srivastava et al., 1995]. The connection between glutathione and HIV disease has been proved *in vitro*. The low content of glutathione in the cells leads to a progress of the disease [2]. The metabolic bio activation of xenobiotics and their bonding to biological molecules can be inhibited using glutathione [3].

By the formation of the complex between glutathione and Cu(II), it has been proved that the copper ions do not bond to the peptide nitrogen, sulfur or the carboxyl group of the glycine residue [4]. The equilibrium system between VO^{2+} and oxidized glutathione in aqueous solutions was studied in the pH interval 2-11 by potentiometric titration, EPR and UV-VIS spectroscopy [5]. To characterize the complexes formed between oxidized glutathione and Al(III) in aqueous solutions, different techniques were used, e.g. potentiometric titration, NMR and electrospray mass spectroscopy. In acidic media, the aluminium ions bond to the carboxyl groups in the glutamine and glycine residues. At physiological pH, a precipitate of $Al(OH)_3$ is formed [6]. The reduced glutathione can form stable complexes with hard and soft ions of transition metals. The soft ions bond predominantly with sulfur while the hard ions bond to the carboxyl or amino group of the glutamine residue.

Uranyl complexes of glutathione formed at different mole ratios were proved by NMR, IR and UV spectroscopy. The uranyl cation binds to the carboxyl group in the form of monodentate complex while the contribution of the amino group and the sulfhydryl group to the process of complex formation is very low [7].

Glutathione reacts with various electrophilic substances and xenobiotics to form different derivatives of the mercapturic acid. These reactions are initiated by glutathione-S-transferase which catalyzes detoxification reactions.

The prevention of the oxidative stress plays a key role in the pathogenesis of many diseases, including Alzheimer, Parkinson, etc. [8].

EXPERIMENTAL

1.*Chemicals*

$Na_2MoO_4 \cdot 2H_2O$, $VOSO_4 \cdot 5H_2O$, $FeCl_2 \cdot 4H_2O$ (*Merck Germany*), $CuCl_2 \cdot 2H_2O$ (*Fluka, Switzerland*) were used. GSH (reduced) was purchased from (Fluka, Switzerland). Toluene was a product of *Lukoil Neftochim* (Burgas, Bulgaria). Toluene was purified through a method described in the literature [9]. Cyclohexene (*Fluka, Switzerland*) was purified by distillation before use. *Tert*-butylhydroperoxide (*t*-BHP) was purchased (Fluka, Switzerland). *t*-BHP was purified by vacuum distillation at 32–33^{0}C and was determined by iodometry.

2. *Preparation of metal complexes of glutathione*

2.1. *Preparation of molybdenum complex*

First, 0.2 g glutathione (6.5×10^{-4} M) was added to 20 c m^3 bidistilled water and the solution obtained was acidified with dilute HNO_3 to reach pH ~ 2.5. Then, 0.078 g $Na_2MoO_4 \cdot 2H_2O$ (3.25×10^{-4} M) was added to 20 cm^3 bidistilled water and the solution was also acidified with dilute HNO_3 to obtain pH ~ 2.5. Both solutions were mixed at room temperature under intense stirring. The precipitate obtained was filtered, washed with bidistilled water and dried to constant weight. The complexes obtained were then subjected to analysis for the presence of molybdenum (0.243 g -87.4%).

2.2. *Preparation of copper complex*

The complex between $CuCl_2$ and glutathione was prepared in aqueous-alcoholic solution at room temperature: 0.2 g glutathione (6.5×10^{-4} M) was dissolved in a small quantity of bidistilled water. The solution was added to a 20 cm^3 alcoholic solution of $CuCl_2 \cdot H_2O$ (0.055 g, 3.25×10^{-4} M). The aqueous-alcoholic solution was stirred with a magnetic stirrer for 4–6 h. The precipitate containing the complex was then filtered and washed several times with ethyl alcohol and dried under vacuum at room temperature to constant weight. The complex obtained was subjected to analysis to determine the Cu^{2+} content yield 0.23 g (90.2%). The other complexes were prepared using the same method [10]. The yields of other complexes were between 0.21 and 0.23 g (82.3–90.0%).

3. *Analyses*

3.1. *FT-IR analysis*

FT-IR spectra of glutathione and their metal complexes were taken using a B ruker spectrophotometer (Germany) FT-IR Tensor-27 in the interval 4000–400 cm^{-1}, and the samples were prepared as KBr pellets.

3.2. *Quantum-chemical calculation*

The geometric optimization of the bidentate complex compounds of Mo(VI) and some transition metal ions with glutathione in vacuum was performed using semi-empiric quantum chemical method ZINDO/1, part of the software package Hyper Chem 5.1 [11], using standard parametrization for the molybdenum atom and the transition metal ions. The structures of the molecules were preliminarily determined by the method of Molecular mechanics of the same package. The optimization algorithm of Fletcher-Reeves was applied by the quantum chemical calculations. The closed-shell molecules are usually computed within the approximation of the Restricted Hartree-Fock method, known also as the spin-restricted method of Hartree-Fock. The computation converges to the most stable electron configuration for the molecule geometry determined by the Z-matrix. After the geometric optimization of the molecules of the compounds, the geometry with the lowest energy was selected. The quantum chemical calculations were carried out by varying the lengths of all the chemical bonds, valent and torsion angles and using the optimization algorithm of Fletcher-Reeves.

RESULTS AND DISCUSSION

Fig. 1 shows the FT-IR spectra of glutathione and its complexes with Cu (№ 2) and Mo (№ 3). The characteristic absorption bands of GSH for $\nu(NH_2)$ at 3348 and 3251 cm^{-1} were not observed after the complex formation, nor were the bands of NH_3 at 3120 cm^{-1} and SH at 2524 cm^{-1}. It is well known that the band at 1714 cm^{-1} indicates >C=O in COOH. After the preparation of the complex, it was shifted to 1732 cm^{-1} [15].

It has been proved [7] that the bands at 1598 cm^{-1} and 1395 cm^{-1} can be attributed to asymmetric and symmetric valence vibrations of the carboxylate anion –COO$^-$.

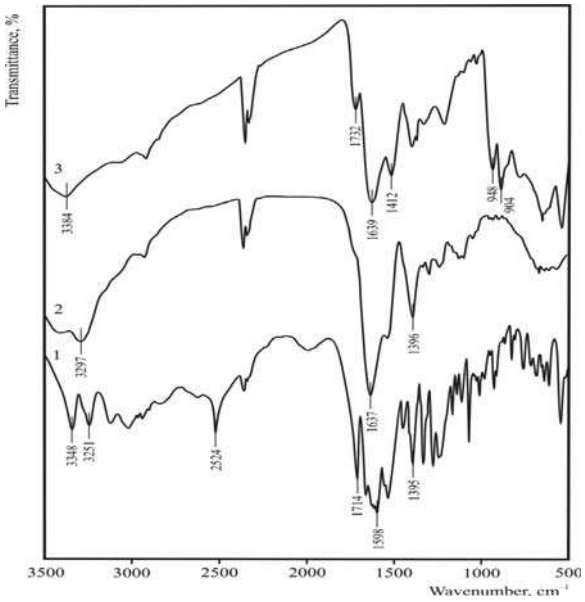

Fig. 1. FT-IR spectra of glutathione and its complexes with Cu (№ 2) and Mo (№ 3).

After the formation of the complex, these bands were shifted in the spectrum to be observed at 1639 and 1412 cm^{-1}. On the other hand, the characteristic bands at 905 and 948 cm^{-1} indicate that the complex contains molybdenyl cation Mo=O [1, 7, 12, 13, 14].

The FT-IR spectrum of the complex between GSH and Cu^{2+} is presented in Fig. 1 (№ 2). There were some significant changes observed after the formation of the complex. The absorption bands at 2524 cm^{-1} attributed to –SH and at 1714 cm^{-1} characteristic of >C=O were missing. The band at 1598 cm^{-1} corresponding to the $–COO^-$ group was shifted to 1639 cm^{-1}. The analytical band characteristic of the asymmetric valent vibrations of COO^- at 1598 c m^{-1}, was shifted to 1637 cm^{-1} after the complex formation. The spectra confirmed that Cu^{2+} ions bond predominantly with –COOH and –SH functional groups of glutathione [15].

Some probable stereostructure of bidentate complexes of glutathione with ions of transition metals, calculated by the semi-empirical method ZINDO/1 are shown in the fig.2 and fig. 3.

Fig. 2. Probable stereostructure of bidentate complex of MoO_2^{2+}-$(GSH)_2$.

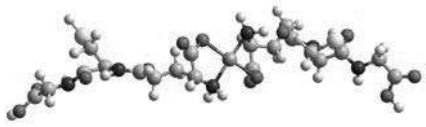

Fig. 3. Probable stereostructure of bidentate complex of Cu^{2+}-$(GSH)_2$.

Table 1. Results obtained from the calculations of the electron structure of bidentate complexes of glutathione with ions of transition metals, carried out by the ZINDO/1 method.

Complex	$E_{HOMO\ (ev)}$	E_{LUMO} (ev)	$\Delta E_{(HOMO-LUMO)}$ (ev)
Cu^{2+}-$(GSH)_2$	-5.9238	3.1256	9.0494
Fe^{2+}-$(GSH)_2$	-5.9491	4.0203	9.9694
MoO_2^{2+}-$(GSH)_2$	-7.0705	3.3599	10.4304
Ni^{2+}-$(GSH)_2$	-6.0705	5.0457	11.1163
Co^{2+}-$(GSH)_2$	-5.6129	5.5398	11.1528

Table 1 shows the energies of the highest occupied molecular orbital (HOMO) and that of the lowest unoccupied one (LUMO). They are called also boundary MO and determine to great extent the properties of the molecular system like the steric behavior by substitution of ligands and its chemical reactivity. In all coordinated compounds, HOMO orbital is composed of the atomic orbitals of the ligands. Unlike HOMO, the LUMO orbitals of all complex compounds is composed mainly from the AO of molybdenum or the transition metal and partially from the p_y-AO of the glutathione oxygen and nitrogen atoms bonded to it.

The energy difference ΔE, (ev) between the highest occupied molecular orbital (HOMO) and the lowest unoccupied molecular orbital (LUMO) showed results varying from 9.0494 for the complex of Cu^{2+}-$(GSH)_2$ to 11.1528 for the complex of Co^{2+}-$(GSH)_2$, (ev).

The values of the valent angle between the metal ion and the nitrogen and oxygen atoms of the bidentate ligand of glutathione in the structure varied from 84.2218 deg for the complex Fe^{2+}-$(GSH)_2$ to 88.8964 deg for the complex Cu^{2+}-$(GSH)_2$, which indicates the influence of the metal ion on the chelate structure.

Tables 2 and 3 show these results.

Table 2. Results obtained from the calculation of the total energy of glutathione with molybdenum (VI) and ions of transition metals - Cu(II), Co(II), Fe(II), Ni(II), arranged by the increase of energy.

Complex	Total energy (a.u)	Total energy (kcal/mol)
Fe^{2+} - $(GSH)_2$	-463.13615	-290628.128
Co^{2+} - $(GSH)_2$	-471.30658	-295755.250
Ni^{2+} - $(GSH)_2$	-481.69394	-302273.548
MoO_2^{2+}- $(GSH)_2$	-482.88124	-303018.606
Cu^{2+} - $(GSH)_2$	-493.76894	-309850.877

Based on the total energy calculated (a.u), the complexes can be arranged by their stability in the following oreder: Cu(II) > Mo(VI) > Ni(II) > Co(II) > Fe(II).

Table 3. Values of the valent angle between the metal ion with the nitrogen and oxygen atoms of complexes of glutathione.

Complex	Valent angle, O-Me-N_{35}, (deg.)	Valent angle, N_{36}-Me-O, (deg.)
Cu^{2+}-$(GSH)_2$	87.8137	88.8964
Fe^{2+}-$(GSH)_2$	84.2218	85.4442
Ni^{2+}-$(GSH)_2$	88.3475	87.4939
Co^{2+}-$(GSH)_2$	85.0503	85.9383
MoO_2^{2+}-$(GSH)_2$	84.7211	84.4849

The electronic charge distribution in a molecule, i.e. the net charges of the atoms, is also connected with the population of the molecular orbitals. If there are n_j electrons on MO χ_j (n_j = 0, 1 or 2) then the value $n_j c^2 \mu j$ ($c_{\mu j}$ – the coefficient in from of AO χ_μ on MO χ_j) is equal to (by approximation of zero differential overlapping) the partial electron population of the corresponding AO.

According to this approximation, which is used also by the method ZINDO/1, the AO of the different atoms are considered to be orthogonal and, therefore, the overlap integrals are assumed to be zero. The total population of an AO is obtained by summing the partial populations across all occupied MO in which this AO takes part. The overall population of an atom in a molecule is the sum of its populations of all of its AO.

The analysis of the populations of the atomic orbitals for the complex of Mo(VI) gave electron configuration of the valent electron layer $4d^{3.211}5s^{0.517}5p^{1.007}$. It indicates that there is significant transfer of electron density from the ligand molecules to the free orbitals of molybdenum with substantial overrating of the populations of 5s- and 5p-atomic orbitals which is typical for the semi-empirical methods.

Table 4. Oxidation of cyclohexene with *tert*-butylhydroperoxide in the presence of complexes of glutathione.

№	Complex	Cyclo-hexene oxide (%)	2-Cyclo-hex-ene-1-ol (%)	2-Cyclo-hexene-1-one (%)
1	GSH+Mo	24.5	1.2	1.8
2	GSH+V	12.4	1.9	1.1
3	GSH+Cu	5.7	5.6	1.7
4	GSH+Fe	1.9	5.8	1.7

Reaction conditions: T = 80°C; $C_{o\ Me} = 1x10^{-3}$ mmol/l; $C_{o\ hp}$ = 0.2 M/l; $C_{o\ cycloxene}$ = 2.0 M/l.
Duration: 90 min.; solvent-toluene

The experimental results of cyclohexene oxidation in the presence of the complexes obtained are presented in Table 4. As can be seen from the table, high yields of cyclohexene oxide were observed with molybdenum and vanadium complexes: 24.5 and 12.4% respectively. This confirms the literature data [16-18] where the authors maintain that the Mo(VI) complexes (including vanadium, tungsten and titanium ones) will probably be effective in epoxidation due to the heterolytic decomposition of the peroxide bond. Lower effectiveness was shown by the copper and iron complexes, where the cyclohexene oxide yield was in the range of 5.7–1.9 %.

CONCLUSIONS

Some probable stereostructure of bidentate complexes of glutathione with ions of transition metals are presented. The total energy, valence angle and populations of the orbitals for the complexes were calculated by the semi-empirical method ZINDO/1. The complexes were investigated as catalysts in the model reaction of oxidation of cyclohexene in the presence of *tert*-butylhydroperoxide. The activities of the com-

plexes obtained toward cyclohexene epoxidation can be arranged in the following order:

Mo(VI) > V(IV) > Cu(II) > Fe(II).

It was found out that only cyclohexene oxide is selectively obtained in this reaction.

REFERENCES

1. Srivastava H., R. Srivastava, Physicochemical Studies of some 3d-Bivalent Transition Metal Complexes of Glutathione (Reduced), *Journal Indian Chemical Society*, v.**72**, (1995), p. 435-438.

2. Jahoor F., A. Jackson, B. Gazzard, G. Philips, D. Sharpstone, M. Frazer, W. Heird, Erythrocyte glutathione deficiency in symptom-free HIV infection is associated with decreased synthesis rate, *American Journal of Physiology*, v.**276**, (1999), p. 205-211.

3. Takakusa H., H. Masumoto, C. Makino, O. Okazaki, K. Sudo, Quantitative Assessment of Reactive Metabolite Formation using ^{35}S-labeled Glutathione, *Drug Metabolic Pharmacokinetics*, v.**24**, (2009), p. 100-107.

4. Pedersen J., C. Steinkuhler, U. Weser, G. Rotilio, Copper-glutathione complexes under physiological conditions: structures in solution different from the solid state coordination, *Biometals*, v. **9**, (1996), p. 3-9.

5. Pessoa J., I. Tomaz, T. Kiss, P Buglyo, The system VO^{2+} oxidized glutathione: a potentiometric and spectroscopic study, *Journal of Inorganic Biochemistry*, v.**84**, (2001), p. 259-270.

6. Yang X., Q. Zhang, R. Chen, R. Shen, Speciation of Aluminum (III) Complexes with Oxidized Glutathione in Acidic Aqueous Solutions, *Analytical Sciences*, v. **24**, (2008), p.1005-1012.

7. Marzotto A., Uranyl complexes of glutathione, *Journal of Inorganic and Nuclear Chemistry*, **39**, (1977), p. 2193-2197.

8. Wu G., Y. Fang, S. Yang, J. Lupton, N. Turner, Glutathione metabolism and Its Implications for Health, *Journal of Nutrition*, v. **134**, (2004), p. 489-492.

9. Tabushi I., M. Kodera, M. Yokoyama, *J. Am. Chem. Soc.* **107**, 15, (1985), p. 4466.

10. Vassilev K., S. Turmanova, M. Dimitrova, S. Boneva, Poly (propylene imine) dendrimer complexes as catalysts for oxidation of alkenes, *European Polymer Journal*, **45**, (2009), p. 2269-2278.

11. HyperChem for Windows, Release 5.1, *Hypercube, Inc*.

12. Vassilev K, S. Tanielyan, S. Ivanov, R. Stamenova, *Oxid. Commun.*, **13**(3), (1990), p. 159.

13. Stamenova R., Ch. Tsvetanov, K. Vassilev, S. Tanielyan, S. Ivanov, Polymer-Supported Molybdenum and Vanadium Catalysts for Epoxidation of Alkenes by Alkyl Hydroperoxides, *J. Appl. Polym. Sci.*, **42**(3), (1991), 807-812.

14. Haight G.P. Jr., T. J. Huang, *J. Am.Chem. Soc* **93**(3), (1971), p.611.

15. Dimitrova M., S. Turmanova, K. Vassilev. Complexes of glutathione with heavy metals as catalysts for oxidation, *Reaction Kinetics, Mechanisms and Catalysis*, v.**99**, Issue 1, (2010), p. 69-78.

16. Sheldon R. A., Synthetic and Mechanistic Aspects of Metal-Catalysed Epoxidations with Hydroperoxides, *Journal of Molecular Catalysis*, **7**, 1, (1980), p. 107- 126.

17. Sheldon A.,: Homogeneous and heterogeneous catalytic oxidations with peroxide reagents, Book: Organic Peroxygen Chemistry, Book Series: Topics in Current Chemistry, **164**, 21, (1993).

18. Jørgensen K. A., Transition-Metal-Catalyzed Epoxidations, *Chemical Reviews*, Vol. **89**, No. 3, (1989), 431-458.

ANNUAL OF ASSEN ZLATAROV UNIVERSITY, BURGAS
BULGARIA, 2018, v. XLVII (1)

SIMULTANEOUS DETERMINATION OF CADMIUM AND ZINC IN DRINKING AND LAKE WATERS BY ANODIC STRIPPING VOLTAMMETRY

Nikolay Zaitsev, Dencho Stanev, Krasimira Stancheva, Viktoria Trifonova, Veska Shivacheva, Hristivelina Jecheva
E-mail: krasimiraangelova@abv.bg

ABSTRACT

The concentrations of Cd and Zn metal ions in drinking and lake waters were simultaneously determined with anodic stripping voltammetry technique at mercury-film electrode. The stripping peaks were obtained at –600 to –700 mV for cadmium(II) and at –900 to –1100 mV for zinc(II), supporting electrolyte 0.1 M HNO_3. The concentrate was stripped by changing the potential from –1400 to +200 mV, at a potential sweep rate 25 mV/s. The calibration graph quantitative method was used and the concentration linear ranges of Cd and Zn were in the range of 0.5–400 ppb and 0.5–500 ppb, respectively. The detection limits and quantitation limits are as follow: for Cd 0.67 μg/L and 2.23 μg/L, and for Zn 0.56 μg/L and 1.86 μg/L. This study shows the concentrations of metals determined are lower than the international permissible limits and there is no a health hazards in the consumption of water in this region.

Key words: *stripping voltammetry, cadmium and zinc determination, drinking and lake waters*

INTRODUCTION

Over the last decade, Anodic Stripping Voltammetry (ASV) has been widely used in various fields as a very versatile and powerful electroanalytical technique. This method is aimed to extend the scope of the sensitivity and selectivity of stripping analysis toward numerous analytes [1]. Electroanalytical procedures have been proposed for the determination of trace metals because they can be a valid option in the multicomponent analysis of several species; they can also be used for natural water, especially seawater [1]. The sensitivity and selectivity of these methods can be improved either by the introduction of new types of electrodes or by the development of new analytical procedures. Electrochemical methods include stripping voltammetric techniques, principally anodic stripping (ASV) and adsorptive cathodic stripping (AdSV) voltammetry, which show numerous advantages, such as minimum sample pretreatment, high speed of analysis, good performance with saline matrix, low cost, and good selectivity and sensitivity [1].

Toxic and heavy metals are the most toxic inorganic pollutants and can be of both natural and anthropogenic origin associated with various sources of harmful emissions. The effects of toxic and heavy metals are particularly pronounced in areas with developed chemical or metallurgical industries [2]. Concerns about their long-term exposure and toxic effects on human health have increased with increasing industrial use and the associated environmental pollution. Major sources of intoxication include air, soil and water [3]. In international practice, the term "environmental disease" has been officially recognized, associated with acute toxic changes in the blood, nervous diseases, and interference with the genetic structure of the cell [4]. As a result, mutagenic and carcinogenic damage to the immune system occurs.

Heavy metals include all metals with a relative atomic mass greater than 40 or more than 5 g/cm^3. Some of them, such as Cu, Zn, Mo, Co, Mn, and Fe, play an important role in the life of living organisms, others, such as cadmium, mercury, lead, etc., are not biologically necessary.

The most dangerous for human health are the heavy metals Hg, Cd, Pb, As, Ti [5]. The poisonous action of heavy metals on humans and animals is the greater the more soluble their compounds are in water and fats. Diluted, they are easier to digest and show their toxicity. The water that reaches our homes usually comes either from surface water (water from small rivers, streams or lakes) or underground water. About 80% of the tap water in Bulgaria comes

from lakes, rivers or other sources on the surface. Underground water sources and municipal wells provide about 20% and the rest are from private wells. The most common chemical pollutants in drinking water are nitrates, pesticides, petroleum products and heavy metals due to different sources [6, 7]:

The World Health Organization recommends that the maximum level of zinc in drinking water should not exceed 5 mg/L (5 ppm) as well as the maximum level of cadmium in drinking water should not exceed 0.005 mg/L (5 ppb) [8]. According to the Bulgarian State Standard [9], the basic methods for determining the metals studied are:

- cadmium - photometric and polarographic (BSS 7320-69, BSS 16777, ISO 8288);
- zinc - photometric and polarographic (BSS 15107-80, BSS 16777, ISO 8288).

Photometric methods in the presence of turbid or colored solutions are inapplicable or less applicable.

Although numerous methods are already established for detecting heavy metals, such as atomic absorption spectroscopy, atomic emission spectroscopy, mass spectroscopy and x-ray fluorescence spectroscopy, voltammetry is preferred over spectroscopic techniques due to some advantages related to their cost, simplicity and the possibility of on-site application. ASV allows simultaneous determination of several metals with sufficient accuracy and sensitivity which are characteristics of atomic absorption [10], as well as it is comparable to the sensitivity of neutron activation analysis [11]. Its resolution is greater than the standard polarographic method for heavy metal analysis in water. Examples of determinations of Cd and Zn by Anodic Stripping Voltammetry are given in the literature [12-16].

The present paper describes an ASV study for determination of cadmium and zinc in drinking and lake waters. The goal of the work is to characterize the method of ASV in terms of selectivity, accuracy, reproducibility and sensitivity for analyses of Cd and Zn in these samples. The parameters studied were: variation of pH solution, accumulation potential and accumulation time. To determine the precision, accuracy, sensitivity and linearity of the method, relative standard deviation (RSD), limit of detection and limit of quantitation were determined. The method was applied for the direct determination of Cd(II) and Zn(II) in waters at optimum condition.

EXPERIMENTAL

Instrumentation. Voltammograms are recorded using an Ekotest –VA (Ekoniks-Ekspert, RF) computer-controlled voltammetric analyzer connected to a three-electrode cell. The electrode system is a three-in-one transducer designed as a single body electrochemical cell with a polycarbon indicator electrode, an auxiliary electrode and a reference electrode located in the same plane [17-19]. The combination "3 in 1" electrode is a whole voltammetric 3-electrode cell in a single body. All component electrodes (work, auxiliary and reference electrodes) are placed coplanarly on top of the sensor. The indicator electrode surface is regenerated by polishing it with an ashless paper filter wetted with ethanol. Voltammograms are recorded in an alternating-current mode with alternating voltage amplitude. The pH is measured using an Ekspert 001, model 3 (0.1) pH meter/potentiometer (Ekoniks-Ekspert, RF) with a glass electrode.

Fig. 1. The set for measurements of heavy metals in the laboratory and field conditions.

Reagents and solutions. All chemicals (Merck, Germany, high purity >99 %) are of analytical-reagent grade and employed without further purification. Double-distilled water was used in the preparation of the various solutions. The following reagents were used: HNO_3; $Hg_2(NO_3)_2 \times H_2O$; $Zn(NO_3)_2 \times 6H_2O$; Na_2SO_3, $Cd(NO_3)_2 \times 4H_2O$. A stock solution of $Hg_2(NO_3)_2$ at a concentration of 5 g/l; a working solution of Hg^{2+} - 100 mg/L; a stock solution of Cd^{2+} - 1 g/L; a Zn^{2+} stock solution - 1 g/L. The working solutions of standard cadmium and zinc solutions having concentrations 100-500 ppb were prepared with appropriate dilution.

Analytical procedure. Water samples were filtered. Then 1 mL water sample was pipetted and transferred in glass vessel containing 25 mL

0.1N HNO_3 supporting electrolyte and 100 μg/L Hg^{2+} solution to form a Hg-film during electrolysis (7 drops of 100 mg/L $Hg(NO_3)_2.H_2O$ were put in the vessel). The electrode was immersed into the solution and the analytes were preconcentrated. The voltammograms were recorded. Consecutively, 1, 2, 3, 4, 5 m L of standard solutions of Cd and Zn (100 ppb) were added and voltammograms were recorded. The concentrations were calculated by the equations of the calibration graphs. All measurements were carried out at room temperatura and 5 duplicates.

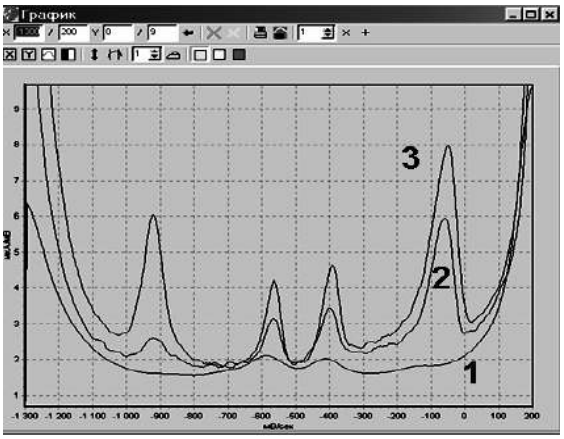

Fig. 2. Examples of measurement of zinc, cadmium, lead, and copper with the complexes «Ecotest-VA». Samples: 1 - blank, 2 - tested sample, 3 - tested sample with standard additions [16].

Table 1. Optimal conditions for voltammetric measurements with the replacement of solutions using a three-in-one transducer.

Stage of analysis	Solution composition	Potential of the working electrode, E_w, mV	The time of exposing the electrode, t_{exp}, s
1.Electrochemical cleaning of the electrode	0.1M HNO_3	+100	100
2.Formation of the mercury film	$Hg(NO_3)_2.H_2O$ 100 mg/L, 0.1M HNO_3	–600	200
3.Electrochemical preconcentration of cadmium and zinc	0.1M HNO_3 0.01M HNO_3	–600	200
4.Electrostripping of the concentrate	0.1M HNO_3 + sample	–1400…+200; potential sweep rate, 25 mV/s	300

RESULTS AND DISCUSSION

Anodic stripping voltammetry has been developed to determine the concentrations of Cd and Zn at ppb level. The preconcentration step is a key for achieving these low detection limits. During accumulation the metal is reduced and forms an amalgam in the mercury film.

1. Electrochemical deposition – preconcentration of analyte at the electrode thin film surface under forced convective conditions (stirring solution):

$M^{2+} + 2e^- + Hg = M(Hg)$

2. Quiet time – the potential is still applied, but the stirring is stopped for 30 seconds prior to analysis.

3. Stripping – the potential is scanned to oxidize the metal back to its original state:

$M(Hg) = M^{2+} + 2e^- + Hg$

Scan in the positive direction peak current is proportional to the analyte concentration.

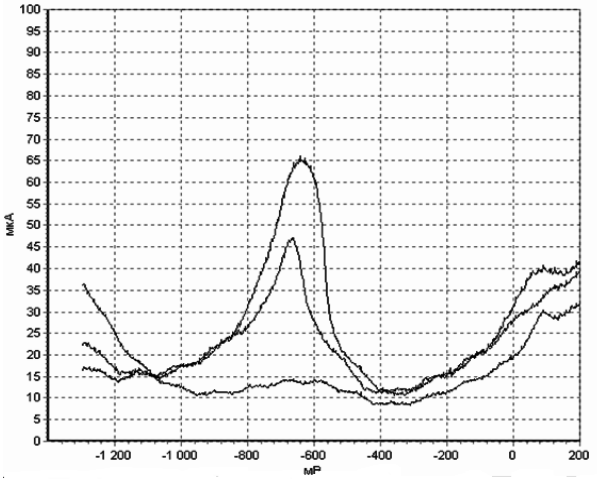

Fig. 3. Voltammograms of drinking water with additives of Cd standard solutions of 100 and 200 μg/L.

Results from the ASV show that the signals from both cadmium and zinc increased linearly with concentration. The linearity of the calibration curves obtained yielded correlation values (R) close to 1. Peak currents were obtained at the potentials between –600 and –700 mV for cadmium(II) and at –900 to –1100 mV for zinc(II), supporting electrolyte 0.1 M HNO_3 at a rate of 25 mV/s in an alternating-current mode. The optimum current range was 2–200 μA. The optimal conditions for voltammetric measurements reported earlier by us [20] are given in table 1.

Linear calibration graphs were obtained in a concentration range 10–400 μg/L for Cd^{2+}, and 10–500 μg/L for Zn^{2+}.

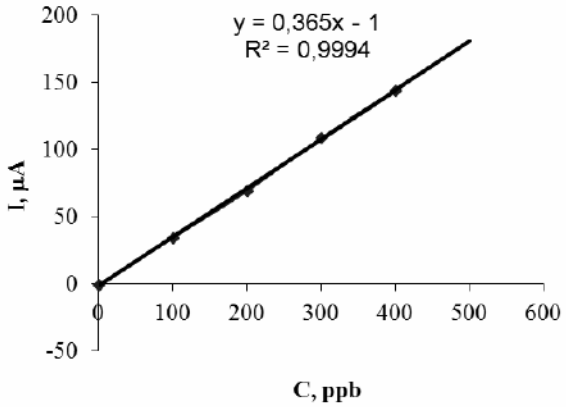

Fig. 4. Calibration graph of cadmium standard solutions.

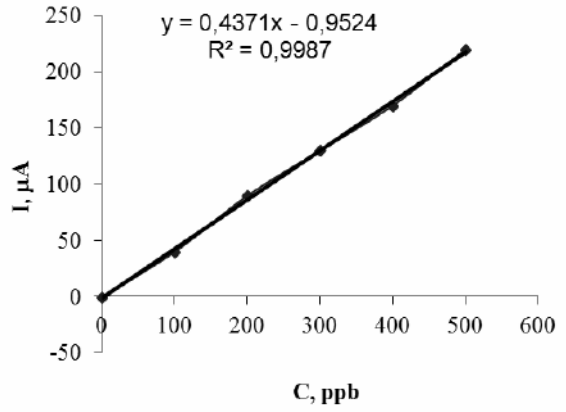

Fig. 5. Calibration graph of zinc standard solutions.

The detection limit (LOD = 3.σ/S) and quantitation limit (LOQ = 10.σ/S), where σ is the standard deviation of the reagent blank (n=5) and S is the slope of the calibration curve for cadmium ions are 0.67 μg/L and 2.23 μg/L and for zinc ions are 0.56 μg/L and 1.86 μg/L, respectively.

Table 2. Analyses of model solutions having 100 μg/L and 200 μg/L standards of Cd and Zn.

Samples	Found $\bar{x} \pm tS/\sqrt{n}$ (μg/L)	RSD $S_r = (S/\bar{x}) \times 100$ (%)
Cd addition 100 μg/L	99.8 ± 1.3	1.10
Cd addition 200 μg/L	199.4 ± 3.1	1.26
Zn addition 100 μg/L	99.6 ± 1.5	1.21
Zn addition 200 μg/L	200.2 ± 2.2	0.89

Table 3. Determination of Cd(II) in waters.

Sample	Cd(II) found $\bar{x} \pm tS/\sqrt{n}$ (μg/L)	RSD $S_r = (S/\bar{x}) \times 100$ (%)
Tap water	98.2 ± 2.7	2.21
Mineral water Hyssar	96.0 ± 3.7	3.13
Mineral water Bankya	97.6 ± 3.9	3.20
Spring water	96.8 ± 5.0	4.16
Lake water	99.2 ± 2.5	2.06

The accuracy and precision of the voltammetric procedure were verified by analyses of model solutions (table 2). The results obtained are given in table 3 and 4.

Table 4. Determination of Zn(II) in waters.

Sample	Zn(II) found $\bar{x} \pm tS/\sqrt{n}$ (μg/L)	RSD $S_r = (S/\bar{x}) \times 100$ (%)
Tap water	291.4 ± 4.0	1.10
Mineral water Hyssar	118.2 ± 6.4	4.12
Mineral water Bankya	102.2 ± 5.1	3.99
Spring water	99.6 ± 5.4	4.41
Lake water	450.0 ± 7.0	1.26

Number of determination $n = 5$; t - Students t-value at 95% probability; S - standard deviation; $\bar{x}$, an average.

Cd^{2+} was not found in any water samples. Zn^{2+} was in the order of 2.2–350 ppb in the samples, which is bellow international permissible limits.

The method proposed is easy and fast and it requires minimal sample pre-treatment. It is generally not affected by salt content. The concentrations of Cd and Zn in various water samples were found to be lower than the drinking water contamination standards issued in the World Health Organization.

CONCLUSIONS

Anodic stripping voltammetry has been developed for the simultaneous determination of cadmium(II) and zinc(II) in drinking and lake waters. Under the optimal conditions alternating-current voltammograms were recorded and the concentrations were determined by calibration graph method. The results obtained show that the method offers advantages as easy sample pre-treatment, good selectivity, sensitivity, reproducibility and linearity

REFERENCES

1. Wang, J. *Stripping Analysis-Principles, Instrumentation and Application*. *VCH, Deerfield Beach, (2006).*
2. Staykova, P. and V. Naydenova. Proceedinds of the anniversary scientific conference of ecology, Plovdiv, 2008, p. 551.
3. Enciclopedia www.greenstudentu.com/ encyclopedia/pollution. Accessed 2/17/2010.
4. Lawrence Wilson M.D. *Toxic metals in human health and disease" (© Revised, July 2008, The Center for Development)*- http://www.drlwilson.com/Articles/TOXIC%20METALS.htm
5. Stoyanov, S. *Heavy metals in the environment and food products. - Toxic damage to the person, clinical picture, treatment and prophylaxis*. *Pensoft Publishing House, Sofia, (1999).*
6. European Council Directive 98/83/EC of 3 November 1998 on the quality of water intended for human consumption, Values of Annex 1, Part B, (1998).
7. Unicef, Common water and sanitation-related diseases. (2003). Available http://www.unicef.org/wash/index_wes_related.html
8. WHO/FAO/IAEA. *Trace Elements in Human Nutrition and Health, "World Health Organization", Geneva, 1996.*
9. Manual. *Bulgarian State Standards, Ed., Standardization, Sofia, 1989.*
10. Bond, A. M. *Electroanalytical methods, ed. Scholtz, Moscow, Binom, 2006.*
11. Drugov Y.S. and A.A. Rodin. *Ecological Analytical Chemistry, St. Petersburg, Anatolia, 2002.*
12. Ensafi, A.A., T. Khayamian, A. Benvildi and E. Mirmontaz. *Anal. Chim. Acta*, **561**, (2006), p. 225.
13. Merkoçi, A., M. Vasjari, E. Fàbregas and S. Alegret. *Microchim. Acta*, **135**, (2000), p.29.
14. Martiniano, L.C., V. R. Abrantes, S. Y. Neto, E. P. Marques, T.C.O. Fonseca, L.P. Paim, A. G. Souza, N. R. Stradiotto and R. Q. Aucélio. *Fuel*, **103**, (2013), p. 1164.
15. Mahesar, S.A., S.T.H. Sherazi, A. Niaz, M.I. Bhanger, S. Uddin and A. Rauf. *Food Chem. Toxicol.* **48**, (2010), p.2357.
16. Jakmunee, J. and J. Junsomboon. *Talanta*, **77**, (2008), p. 172.
17. Zaitsev, N.K., E. B. Sviderskii and V.V. Yuritsyn RF Patent 2 239 825, (2004).
18. Zaitsev, N.K., E.A. Osipova and E. B. Sviderskii, *J. Anal. Chem.* **59**, (2004), p. 649.
19. Shvedene N.V., V.V. Sviridov, N.K Zaitsev, M.V. Roslova and I.V. Pletnev. *Moscow University Chem. Bulletin*. **67**, (2012), p. 192.
20. Zaitsev, N., D. Stanev, K. Stancheva, V. Trifonova, V. Shivacheva and H. Jecheva. *Annual of Assen Zlatarov University, Burgas, Bulgaria* **XLVI** (1), (2017), p. 7.

ANNUAL OF ASSEN ZLATAROV UNIVERSITY, BURGAS
BULGARIA, 2018, v. XLVII (1)

INFLUENCE OF DENSITY ON THE EVAPORATION KINETICS OF VOLATILE COMPOUNDS FROM WASTE WATER TREATMENT PLANTS

Ivan Chobanov, Zilya Mustafa
E-mail: ichobanov@btu.bg, zmustafa@abv.bg

ABSTRACT

The influence of density on the evaporation kinetics of volatile compounds from waste water treatment plants was investigated. Calculations for five compounds (benzene, toluene, styrene, chloroform and tribromomethane) were performed. Algorithm of US EPA was used. Kinetic curves for all investigated compounds were obtained. The results indicate that the density has a direct effect on the emissions of those compounds for which mass transfer is controlled by the gas-phase resistance (small K_G values). Density does not have a great influence on the liquid-phase controlled compounds.

Key words: *air emissions, mass transfer*

INTRODUCTION

Many different industries generate waste water streams that contain organic compounds. The organics volatilize into the air in an attempt to reach equilibrium between aqueous and vapor phases. The factors that can affect the rate of volatilization include waste water surface area, temperature, turbulence, waste water retention time in the system, the depth of the waste water in the system; the concentration of organic compounds in the waste water and their physical properties, such as volatility and diffusivity in water; the presence of a competing mechanism, such as biodegradation and so on.

When the amount of organic compounds is greater than their solubility in water then density appears to be a very important factor that affects the rate of evaporation. Hydrocarbons are non-polar and water is polar therefore the solubility of hydrocarbons in water is slight. When they are mixed, they form layers which are normally arranged according to density, with the least dense masses sitting above the more dense layers.

In this study the influence of density on the evaporation kinetics of volatile liquid compounds was investigated.

EXPERIMENT

Calculations:

The rate of volatilization can be determined by using mass transfer theory. Individual gas phase and liquid phase mass transfer coefficients (K_G and K_L, respectively) are used to estimate overall mass transfer coefficients (K and Koil) for each VOC [1-2].

The general approach that is used is described in AP-42 – a compilation of air pollution calculation methods published by the United States Environmental Protection Agency (US EPA) [3]. According to it, the first step is to calculate individual gas phase and liquid phase mass transfer coefficients K_G and K_L. These individual coefficients are then used to calculate the overall mass transfer coefficient, K. Exceptions to this procedure is the calculation of overall mass transfer coefficients in the oil phase, K_{oil}, which requires only K_G. The overall mass transfer coefficient is then used to calculate the emissions rates [4-8].
The chosen wastewater treatment equipment was a tank without aeration, biodegradation and recirculation of water. It was assumed that the tank had depth 3 m and area 700 m^2.

The used algorithm is as follows:

Calculations for water without oil film on the surface

1. Finding the equivalent diameter:

$$D_e = \sqrt{\frac{4.A}{\pi}} \quad (1)$$

Where: D_e is the equivalent diameter, m; A is water surface area, m^2.

2. Calculating the liquid phase mass transfer coefficient:

For $U_{10} > 3{,}25\ m.s^{-1}$ and $D_e/Depth < 14$ (2)

$$K_L = 10^{-6} + 144.10^{-4}.(U^*)^{2,2}.(Sc)^{-0,5};\ U^* < 0{,}3$$
$$K_L = 10^{-6} + 34{,}1.10^{-4}.U^*.(Sc)^{-0,5};\quad U^* > 0{,}3$$

Where K_L is the liquid phase mass transfer coefficient, m.s^{-1}; U_{10} is the wind speed at 10 m over the liquid surface, m.s^{-1};

Sc_L is Schmidt number on liquid side represented by the expression:

$$Sc_L = \frac{\mu_L}{\rho_L D_w} \quad (3)$$

Where μ_L is liquid phase viscosity, g.cm^{-1}.s^{-1}; ρ_L is liquid phase density, g.cm^{-3}; D_w diffusivity of constituent in water, cm^2.s^{-1}. Since the quantity of water diffused components is small (below the solubility threshold), therefore for μ_L and ρ_L the values obtained for the water have been used.

The U^* parameter (friction velocity) is calculated using the following equation:

$$U^* = 0{,}01.U_{10}.(6{,}1 + 0{,}63.U_{10})^{0,5}, m.s^{-1} \quad (4)$$

3. Calculating the gas phase mass transfer coefficient:

$$K_G = 4{,}82.10^{-3}.(U_{10})^{0,78}.(Sc_G)^{-0,67}.(D_e)^{-0,11} \quad (5)$$

Where K_G is the gas phase mass transfer coefficient, m.s^{-1}; Sc_G is Schmidt number on gas side represented by the expression:

$$Sc_G = \frac{\mu_G}{\rho_G D_a} \quad (6)$$

Where μ_G – gas phase viscosity, g.cm^{-1}.s^{-1}; ρ_G – gas phase density, g.cm^{-3}; and D_a – coefficient of component's air diffusion, cm^2.s^{-1}.

4. Calculating the equilibrium constant of liquid-vapor phase:

$$K_{eq} = \frac{H}{R.T} \quad (7)$$

Where K_{eq} is the equilibrium constant; H is Henry's law constant, atm.m^3.mol^{-1}; R – universal gas constant, which, for the above equation, has the following value 8,21.10^{-5}atm.m^3.mol^{-1}.K^{-1}

5. Overall mass transfer coefficient

$$K = \frac{K_L K_{eq} K_G}{K_L + K_{eq} K_G} \quad (8)$$

6. Concentration of contaminant in the liquid phase

$$C_L = \frac{Q.C_0}{K.A + Q} \quad (9)$$

Where: C_L is concentration of constituent in the liquid phase, g.m^{-3}; C_0 is initial concentration of constituent in the liquid phase, g.m^{-3}; Q is volumetric flow rate, m^3.s^{-1}.

7. Calculation of emission

$$E = K.C_L.A \quad (10)$$

Where: E is emission, g.s^{-1};

Calculations for water with oil film on the surface

1. Finding the equivalent diameter:

$$D_e = \sqrt{\frac{4.A}{\pi}} \quad (11)$$

Where: D_e is the equivalent diameter, m; A is water surface area, m^2.

2. Calculating the gas phase mass transfer coefficient:

$$K_G = 4{,}82.10^{-3}.(U_{10})^{0,78}.(Sc_G)^{-0,67}.(D_e)^{-0,11} \quad (12)$$

Where K_G is the gas phase mass transfer coefficient, m.s^{-1}; Sc_G is Schmidt number on gas side represented by the expression:

$$Sc_G = \frac{\mu_G}{\rho_G D_a} \quad (13)$$

Where μ_G – gas phase viscosity, g.cm^{-1}.s^{-1}; ρ_G – gas phase density, g.cm^{-3}; and D_a – diffusivity of constituent in air, cm^2.s^{-1}.

3. Calculating the overall mass transfer coefficients for oil phase:

$$K_{oil} = K_G.Keq_{oil} \quad (14)$$

Where K_{oil} is overall mass transfer coefficient for transfer of constituent from oil phase to gas phase, m.s^{-1}; Keq_{oil} is equilibrium constant or partition coefficient (concentration in gas phase/concentration in oil phase).

$$Keq_{oil} = \frac{P^*.\rho_a.MW_{oil}}{P_0.\rho_{oil}.MW_a} \quad (15)$$

Where P* is vapor pressure of the constituent, atm; ρ_a is density of air, g.cm^{-3}; MW_{oil} is molecular weight of oil; ρ_{oil} is density of oil, g.cm^{-3}; MW_a is molecular weight of air; P_0 is total pressure, atm;

4. Concentration of constituent in the oil phase:

$$C_{L_{oil}} = \frac{Q_{oil}.C^*_{0_{oil}}}{K_{oil}.A + Q_{oil}} \quad (16)$$

$$C^*_{0_{oil}} = \frac{C_0}{FO} \quad (17)$$

$$Q_{oil} = FO.Q \quad (18)$$

5. Calculation of emission:

$$E = K_{oil}.C_{L_{oil}}.A \quad (19)$$

Table 1. Values of some properties used in calculations

Properties	Value	Dimension
Air density	0.0012	g.cm^{-3}
Water density	1	g.cm^{-3}
Air viscosity	0.000181	g.cm^{-1}.s^{-1}
Water viscosity	0.00893	g.cm^{-1}.s^{-1}
Molecular weight of air	29	g.mol^{-1}
Molecular weight of water	18	g.mol^{-1}

RESULTS AND DISCUSSION

Evaporation kinetics of volatile compounds from water solutions gives information about changing of contaminants concentration and emissions with time. The calculations were performed for the following compounds: benzene, toluene, styrene, chloroform and bromoform (tribromomethane). The initial amounts of all compounds in the tank were bigger than their solubility in water, therefore in all cases there were two liquid layers in the system.

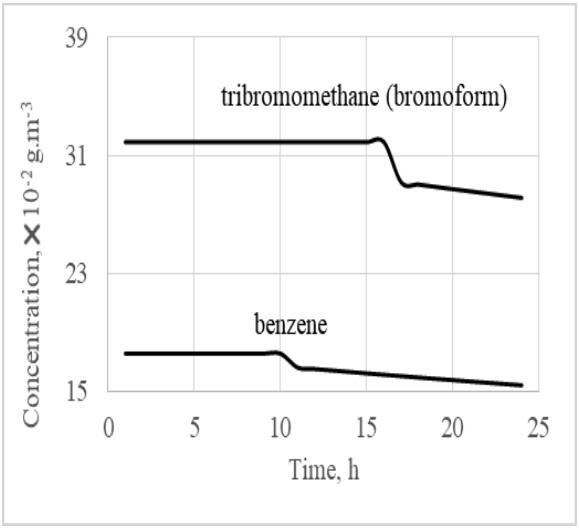

Fig. 1. Kinetic curves for benzene and tribromomethane

All obtained results can be grouped in two groups, which are presented in Fig. 1, by concentration change of benzene and tribromomethane. The density of benzene is less than the density of water and it forms an oil film on the water surface. Tribromomethane has bigger density than water and it lies at the bottom of the tank. All calculated kinetic curves have two clearly distinguished stages. The mechanism of evaporation during the first stage is different for light and heavy components. For the heavy components lying at the bottom of the tank, overall mass transfer resistance is the sum of liquid phase resistance and gas phase resistance. For the light components which form oil films on t he water surface, the overall mass transfer resistance is equal to gas phase resistance.

The mechanism of evaporation during the second stage is the same for light and heavy components because there is only one liquid phase. During this stage concentration decreases exponentially. For small periods of time this decrease can be approximated by linear function, but for long periods this is inaccurate.

Comparison of all kinetic curves shows that not all heavy compounds are affected by density. For example, chloroform is not influenced by density in contrast to tribromomethane, which is deeply affected. Therefore there is a need for analysis to determine the conditions in which compound emissions are influenced by density.

Table 2 contains the obtained results for gas phase mass transfer coefficient (K_G) and overall mass transfer coefficient (K). Analysis of the data shows that the density has a direct effect on the emissions of those compounds for which mass transfer is controlled by the gas-phase resistance (small K_G values). Density does not have great influence on the liquid-phase controlled compounds

Table 2. Results for gas phase mass transfer coefficient (K_G) and overall mass transfer coefficient (K)

Compounds	K_G, $m.s^{-1}$	K, $m.s^{-1}$
benzene	$6.817.10^{-3}$	$3.152.10^{-6}$
toluene	$6.765.10^{-3}$	$1.128.10^{-6}$
styrene	$5.904.10^{-3}$	$2.437.10^{-7}$
chloroform	$7.624.10^{-3}$	$5.312.10^{-6}$
tribromomethane	$1.583.10^{-5}$	$3.795.10^{-7}$

CONCLUSIONS

The influence of density on the evaporation kinetics of volatile compounds from waste water treatment plants was investigated. Calculations for five compounds (benzene, toluene, styrene, chloroform and tribromomethane) were performed. Algorithm of US EPA was used. Kinetic curves for all investigated compounds were obtained. The results indicated that the density has a direct effect on the emissions of those compounds for which mass transfer is controlled by the gas-phase resistance (small K_G values). Density does not have great influence on the liquid-phase controlled compounds.

REFERENCES

1. Bianchi, A. P. and M. S. Varney. *Annals of Occupational Hygiene*, **41**, (1997), p. 437.
2. Aliabadi, M., A. Aroujalian and A. Raisi. *Desalination*, **284**, (2012), p. 116.
3. EPA, AP-42, *Compilation of air pollutants emission factors*, Fifth edition, Volume I: Stationary Point and area sources, 4.3 Waste Water Collection, Treatment and Storage, Office of Air Quality Planning and Standards, Office of Air and Radiation, Research Triangle Park, NC 27711, (Last Edition - 2017).
4. Santos, J. M., V. Kreimb, J.-M. Guillot, N. C. Reis Jr., L. M. de Sá and N. J. Horan. *Atmospheric Environment,* **60**, (2012), p. 18.
5. Gebicki, J., H. Byliński and J. Namieśnik. *Environmental Monitoring and Assessment,* **188:32**, (2016).
6. Liao, Q., X. Tian, R. Chen and X. Zhu. *International Journal of Heat and Mass Transfer*, **51**, (2008), p. 1780.
7. Qasim M. and Z Shareefdeen. *Advances in Chemical Engineering and Science,* **3**, (2013), p. 57.
8. Chobanov I., R Kutsarov. *Annual Assen Zlatarov University, Burgas,* **39**, (2010), p. 63.

ANNUAL OF ASSEN ZLATAROV UNIVERSITY, BURGAS
BULGARIA, 2018, v. XLVII (1)

VACUUM METALLIZATION OF POLYMER MEMBRANES OF DIFFERENT MORPHOLOGY WITH TITANIUM

Milena Miteva, Violeta Slavova, Stoiko Petrov
E-mail:rmkpetrovi@abv.bg

ABSTRACT

Samples of polyacrylonitrile membranes with different structural and technological characteristics were surface modified with titanium deposited by vacuum metallization at different metallization periods. They were studied for permeability and selectivity towards water and a calibrant and observed by SEM. It was found out that the metal used deposited predominantly on the surface of the membranes and, depending on exposition duration, penetrates in the bulk, thus affecting the porous structure and the characteristics of the membranes.

Key words: *polyacrilonitrile, polymer membranes, modification with titanium, vacuum metallization*

INTRODUCTION

Polymer membranes are used nowadays in many branches of the industry and technological processes [1]. Various possibilities and methods of their modification are used to improve their properties and widen the range of their application [2]. Due to its specific characteristics, polyacrylonitrile is the most widely used material for preparation of membranes for UF, MF, NF [3,4], namely because of the possibilities for additional modification. Metallization is a method [5,6] successfully used for polymeric surfaces but, applied to a membrane, proceeds by entirely different mechanism depending on the conditions of the vacuum metallization, type of the metal and surface characteristics. Different metals can be deposited on the surface by metallization. Recently, titanium and its oxides attracted the interest for practical purposes and polymer membranes are being successfully metalized with TiO_2.

The aim of the present paper is to study the modifying effect of the metallization of PAN membranes of different morphologic characteristics with titanium.

It is well known that titanium is a biologically compatible material but it is known also that TiO_2 used as a modifier significantly decreases the concentration polarization on the surface of the membranes by changing it from hydrophobic to hydrophilic. It has a remarkable bactericidal effect: it decreases the total number of microorganisms, especially that of Escherichia coli**,** accompanied by a significant decrease of the permeability of the modified membranes [7,8].

EXPERIMENT

The membranes studied were prepared by the dry-wet phase inversion method with coagulant deionized water from polymeric solutions of polyacrylonitrile (PAN), product of "LUKOIL Neftochim Bourgas" Co., with concentration of 16 mass %. The solvents dimethyl sulfoxide (DMSO) and dimethyl formamide (DMF) p.a., purchased from Fluka (Switzerland), were used separately and in ratio 1:1. The sample membranes were marked I, II and III, depending on the composition of the forming solution

The surface of the membranes was preliminarily activated with alkali solutions of $SnCl_2.2H_2O$. The Ti coatings were deposited on the samples in a specially redesigned vacuum installation TITAN 22, product of SPF Vacuum technics Yambol. The vacuum chamber volume was 216 dm^3. Direct current unbalanced magnetron with permanent magnets was used. It operates with flat targets ∅100 mm and was powered by power supply providing direct current up to 10 Å at voltage up to 800V. The maximal operating temperature of the heated mass was 500^oC and it was measured by thermocouples. The magnetron sputtering of the metal was carried out at initial vacuum in the working chamber P_i= 1.10^{-3} Pa, working medium Ar with purity 99.99% and working pressure in the chamber P_w= 4.10^{-2} Pa. Three metal exposition times were employed: 5, 15 and 25 sec. After completion of

the sputtering process, the membranes were cooled to room temperature.

The selectivity (φ,%) and permeability (G, l/m^2.h) of the metalized membranes towards water and albumin as calibrant were measured on a laboratory module "Sartorius" SM-165, England. The albumin concentration was determined in the Central Scientific Research Laboratory of Prof. Asen Zlatarov University on a spectrophotometer Evolution 300 UV-VIS, product of Thermo Scientific, at wavelength λ = 280 nm. The scanning electron microscope observations were performed on apparatus JSM-5510, product of "JEOL", Japan.

RESULTS AND DISCUSSION

The selection of membranes for surface modification with titanium was made on the basis of previous studies of the working team [9,10]. The wide variety of compositions of the polymer solutions from which membranes of various structural and technological characteristics prepared by phase inversion provided a possibility to choose the ones suitable for the present study, which required membranes of different porosities. The results obtained from the study of the permeability and selectivity of the polymer membranes selected for modification which was carried out at 0.3 MPa immediately after their formation and preparation for the experiments are shown in Table 1.

Table 1. Permeability and selectivity of non-metalized membranes measured at 0.3 MPa

Membranes	G_{H2O} l/m^{2}h	$G_{alb.}$ l/m^{2}h	$\varphi_{alb.}$, %
I	716	119	91
II	119	68	90
III	143	74	93

The three membranes had permeability in a wide range, with permeability for water from 716 to 119 l/m^2 .h and for albumin from 119 to 68 l/m^2 .h. Membrane I had the highest permeability for water and albumin, followed by membrane III and the lowest values were registered for membrane II. A characteristic of asymmetric membrane porous structure is that the in-depth profile is different, consisting of a denser upper layer and a highly porous lower sublayer.

Analyzing and comparing the values for the membranes, it can be seen that the percentage values were very close. It means that substances with molecular weight higher than that of the calibrant albumin (MM 76 KDa) will be retained by the membrane surfaces equally well, which proves their asymmetric structure (Fig. 2).

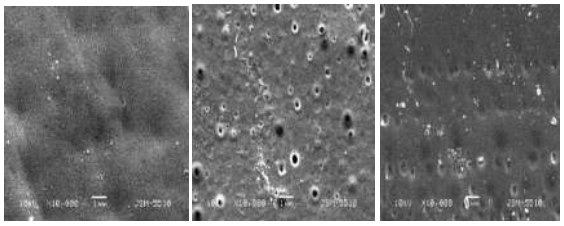

I. II. III.

Fig. 2. SEM images of membrane surface before metallization

The porosity increases gradually from the surface to the bulk of the membrane (Fig. 3). The upper layer provides predominantly the selectivity, the sublayer provides the permeability and the two together ensure the stability of the structure under operation.

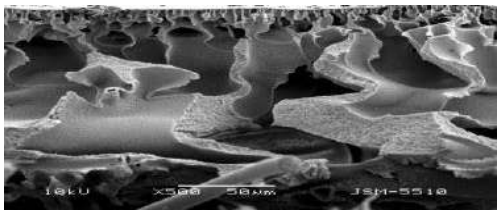

Fig. 3. SEM mage of cutoff of asymmetric membrane

The structures formed under the corresponding phase inversion conditions showed visible differences in pore sizes on the surface. Towards the calibrant, these structures showed similar efficiency with respect to selectivity (Table 1) but quite different morphological characteristics with respect to the processes of vacuum metallization.

The structural permeability of pure and metalized membranes was compared and analyzed on the basis of the hysteresis curves (Figs. 4,5,6). They were drawn using the results obtained from studies of water permeability G = f(P) under stepwise increase and decrease of the pressure from 0 to 0.5 MPa. These curves characterize the stability of the membranes and the changes taking place after their surface modification. All three membranes showed substantial decrease of

the permeability with the increase of the exposition period, i.e. with the densification of the metalizing layer. The greatest changes were observed for membrane III (Fig. 7B). This accumulation is also associated with the destruction of the selective surface of the membrane, which is the reason for the significant decrease of selectivity (Table 2). The consequences of the influence of the metalizing titanium layer, with respect to exposition period, can be confirmed by the values of the permeability and selectivity determined towards albumin and presented in Table 2.

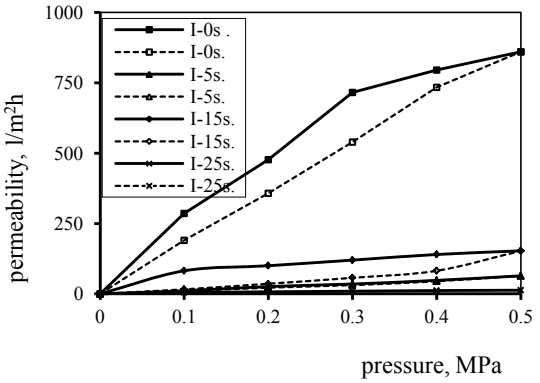

Fig. 4. Hysteresis curves of water permeability of membrane I, before and after metallization at different exposition periods

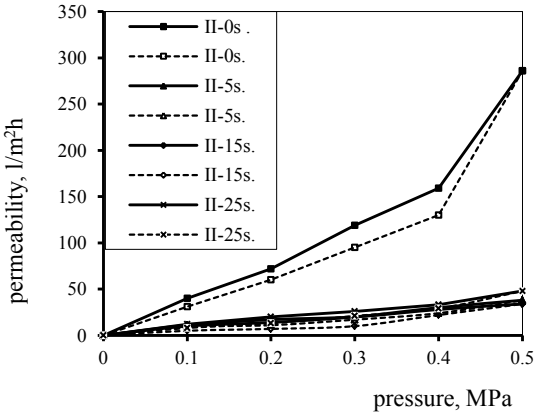

Fig. 5. Hysteresis curves of water permeability of membrane II, before and after metallization at different exposition periods

At exposition period of 5 sec (Fig. 4), the water permeability decreased to 150 - 180 l/m^2.h. At 15 sec it reached 25 - 30 l/m^2.h and at 25 sec it remained the same. Therefore, the optimal period of treatment should not exceed 15 sec. Obviously, the prolonged treatment period resulted in changes of the mechanical strength of the selective layer.

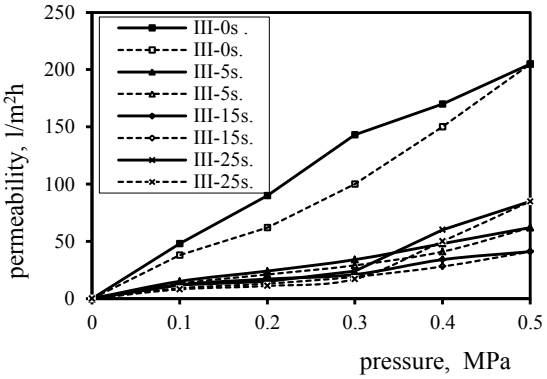

Fig. 6. Hysteresis curves of water permeability of membrane III, before and after metallization at different exposition periods

However, not with all samples the titanium coating was only deposited as a second layer which has certain effect on the values of permeability and selectivity towards the calibrant (Table 2). Depending on the metallization period, metalizing structures of different densities and different penetration in the bulk of the samples are formed.

Table 2. Permeability and selectivity of membranes metalized at different exposition periods, determined at pressure of 0.3 MPa

Membranes		**I**	**II**	**III**
5 sec	$G_{H2O,}$ l/m^{2}h	35	20	34
	$G_{alb,}$ l/m^{2}h	12	12	15
	$\varphi_{alb,\%}$	92	61	43
15 sec	$G_{H2O,}$ l/m^{2}h	120	20	21
	$G_{alb,}$ l/m^{2}h	33	11	27
	$\varphi_{alb,\%}$	90	81	24
25 sec	$G_{H2O,}$ l/m^{2}h	10	26	24
	$G_{alb,}$ l/m^{2}h	24	16	15
	$\varphi_{alb,\%}$	90	90	61

All three membrane structures changed their characteristics, with membrane III showing negative influence of the metallization on its characteristics for all three exposition periods.

The change of the selective layer of the membrane in the process of metallization was confirmed also by the changed structure studied by SEM. In the first stage, the metallization takes

place only on the surface of the selective layer (fig. 7A).

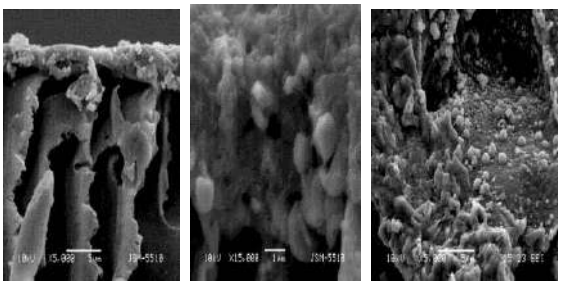

A/ B/ C/

Fig. 7. SEM images of membrane III after metallization for 5 sec (A), 15 sec (B) and 25 sec (C)

Further, the metal atoms start penetrating in depth but without reaching the selective zone (Fig. 7B). At the longest exposition, they penetrate into the pores (Fig. 7C), which leads to decreased selectivity and permeability of the membranes.

CONCLUSIONS

1. The vacuum metallization of membrane surface with titanium ions results in changes in the structure of the selective layer of the membranes and depends on pore size. At 5 sec treatment, the shortest exposition period, the water permeability decreased to 140 l/m^2.h at 25 sec treatment period, beside the decreased permeability, the selectivity also decreased to 24%.

2. Depending on the membrane structure and exposition duration, the titanium coating forms a second surface layer with different density and the selectivity remains high. The metal atoms penetrate the membrane and the pores at metallization periods longer than 15 sec.

3. The optimal duration of membranes metallization should not exceed 15 sec so that the membranes technological parameters are preserved even in the presence of the metalizing titanium layer.

REFERENCES

1. Baker, R.W., *Membrane technology and applications, John Wiley & Sons, Ltd, West Sussex, England, 2004.*

2. Drioli, E. and Giorno L., *Membrane opera-tions: innovative separations and transformations, Wiley-VCH, 2009.*

3. Fang, C.-P., Su, Y., Wan, Y.-H., *Chem Eng,* 39, (2011), p.658.

4. Lalia, B. S., Kochkodan, V., Hashaikeh, R., Hilal, N., *Desalination*, 326 (2013), p.77.

5. Kanev, M., Uzunov, Ts., Hovsepyan, P., Tehnologiya za nanasyane na pokritiya, VTU "Angel Kanchev", Ruse, 1986.

6. Zhang, G., Gao, X., Ji, S., Liu, Z., *J Membrane Sci*, 307, (2008), p.151.

7. Vatanpour, V., Madaeni, S., Moradian, R., Zinadini, S., Astinchap, B, *Sep Purif Technol,* 90, (2012), p. 69.

8. Rahimpour, A., Jahanshahi, M., Rajaeian, B., Rahimnejad, M., *Desalination*, 278, (2011), p.343.

9. Slavova, V., Poluchavane, modifikatsiya, i izsledvane na ultrafiltratsionni polimerni membrani chrez himicheska i vakuumna metalizatsiya, disertatsiya za stepen doktor, U "Prof.d-r. As. Zlatarov, Burgas, 2013.

10. Miteva, M., Poluchavane i izsledvane na poliakrilonitrilni membrani na osnova na mnogokomponentni polimerni raztvori, disertatsiya za stepen doktor, U "Prof.d-r. As.Zlatarov, Burgas, 2014.

ANNUAL OF ASSEN ZLATAROV UNIVERSITY, BURGAS
BULGARIA, 2018, v. XLVII (1)

STUDY OF THE GRANULATION OF FLY ASH FROM THERMAL POWER STATIONS

Ganka Kolchakova, Nikolay Enev, Milena Ivanova, Snejana Koruderlieva
E-mail: gkolchakova@gmail.com

ABSTRACT

The effect of the type and amount of binding substance on the yield and strength of granules prepared from fly ash was studied. The highest yield of granules was achieved with clayish slip used as binder. The granules obtained are brittle, with compression strength 0.1 MPa. The apparent density of the sintered granulates was in the range of 1200-1500 kg/m^3 and the total porosity was 55-40%.

Key words: *waste, fly ash, granulation, properties, compression strength*

INTRODUCTION

Thermal power stations (TPP) generate great amounts of various types of waste. A substantial part of them is the fly ash which is often deposited on arable land and is a major source of environment contamination [1]. It can be used for production of building materials such as additives and fillers (bricks, ceramic articles, cement, concretes, etc.), dry building mixtures, etc. [2-6].

The main direction in the production of artificial porous fillers is connected with the wide use of industrial waste materials – mainly sols and slags from TPP, wastes from metallurgy, chemical production plants, etc. [7-11].

The production of porous fillers from TPP sols helps solving problems with the utilization of natural resources, reduction of industrial wastes, development of no-waste technologies, recultivation of arable land, etc. [12].

From the analysis of numerous scientific research works, it was found that the granulation of finely dispersed ashes generated from coal combustion in thermal power stations is a perspective method for utilization of this waste material [13]. The granulation methods comprise a large group of processes for formation of aggregates of spherical or cylindrical form from powders, pastes, melts and solutions of the processed materials [14]. These processes are based on different ways of treatment of the materials.

The aim of the present work is to study the possibility for granulation of fly ash generated by thermal power stations.

EXPERIMENT

The ash used in the experiments had the following composition: mass%: SiO_2-48.32; Al_2O_3-17.90; Fe_2O_3-18.01; CaO-4.52; MgO-2.34; K_2O+Na_2O-2.40; TiO_2-0.87; MnO-0.04; LOI-5.6. The X-ray phase analysis of the ash is shown in Fig. 1.

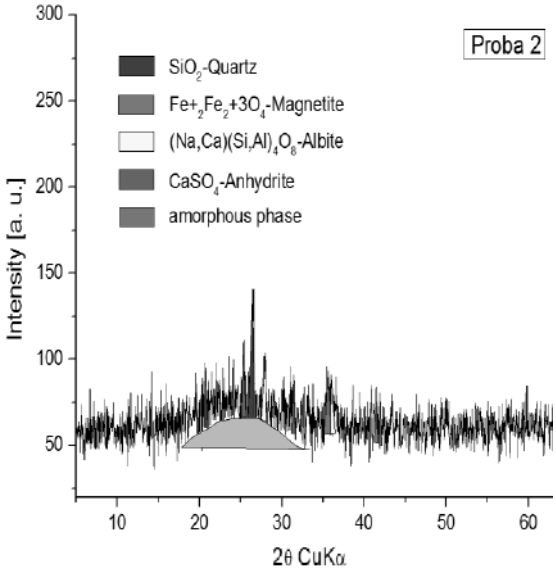

Fig. 1. Diffractogram of ash

The most intensive reflexes registered from the ash were quartz, magnetite, albite and amorphous phase.

The modulus of basicity of the ash calculated from the data on the chemical composition was 0.1, which classified the ash in the group of highly acidic substances. The ash was highly dispersed, with specific area of 8 m^2/g.

The studies of ash granulation were carried out on a drum granulator. The initial ash was mixed with the calculated amount of binding substance and homogenized. The moisture content of the resultant blend was 15-20%. The

blend obtained was then charged into the granulator and processed for 2-3 h. The granules obtained were taken out, dried in air for one day and then the granulometric composition was determined.

RESULTS AND DISCUSSION

The type and the amount of the binding substance are of special importance for the granulation process. For these experiments, 65% clayish slip and 20% aqueous solution of water soluble polymer "Laxin" were used. The results obtained are presented in Table 1.

Table 1. Fraction composition of the granules depending of the type and amount of the binding substance

Binding substance mass%	Granulometric composition, %			Yield of working fraction,%
	5-10 mm	10-20 mm	20-30 mm	
65% clayish slip				
2,5	55,2	35,6	9,2	90,8
3,5	68,3	27,2	4,5	65,5
4,5	72,4	25,0	2,6	97,4
5,5	32,5	43,3	24,2	75,8
20% aqueous solution of „Laxin				
1	62,3	13,2	24,5	75,5
2	58,3	22,4	19,3	80,7
3	69,1	22,7	8,2	91,8
4	43,4	32,8	1,8	76,2

The highest yield of granules was achieved with clayish slip used as binder.

The granules obtained are brittle, with compression strength 0.1 MPa.

According to data in the scientific literature, the strength of the granules can be increased by increasing the drying temperature to 300ºC, as well as by introducing special hardening additives.

It is advisable to use sodium phosphates because of the structural characteristics of the phosphate ions. For the experiments, $Na_5P_3O_{10}$ was used. As a binding substance, 20% solution of "Laxin" was added in amount of 1 mass%. The results obtained are shown in Table 2.

Table 2. Effect of the quantity of $Na_5P_3O_{10}$ on the yield, by fractions

$Na_5P_3O_{10}$, mass %	Yield of granules, %	Compressive strength, MPa
-	75,5	0,11
1	89,2	0,24
2	93	0,30
3	98	0,50

It can be seen from Table 2 that the addition of $Na_5P_3O_{10}$ increased the yield of granules of fraction 5-20 mm by about 15% and granules strength almost 4 times.

The effect of the sintering temperature on the tensile properties of the granules was also studied.

Aiming to preserve the initial shape of the granules, it is advisable to heat them in one layer. The sintering was carried out with granulate containing 4.5% clayish slip as binder.

The sintering was performed in a chamber super kanthal furnace „Naber" with programmable regulator for controlled proceeding of the process to temperatures 1100 and 1175°C and isothermal period of 15 min at 700°C. The heating rate employed was 25°C/min with isothermal period and the maximal temperature 0,5 h.

Figure 2 presents a photograph of the obtained granules.

The color of the non-sintered granules is grey-black. With the increase of the temperature, the granules color changed to brick-colored to red-brown (Fig. 2).

The apparent density of the sintered granulates was in the range1200-1500 kg/m^3 and the total porosity was 55-40%.

To determine the compression strength, the fraction 5 – 20 mm was used as it is the preferred one for fillers in light concretes.

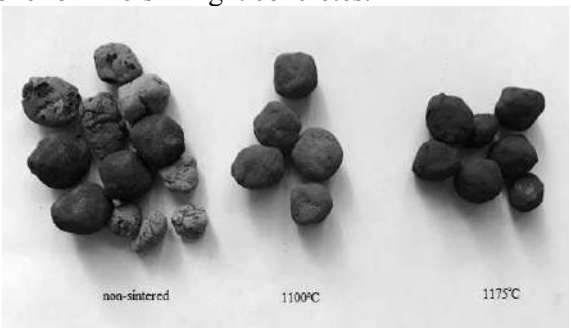

Fig. 2. Picture of the granules

At 1100ºC, the compression strength was measured to be 1.1 MPa, while for granules sintered at 1175°C it was 2.2 MPa which is comparable to the data on fillers used in construction.

CONCLUSIONS

The effect of the type and amount of binding substance on the yield and strength of granules prepared from fly ash was studied.

The highest yield of 5-20 mm sized granules was observed with binder 65% clayish slip.

The use of $Na_5P_3O_{10}$ as reinforcing additive, the yield of granules increased and their strength increased when 20% solution of Laxin was used as binder.

The sintering of the granules resulted in increased apparent density of the granules, decrease of porosity and substantial increase of their compression strength up to 2.2 MPa which is a good prerequisite for their use as a filler in light concretes.

REFERENCES

1. Pandey V. C., B. Singh, *Ecol. Eng.,* **49**, (2012), p. 190.
2. Cao J., X. Dong, L. Li, Y. Dong, *J. Eur. Ceram. Soc.,* **34**, (2014), p. 3181.
3. Qin J., C. Cui, X. Y. Cui, A. Hussain, C. M. Yang, *Constr. Build. Mater.,* **95**, (2015), p.10.
4. Zoorob S. E. , J. G. Cabrera, *Environ. Sci.*, **71**, (1997), p. 149.
5. Kockal N. U., T. Ozturan, *J. Hazard. Mater.*, **197**, (2010), p. 954.
6. Weinecke M. H., B. P. Faulkner, *Miner Eng,* **54**, (2002), p. 39.
7. Chiou I. J., K. S. Wang, C. H. Chen, Y. T. Lin, *Waste Manage.,* **26**, (2006), p. 1453.
8. Liao Y. C., C. Y. Huang, Y. M. Chen, *Constr. Build. Mater.,* **46**, (2013), p. 79.
9. Chen H. J., M. D. Yang, C. W. Tang, S. Y. Wang, *Constr. Build. Mater.*, **28**, (2012), p. 387.
10. Corrochano B. G., J. A. Azcárate, M. Rodas, F. J. Luque, J. F. Barrenechea, *Cem. Concr. Compos.*, **32**, (2010), p. 694.
11. Frankovič A., V. B. Bosiljkov, V. Ducman, *Adv. Mat. Res.,* **51**, (2017), p. 267.
12. Parab N., S. Mishra, S. R. Bhonde, *Bull. Nat. Inst. Ecol.,* **23**, (2012), p. 31.
13. Agusta H., F. N. Nisya, R. N. Iman, D. B. C. Bilad, *IOP Conf. Series: Earth and Environmental Science*, **65**, (2017), p. 012023
14. Geetha S., K. Ramamurthy, *Waste Manage.*, **30**, (2010),p, 1528–1535.

ANNUAL OF ASSEN ZLATAROV UNIVERSITY, BURGAS
BULGARIA, 2018, v. XLVII (1)

SYNTHESIS AND CHARACTERIZATION OF WILLEMITE CERAMIC PIGMENTS OBTAINED BY UTILISATION OF BIO-WASTE

Tsvetalina Ibreva, Irena Markovska, Tsvetan Dimitrov

Assen Zlatarov University, Burgas 8010, Bulgaria
E-mail: imarkovska@btu.bg

ABSTRACT

This study shows the possibility to synthesisze ceramic pigments via solid-state high temperature sintering. Willemite ceramic pigments, doped with Co and Ni as well as Fe-Zn spinel ceramic pigments were synthesized. The starting materials used for the synthesis are CoO, ZnO, CoO, Fe_2O_3, NiO and SiO_2 obtained from bio waste - rice husk ash. The optimal parameters of the synthesis process have been determined. Willemite is a mineral (zinc silicate) having a chemical formula Zn_2SiO_4. For the production of willemite ceramic pigments in the system MeO–ZnO–SiO_2 the following main materials were used: ZnO, CoO, NiO. With the addition of Fe_2O_3, both minerals willemite and iron-zinc spinel - $ZnO.Fe_2O_3$ were simultaneously synthesized. In our work, as a source of SiO_2, we used white rice husk ash, a by-product of rice milling process. The use of bio-waste as a raw material in the ceramic industry has been studied for many years due to the economical, energy-saving and environmental advantages.

The colour of the pigments was determined using a Lovibond Tintometer RT 100 Color. The willemite ceramic pigments and rice husk ash were studied by X-ray analysis, scanning electron microscopy (SEM). It has been found out that the synthesized pigments are suitable and can be successfully applied in glaze tiles and sanitary ceramics.

Key words: *CIELab color measurement, oxide additives, rice husk, willemite pigments, spinel willemite pigments*

INTRODUCTION

The object of the present study is the investigation of the possibility to obtain ceramic pigments by utilizing a widespread bio-waste: rice husk. The use of industrial waste (by-products) as a raw material in the ceramic industry has been under study for decades due to its economical, energy-saving and environmental advantages [1-7]. The combustion of rice husk in air medium results in the production of white rice husk ash (RHA). Rice husk ash contains a high amount of SiO_2, more than 90% [1]. In our work, as a source of SiO_2, we used white rice husk ash. Rice husk is waste product containing about 20% SiO_2. Rice husk is a by-product of the rice milling process. Annually, about 500 million tons of rice are processed to obtain 100 million tons of rice husk. The latter contain 70-75% organic components and the rest is inorganic components, mainly SiO_2.

Ceramic pigments are inorganic coloured, finely dispersed powders which, when added to some medium, impart certain colour and change some of its properties. Beside their colouring ability, ceramic pigments are resistant to atmospheric and chemical influences, high temperatures, decomposing activity of silicate melts and the effects of light [8-12]. These coloured inorganic substances have high coefficient of light refraction, they are insoluble in water, organic solvents and binding materials but possess the ability to disperse in them and impart specific colour.

Ceramic pigments must have the following properties: resistance to high temperatures, resistance to the eroding effects of silicate melts at the temperatures of sintering, high colour intensity, cover ability, light stability. Most of the compounds obeying these requirements are colourless. To make them play the role of pigment, they are artificially coloured by introducing substances imparting the desired colour. Such prop-

erties have the compounds of transition d- and f-elements, e.g. vanadium, iron, cobalt, manganese, nickel, chromium, copper, praseodymium, etc.

One of the most suitable materials complying with the requirements for pigments mentioned above is willemite. For this reason, it is incraesingly used for these purposes. Willemite is a mineral, zinc silicate. It was discovered in the form of small brown crystals and in 1830 was named after the King of Holland Willem I (Willem Frederik). Willemite can be green, yellow, brown, red-brown, orange and blue. It can be found in nature as small prismatic or stubby crystals. It is one of not many silicates with trigonal singony which is more characteristic of the carbonates.

In our earlier studies, we have proved the effect of CoO as an oxide imparting saturated blue colour to the willemite pigments [13]. In the present work, the efforts were focused on the effects of other oxides, e.g. NiO and Fe_2O_3, besides CoO, on the synthesis and properties of willemite pigments suitable for the ceramic industry.

MATERIALS AND METHODS

Materials

The synthesis of pigments is carried out in a solid state reaction using the following chemically pure initial materials: ZnO, CoO, Fe_2O_3, NiO. In the synthesized pigments ZnO was substituted particularly by CoO, Fe_2O_3, NiO. As a source of SiO_2, white rice husk ash was used.

Methods

The willemite ceramic pigments and rice husk ash were studied by X-ray analysis, scanning electron microscopy (SEM) as well as by CIELab, the system of colour measurement.

The X-ray analyses were carried out by the method of powder diffraction using X-ray apparatus equipped D2 PHASER AXS- Bruker, with Cu anode and K_α emission, (CuKα, λ=1.5406Å). The following operating regime was used during the experiments: current 10 mA and voltage 30 kV.

The morphology of samples was examined by scanning electron microscopy (SEM). The electron microscope photographs of rice husk were taken using scanning electron microscope Philips SEM525M/EDAX9900 with attached X-ray microanalyst. The microphotograhps were made in a regime of secondary electrons at acceleration of 20 kV.

Colour is one of the most important indicators of pigment quality. Coloured substances absorb and convert light rays of a certain wavelength into the visible portion of the spectrum, due to their atomic structure. The CIELab system defines colours not only of ceramic pigments but also of other materials, which indicates that this system is universal and widely used. In the present paper the colour determination of the pigments is determined spectrally by a tintometer of Lovibond Tintometer RT 100 Color. The colour space of the CIELab system is shown in Figure 1.

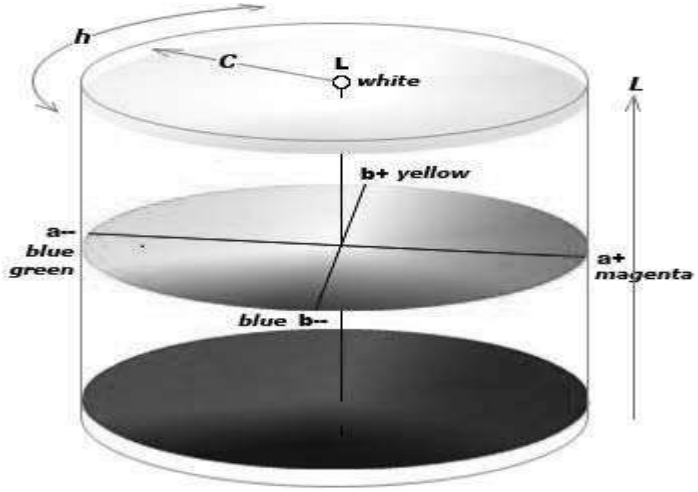

Fig. 1. The colour space of CIELab system

The colour measurements were performed using the CIELab method. This method, which is the standard analysis in the ceramic industry, especially for ceramic pigments, allows to determine the whiteness and colour degree of tiles by measuring the three parameters: L^*, a^* and b^*, where:

- L^* (brightness), from absolute white $L^* = 100$ to absolute black $L^*=0$
- a* - green color (-) / red color (+)
- b* - blue color (-) / yellow color (+)

EXPERIMENT

The composition of the samples is shown in Table 1. Quantities of the starting oxides (ZnO, CoO, Fe_2O_3, NiO) in the 100 g batch recipe are weighed to the nearest 0.1 g, then mixed and homogenized in a PULVERIZETE6 planetary

mill of FRITCH. The blends recipes are calculated as to partially replace ZnO with CoO, Fe_2O_3, NiO in the formation of the willemite. As a source of SiO_2 in the feedstocks, we added rice husk oxidized at 650°C in air: rice husk ash (RHA). The present study was carried out with rice husk obtained during processing of the Krasnodarski 424 rice variety grown in Bulgaria. The husks are arc-shaped and size approximately: 8 mm length, 2-3 mm width and 0.10÷0.15 mm thickness. The husks contain 74.5% organic matter (cellulose, hemicellulose and lignine) and water, and the rest is inorganic matter comprising 20% SiO_2 and 5.5% mixture of the following oxides: CoO, Fe_2O_3, MgO, Al_2O_3, Na_2O, K_2O, MnO_2, as well as traces of Cu and Pb [14-16]. These oxides accompanying SiO_2 play the role of a mineralizer in the synthesis of pigments.

Table 1. Composition of the samples

№ of the sample	Composition	*T*, ^{0}C
C1	$CoO.ZnO.SiO_2$	1000
C2	$CoO.ZnO.SiO_2$	1150
C3	$0.375CoO.1.625ZnO.SiO_2$	900
C4	$0.375CoO.1.625ZnO.SiO_2$	1000
C5	$0.375CoO.1.625ZnO.SiO_2$	1100
F1	$Fe_2O_3.ZnO.SiO_2$	1000
F2	$Fe_2O_3.ZnO.SiO_2$	1150
N1	$NiO.ZnO.SiO_2$	1000
N2	$NiO.ZnO.SiO_2$	1150

The synthesis of pigments was carried out by the method of solid state sintering. The sintering of the initial blends, the compositions of which are presented in Table 1, was performed in a laboratory muffle furnace at a heating rate of 6^{o}C\min and 2 h isothermal period at the final temperature. The pigments were sintered at 900^{o}C, 1000^{o}C, 1100°C and 1150°C. After sintering, additional homogenization was carried out in a planetary mill PULVERIZETE6, product of FRITCH Co.

RESULTS AND DISCUSSION

SEM analysis

Figs. 2 and 3 show the electron micrographs of Co-willemite pigments synthesized at 1000 and 1150°C.

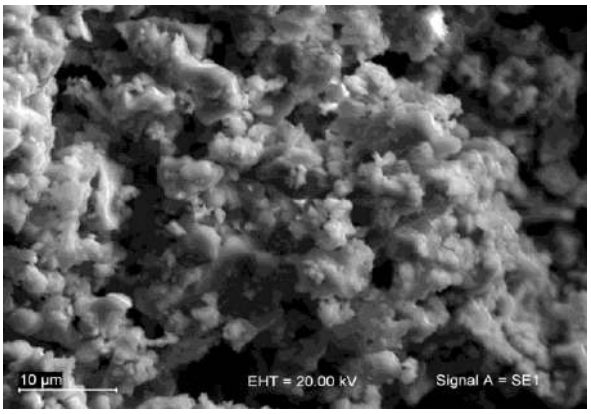

Fig. 2. SEM of Co-willemite pigments (1000^{0}C)

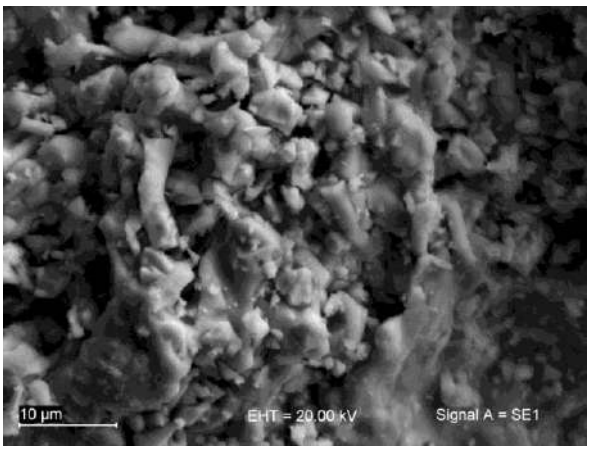

Fig. 3. SEM of Co-willemite pigments (1150^{0}C)

The particles are opaque to the electron beam, so from the photographs taken, only the shape and size of the crystals can be drawn. The great tendency of particles to aggregation is noticeable. The figures show that the samples are polydispersed and two types of crystals are observed: with a particle size of 2-5 μm and between 6 - 8 μm.

X-ray analysis

The X-ray analysis carried out showed that cobalt-willemite ceramic pigments were synthesized in the system $x.CoO.(2-x).ZnO.SiO_2$, where x=0.375 and 1.00, as well as nickel-willemite ceramic pigments in the system $NiO.(2-x).ZnO.SiO_2$, where x=1.00 (Figs. 4-7). The addition of iron resulted in synthesis of spinel pigments containing smaller amounts of willemite. (Fig. 6). The results shown in Figs. 4-7 correlate excellently with those for colour and luminance presented in Table 1.

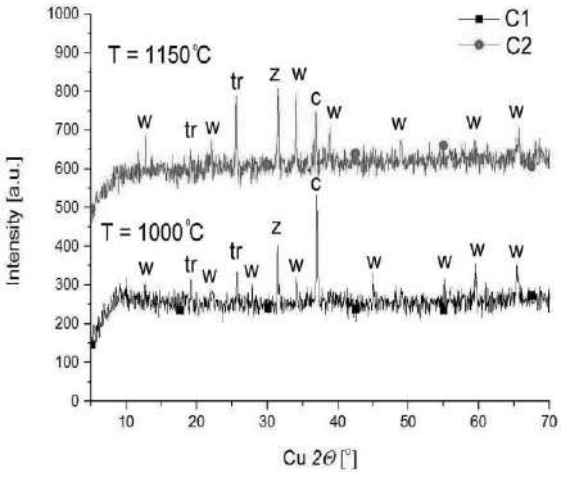

Fig. 4. XRD parents of Co-doped zinc silicate annealed at 1000 and 1150°C. Legend: w- willemite, tr- trydimite (SiO_2), z- ZnO, c- CoO

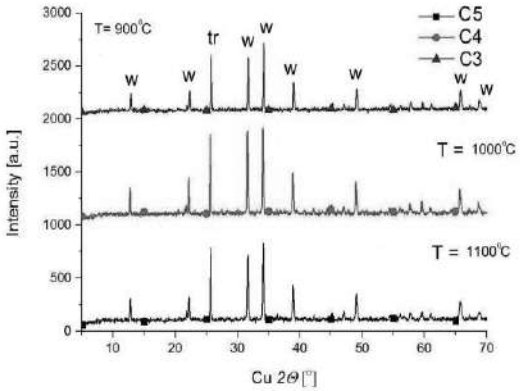

Fig. 5. XRD parents of Co-doped (0,375CoO) zinc silicate annealed at 900, 1000 and 1100 °C. Legend: w- willemite, tr- trydimite (SiO_2)

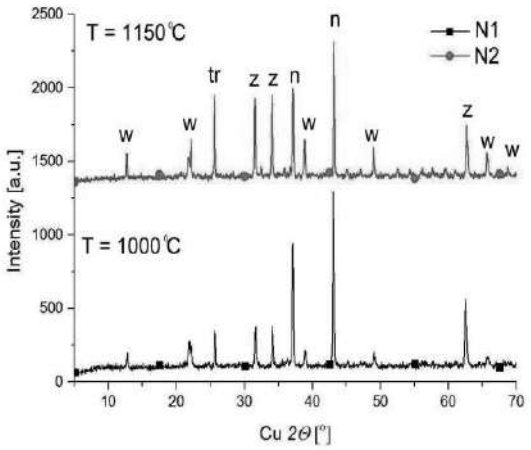

Fig. 6. XRD parents of Ni-doped zinc silicate annealed at 1000 and 1150 °C. Legend: w- willemite, tr- trydimite (SiO_2), z- ZnO, n – NiO

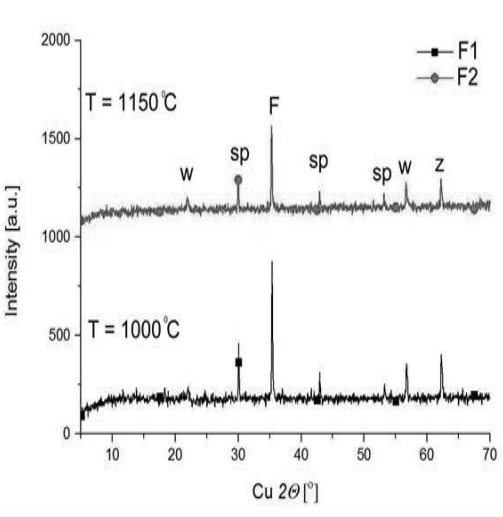

Fig. 7. XRD parents of Fe-doped zinc silicate annealed at 1000 and 1150 °C. Legend: w- willemite, sp– spinel ($ZnO.Fe_2O_3$), z- ZnO, f- Fe_2O_3

The diffraction patterns shown above (Fig. 4 - 7) indicated that it is possible to obtain willemite pigments by substitution of ZnO with CoO and NiO. It can be concluded from the four figures that the best results were obtained for the mixtures with 0,375 CoO – C3÷C5. The powder heated at 900 ^{0}C, 1000 ^{0}C and 1100 ^{0}C consisted mainly of crystalline Zn_2SiO_4 (willemite). X-ray data shows that the quality of Zn_2SiO_4 is achieved at 1000ºC – composition C4 (Fig. 5). This fact is confirmed by the work of T. Pangilinan-Ferolin and R. Vequizo [18], who studied the synthesis of zinc silicate by solid-state reaction using silica from rice husk ash (RHA). In mixture C4 sintered at 1000ºC, obviously, complete substitution of zinc by cobalt in the crystal lattice of zinc silicate was achieved to form willemite-cobaltine and this is the reason for the better values determined by the measurement of colour coordinates of the pigments (b* = - 41.24 and L*=39.08). Significant amount of cobaltine was obtained with the mixtures containing 1 mole CoO but the colour coordinates measured were worse than these for the compositions with 0,375 CoO.

With the addition of NiO in the initial mixture, a weaker interaction was observed between ZnO and SiO_2 from the rice husks and, respectively, less zinc was substituted by nickel in willemite lattice (Fig.6).

The smallest amount of willemite was obtained with the addition of Fe_2O_3 to the initial mixtures. In this case, Fe_2O_3 bonds predominantly with ZnO to form a new compound – chemically bonded spinel $ZnO.Fe_2O_3$ (Fig. 7). Most

probably, the reason for this was the preservation of the electroneutrality of the lattice.

In the system Fe_2O_3 - ZnO - SiO_2, practically brown spinel pigments with very good characteristics were obtained. The pigments synthesized at 1000°C – mixture F1 (b* =44.16, L*=53.14) had better colour characteristics. With this composition, the amount of the spinel phase predominates the willemite phase (Fig. 8). The works of Masslennikova et al. confirm our results for Ni and Fe doped pigments [19-20].

In the high temperature sintering of the four initial mixtures, beside the newly formed chemical compounds – willemite or spinel, there remained unreacted initial oxides the peaks of which can be observed in the diffraction patterns. The results obtained from the XRD analysis showed that almost all of the SiO_2 from the rice husks reacted with ZnO in mixtures C1 – C5, N1 and N2 to give willemite, while in mixtures F1 and F2 (Fig. 7) SiO_2 binds to ZnO mainly before the formation of spinel - $ZnO.Fe_2O_3$ so the willemite synthesized was less. It can be seen in all four figures 4 -7 that due to the presence of alkali impurities in the rice husks (Na_2O, K_2O), the high temperature modification of SiO_2 was α-tridymite but not α- cristobalite, as it usually occurs in practice.

Colour Measurement

One of the most characteristic properties of pigments is their colour. In this respect, one of the most important studies of pigments is connected with the determination of their colour coordinates. The colouring of the pigment occurs due to the selective absorption of certain wavelengths of light by its crystal lattice. As a result, the pigments are coloured in a color complementary to the absorbed one. Most often, the colour carriers in the pigments are the chromophores. These are atoms and atomic agglomerates which have the ability to impart one or other colour to the substances where they are present.

The results obtained for colour coordinates of the pigments synthesized from mixtures C1 – C5, F1 – F2 and N1 – N2 were determined in the system CIELab. It was found out that the best results were obtained in the synthesis of the Co-willemite pigments. The most saturated colour was that of the pigment with composition C4 (0,375CoO.1,625ZnO. SiO_2) sintered at 1000°C where the amount of blue colour measured in the CIELab system was b* = -41.24. The results shown in Table 1 indicated that the optimal temperature for synthesis of cobalt-willemite pigments is 1000°C.

The pigments synthesized which contained iron – mixtures F1 and F2 had brown colour with the values of the coordinates a* and b* decreasing with the increase of the sintering temperature – they were a* - 23,23 and b* -44,16 at 1000ºC and a* - 14,12 and b* -17,17 at 1100°C.

The colour observed for the nickel-willemite pigments was green and the amount of green colour increased with the increase of the sintering temperature (-a*) while parameter (+b*) decreased.

A tendency of decrease of luminance L* was observed for all the pigments (they became darker) with the increase of the sintering temperature.

CONCLUSIONS

Ceramic pigments were synthesized via solid-state high temperature sintering.

The optimal parameters for the process of synthesis of all initial mixtures were established.

The starting materials used for the synthesis are CoO, ZnO, CoO, Fe_2O_3, NiO and SiO_2 obtained from bio waste – rice husk ash.

It was found that the best results were obtained with the cobalt doped pigment with composition C4 (0,375CoO.1,625ZnO.SiO_2) synthesized at temperature of 1000°C. In this case, zinc was totally substituted by cobalt in the crystal lattice of the zinc silicate to form willemite-cobaltine and this stipulates the better result obtained by the measurement of the colour coordinates of the pigments where the amount of blue colour measured in the system CIELab was b* =-41.24. The same composition showed also the highest luminance (L* =39,08) and saturation of the colour.

The X-ray analysis shows that the addition of NiO to the initial mixture leads to worse substitution of zinc by nickel in the willemite lattice so the amount of willemite formed was less. The pigments synthesized had green colour.

The synthesized pigments are suitable and can be successfully applied in glaze tiles and sanitary ceramics.

REFERENCES

1. Serra, M., M. Conconi, M. Gauna, G. Suárez, E. Aglietti and N. Rendtorff. *J. Asian Ceram. Soc.,* **1**, (2016), p. 61-67.

2.Sutcu, M. and S. Akkurt. *Ceram. Int*., **7**, (2009), p. 2625-2631.
3. Quaranta, N., M. Unsen, H. López, C. Giansiracusa, J. Roether and A. Boccaccini. *Ceram. Int.,* **1**, (2011), p. 377-385.
4. Vieira, L., M. Folgueras, M. Tomiyama and S. Prim. *Mater.Sci. Forum*, **912**, (2018), p.44-49.
5. Svetlana Genieva, Annual of Assen Zlatarov University, **XLI,** (2012), p. 19-24.
6. Kumar, P., A. Srivastava, V. Kumar, M. Majhi and V. Singh, *J. Asian Ceram. Soc.,* **2**, (2014), p. 169-175.
7. Sultana, M., A. Ahmed, M. Zaman, M. Raman, P. Biswas and P. Nandy. J. *Asian Ceram. Soc*., **1**, (2015), p. 22–26.
8. Ozel, E., H. Yurdakul, S. Turan, M. Ardit, G. Cruciani and M. Dondi. *J. Eur. Cer. Soc*., **30,** (2010), p. 3319-3329.
9. Galindo, R., M. Llusar, A. Tena, G. Monros and J. Badenes. *J. Eur. Cer. Soc.,* **1**, (2007), p. 199-205.
10. Alarcon, J., P. Escribamo and J. Gargallo. *Br. Ceram. Trans. J.,* **3**, (1984), p. 81-83.
11. Carda, J., G. Monros, P. Escribano and J. Alarcon. *J. Am. Cer. Soc.,* **1**, (1989) p.160-162.
12. Klemme, S., J. Miltenburg, P. Javorsky and F. Wastin. *Am. Miner.,* **90**, (2005), p. 663-666.
13. Dimtrov, Ts., I. Markovska, Ts. Ibreva. *Eur. Un. Sci. (EUS),* **50,** (2018) p. 55-58.
14. Vlaev, L., I. Markovska and L. Lyubchev. *Thermoch. Acta,* **406**, (2003) p. 1-7.
15. Markovska I. and L. Lyubchev. *J. Therm. Anal. and Cal.*, **3,** (2007), p. 809-814.
16. Vlaev, L., I. Markovska and L. Lyubchev. *Oxidation com.,* **2**, (2004), p. 444-452.
17. Cannio, M. and F. Bondioli. *J. Eur. Cer. Soc.,* **3,** (2012) p. 643-647.
18. Pangilinan-Ferolin, T., R. Vequizo, Proceedeing of coference IETEC'13, Ho Chi Minh City Vietnam, 2013, p. 67.
19. Masslennikova., G., A. Glebicheva and N. Fomina. *Glass and Ceram.,* **8**, (1974), p. 23-25.
20. Masslennikova, G., N. Fomina and A. Glebicheva. *Glass and Ceram.*, **4**, (1975), p. 26-27.

ANNUAL OF ASSEN ZLATAROV UNIVERSITY, BURGAS
BULGARIA, 2018, v. XLVII (1)

ALKYD RESINS BASED ON GLYCEROL PHASE FROM RAPESEED OIL BIODIESEL PRODUCTION

Nikola Todorov, Krasimira Yaneva, Yordan Denev
E-mail: steel_nick@yahoo.com

ABSTRACT

The possibility for utilization of all organic substances in glycerol phase obtained from rapeseed oil biodiesel production was investigated. The complex composition of the glycerol phase (GPh –1R) was simplified through saponification and neutralization processes. Two liquid fractions crude glycerol (CGly–1R) and free fatty acids (FFA-1R) were obtained. Medium-oil alkyds ware synthesized from the CGly –1R, FFA-1R and phthalic anhydride.

The alkyd resins were obtained as 60% solutions in xylene. For the acceleration of their drying, 1% Pb and varying amounts (0.1-0.5 %) Co were added. Films cast by 50 applicators from the solutions were dried at 25±1 ◦C for 24 hours, and then were heated to 120°C for 3 hours. The physical properties (drying degree, hardness and adhesion) were studied.

Keywords: *rapeseed oil biodiesel, glycerol phase, alkyd resins, coatings*

INTRODUCTION

Biofuels are a promising alternative to fossil fuels due to their abilities - lowering greenhouse gas emissions, providing sustainable supplies of energy and creating cleaner environments. Nowadays, rapeseed is still the main feedstock for biodiesel production in Europe.

For the production of 1 ton of rapeseed fatty acids methyl esters (FAMEs), about 2.5 tons of rapeseed are needed, which requires a land area of 0.77 hectares. Biodiesel from rapeseed oil shows good stability and winter performance because the oil contains around 60% mono-unsaturated oleic fatty acids and only around 6% saturated fatty acids. New varieties contain up to 87% mono-unsaturated oleic fatty acids [1].

The main disadvantage of biodiesel is its price, which is higher than that of petroleum diesel. One possibility to reduce the price of biodiesel is the utilization of the glycerol phase (GPh). Due to its complex and unknown (varying) composition, its use is fairly limited and it already causes ecological problems [2]. The typical refining process of crude glycerol includes neutralization to remove soaps and salts, and vacuum evaporation to eliminate methanol and water. As a result, crude glycerol with a glycerol content of over 80% is obtained [3, 4].

There are many investigations into alternative uses of crude glycerol [5-11].

However, there is little information about the utilization of all organic substances in glycerol phase. Therefore, researchers are seeking applications of the glycerol phase. Among the possibilities, attention is drawn to polymer chemistry and technology [12]. Methods for the synthesis of polyurethanes [13] and polyesters [14] are known.

No data are available about the preparation of alkyds from glycerol phase in the literature. In the present work, we report the results from our investigations on the possibility for using all the organic substances in glycerol phase in alkyd resins manufacturing.

2. MATERIALS AND METHODS

1. Materials

Glycerol phase (GPh-1R) was purchased from Biogas Engineering, Bulgaria. Other materials - phthalic anhydride (PhA), methanol, potassium hydroxide, sodium hydroxide, xylene, Pb acetate and Co naphthenate, hydrochloric acid were purchased from Aldrich and used without further purification.

2. Analyses

♦ The compositions of both the GPh–1R and crude glycerol CGly–1R were determined according to the following internationally standardized methods of analysis: glycerol content – ISO

1066; content of methanol – EN 14110; water content (Karl Fischer) – EN ISO 12937; ash content – ASTM D 482; free fatty acids (FFAs) - ASTM standard method D4662-08; content of soaps – RCPL-012-B; content of soaps + FAMEs + FFAs – DGF-E- III9a; non-glycerol organic matter(MONG) content - ISO 2464.

♦ The basic characteristics of free fatty acids (FFAs-1R), obtained from GPh – 1R were determined according to the following standardized methods of analysis: iodine value -BDS EN ISO 3961:2013; Gardner color - BDS EN ISO 15305:2003; density - BDS EN ISO 6883:2014; saponification value - BDS EN ISO 3657

♦ The initial acid value of alkyds was determined by the formula:

$$Initial\ AV = \frac{56100eA}{\Sigma W} \qquad (1)$$

where *e*A - acid equivalent, W – total mass of the reagents used.

3. Simplifying the composition of the glycerol phase GPh-1R

200g GPh – 1R was filtered to remove all solid materials. Then 10 M NaOH was added until the pH reached 11. The saponification process was carried out for 60 min at temperature of 50°C. The flask content was cooled to room temperature, hydrochloric acid was slowly added until pH was 5 and the mixture was stirred for another 15 min. The obtained solid phase was filtered. Methanol and water were removed by vacuum evaporation at 60-80°C for 2 h using a rotary evaporator. Then the sample was placed in a separating funnel for phase split overnight. Two liquid layers were obtained. The light one FFAs-1R contained mainly free fatty acids (FFAs) and heavy layer CGly-1R contained mainly glycerol.

Then methanol was removed by vacuum evaporation using a rotary evaporator EV311PLUS-V. VP30 LabTech

4. Synthesis of alkyds

The calculated amount of CGly-1R was poured in a 500 ml round-bottomed flask equipped with a mechanical stirrer, contact thermometer, inert gas bubbler and Dean-Stark piece. Xylene was used as azeotropic solvent. The mixture was heated up to 120°C with constant stirring. This temperature was maintained until the water contained in crude glycerol completely evaporated.

The temperature was then increased to 170°C and the calculated amounts of FFAs-1R and phthalic anhydride were added. When the viscosity of the system started increasing, the temperature was gradually raised to 240°C and the stirring was intensified The reactions were followed with acid value (AV). The acid values were determined by titration of samples dissolved in ethanol–toluene with 0,1NKOH solution. Condensation reaction was allowed to continue until the acid value of the resin was approximately 10mgKOH/g. The alkyds were labelled as Alk-1R.

5. Preparation of films from alkyd resins and testing

The synthesized alkyds Alk-1R were cooled to 70°C and accurate amount of xylene was added to obtain 60% solutions (alkyd resins). Then hot filtration was carried out for separation of the NaCl, which is the last contaminant in the alkyd resins resulting from the use of CGly-1R and the glycerol phase.

Glass plates (150x30 mm) were degreased by dipping into petroleum ether, then the surfaces were cleaned by fine cloth, washed and whipped. The plates were washed with ethyl alcohol and allowed to dry in air.

To accelerate drying of alkyd resins, 1% Pb and varying amounts (0.1-0.5) % Co were added. Using 50μm applicator, the prepared solutions were applied on glass plates. Films were air-dried at 25°C for 24 hours and following 2 hours at 120°C. The drying degree was determined by Ericsen 415 apparatus since the results are given according to Standard EN ISO 9117-5. The hardness was determined by a Pencil hardness tester (Model- B-3084) in scale from 6B to 6H with a standard set of pencils by dragging the pencil along the films by following according to ASTM D-3363.92, 2004. The adhesion strength was measured by Cross Hatch Cutter tester according to ASTM D-3359.

3. RESULTS AND DISCUSSION

1. Simplifying the composition of the glycerol phase GPh-1R

By certified method analysis the glycerol phase GPh-1R composition was determined (Table 1)

Table 1. Composition of the Glycerol phase GPh–1R (wt.%)

Composition	Values, wt.%
Glycerol content	45,1
Content of methanol	12,8
Water content	9,8
Content of soaps	16,6
Content of soaps+FAMEs+FFAs	29,8
Ash content	2,5

The results show that the composition of GPh-1R corresponds to the specification of quality glycerol phase [15].

It can be seen (Table 1) that the glycerol content was 45.1 wt.% and the one of non-glycerol organic matter was 29.8% wt.%. Their utilization is important for the stability of the biodiesel industry and for the protection of the environment. However, their direct use for alkyd synthesis is not possible. Employing two easy chemical processes, the composition can be substantially simplified. The first one is saponification. It is carried out with aqueous solution of NaOH. For the proper completion of the process, it is necessary to keep the mole ratio NaOH/(FAMEs + glycerides) = 1,2/1. As a result from the saponification, FAMEs and the glycerides are converted to soaps (Scheme 1).

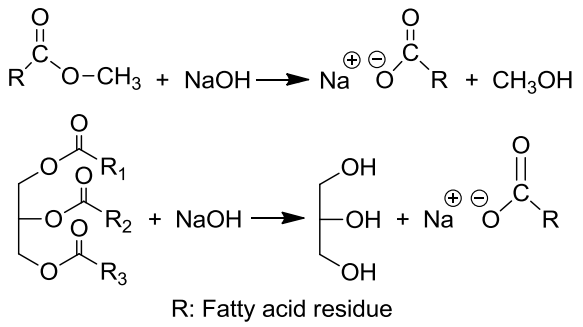

Scheme 1. Interaction of FAMEs and the glycerides with NaOH

The second process is neutralization. Hydrochloric acid was used for the present work. This process transforms the soaps into free fatty acids while NaOH reacts to give NaCl (Scheme 2).

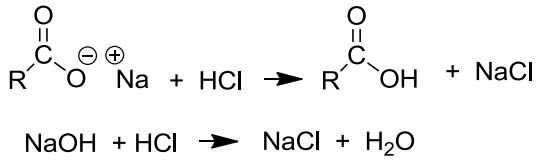

Scheme 2. Interaction of sodium hydroxide and soaps with hydrochloric acid

As a result, from the processes taking place in the liquid phase, a solid phase of salts (NaCl) was formed. NaCl is the main contaminant in the reaction mixture, it was removed by storing the solution (for about 2 hours).

The second contaminant is methanol. It was removed by distillation and can be used again in the process. Thus, the liquid phase obtained contained aqueous solution of glycerol and FFAs**.** They are mutually insoluble and quite different by relative weight. If stored overnight, they form layers. The process was facilitated by adding an optimal amount of deionized water**.** Two liquid layers were obtained. The light one FFAs-1R contains mainly free fatty acids (FFAs) and heavy layer CGly-1R contains mainly glycerol. Some basic characteristics of the two fractions were determined (Table 2).

Table 2. Some basic characteristics of the CGly-1Rn and FFAs-1R obtained from the glycerol phase.

Characteristics	value
CGly-1R	
Glycerol content, wt.%	80,4
Density at 20°C, g/cm^3	1,27
Water content, wt.%	9,4
M.O.N.G. content, wt.%	2,5
Ash content, wt.%	7,7
Gardner Color	6
FFAs-1R	
FFAs content, wt.%	98
Density at 20°C, g/cm^3	0,918
Saponification value (mg KOH/g)	171
Iodine number, g I_2/ 100 g oil	108
Average molecular weight, (g/mol)	282
Gardner Color	8

It can be seen that the fatty acids obtained were comparatively pure but a full removal of MONG and sodium chloride from the glycerol cannot be achieved.

2. Theoretical calculation of alkyds compositions

Alkyds were formulated according to Patton's gel point calculation [16]. Alkyds formulated to have FFAs content 50% were prepared with FFAs-1R, CGly-1R and phthalic anhydride. The alkyds were labeled as Alk-1R.

Table 3. Composition of the alkyds Alk-1R

Ingredient	W(g)	m0
FFAs-1R, g which contained:	51	
FFA	50	0,1773
Gly	1	0,0109
CGly-1R,g which contained:	29,1	
Gly	22,4	0,2432
Glycerides	0,3	0,0005
FAMEs+ FFAs	0,4	0,0013
PhA	33,9	0,2291
Total	108	0,6623
Separated water	7,3	

The *K* constant was 1.04 and the ratio of basic equivalents to acid equivalents (*R*) was 1.2.

3. Synthesis of alkyds Alk-1R

Alkyds Alk-1R were obtained by a one-step process (fatty acid method) taking place by the addition of CGly-1R, FFAs-1R and phthalic anhydride simultaneously into the reactor. Generally, the process can be described with Scheme 3.

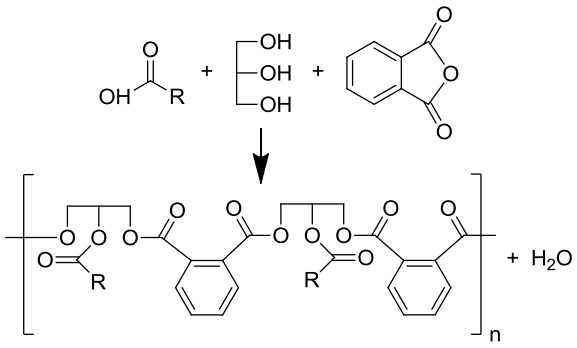

Scheme 3. Esterification reaction

Under the defined reaction conditions, may also occur with impurities in crude glycerol – FAMEs and glycerides. They can also interact under the established conditions to structure chemical bonds characteristic of the alkyds.

The alkyd reactions were followed by acid value (AV) determinations. The change of acid value with time in the process of polyesterification is shown in Fig. 4.

It can be observed that the acid value rapidly decreased in the early stages of the process, due to the interaction of the more active primary OH groups in the glycerol with phthalic anhydride. Later, the acid value decrease became slower because the primary hydroxyl groups had already interacted and the reactivity of the secondary groups was lower. The mobility of the molecules

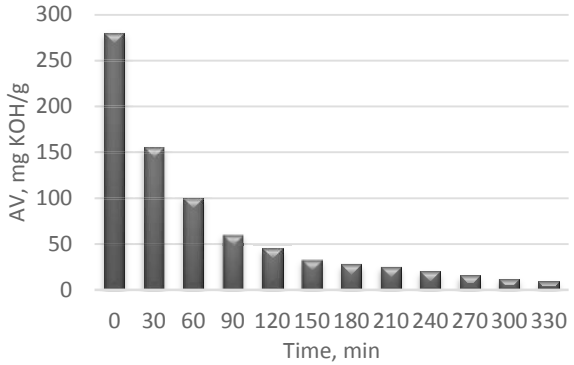

Fig. 4. The change of the acid value during reaction time.

also decreased due to their increased length and formation of branches. To activate the process, the temperature was increased from 170 to 220 - 240°C. The interaction was carried on until the acid value became < 10 mg KOH g^{-1}.

4. Preparation and testing of alkyd resin films

The synthesized alkyds were cooled to 70°C and accurate amount of xylene was added to them to obtain 60% solutions. Then hot filtration was carried out for separation the NaCl, which are the last contaminant in the alkyd resins resulting from the use of CGly 1R.

To accelerate drying, 1% Pb and and varying amounts (0.1-0.5% with respect to the dry substance*)* Co were added to the alkyd resins. The films were prepared from the solutions on glass plates using 50 μm applicator. The films were air-dried at 25°C for 24 hours and then were heated to 120°C for 3 hours. The drying degree, the hardness and adhesion were studied /Table 4/.

Table 4. Some mechanical properties of dried films, obtained with varying amounts Co accelerator.

Mechanical Property	0,1%	0,3%	0,5%
Drying degree	2	3	3
Hardness	B	HB	HB
Adhesion	4b	4b	3b

The results show (Table 4) that the optimal physico-mechanical characteristics were obtained by accelerating the drying with 1% Pb and 0.3% Co.

CONCLUSION

At present, rapeseed is the main feedstock for biodiesel production in Europe. Production of

biodiesel as a by-product produces a glycerol phase. Its utilization is a very important for stabilization of the biodiesel industry. The main purpose of this work is investigation on the possibility for utilization of all organic substances in the glycerol phase. The saponification and neutralization processes are used to simplify the complex composition of glycerol phase. Two products were obtained: crude glycerol and free fatty acids. The results showed that crude glycerol and free fatty acids can be successfully used in the synthesis of alkyds by the fatty acid method. Thin films were prepared from the obtained medium oil alkyd resins. Their drying was accelerated with 1% Pb and varying amounts of Co. Optimal physicochemical characteristics were found to have films obtained under accelerating of drying with 1% Pb and 0,3% Co.

REFERENCES

1. http://www.eubia.org/cms/wiki-biomass/biofuels/biodiesel

2. Hájek, M. and F. Skopal, Purification of the Glycerol phase after transesterification of vegetable Oils, 44th International Petroleum Conference, Bratislava, Slovak Republic, (2009), p.21-22.

3. Tan H., A. AbdulAzizn, M. Aroua, Glycerol production and its applications as a raw material:Areview, *Renew Sustain Energy Rev*, **27**, (2013), p.118–127.

4. Hájek, M.; Skopal, F. Treatment of glycerol phase formed by biodiesel production. *Bioresour. Technol*., **101**, (2010), p.3242–3245.

5. Ayoub M.and A. Abdullah, Critical review on the current scenario and significance of crude glycerol resulting from biodiesel industry towards more sustainable renewable energy industry. *Renew Sustain Energy Rev,* **16**, (2012), p.2671–2686.

6. Leoneti A., V. Aragão-Leoneti de Oliveira SVWB. Glycerol as a by-product of biodiesel production in Brazil: alternatives for the use of unrefined glycerol. *Renew Energy*, **45,** (2012), p.138.

7. Todorov N., M. Radenkov, D. Todorova, Synthesis of unsaturated polyester resins by utilization, based on PET waste and crudeglyceol, Annual of Assen Zlatarov University, Burgas, Bulgaria, v. XLI (1), (2012), p.86-91.

8. Todorov N., Utilization of Crude Glycerol and Waste Poly(ethylene terephthalate) for Production of Unsatured Polyester Resins – *International journal of scientific research, Environmental Science*, 5 (3)(2016), p.87-89.

9. Todorov N., D.Todorova, Study on the possibility to utilize crude glycerol and waste polyethylene terephthalate for production of alkyd resins, *International journal of scientific research, Environment science*, 3 (10), (2014), p.188-190.

10. Todorov N., M. Radenkov, D. Todorova, Utilization of crude glycerol and waste polyethyleneterephthalate for production of alkyd resins, *Journal of Chemical Technology and Metallurgy*, 50, 3, (2015),240-248.

11. Todorov N., B. Dzhundzhurova and Donka Todorova, Alkyd resin obtained from crude glycerol and waste polyethylene terephthalate, *International Journal of Applied Research,* 2(10), (2016), p. 101-103.

12. Hejna A., P. Kosmela, K. Formela, Ł. Piszczyk, J.Haponiuk, Potential applications of crude glycerol in polymer technology–Current state and perspectives, *Renew Sustain Energy Rev*, **66,** (2016), p.449-475

13. Li Y. Development of Polyurethane Foam and Its Potential within the Biofuels Market, *Biofuels*, **2(4)**, (2011), p. 357-359.

14. Valerio, O., T. Horvath, C. Pond, M. Misra, A.Mohanty, Improved utilization of crude glycerol from biodiesel industries: Synthesis and characterization of sustainable biobased polyesters, *Industrial Crops and Products,***78**, (2015),p.141-147

15. https://www.enviengroup.eu/images/specifikacie-kvality/g-faza/Quality-specification-of-glycerol-phase-Biodizel-Vukovar.pdf, 2015.

16. T.C. Patton, Alkyd Resin Technology, John Wiley and Sons, NewYork, USA, 1962.

ANNUAL OF ASSEN ZLATAROV UNIVERSITY, BURGAS
BULGARIA, 2018, v. XLVII (1)

MULTILAYER POLYMER FILMS BASED ON RECYCLED HIGH DENSITY POLYETHYLENE (HDPE)

Krasimira Georgieva, Yordan Denev
E-mail: krasiianeva@yahoo.com

ABSTRACT

The problem of polymer recycling is a very important stage of the global utilization strategy for waste materials. The aim of the present work is study on the possibility for secondary usage of waste high density polyethylene (HDPE) as main component in the polymer mixture with ethylene-propylene copolymer and mineral filler ($CaCO_3$). In the present work the results of characterization of multilayer polymer films based on recycled high density polyethylene (HDPE) are presented. Characterization of polymer films was performed using mechanical testing and spectroscopic IR-methods. The recipes for blends obtaining optimal properties were proposed. The results of present study show a perspective possibility for utilization of huge amounts of waste HDPE as main component in multilayer films with good characteristics, suitable for packaging purposes of foods.

***Key words**: HDPE, polymer blends, recycling, multilayer film, mechanics, FT-IR*

INTRODUCTION

High density polyethylene (HDPE) is widely used due to its low price, good processing, high impact strength, excellent chemical resistance and good electrical insulating properties [1]. The widest usage of high density polyethylene (HDPE) and low-density polyethylene (LDPE) found as packaging films, is mainly for food products [3-5]. The scientific developments and application progress in the field of polymer mixtures in the past two decades are extensive and mixing is economically more effective than developing new polymers [6-8]. Polyolefins are usually modified by the addition of elastomers in order to improve their properties at low temperatures as well as their relative elongation [9-11].

The extensive production of HDPE, which accounts for 17.9% of the world production of polymers, has lead to the deposition of colossal quantities of these materials as waste, and at present, in the world about 26 million tons of HDPE are thrown away annually, but only 8 million of them are subject to recycling and secondary processing [12-14]. The aim of the present work is to study and prove the possibility for utilization of waste high density polyethylene (HDPE) as a component of a polymer mixture used as a core layer in the manufacture of multilayer films with good barrier characteristics.

EXPERIMENT

The main materials used for the production of the multilayer films, which are the subject of research, is high density polyethylene (HDPE), linear low density polyethylene (LLDPE), polyamide (PA), ethylene-propylene copolymer (EPDM), adhesive, filler ($CaCO_3$) and masterbatch. The characteristics of these components mixed in different mass ratios in the developed formulations are presented in the list below.

1. High Density Polyethylene (HDPE) Mark „HIPLEX“ TR 130, produced by „PetroHemija“;
2. Polyamide Mark Ultramid C40 LN 01, produced by BASF;
3. Ethylene-Propylene Copolymer Mark Vistamaxx 6102FL, produced by ExxonMobil;
4. Linear Low Density Polyethylene (LLDPE) Mark Aramco LLDPE F2111BS, produced by Aramco Trading;
5. Adhesive – Ethylene-Acrylic Acid, Primacor 1321, produced by Dow Chemical Company;
6. Mineral Filler - $CaCO_3$ Mark Schulcarb 380AR, produced by A. Schulman;
7. Masterbatch PE Blue B1337.

Table 1 presents the components and their mass ratios in the developed polymer mixtures for production of multilayer films.

Table 1. Components and recipes of multilayer films

Base Layer (Core Layer)	
Component	mass, %
HDPE, %	70/0
R-HDPE, %	0/70
Vistamaxx, %	0 – 15
Filler, %	0 – 10
LLDPE, %	0 – 20
R-PAPE, %	12
Adhesive, %	3
Side Layer (Skin Layer)	
Component	mass, %
MDPE	82
LLDPE	15
Blue	3

The structure of a multilayer film in terms of location and the thickness of individual layers is as follows: 1/3/1. The average thickness of the resulting three-layer film is 24 μm. Mechanical tests were conducted according to the standard BS ISO 527.3 on Lloyd Instruments Ltd JJ apparatus, Machine Type T5000. Research on the mechanical properties was carried out, preparing the tensile specimens of multi-layer films, in the direction of extrusion of the film (parallel to the direction of extrusion) – MD (machine direction), and in a direction perpendicular to this direction – TD (transverse direction).The infrared spectroscopy studies were carried out in the middle infrared region (4000-400 cm^{-1}) on Bruker Tensor 27 apparatus. Spectra were recorded in the mode of transmission, then held for the purpose of processing, eliminating the influence of moisture and CO_2, recalculated and displayed with the absorption mode. For the processing of the spectra OPUS 6.5 software application was used.

RESULTS AND DISCUSSION

The typical three-layer film structure consists of a base layer (layer core) and a two-side layer (skin layers). The packaging industry usually requires films that can be printed on and this is normally done thermally. The most typical polymers for the printed layer are low density polyethylene (LDPE), polypropylene (PP) or ethylene vinyl acetate with linear low density polyethylene (LLDPE). The important factors in the choice of a printable layer are good heat resistance, high speed printing, economic considerations, the temperature of ignition of the printing and coefficient of friction.

The main task in the study of polymer blend composition is to establish the influence of individual components and the nature of HDPE (neat and recycled). First, completely identical mixtures containing 70% neat HDPE and 70% recycled HDPE were prepared. The final film structure was prepared with the side layers using a joint blow extrusion production method. The mechanical properties of the resulting films depending on the nature of the HDPE are presented in Table 2.

Table 2. Comparative values of mechanical properties of blends based on neat and recycled HDPE

Tensile Strength, MPa	70 % neat HDPE	70 % r-HDPE
MD	40.0	34.5
TD	33.6	32.3
Relative Elongation, %	70 % neat HDPE	70 % r-HDPE
MD	350	350
TD	490	490

The results show that the values of the relative elongation keep constant, which might be an indication that the ongoing processes in the course of the secondary treatment do not affect the length of the macromolecules substantially and the molecular-mass distribution in recycled material, and the changes are more of a structural nature. Confirmation of this hypothesis is the almost negligible change in the value of the tensile strength in direction TD.

The influence of the main components in the middle layer (core) of multilayer films, the amount of the elastomeric component (ethylene-propylene copolymer) and quantity of the imported mineral fillers ($CaCO_3$) were examined. Polymer mixtures were prepared in which the quantity of ethylene-propylene copolymer is in the range from 0 to 15 mass %, as well as mixtures containing mineral filler $CaCO_3$ in the interval of 0 to 10 mass %. In all the above described polymer blends the amount of recycled HDPE is 70 mass %.

The side layers (skins) possessed small constant thickness and its effect was not taken into account during the characterization processes. The dependence of the tensile strength of the core layer of the film as a function of the quantity of the imported ethylene-propylene rubber

copolymer was studied [15]. The changes of tensile strength in both directions of deformation (MD and TD) are presented in Fig. 2.

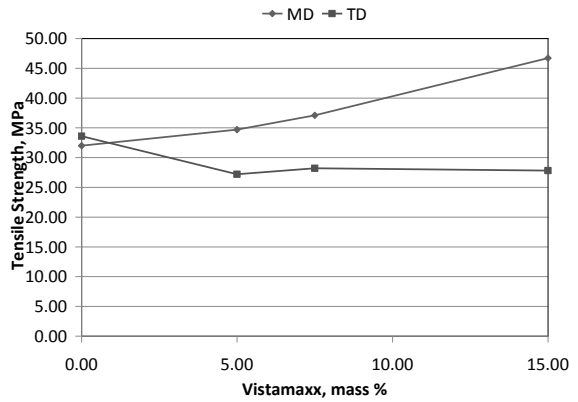

Fig. 2. Tensile strength of the film as a function of contained ethylene-propylene copolymer

In direction MD the tensile strength grows monotonous, while in the perpendicular direction TD the values are lower and maintain a constant value after an imported quantity of ethylene-propylene copolymer of 5 mass %. A slight decrease in the tensile strength after the addition of 7.5 mass % ethylene-propylene copolymer was observed.

This fact proves the optimal quantity of the imported ethylene-propylene copolymer: 7.5 mass %. The dependence of the values of the relative elongation at the break time of the film as a function of the quantity of contained ethylene-propylene copolymer was studied and the results are shown in Fig. 3.

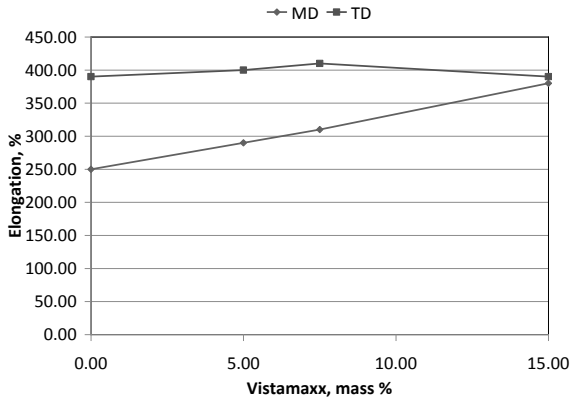

Fig. 3. Relative elongation of the film as a function of contained ethylene-propylene copolymer

Ethylene-propylene copolymer has flexible macromolecules with a typical rubber behaviour. With the increase of its amount in the polymer blend the relative elongation at break in direction MD increases its value by more than 50 %, reaching up to 370 % on added amount of 15 mass %. At the same time the relative elongation in direction TD has a strong extreme behaviour. In a narrow range the elongation passes through a maximum at addition of ethylene-propylene copolymer in the amount of 7.5 mass %.

From the results for the mechanical properties as a function of imported ethylene-propylene copolymer it can be strongly argued that the core layer of the film based on recycled HDPE must contain 7.5 mass % of ethylene-propylene copolymer.

The dependence of the core layer tensile strength as a function of the quantity of the imported mineral filler ($CaCO_3$) was analyzed and the results for both testing directions (MD and TD) are presented in Fig. 4.

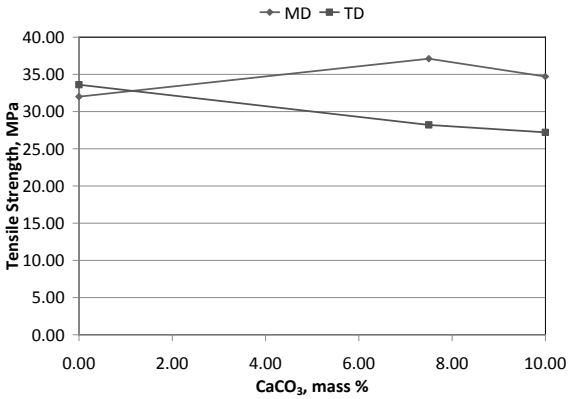

Fig. 4. Tensile strength of the film as a function of contained mineral filler

The tensile strength in MD direction has a maximum at 7.5 mass % $CaCO_3$, while in direction TD the values decrease monotonically for the whole reinforcement interval. The tensile strength lowering is fully anticipated and logical regarding the material inhomogeneity caused by the introduction of mineral phase of a totally different chemical nature. The main problems of the phase boundary polymer-filler are related to the structure of the border polymer layer surrounding the filler particles.

The relative elongation as a function of the quantity of the imported $CaCO_3$ is illustrated in Figure 5. It is known from the polymer reinforcement theory that the introduction of mineral fillers severely disrupts the lyophilic-lyophobic balance in the resulting composite, which is most significantly reflected in sharply lower values of

relative elongation, even at low degrees of reinforcement.

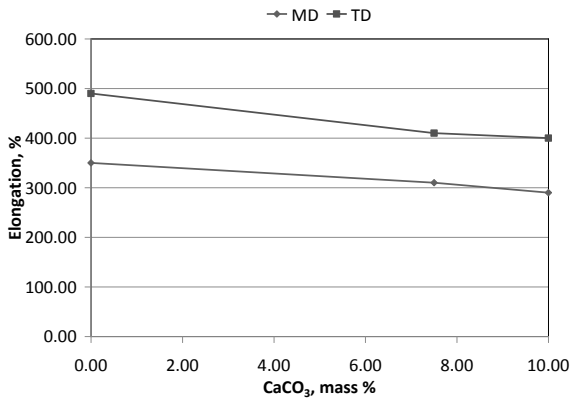

Fig. 5. Relative elongation of the film as function of contained mineral filler

The obtained results confirm the theory and the rapid decrease of relative elongation at reinforcement degree of 7.5 mass % and further change is almost insignificant. In the complex analysis of tensile strength and relative elongation data, as a function of the filler amount, it is concluded that the optimal degree of reinforcement with $CaCO_3$ is 7.5 mass %.

As a result of the studies, the optimum formulations of polymer mixtures are determined. They have nearly the same values as those based on neat HDPE. The recipes of polymer mixtures used as a core layer are presented on Table 3.

Table 3. Recipes of multilayer films with optimal properties

Base Layer (Core Layer)			
Component	Sample 1	Sample 2	Sample 3
HDPE, %	70	-	-
R-HDPE, %	-	70	70
Vistamaxx, %	-	7.5	5
Filler, %	10	7.5	10
LLDPE, %	20	-	-
R-PAPE, %	-	12	12
Adhesive, %	-	3	3
Side Layer (Skin Layer)			
Component	Sample 1	Sample 2	Sample 3
MDPE	82	82	82
LLDPE	15	15	15
Blue	3	3	3

HDPE is a representative of semicrystalline thermoplastic materials and in the recycling technology it is of practical interest in view of the change in the crystallinity degree of homopolymers, as well as of mixtures with ethylene-propylene copolymer and $CaCO_3$.

Some aspects of the structural behaviour of polymers can be analyzed using data from FT-IR spectroscopy [17, 18].

The IR-spectra of the multilayer films based on the optimal recipes are presented in Fig. 6.

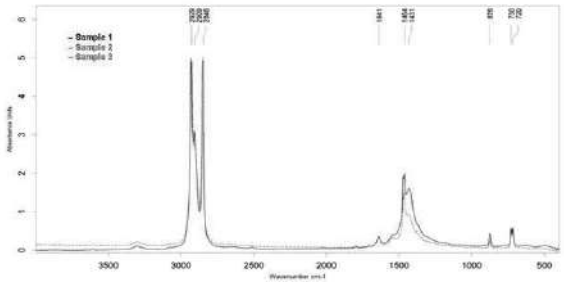

Fig. 6. IR-spectra of multilayer films in the range 4000 – 400 cm^{-1}

A well known method for the determination of polyolefins crystallinity degree using methods of FT-IR spectroscopy can be found in the literature [19, 20].

The procedure consists of calculating the ratio of the characteristic absorption band for crystal area in 730 cm^{-1} to the absorption band associated with the amorphous area in 1268 cm^{-1}.

The degree of crystallinity was calculated using the following equation:

$$\chi_C = \frac{A_{c(730)}}{A_{a(1268)}} \quad (1)$$

The calculated values for crystallinity degree are presented in Table 4.

Table 4. Calculated values of crystallinity degree

Polymer film	χ_c, %
Sample 1	52
Sample 2	49
Sample 3	40

The calculated values for crystallinity degree have the highest value in the absence of recycled HDPE modification with ethylene-propylene copolymer or mineral filler. The value of 52 % is significantly reduced compared to the high crystallization tendency of polyolefins which increases to 70 – 80 % regarding the processes of

destruction of the crystal formations in the secondary polymer processing.

The addition of a highly amorphous component, such as ethylene-propylene copolymer, lowers the degree of crystallinity (to 49% in Sample 2) and the polymer cold flow limit. The amount of crystal phase of $CaCO_3$ in Sample 3 is the highest, but the crystallization of polymer matrix leads to a sharp decrease and reaches crystallinity degree of only 40 %.

CONCLUSIONS

Polymer mixtures containing 70 mass % recycled HDPE and different ratios of other components (ethylene-propylene copolymer and mineral filler) are developed. Three layer extruded films were produced and mechanical testing and spectroscopic characterization were carried out. A study the influence of the quantity of the components on the mechanical properties of polymer blends was performed. It was proved that the optimal mechanical properties, closest to the usage of neat HDPE, are obtained in the polymer mixture containing: recycled HDPE – 70 mass %, ethylene-propylene copolymer – 7.5 mass % and mineral filler ($CaCO_3$) – 7.5 mass %. Through a computational procedure based on the IR spectroscopy data multilayer polymer films were structurally characterized and their crystallinity degree was calculated.

REFERENCES

1. Mark A. Spalding and Ananda Chatterjee. *Handbook of Industrial Polyethylene and Technology: Definitive Guide to Manufacturing, Properties, Processing, Applications and Markets Set, Wiley-Scrivener, 2017.*
2. Cantor K. *Blown Film Extrusion, Carl Hanser Verlag, Munich, 2011.*
3. Morris B. *Science & Technology of Flexible Packaging, William Andrew Publishing, 2016.*
4. Wagner J. *Multilayer Flexible Packaging, William Andrew Publishing, 2016.*
5. Butler, T.I. & Morris, B.A. *Chapter 15 - PE based multilayer film structures, in: Wagner, J.R. (ed.), Multilayer Flexible Packaging, William Andrew Publishing, 2016.*
6. Muralisrininivasan. *Polymer Blends & Composites, 2017.*
7. Paul D, S. Newman. *Polimernye smesi, Mir, Moskva, 1981.*
8. Robeson L. *Polymer Blends, Hanser, 2007.*
9. Abitha V.K. and A.V.Rane. *A review on EPDM/ polyolefinic blends and composites, Research & Reviews in Polymer Review.* **5(3)**, (2014), p. 102-114.
10. Penava N.V., V. Rek and I. F. Houra. *Effect of EPDM as a compatibilizer on mechanical properties and morphology of PP/LDPE blends, Journal of Elastomers & Plastics*. **45(4)**, (2012), p. 391–403.
11. Tall S., S. Karlsson, Ann-Christine Albertsson. *EPDM elastomers as impact modifiers for contaminated recycled HDPE, Polymer and Polymer Composites*. **5(6)**, (1997), p. 417-422
12. Mantia F. *Vtorichnaya pererabotka plastmass, Moskva, 2006.*
13. WRAP Large Scale HDPE Recycling Trial Report.
14. Francis R. *Recycling of Polymers: Methods, Characterization and Applications, John Wiley & Sons, 2016.*
15. Zhao L., P. Choi. *A Review of the Miscibility of Polyethylene Blends, Materials and Manufacturing Processes*. **21(2)**, (2006), p. 135-142.
16. Ishida, H. *Fourier Transform Infrared Characterization of Polymers, 1987.*
17. Stuart B. *Chapter 6. Polymers, in: Infrared Spectroscopy: Fundamentals and Applications, 2005.*
18. Eidelman N. and C. G. Simon, *Characterization of Combinatorial Polymer Blend Composition Gradients by FTIR Microspectroscopy, Journal of Research of the National Institute of Standards and Technology*. **109**, (2004), p. 219-231.
19. Rabek Y. *Eksperimentalniye metody w himii polimerov, Mir, Moskva, 1983.*
20. Thomas S., *Characterization of Polymer Blends, Wiley, 2014*

ANNUAL OF ASSEN ZLATAROV UNIVERSITY, BURGAS
BULGARIA, 2018, v. XLVII (1)

DETERMINATION OF HYDRODYNAMIC PARAMETERS OF FIBER SORBENTS

Aleksandar Dimitrov, Dimitrinka Ivanova, Stela Naydenova, Marina Dimitrova, Dimitar Gogov
E-mail: al_dim_2000@abv.bg

ABSTRACT

At different flow rates, the hydrodynamic properties of the fixed layer of fibrous adsorbent were investigated with high content of silicon dioxide, with different fiber lengths, and varying degrees of layer density. The parameters of the layer were defined: porosity, equivalent diameter of the channel and specific geometric and usable surfaces.

***Key words**: flow rate, hydrodynamic, fibrous adsorbent, channels, usable surface*

INTRODUCTION

The implementation of multiple technological processes requires the intensification of the accompanying adsorption ones. This requires the development of materials which have both high absorption capacity and a small bulk density, high thermal and chemical resistance. The materials that could satisfy this set of requirements are fibrous sorbents: active carbon fibers [1-3], synthetic fiber-based chemosorbents [4] and inorganic fibers with high silica content [5, 6].

Characteristic of fibrous adsorbents with a high silica content is that they are distinguished by high velocity and completeness of adsorption-desorption processes related to many substances - water vapors, ammonia, oxides of nitrogen and sulfur [7-11], etc.

The purpose of the present study is to investigate the hydrodynamics of a fixed layer of high density silica adsorbent.

EXPERIMENT

The hydrodynamic studies were conducted in laboratory conditions. For a fixed layer of adsorbents fibers with a high content of silica [6] - samples 1 to 4, synthetic zeolite 3A with spherical and cylindrical form - samples 5 and 7 and natural zeolite (clinoptilolite) with irregular shape - sample 6 were used. Compressed air which passes through a gear-filter, rotomer and enters a model of organic glass tube was also used. The adsorbent hydrodynamic characteristic was determined and deposited on a grid whose resistance was commensurate with the layer resistance. Sensors before and after the layer received impulses that were recorded with a differential pressure gauge. To limit the influence of wall effect, the diameter of the model tube was 0.005 m, as a result of which the tube diameter was 30 times and more larger than the particle diameter. The different bulk density of the fiber adsorbent layers was achieved by wetting the fibers during sample loading, bending - fixing the height of the layer and then drying it using warm air.

RESULTS AND DISCUSSION

Fibers with high percentage of silicon dioxide are adsorbents with a microporous structure, which is predetermined by the microheterogenic structure of the starting glass fibers and by the peculiarities of their way of production. The results of the study are presented in Tables 1 and 2 and Fig. 1. A comparative characteristic of the parameters of the fixed layer formed by adsorbents with fibrous, spherical, cylindrical and irregular shape is made. The selection is not random. Typical for all of these is that they have a microporous structure and close structural-sorption characteristics.

The main structural features of the fixed layer are its porosity and specific geometric surface area in a unit of volume S_o. The formation of a fixed layer of geometric elements of different shape, number, position, and volume creates a complex system whose description is very complex and unnecessary. It is more appropriate to treat the fixed layer as a uniform environment with isotropic properties.

Table 1. Parameters of fibrous and granular adsorbents.

Sample	Bulk density, $\rho_{н}$, g/cm^3	Real density, $\rho_{ист}$, g/cm^3	Porosity of the layer, E, m^3/m^3	Geometric surface of the layer, S_o, m^2/cm^3	Equivalent channel diameter d^k_{ek} x 10^{-5}, m	Usable surface $S_и$, m^2/cm^3	Height of layer, H x 10^{-3}, m
Fibrous adsorbent with a high content of silicon dioxide, $d^{вл}_{ср}$ = 12 μm							
1	0,0743	0,9962	0,960	30414	*11,70*	21724	50
2	0,0815	1,9962	0,963	32000	12,60	22857	100
3	1,5286	2,4323	0,170	63540	1,07	52730	50
4	2,0385	2,4323	0,158	99300	0,64	61566	100
Molecular Sieve Zeolite ZA (Spheres), $d^4_{ср}$ = 2,36 x 10^{-3} m							
5	0,8846	2,2729	0,610	992	240	387	50
Natural zeolite (clinoptilolite) with irregular shape, $d^4_{ср}$ = 3,5 x 10^{-3} m							
6	0,866	1,7578	0,492	1193	164	606	50
Molecular sieve-zeolite ZA with cylindrical shape, $d^4_{ср}$ = 2 x 10^{-3} m							
7	0,4187	1,4267	0,706	1208	234	1642	50

It is obvious that the porosity of the layer is directly dependent on the particle configuration, the nature of its surface and the degree of sealing of the layer.

It is calculated on the basis of the determined values for the bulk ($\rho_{н}$) and the real ($\rho_{ист}$) density, and the pore volume is not included in it:

$$\varepsilon = 1 - \frac{\rho_{н}}{\rho_{ист}} \qquad (1)$$

For this reason, porous bodies such as adsorbents ($\rho_{ист}$) can be expressed as seemingly - with the ratio between the mass of the fibers and their volume. The highest values for the porosity of the layer formed by the fibrous adsorbents with a high content of silicon dioxide have a sample of 1 (0.960 m^3/m^3), while in sample 4 it is the lowest (0.158 m^3/m^3) due to the high Patching of the layer.

The values of the specific geometric surface of the layer depend on both the size of the layer and the size and configuration of the adsorbent particles. The calculations for S_o of samples 1 ÷ 4 are made in two independent ways. The deviation between the values obtained is less than 2%:

$$S_o = \frac{6(1-\varepsilon)K_ф}{d^4_{ср}} \qquad (2)$$

where:
$K_ф$ = 1 - for spherical particles;
$K_ф$ = 1.37 - for irregularly shaped particles.

$$g = cd^{вл}_{ср} \qquad (3)$$

The mass thus determined corresponds to a fiber area of 0.5 m^2:
g - mass of the fiber adsorbent sample, g;
$d^{вл}_{ср}$ - average fiber diameter, μm;
c = 0.3125.

It is noteworthy that fibrous adsorbents (samples 1÷4) are distinguished by extremely high values for their specific geometric surface - from 30,000 to 100,000 m^2/m^3. They are, respectively, one or two orders of magnitude larger than those of traditional granular (samples 5 and 7) and those of irregular shape (sample 6).

This is a great advantage for the adsorption processes, as the usable surface ($S_и$) is many times greater than 20,000 to 60,000 m^2/m^3 against 380-1,600 m^2/m^3 for the granulated.

Table 2 and Fig. 1 depict the results of the studies related to determining the hydrodynamic resistance of a layer of fibrous and granular adsorbents at different flow.

The passage of the air flow through the immobile layer of adsorbents is associated with an external flow of the geometric forms of the particles and internally to the channels formed between the geometric shapes.

The complex nature of fluid movement through the immobile layer is defined by the diversity of the shape of the channels that go through it.

Table 2. Hydrodynamic characteristics of a fixed layer of adsorbents.

Sample	Layer length *(mm)*	Indicators	Flow rate (m/s)				
			0,1	0,2	0,3	0,4	0,5
Fibrous adsorbent with a high content of silicon dioxide, $d^{вл}_{ср}$ = 10÷12 μm							
		Re_i	0,80	1,80	2,70	3,60	4,50
1	50	λ_i	30,48	13,81	9,36	7,14	5,81
		fx_i	45,58	20,58	13,9	10,58	8,58
		Re_i	0,94	2,00	3,00	4,00	5,00
2	100	λ_i	24,29	12,48	8,48	6,48	5,28
		fx_i	38,80	18,58	12,58	9,58	7,78
		Re_i	0,43	0,85	1,27	1,70	2,44
3	50	λ_i	56,55	28,70	19,37	19,37	10,37
		fx_i	84,69	42,93	28,92	21,75	15,33
		Re_i	0,27	0,54	0,82	1,09	1,30
4	100	λ_i	44,92	44,92	29,74	22,49	18,94
		fx_i	133,94	67,24	44,48	33,60	28,27
Molecular Sieve Zeolite ZA (Spheres), $d^4_{ср}$ = 2,36 x 10^{-3} m							
		Re_i	54,93	82,40	109,87	137,33	192,27
5	50	λ_i	1,35	0,92	0,77	0,70	0,65
		fx_i	1,89	1,23	1,06	0,90	0,84
Natural zeolite (clinoptilolite) of irregular shape, $d^4_{ср}$ = 3,5 x 10^{-3} m							
		Re_i	22,80	45,60	68,50	91,30	114,09
6	50	λ_i	1,55	1,00	0,80	0,74	0,69
		fx_i	2,15	1,36	1,10	0,97	0,89
Molecular sieve-zeolite ZA with cylindrical shape, $d^4_{ср}$ = 2 x 10^{-3} m							
		Re_i	10,00	20,00	30,00	40,00	50,00
7	50	λ_i	2,74	1,64	1,26	1,07	1,02
		fx_i	4,56	2,38	1,80	1,50	1,34

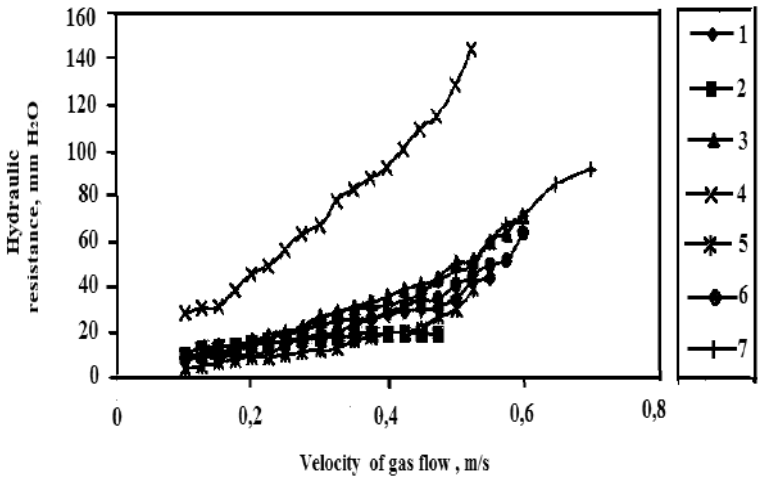

Fig. 1. Dependence of the hydraulic resistance on the layer of linear velocity of gas flow

By analogy with the calculation of the equivalent particle diameter of irregular shape, the equivalent diameter of the non-circular cross-sectional channels is also calculated:

$$d_e^k = \frac{4\varepsilon}{S_o(1-\varepsilon)} \quad (4)$$

On the basis of d_e^k (the mean fictitious and true velocity of fluid movement through the immobile layer) the equivalent Reynolds criterion is defined. It is evident (Table 2) that in the fibers it does not exceed the number 5. The turbulence, consisting of the continuous breaking of whirlwinds, starts at Reynolds values of 20.

Therefore, the greater the fibrillation of the fibrous layer, the influence in the neighboring fibers is more pronounced and *Re* is of lower values. For fiber layers, the values for *Re* are in the range of 0.05 to 20, corresponding to the inertial flow. This explains the fact that increasing the flow of the fluid increases the resistance ΔP (Fig. 1). Small fiber sizes (10 ÷ 12 μm) and grooves cause the number of contact points among the fibers to grow. By increasing the porosity of the layer (ε), the number of contact points decreases. Parallel to (ε) the volume of the concealed zones increases, as a result of which the fluid velocity decreases. The stagnant areas retain some of the fluid passed and their volume becomes unusable in macro-kinetic processes.

Based on the values of the *Re* criterion, the coefficients of the total (λ) and the hydraulic (*fx*) impedance are defined as:

$$\lambda_{\text{i}} = \frac{24}{Re_{\text{i}}} + K \quad \text{and} \quad \lambda_{\text{i}} = \frac{8K}{Re_{\text{i}}} + K_{\text{и}} \qquad (5)$$

where:
K = 0,48; $K_{\text{и}}$ (inertial) = 0,58 (for $Re < 1500$).

For values of $Re < 100$, the flow is characterized by a laminar mode and the hydrodynamic resistance is almost directly proportional to the linear velocity (Fig. 1).

Regardless of the adopted approach for determination of hydrodynamic resistance (ΔP), the determining influence of porosity (ε) and the size of the fibers ($d_{\text{ср}}^{\text{вл}}$) on the dimension of ΔP and the geometric surface which participates in the mass and heat transfer processes. It should be noted that not the whole geometric surface is involved in them, but only that part which is not shielded from the inter-particle contact points, i.e. the so called usable surface (Table 1). It is determined based on the ΔP, ε, V values:

$$S_{\text{и}} = \left[\frac{\Delta P}{H} . \frac{\varepsilon^3}{V \mu K} \right]^{1/2} \qquad (6)$$

where:
$S_{\text{и}}$ - usable surface of the fibrous adsorbent;
K - Kozeni-Karman constant (K = 4.5);
μ - dynamic viscosity;
H - adsorbent bed height:
ΔP - hydraulic resistance of the layer;
V - linear flow velocity.

CONCLUSION

The purpose of the conducted study is to observe the hydrodynamic behavior of a immobile layer of fibrous adsorbent with a high content of silicon dioxide. It has been found that the parameters characterizing the immobile layer - specific and usable surface, are several orders of magnitude larger than those of the traditional granules, and the porosity of the layer formed by the fibrous sorbents can be purposefully regulated within wide limits.

The good hydrodynamic performance and the high sorption capacity of high silica fibers indicate that they can be used for sorption, separation and deep-drying gas and liquid streams.

REFERENCES

1. Ermolenko, I., I. Lyubliner and N. Gulko. Element containing coal fibrous materials. Minsk, Science and technology, 1982.
2. Burchell, T.D. Carbon Materials for Advanced Technologies. Elsevier, 1999.
3. Peebles, L.H. Carbon Fibers Formation, Structure, and Properties. eBook, Taylor & Francis Group, Reissued 2018 by CRC Press.
4. Zverev, M. Chemisorption Fibers. Moscow, Chemistry, 1981.
5. Gopinath, A. and K. Kadirvelu. Strategies to design modified activated carbon fibers for the decontamination of water and air. *Environmental Chemistry Letters,* 2018, p. 1.
6. Patent №30801, Bulgaria.
7. Yoshikawa, M., A. Yasutake and I. Mochida. Low-temperature selective catalytic reduction of NO_x by metal oxides supported on active carbon fibers. *Applied Catalysis A: General,* vol. 173, Issue 2, 1998, pp. 239-245.
8. Jae, W.S., J.P. Soo and K.R.Seung. Effect of modification with HNO_3 and NaOH on metal adsorption by pitch-based activated carbon fibers. *Carbon*, vol. 39, Issue 11, 2001, pp. 1635-1642.
9. Mangun, C.L., K.R. Benak, J. Economy and K.L. Foster. Surface chemistry, pore sizes and adsorption properties of activated carbon fibers and precursors treated with ammonia. *Carbon*, vol.39, Issue 12, 2001, pp. 1809-1820.
10. Qing, S.L., T.Zheng, P.Wang, J.P.Jiang and N.Li. Adsorption isotherm, kinetic and mechanism studies of some substituted phenols on activated carbon fibers. *Chemical Engineering Journal*, vol.157, Issues 2–3, 2010, pp. 348-356.
11. Gogov D., Symposium on ecology, Burgas, Bulgaria, 2002

ANNUAL OF ASSEN ZLATAROV UNIVERSITY, BURGAS
BULGARIA, 2018, v. XLVII (1)

EVALUATION OF HEAVY FUEL OILS

Yordanka Tasheva, Todor Palichev
E-mail: jtasheva_2006@abv.bg

ABSTRACT

Characterization and evaluation of eight heavy fuel oil were made. The purpose of this study was to develop a better understanding of the chemical composition of residues through the coordinated application of existing characterization methods.

Key words: *heavy fuel oil, evaluation, deep refining*

INTRODUCTION

The precise chemical and physical constitution of petroleum residues is not well understood because of the overall lack of well-documented and acceptable analytical procedures. Many techniques are applicable for the characterization of residues, but few have been developed to a satisfactory stage of systematic methodology [1]. Information is needed to enhance understanding of the nature and interrelationships of residue constituents which can be employed to develop models that explain and predict refining characteristics. Since the major complex constituents of crude oils are concentrated in the residua, this study demonstrated the application of a characterization scheme using eight residues from different heavy fuel oils.

The use of heavy oils as refinery feedstock is increasing. Heavy oils are distinguished from light oils by API gravity, with heavy oils being less than 20 API [2]. Geochemically, many heavy oils are immature crudes and/or biodegraded crudes. The combination of high viscosity at operational temperatures and high concentrations of elements other than carbon and hydrogen causes unique difficulties in the processing of these materials [3].

Low atomic hydrogen-to-carbon ratios mean that hydrogenation or coking steps will be necessary. Asphaltene contents, defined by precipitation with added n-pentane or *n*-heptane, usually are large. High concentrations of sulfur, nitrogen, oxygen, and metals indigenous to crudes (Ni, V, Fe) also result in considerable hydrogen demand. Some heavy oils also contain components that are highly corrosive to refinery equipment.

The strategies for upgrading residues emphasize the differences among their compositions, which will influence the selection of methods for their conversion to products [4]. Hydrodesulfurization (HDS) and hydrodemetallization (HDM) efficiencies cannot be predicted by such conventional measurements as total sulfur, metals, or asphaltene contents, or Conradson carbon residue (CCR) values [5]. Properties of residues determined by conventional methods are not good predictors of their behavior in upgrading processes [6]. Moreover. knowledge about the components of residues that cause specific problems in processing is needed [7].

EXPERIMENT

The experimental investigations were done with eight heavy fuel mixtures. They were labeled from 1 to 8. Each blend was deashphalted with n-hexane. The obtained results are presented in the following tables.

They also studied hydrocarbon group composition. The data are given in Table 9.

The next table shows density, C: H ratio and toluene equivalent of studied blends of heavy fuel oils.

The analyses were done by standard methods and were demonstrated in a previous work [7].

RESULTS AND DISCUSSION

Tables from 1 to 8 show the distillation characteristics of heavy fuel oil 1 according to BSS EN ISO 3405.

Table 1. Distillation characteristics of heavy fuel oil 1

Distillation characteristics	Temperature, °C
i. point	245

e. point	360
Yield, ml	4,2

Table 2. Distillation characteristics of heavy fuel oil 2

Distilation characteristics	Temperature, °C
i. point	258
e. point	360
Yield, ml	3,8

Table 3. Distillation characteristics of heavy fuel oil 3

Distillation characteristics	Temperature, °C
i. point	268
e. point	360
Yield, ml	3,6

Table 4. Distillation characteristics of heavy fuel oil 4

Distillation characteristics	Temperature, °C
i. point	258
e. point	360
Yield, ml	3,8

Table 5. Distillation characteristics of heavy fuel oil 5

Distillation characteristics	Temperature, °C
i. point	262
e. point	360
Yield, ml	4,0

Table 6. Distillation characteristics of heavy fuel oil 6

Distillation characteristics	Temperature, °C
i. point	256
e. point	360
Yield, ml	3,8

Table 7. Distillation characteristics of heavy fuel oil 7

Distillation characteristics	Temperature, °C
i. point	254
e. point	360
Yield, ml	4,0

Table 8. Distillation characteristics of heavy fuel oil 8

Distillation characteristics	Temperature, °C
i. point	245
e. point	360
Yield, ml	4,2

Table 9. Hydrocarbons group composition on studied blends

mixture	saturate	arene	polar
1	43,5	21,1	35,4
2	39,8	23,2	37,0

3	42,4	19,8	37,8
4	50,1	12,4	37,5
5	50,6	17,6	31,8
6	48,8	20,2	31,0
7	46,4	23,8	29,8
8	49,2	19,1	31,7

Table 10. Physicochemical characteristics of studied blends

mixture	Density, kg/m^3	C:H ratio	Toluene equivalent
1	934,7	6,80	17
2	939,9	6,82	19
3	936,3	6,84	15
4	938,3	6,86	21
5	940,3	6,88	13
6	940,6	6,90	15
7	936,8	6,82	17
8	948,7	6,90	19

The presented data show the possibility for deep refining of studied blends.

This involves demonstrating a standardized approach for a well-balanced, cost-effective characterization program. Application of the characterization and evaluation of heavy fuel oils is expected to provide data that can be used to improve the economic viability of processing operations.

REFERENCES

1. Ting D., Thermodynamic stability and phase behavior of asphaltenes in oil and of other highly asymmetric mixtures (Ph.D. thesis), Rice University of Houston, Texas, (2003).

2. Guilherme, P., M. Magorie, M., R. Vinicius, *Fuel* **115**, (2014), p. 190.

3. Petkova, N., M. Angelova, P. Petkov, *Petroleum & Coal*, **51**, (2009) p. 286.

4. Stratiev, D., I. Shishkova, T. Tsaneva, M. Mitkova, D. Yordanov, *Fuel,* **170**, (2016), p. 115.

5. Balabin R., R. Syunyaev, T. Schmid, J. Stadler, *Energy Fuels,* **25**, (2010), p. 189.

6. Ashoori S., M. Sharifi, M. Masoumi and M.Salehi, *Egyptian Journal of Petroleum,* **26,** (2017), p. 209.

7. Tasheva Y., A. Palichev, T. Palichev, *Industrial Technologies*, **4**, (2017), p. 132.

ANNUAL OF ASSEN ZLATAROV UNIVERSITY, BURGAS
BULGARIA, 2018, v. XLVII (1)

PREPARATION AND CHARACTERIZATION OF CHITOSAN-ANTIBIOTIC-ZEOLITE NANOCOMPOSITE FILMS

Dilyana Zvezdova, Ivaylo Tankov, Stefan Harkov, Radoslava Nikolova, Anife Veli

E-mail: zvezdova@abv.bg

ABSTRACT

A series of novel chitosan-anthibiotic-zeolite nanocomposite (CAZN) films were prepared for wound healing application by using the solvent casting method. Their physicochemical properties, namely thickness, folding endurance, water absorption capacity, and water vapour transmission rate (WVTR) were studied. Fourier transform infrared spectroscopy (FTIR) was employed to ascertain the interaction between the negatively charged zeolite and positively charged chitosan. Due to the strong hydrophilic nature of zeolite, it greatly enhances the water absorption capacities of the prepared nanocomposite films. In addition, the presence of zeolite in the films also increases their mechanical strength.

Key words*: chitosan, zeolite, chitosan-tertsef-zeolite nanocomposite films, FTIR*

INTRODUCTION

Chitosan, a linear copolymer of β-(1 – 4)-linked 2-acetamido-2-deoxy- β-d-glucopyranose and 2-amino-2-deoxy- β-d-glycopyranose (N-deacetylated derivative of chitin as a main component of the exoskeleton of crustaceans), has been used in a variety of biomedical and pharmaceutical applications because of its potential beneficial properties, such as biodegradability, non-toxicity, antimicrobial activity [1], and boosting of wound healing [2, 3]. These properties have resulted in the use of chitosan as a raw compound for wound-dressing materials [4 – 7]. However, the strong intermolecular hydrogen bonds on chitosan backbones make the chitosan rigid, insoluble, and resistant to the construction of chitosan hydrogels. Furthermore, a combined use of chitosan-based materials and antibacterial agents increases the wound-healing effects of the materials [8]. In the combined-use therapy, antibacterial agents do not easily persist in effective concentration levels at wound sites. An efficient approach to perform the therapy is to place wound-dressing hydrogels having drug-release functions at wound sites. However, the controlled sustained release of drugs from hydrogels is difficult because the release mechanism depends mainly on two phenomena: the degradation of polymeric networks and the diffusion of compounds through the hydrogel medium [9, 10]. We have developed a novel approach for constructing functional biomaterials: the chemical or physical conjugation of such functional units as inner spaces, surfaces, and interfaces to materials. The approach includes the incorporation of an antibiotic in base materials (such as tissue-adhesive "hydrogels", biodegradable "sheets", and "particles" for drug delivery systems).

EXPERIMENTAL

1. Materials.

Chitosan (Cs) with a degree of deacetylation 79% was obtained as a gift sample from shrimp shells, antibiotic Tertsef was acquired from Actavis (Bulgaria) (T), and Zeolite (Z) was purchased from Kardzhali region. All chemicals were used as received without further purification.

2. Preparation of chitosan film.

First, 1% (w/v) chitosan solution was prepared by dissolving 1 g of chitosan in 100 mL of 1% (v/v) aqueous acetic acid under continuous magnetic stirring. Then the solution was allowed to keep at room temperature for one or two days to remove the air bubbles formed during stirring so as to obtain a clear solution. After that the clear solution was cast evenly into a petri plate and allowed to dry at 60 °C in an oven. After drying, the chitosan film was peeled off and stored in desiccator for further study.

3. Preparation of chitosan-anthibiotic-zeolite films (CTZ).

The nanocomposite films were prepared by using the above-mentioned method. In brief, 1% (w/v) Cs solution, 0.25% (w/v) Tertsef (T) and 0.25% (w/v) zeolite (Z) solution were prepared separately. Then Cs solution was added dropwise into the mixture of T and Z solution in different ratios under continuous magnetic stirring at 52°C to obtain a solution mixture (Table 1). Finally, the solution mixture was cast into a petri plate and dried at 60 °C to evaporate the solvent for the formation of CTZ film.

Table 1. Proportion of chitosan and tertsef-zeolite in nanocomposite films.

S. No.	Sample code	Chitosan (mL)	Tertsef-Zeolite (mL)
1	Cs	25	-
2	CTZ11	10	10
3	CTZ12	20	10
4	CTZ13	30	10
5	CTZ14	40	10
6	CTZ15	50	10

3. Characterization of CBN film

The IR spectrum of the pellets was acquired using infrared spectrometer Nicolet iS 50 FTIR in the range of 4000-400 cm^{-1}. Approximately 1mg of the sample was well mixed into 300 mg KBr powder and then finely pulverized and put into a pellet-forming die. A force of approximately 6 tons was applied under vacuum for several minutes to form transparent pellets.

4. Folding endurance

The folding endurance of the CTZ films was measured to find the flexibility needed to handle the films comfortably, safely, and carefully on the wound surface. The folding endurance was determined manually by repeatedly folding the film at the same point until it broke or folded up to 300 times. The number of times of folding without any breakage gave the exact value of folding endurance of the CTZ film. It was performed three times for each film to obtain an average value.

6. Thickness and mass measurement of the CTZ films

Thickness is a major factor that greatly affects the functional properties of wound dressing materials. The thicknesses of the CTZ films were measured using an electronic digital micrometer (Kinex CZ) and randomly selecting four positions on each film. The mean was used to express the thickness of the films. To determine the mass uniformity of each CTZ film, four pieces of equal sizes were cut from different positions of each CTZ film followed by weighing their respective masses with electronic balance and eventually, these values were used to calculate the average mass.

7. Water absorption capacity

For water absorption capacities, the pre-weighed CTZ films (25 mm x 25 mm) were individually immersed in 20 mL of freshly prepared 0.9% saline solution at room temperature. Then, the soaked films were withdrawn from the medium at pre-determined time interval. The swollen weights of the CTZ films were determined after removing excess surface water on the films with filter paper followed by placing them back into the same saline solution. Percentage swelling of the CTZ films was calculated according to the following equation:

$$\text{Swelling (\%)} = [W_f - W_i/W_j] \times 100 \quad (1)$$

where W_f is the weight of the wet film and W_j is the initial weight of the film.

8. Water vapour transmission rate

Water vapour transmission rate (WVTR) was determined gravimetrically according to the modified ASTM E96-95 standard method. Succinctly, a CTZ film of a suitable dimension was mounted on a circular opening of a WVT cup containing 20 mL of distilled water. The WVT cup was accurately weighed and placed in an incubator at 25 °C. Then the WVT cup was re-weighed periodically at 24, 48, and 72 h and then a rate of change in mass was plotted as function of time for each CTZ film. Finally, the WVTR was calculated using the following equation:

$$\text{WVTR}(gm^{-2}\ day^{-1}) = [M \times 24/T\text{-}A] \quad (2)$$

where M represents change in weight, T is time during which the change in weight occurred, and A is the exposed area of the film (m^2).

9. Dressing pH

First, the CTZ films were separately immersed in normal saline solution until it reached equilibrium. After that each CTZ film was removed from the normal saline solution and the same solution was taken into consideration for determining the dressing pH of the said films using a digital pH meter. All tests were per-

formed three times and the average values were recorded.

10. Porosity measurement

The porosity of the CTZ films was determined using the liquid displacement method. In brief, the weight of each CTZ film with a dimension of 1cm x 1 cm was recorded and then the film was put into a beaker containing 5 mL of absolute ethanol for 24 h or until it reached equilibrium. After that the CTZ film was taken out and further weighed. The porosity of the CTZ films was calculated using the following equation:

$$\text{Porosity} = [(W_2 - W_1 - W_3)/(W_2 - W_3)] \times 100 \quad (3)$$

where W_1 represents the initial known weight of a film, W_2 is the sum of the weights of ethanol and the immersed film, and W_3 is the weight of ethanol after the removal of each film.

Chitosan-tertsef-zeolite solution mixture

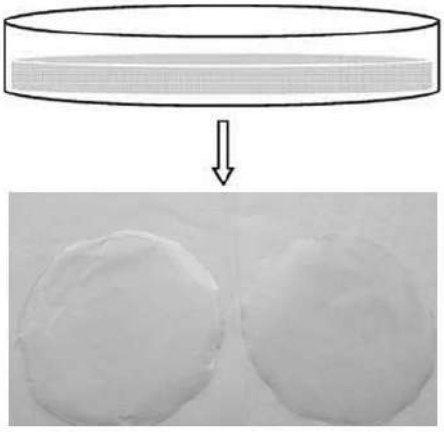

Chitosan-tertsef-zeolite nanocomposite film

RESULTS AND DISCUSSION

1. Characterization of CTZ films

1.1. Fourier transform infrared spectroscopy (FTIR)

FTIR spectra of chitosan (Cs), tertsef (T), zeolite (Z), and chitosan-tertsef-zeolite nanocomposite (CTZ) films are displayed in Fig. 1. As can be seen in Fig. 1(a), the FTIR spectrum of Z shows a peak at 1065.61 cm^{-1} that belongs to Si-O-Si linkage. In addition, the characteristic absorption peaks are found at ~3628.71 cm^{-1} (stretching vibration of Al OH and Si—OH), at 3446 cm^{-1} (stretching vibration of O H and H—O—H groups), at 1636.41 cm^{-1} (H—O—H bending vibration), at 794.54 cm^{-1} (Al—Al—OH bending frequency), and at 507 cm^{-1} (bending vibration of Si—O). The spectrum of CTZ nanocomposite film [Fig. 1(c)] shows a characteristic band at 3431.78 cm^{-1} that is due to a hydrogen bonding formation between the functional groups of C (O—H and N—H groups) and Z (O—H groups). The peak observed in the C spectrum at 1654.9 cm^{-1} shown in Fig. 1(a) is shifted to 1644.1 cm^{-1} in the CTZ spectrum (Fig. 1(c)), which corresponds to the deformation vibration of amine groups of chitosan. An FTIR spectrum of the tertsef shows a sharp intense peak at 1742.48 cm^{-1} (which clearly shows the presence of a carbonyl group), which confirms the carboxylic group in tertsef. Some of the other notable peaks seen in tertsef containing samples include that at 1649.7 cm^{-1} and 1605 cm^{-1} indicating C-N stretching and the presence of amide. The proof of interaction between COOH group in tertsef and NH_2 group in chitosan is also indicated by the fact that the strong peak is at 1758.85 cm^{-1}. The amide and C-N functional groups appear to have a shift in their wave number to 1632 cm^{-1} and 1562 cm^{-1}, respectively, indicating interaction between cefazolin and chitosan microparticles.

2. Thickness and mass measurement of CTZ films

The analysis of thicknesses of pure chitosan and CTZ films with varying ratios of C and Z is portrayed in Table 2. To obtain uniform thickness throughout the nanocomposite films, petri plates with the same diameters and equal volumes of all the prepared solutions were used. The thicknesses of all CTZ films were in the range between 17.5 ±10 μm and 47 ±19 μm. It was found out that the thicknesses of the nanocomposite films increased with increasing the chitosan content in the film forming solution that might be due to enhanced viscosity of C. The mass of 1 cm x 1 cm of the CTZ film was calculated for each prepared film, and it was in the range between 17.00 ± 1.00 mg and 23.00 ± 2.06 mg. From the result, it was found out that there was no significant variation in the masses of the CTZ nanocomposite films. This result indicated that the method adopted for the preparation of the CTZ films was consistent.

3. Folding endurance

Each CTZ film was individually folded repeatedly in the same place to find their folding strength and data are displayed in Table 2.

Table 2. Physical properties of CTZ films in terms of thickness, mass, and folding endurance

Sample code	Thickness (μm)	Mass (mg)	Folding endurance
Cs	22.00	21.50	235.70
CTZ 11	18.30	16.00	200.03
CTZ 12	26.00	19.00	225.75
CTZ 13	28.50	20.50	245.50
CTZ 14	30.80	22.70	267.25
CTZ 15	38.50	25.00	282.50

The table shows that the folding strength of the CTZ films increases with decreasing the content of zeolite from 50% to 20% with respect to chitosan in the said films. Further reduction of the zeolite content may decrease the folding strength of the nanocomposite films. It can be seen from Table 2 that CTZ15 nanocomposite film (282.50) shows the highest folding strength, whereas the CTZ11 nanocomposite film (200) shows the lowest one among all prepared nanocomposite films. Therefore, it can be said that the presence of zeolite in the right proportion in the solution mixture greatly enhances the mechanical strength of the nanocomposite films.

4. Water absorption capacity

Ideally, a wound dressing material should absorb wound fluid while it is applied on the wound bed and thus, it maintains a certain level of moist environment at the wound bed. Water absorption capacity is an important factor of any wound dressing material and prevents dehydration of the tissue, inhibits microorganism growth, and also protects wound maceration. As depicted in Fig. 2, it was found out that the water absorption capacities of all CTZ films increased over a period of time. Apart from this, it also showed that CTZ 14 had the highest water absorption capacity among all prepared CTZ films. It is expected that due to the hydrophilic nature and water holding capacity of zeolite, it enhances the water absorption capacity of the CTZ 14 nanocomposite film. Furthermore, the results showed that the water absorption capacity of the prepared CTZ films increased with increasing the content of C in the composites.

5. Water vapour transmission rate (WVTR)

A dressing used for wound healing purposes should maintain water loss from the wound surface at an optimal rate. The high value of water vapour loss may lead to dehydration of the wound and adherence of the dressing to the wound surface, whereas the low value of water vapour loss might lead to accumulation of wound exudates that may accelerate the risk of bacterial growth and also delay the wound healing process. The WVTR values of the pure C and CTZ films are shown in Fig. 3. The pure CS shows reasonably good WVTR, which is further increased by the addition of tertsef and zeolite. The WVTR value of the CTZ 14 nanocomposite film is near the above-mentioned recommended range of an ideal wound dressing.

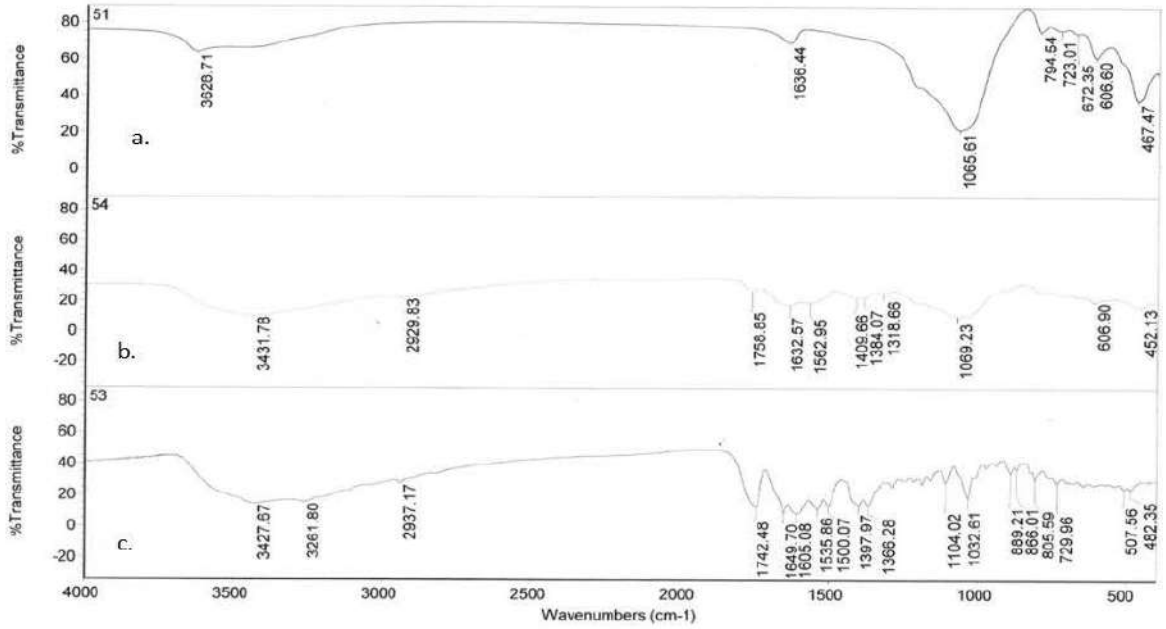

Fig. 1. FTIR spectra of (a) chitosan, (b) zeolite, and (c) CTZ film.

5. Dressing pH

Dressing pH is an important parameter for wound dressing, which facilitates not only the control of infection at the wound surface but also accelerates the formation of fibroblast proliferation. Ideally, a wound dressing should maintain a slightly acidic environment at wound surface (because the pH of normal human skin ranges between 4.0 and 6.8) and thus it would accelerate the wound healing process compared to neutral and alkaline environments. The CTZ films show dressing pH in the range between 5.60 and 6.80, which is presented in Fig. 4. From this result, it can be concluded that the CTZ nanocomposite film has an ability to provide an acidic environment to the wound surface, where CTZ can enhance cell proliferation and fibroblast formation as well.

4. Porosity measurement

The porosity of the CTZ films was determined by the liquid displacement method using absolute ethanol and the results are shown in Fig. 5. The porosity of pure chitosan film increased from 70%t o 90% significantly with the incorporation of tertsef and zeolite. The porosity of the nanocomposite films affected not only their swelling abilities but also their WVTRs. The decreasing values of water absorption capacity and WVTR might be due to low porosity as shown in Fig. 3 and 4, respectively. This result confirmed that there was a direct influence of porosity on water absorption capacity and WVTR as well.

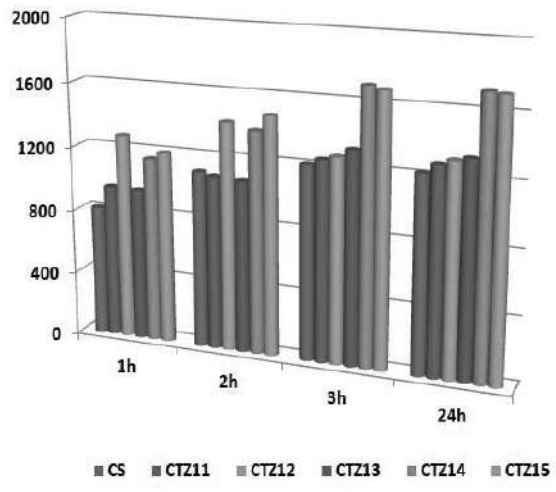

Fig. 2. Water absorption capacity of pure chitosan (C) and CTZ films.

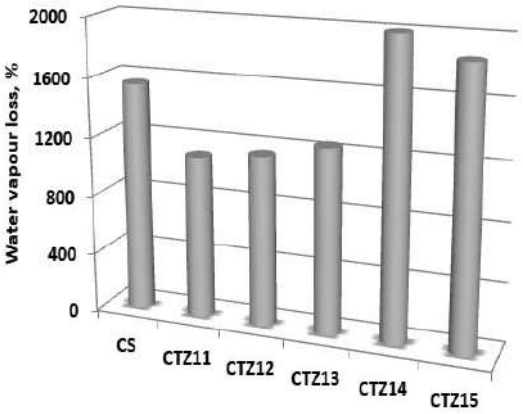

Fig. 3 Water Vapour Transmission Rate value of chitosan and CTZ film

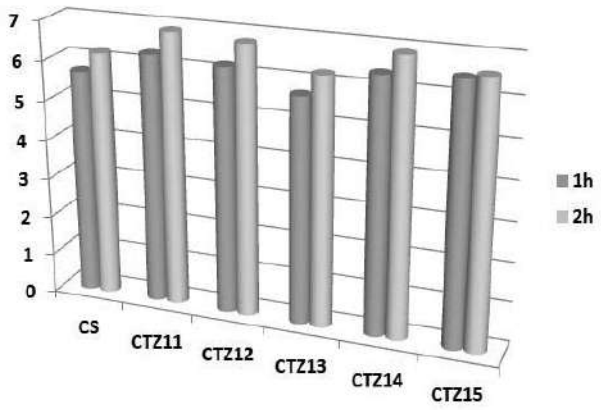

Fig. 4. Dressing pH of pure CS and CTZ films.

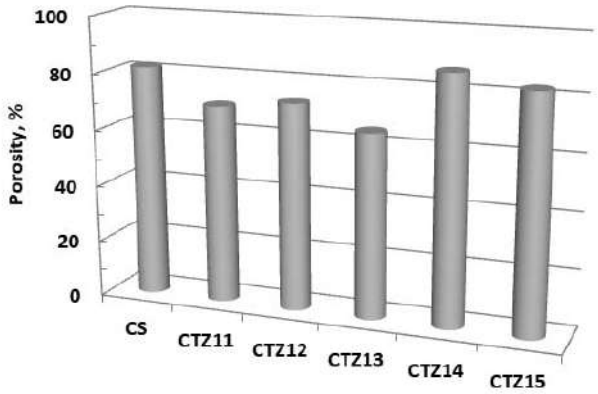

Fig. 5. Porosity evaluation of the nanocomposite films.

CONCLUSION

A series of novel chitosan-tertsef-zeolite nanocomposite films were prepared for wound healing application by using the solvent casting method. The contents of chitosan, tertsef and zeolite in the solution mixture were optimized on the basis of folding endurance of the prepared nanocomposite films, followed by studying water absorption capacities, WVTRs, and porosity

measurements. More interestingly, the incorporation of an appropriate amount of zeolite in the solution mixture with respect to chitosan in order to produce the nanocomposite films dramatically improved almost all properties which are required from an ideal wound dressing material. FTIR spectra confirmed the H-bonding interactions between the hydroxyl groups of zeolite with the hydroxyl and amino groups of chitosan.

REFERENCES

1. Pillai C., W. Paul and C. Sharma. *Prog. Polym. Sci.,* 34, (2009), p. 641–678.
2. Murakami K., H. Aoki, S. Nakamura, S.I. Nakamura, M. Takikawa, M. Hanzawa, S. Kishimoto, H. Hattori, Y. Tanaka, T. Kiyosawa, Y. Sato and M. Ishihara. *Biomaterials,* 31, (2010), p. 83–90.
3. Boucard N., C. Viton, D. Agay, E. Mari, T. Roger, Y. Chancerelle and A. Domard. *Biomaterials*, 28, (2007), p. 3478–3488.
4. Patrulea V., V. Ostafe, G. Borchard and O. Jordan. *Eur. J. Pharm. Biopharm*., 97, (2015), p. 417–426.
5. Usman A., K. M. Zia, M. Zuber, S. Tabasum, S. Rehman and F. Zia. *Int. J. Biol. Macromol*., 86, (2016), p. 630–645.
6. Jayakumar R., M. Prabaharan, P.T. Sudheesh Kumar, S.V. Nair and H. Tamura. *Biotechnol. Adv*., 29, (2011), p. 322–337.
7. Bano I., M. Arshad, T. Yasin, M.A. Ghauri and M. Younus. *Int. J. Biol. Macromol*., 102, (2017), p. 380–383.
8. Chen H., X. Xing, H. Tan, Y. Jia, T. Zhou, Y. Chen, Z. Ling and X. Hu. *Mater. Sci. Eng. C*, 70, (2017), p. 287–295.
9. Arifin D.Y., L.Y. Lee and C.H. Wang. *Adv.Drug Deliv. Rev*., 58, (2006), p. 1274–1325.
10. Lin C.C. and A.T. Metters. *Adv. Drug Deliv. Rev*., 58, (2006), p. 1379–1408.

ANNUAL OF ASSEN ZLATAROV UNIVERSITY, BURGAS
BULGARIA, 2018, v. XLVII (1)

CHITOSAN NANOCOMPOSITE FILMS AS ANTIMICROBIAL AGENT: APPLICATIONS AND MODE OF ACTION

Dilyana Zvezdova

E-mail: zvezdova@abv.bg

ABSTRACT

Chitosan, a hydrophilic biopolymer industrially obtained by N-deacetylation of chitin, can be applied as an antimicrobial agent. The present paper highlights the applications of chitosan as an antimicrobial agent against fungi, bacteria, and viruses and as an elicitor of plant defence mechanisms. A series of novel chitosan-zeolite nanocomposite (CZN) films were prepared by using solvent casting method for wound healing application. The antibacterial activity of the films was investigated against gram positive and gram negative microorganisms. It was found out that all CZN films showed good inhibitory activity against all tested bacteria as compared to control samples. The above analysis suggested that the CZN films could be used as potential candidates for wound healing application.

Key words*: chitosan, zeolite, chitosan-ceftriaxone-zeolite nanocomposite films, Bacillus subtilis, Escherichia coli*

INTRODUCTION

Pathogenic bacterial infection is one of the most crucial problems in wound care management. Infection of wound surface not only changes a normal healing wound into a non-healing wound or a chronic wound but also causes a serious problem to public health. To overcome this problem, scientists are aggressively working to prepare advanced wound dressing materials. Nowadays, natural polymers based wound dressing materials play a decisive role to prevent microbial infection at wound surface. Among them, chitosan is a very promising candidate for wound healing due to its strong antibacterial properties against a broad spectrum of gram negative and gram positive bacteria. Moreover, it is biodegradable, non-toxic, biocompatible, and hemocompatible, which are essential properties for acceleration of wound healing [1-7]. The N-acetyl glucosamine units present in chitosan and chitin also play a significant role not only in enhancing the reepithelization process but also in repairing wound tissues [8]. Further, chitosan finds a wide variety of applications ranging from tissue engineering to drug delivery to gene delivery to medicine to agriculture to pharmaceutical to wound healing to bone healing application because of its ease of moulding into gel, sponge, nanocomposite, scaffolds, powder, beads, and films [9-13]. Till now various blends of chitosan with natural polymers, synthetic polymers, nanomaterials have been investigated to prepare dressing materials for wound healing applications such as chitosan and collagen artificial skin incorporated with nano particles [14]. But still, there is a shortcoming of using chitosan as a wound dressing material as a consequence of its poor mechanical strength and water absorption capacity. Therefore, in the present study, we selected zeolite as one of the most promising reinforcing materials due to its non toxicity, high cation-exchange capacity, low cost, ease of availability, and antimicrobial activity. In addition, it also has the ability to absorb large amounts of wound fluid and thus maintains a moist environment, which is extremely important for any wound dressing material. Moreover, it is used for the treatment of various skin problems such as boils, wound, ulcers, and sores. On the other hand, due to the polycationic nature of chitosan, it can interact with negatively charged zeolites, thus resulting in the formation of a polyelectrolyte complex. The interaction between chitosan and zeolite not only improves the mechanical strength but also enhances the overall wound healing properties of the nanocomposite films. The purpose of the present investigation is to show and explain the effect of a synthesized chitosan nanocomposite material on human pathogenic bacteria and its growth inhibition effect against them.

EXPERIMENTAL

Sample preparation

Shrimp shells were washed thoroughly under running tap water followed by washing with distilled water to remove all intact proteins, tissues, soluble organics and inorganics and other impurities. The shells were then collected and boiled in water for 1 h to remove the adherent tissues. The shells were then oven dried at 160°C in hot air oven for 2 h so as to make them brittle, which in turn helped to break the crystalline structure of chitin. After 2 h the shells were ground to fine powder.

1.1. Demineralization

The main inorganic compound of the shell includes calcium carbonate and various other trace elements. In order to remove calcium carbonate only dilute hydrochloric acid is used to prevent chitin hydrolysis [18]. 7% of hydrochloric acid was added to shell powder and constantly stirred at 250 rpm for 60 min at room temperature. The ratio of dried shells to acid solution used for demineralization was 1/30 (w/v). The demineralized shells were then filtered and collected in filter paper, washed to neutrality with distilled water thrice and oven dried at 60 °C for 24h.

1.2. Deproteinization

Shrimp shell powder was then subjected to the same process similar to demineralization for deproteinization. Adherent proteins were removed with sodium hydroxide. 40% of sodium hydroxide was added to demineralized shell powder and constantly stirred at 250 rpm at 60 °C for 1 h at room temperature. The ratio of demineralized shells to sodium hydroxide solution for deproteinization was 1/30(w/v). The demineralized shells were then filtered and collected in filter paper, washed to neutrality with distilled water thrice and dried for 24 h in the oven at 80 °C to get the chitin residue.

1.3. Deacetylation

Chitosan was converted from chitin by deacetylation process. 1 g of chitin was treated with 50 ml of 50% sodium hydroxide. The mixture was constantly stirred at a fixed temperature of 60°C. 50 min after the occurrence of a foamy texture the mixture was filtered, and neutralized with distilled water. The chitosan residue was then treated with 80% alcohol with solid to solution ratio of 1/30(w/v) followed by oven drying at 80°C for 24 h. The chitosan was then stored in air tight containers.

1.4. Preparation of chitosan film

First, 1% (w/v) chitosan solution was prepared by dissolving 1 g of chitosan in 100 mL of 1% (v/v) aqueous acetic acid under continuous magnetic stirring. Then the solution was allowed to stay at room temperature for one or two days to remove the air bubbles formed during stirring so as to obtain a clear solution. After that the clear solution was cast evenly into a petri plate and allowed to dry at 60°C in an oven. After drying, the chitosan film was peeled off and stored in desiccator for further study.

1.5. Preparation of chitosan-zeolite-ceftriaxone film (CZCF)

The nanocomposite films were prepared by using the above-mentioned method. In brief, 1% (w/v) CS solution, 0.025% (w/v) ceftriaxone (C) and 0.025% (w/v) zeolite (Z) solution were prepared separately. Then CS solution was added dropwise into C and Z solution in different ratios under continuous magnetic stirring at 52°C to obtain a solution mixture (Table 1). Finally, the solution mixture was cast into a petri plate and dried at 60°C to evaporate the solvent for the formation of CZN film.

1.6. Antibacterial study (Agar disc diffusion method)

The antibacterial activity of CS and CZCF films was determined by using agar disc diffusion method against gram positive (B. subtilis) and gram negative (E. coli) bacteria. For antibacterial activity, first of all, the respective nutrient agar medium and nutrient broth medium were prepared by adding 2.8 g of agar and 1.3 g of broth separately in each 100 mL of distilled water and sterilized. The nutrient agar media was then poured into sterilized petri plates. A loopful of each bacterial strain was spread on nutrient agar and incubated at 37 °C for 24 h to produce a single colony. A representative bacteria colony was picked off with a wire loop and then placed in pre-sterilized nutrient broth and incubated overnight at 37 °C for 12 h. After that the cultured bacterial medium B. subtilis and E. coli suspension of 107-108 CFU/mL were inoculated on petri plates and bacteria was spread evenly over the surface of the agar media. Then each film with a dimension of 10 mm x 10 mm was placed on inoculated agar plates. These plates were incubated at 37°C for 24 h and zone of

inhibition around disc was measured to determine the antibacterial activity.

1.7. In vitro nonenzymatic hydrolytic degradation

The degradation of the CZCF films was studied in a phosphate buffered saline solution (PBS) (pH 7.4) at 37°C. The prepared films of equal weights were immersed separately in glass beaker containing PBS and incubated at 37 °C for 3 weeks. Then the CZCF films were removed at predetermined time interval (after one week) from PBS and washed with distilled water to remove residual buffer salts. Finally, the weight of each film was measured. All the hydrolytic degradation studies were performed in triplicate and the percentage of hydrolytic degradation was calculated by using the following equation:

$$\text{Hydrolytic degradation (\%)} = [W_j - W_d/W_J]\text{x}100 \quad (1)$$

where W_j represents initial weight of the film and W_d is dry weight of the film.

1.8. Hemocompatibility test

The hemocompatibility of the so prepared CZCF films were investigated according to the method described elsewhere. In brief, first of all, fresh anticoagulated blood was prepared by adding 1 mL of anticoagulated acid citrate dextrose solution (ACD) into 9 mL of fresh human blood. Before performing this test, each CZCF film with a dimension of 1 cm x 1 cm was placed in a test tube containing 4 mL of saline water and incubated for 30 min at 37 °C. After that ACD blood (200 µL) was added to the test tube and further incubated for 60 min at 37 °C. Similarly, positive and negative controls were prepared by adding the same amount of ACD blood in 4 mL of distilled water (100% hemolysis) and 4 mL of saline solution (0% hemolysis) respectively. After the incubation, each test sample was centrifuged at 2000 rpm for 5 min. The hemoglobin released during hemolysis was determined by the optical density (OD) of the supernatant at 540 nm using UV-VIS spectrophotometer. The percentage of hemolysis was calculate:

$$\text{Hemolysis (\%)} = [OD_{test}\text{-}OD_{neg}/\text{OD}_{pos}\ OD_{neg}] \text{x}100..(2)$$

where OD_{test}, OD_{neg}, and OD_{pos} denote the absorbance of test sample, negative control, and positive control respectively.

RESULTS AND DISCUSSION

2.1. Antibacterial study

A wound generally provides a conductive environment for the growth of microorganisms, which trigger infection and delay the natural wound healing process. Therefore, it is mandatory to conduct an antibacterial study to investigate the efficacy of the dressing material to be used for wound healing application. The antibacterial activity of the CZCF films were evaluated against gram positive (Bacillus subtilis) and gram negative (Escherichia coli) bacteria and the data of the zone inhibition of bacteria are shown in Table 1. The antibacterial result indicated that CZCF 14 (38 mm) film showed the highest antibacterial activity against gram positive bacteria (B. subtilis) as compared to other CZCF films namely CZCF 11 (29 mm), CZCF 12 (33 mm), CZCF 13 (38 mm), CZCF 15 (38.5 mm), and CZCF 16 (33.5 mm). Furthermore, the result also indicated that the zone of inhibition for pure chitosan increased against E. coli from 34 mm to 41 mm (CZCF 16) with the incorporation of zeolite. Chitosan interacts with the membrane of the cell to alter cell permeability. Chitosan also acts as a chelating agent that selectively binds trace metals and thereby inhibits the production of toxins and microbial growth. It also activates several defence processes in the host tissue, acts as a water binding agent, and inhibits various enzymes. Binding of chitosan with DNA and inhibition of mRNA synthesis occurs through chitosan penetration toward the nuclei of the microorganisms and interference with the synthesis of mRNA and proteins. It has been proposed that when chitosan is released from the cell wall of bacterial pathogens host hydrolytic enzymes, it then penetrates the nuclei of bacteria and interferes with RNA and protein synthesis.

Chitosan, however, shows its antibacterial activity only in an acidic medium because of its poor solubility above pH 6.5. Thus, water-soluble chitosan derivatives (soluble in both acidic and basic physiological circumstances) may be good candidates as a polycationic biocide.

In addition to the formation of gas-permeable films, chitosan has a dual function: (a) to direct the interference of bacterial growth and (b) to activate several defence processes.

Table 1. Data of zone of inhibition for CZCF films against Gram positive and Gram negative bacteria.

Sample	Diameter of zone of inhibition (in mm)	
	Gram positive bacteria (Bacillus subtilis)	Gram negative bacteria (Escherichia coli)
CS	37.6	34
CZCF 11	29.0	37.5
CZCF 12	33	39
CZCF 13	38	37.5
CZCF 14	43	38
CZCF 15	38.5	36.8
CZCF 16	33.5	41

2.2. In vitro nonenzymatic hydrolytic degradation

The degradation rate of nanocomposite films was measured at 1st, 2nd, and 3rd week after incubation in PBS (pH 7.4) and was plotted as a function of time (Fig. 1). It was found out that all the CZCF films as well as pure chitosan (control) showed 6-17% degradation after one week of incubation. The CZCF films showed faster degradation after second (22-30%) and third week (30-40%) of incubation. As shown the weight loss was more in the CZCF films containing larger zeolite content. It might be due to easy removal of loosely bound zeolite particles adhered to the surface of the nanocomposite films during incubation in PBS solution and this phenomenon was also confirmed from the SEM analysis.

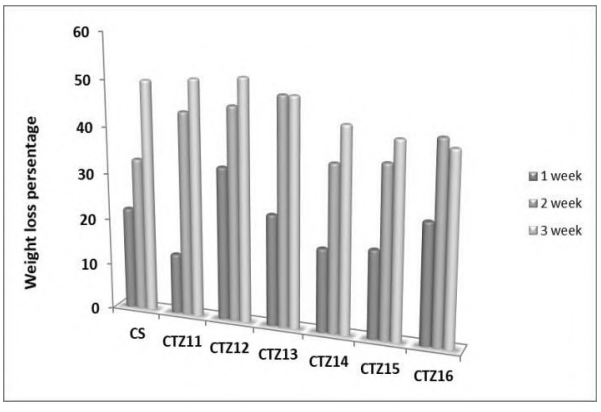

Fig. 1. In vitro nonenzymatic hydrolytic degradation data for CS and CZCF films.

2.3. Hemocompatibility test

The hemocompatibility test is considered to be a very simple and reliable process to measure the hemostatic potential of wound dressings (Fig.2). According to ASTM F material can be divided into three different categories according to hemolytic index (hemolysis%), which are as follows: (1) the materials with percentages of hemolysis over 6% are considered to be hemolytic, (2) the materials with percentages of hemolysis between 2% to 6% are classified as slightly hemolytic, and (3) the materials which show a hemolysis percentage below 2% are considered as non-hemolytic material. Fig. 8 represents the hemolysis percentage values of the CZCF nanocomposite films and the result showed that the hemolysis percentage for all prepared CZCF films were below 1.20%, which indicated that the CZCF films were non-hemolytic in nature.

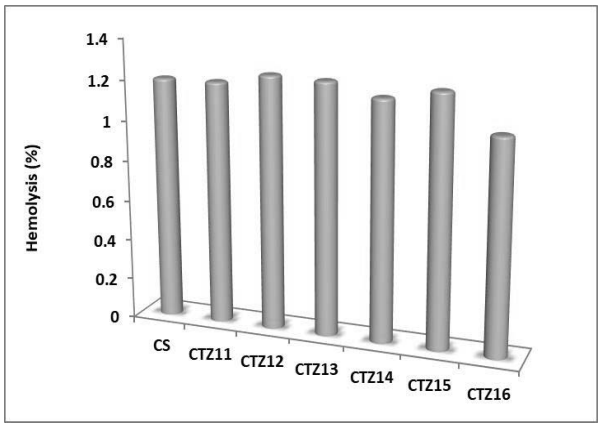

Fig. 2. Hemolysis index of pure chitosan and CZCF films.

CONCLUSION

A series of novel chitosan-ceftriaxone-zeolite nanocomposite films were prepared by using a solvent casting method for wound healing application. FTIR spectra confirmed the H-bonding interactions between the hydroxyl groups of zeolite with the hydroxyl and amino groups of chitosan. On the other hand, all the CZCF films exhibited good antibacterial activity against gram positive (B. subtilis) and gram negative (E.coli) bacteria as well compared to control. Moreover, hemocompatibility results indicated that all the prepared nanocomposite films were highly blood compatible in nature. Finally, all the results indicated that the so prepared CZCF nanocomposite films, especially the CZCF 14 film, have all the required properties for wound healing application. Therefore, it is recommended that the combination of these materials should be employed for the production of wound care products.

REFERENCES

1. Archana D., J. Dutta and P. K. Dutta. *Carbohydrate Polymers*, **95**, (2013), p.530-539.

2. Archana D., B. K. Singh, J. Dutta, P. K. Dutta . *International Journal Biological Macromolecules*, **73**, (2015), p.49-57.
3. Devi N., J. Dutta . *Jornal of Indian Chemical Socaety*, **93**, (2016), p.907-912.
4. Dutta, P., J. Dutta , V. Tripathi. *Jounal Scientific Industrial Research*, **63**, (2004), p.20-30.
5. Paul W., C. P. Sharma. *Trends Biomater. Artif. Organs*, **18**, (2004), p.18-23.
6. Peng C. C., M. H. Yang, W. T. Chiu, C. H. Chiu, C. S. Yang, Y. W. Chen, K. C. Chen, R. Y. Peng . *Macromolecular Bioscience*, **8**, (2008), p.316-327.
7. Singh J., P. K. Dutta. *International Journal Polymer Materials and Polimeric Biomaterials*, **59**, (2010), p.793-807.
8. Singh D., A. Ray. *Journal Macromolecular, Science Polymer Reviwers Part C*, **40**, (2000), p.69-83.
9. Singh J., P. K. Dutta. *International Journal Biological Macromolecules*, **45**, (2009), p.384-392.
10. Yang X., Q. Liu, X. Chen, F. Yu, Z. Zhu. *Carbohydrate Polymers*, **73**, (2008), p.401-408.
11. Upadhyaya L., J. Singh, V. Agarwal, A. C. Pandey, S. P. Verma, P. Das, R. P. Tewari. *Jornal of Controlled Release*, **186**, (2014), p. 54-87.
12. Viseras C., C. Aguzzi, P. Cerezo, A. Lopez-Galindo. *Applied Clay Science*, **36**, (2007), p. 37-50.

ANNUAL OF ASSEN ZLATAROV UNIVERSITY, BURGAS
BULGARIA, 2018, v. XLVII (1)

PREPARATION OF ANTI-CD34 ANTIBODY-FITC AND ANTI-CD45 ANTIBODY-ATTO 465 CONJUGATES FOR IMMUNOFLUORESCENCE IMAGE CYTOMETRIC ASSAY OF LEUKOCYTE AND STEM BLOOD CELLS

Dimitrina Krasteva, Katya Gabrovska, Tzonka Godjevargova
E-mail: godjevargova@yahoo.com

ABSTRACT

Fluorescent conjugates of antibodies specific to CD45 and CD34 cells were made: anti-CD34 antibody-FITC and anti-CD45 antibody-ATTO 465. Purification of the obtained conjugates was carried out by gel filtration chromatography through Sephadex G-25 column. The conjugate fraction characteristics: absorbance and emission were analyzed. The emission characteristics of the obtained conjugates and fluorescent dyes FITC and ATTO 465 NHS were analyzed. A single-step method for leukocyte isolation from human blood was performed. The isolated cells were proved by Giemsa-Eosin staining using an optical microscope. A rapid immunofluorescence image cytometric assay of mature and immature stem cells with these conjugates was made. The cell count was estimated for only 20 min.

Key words: *$CD34^+$, $CD45^+$, antibody, FITC, ATTO465, conjugate, immunofluorescence*

INTRODUCTION

White blood cells (leukocyte) are cells with immunological functions [1,2]. The reference values of white blood cells for an adult human are from 4 x 10^9 to 11 x 10^9 cells/L blood [1]. The determination of a total leukocyte count beyond the above reference values is indicative of various diseases such as Leukemia, Multiple myeloma, Tuberculosis, Infectious mononucleosis, etc [3, 4]. The common leukocyte antigen, CD 45, is a complex family of high molecular weight glycoproteins expressed on all lym-phohematopoietic cells. CD 45 exhibits protein tyrosine phosphatase activity and plays a role in the regulation of cell differentiation. It is present on normal and malignant cells of the myeloid, T- and B-cell lineage [1–5]. CD 34 is a transmembrane phospho-glycoprotein, which is expressed on the surface of immature (stem) cells. Stem cells have been applied in the treatment of serious diseases for more than 55 years. They are applied especially to treat cancers. Stem cell therapy offers a great potential for the treatment of dementia, cardiac infarction, stroke, arthritis and diabetes [6].

Determination of leukocytes and stem cell count and their viability is very important. Based on the expression of CD 45 antigen and CD 34 antigen onto the cell surface, a screening could be made for the number of mature leukocytes and immature stem cells. The determination of cell viability has been performed by several methods including methylene blue dye exclusion (optical microscopy), propidium iodide and 7-amino-actinomycin D using fluorescence microscopy, [7–9]. Fluorescence microscopy methods have been adapted for use on flow cytometers [10–15]. Optimization of the flow cytometric determination requires the use of one fluorescent dye to select nucleated cells and another to determine viability. The determination of cell concentration using a flow cytometer has been well established [16].

Measurement of these cells using a specific monoclonal antibody might provide a more specific indicator for leukocytes and stem cell count and determination of variety diseases.

Immunofluorescence (IF) method using conjugates of antibody specific to CD 45 and CD34 cells with different fluorescent dyes is a perspective method for this purpose. In this study, two conjugates anti-CD34 antibody-FITC and anti-CD 45 antibody-ATTO 465 were prepared. Purification of the obtained conjugates was carried out by gel filtration. Fluorescence image analyses of mature leukocytes and immature stem cells were performed.

MATERIALS AND METHODS

Reagents

Sephadex G25 Medium was purchased from Pharmacia Fine Chemicals, Sweden. Giemsa; Eosin yellowish (Eosin Y, for Microscopy); methylene blue; fluorescein 5(6)-isothiocyanate (FITC); ATTO 465 NHS ester; bovine serum albumin (BSA); anti-CD 34 antibody and anti-CD 45 antibody; methanol; glycerin; dimethylformamide (BSA); 2-amino-2-(hydroxymethyl) - 1,3- propanediol (Tris); Ethylenediaminetetraacetic acid (EDTA); Triton X-100 were delivered by Sigma-Aldrich, Germany. Stem cells were purchased from Allcells. Human peripheral blood was taken from healthy volunteer donors.

Leukocyte isolation from human peripheral blood

A single-step method for leukocyte isolation from human peripheral blood which includes the use of 0.87%NH_4Cl with subsequent centrifugation (400xg for 40 min at 20°C) was used. The isolated leukocytes were observed with Giemsa-Eosin staining by an Olympus BX51 microscope [17].

Preparation and purification of anti-CD34 antibody - FITC conjugate

Antibody-fluorescent dye conjugate was prepared by the method described in our previous paper [18]. Anti-CD 34 antibody 54 µL (1 mg/ml) in 250 µl Reaction buffer (500 mM carbonate buffer, pH 9.5) was shaken at 7 000 rpm for 20 min. Then it was mixed with FITC in DMF (1 mg/mL). The tube was wrapped in foil and was incubated in a shaker for 120 min at room temperature. Then it was left to react at 4°C, overnight. Finally, the conjugate was filtrated from uncoupled reagents.

Sephadex G25 Medium column was used (18 x 1 cm). Flow rate was 0.2 mL/min and fractions were 2 mL each. Elution was performed with Storage buffer (10 mM Tris, 150 mM NaCl, pH 8.2). Fractions were analyzed at 280 nm and 495 nm wavelength for protein and FITC, respectively.

Preparation and purification of anti-CD45 antibody - ATTO465 conjugate

Anti-CD45 antibody – ATTO465 conjugate was obtained following the manufacturer's instructions with some modifications. Briefly, anti-CD 45 antibody was dissolved in reaction buffer with pH 8.3, which contains 20 parts Solution A (1000 mL contains: 8g NaCl, 0.2g KCl, 1.15g Na_2HPO_4, 0.24g KH_2PO_4 , pH 7.4) and 1 part Solution B (0.2 M sodium bicarbonate solution, pH 9.0). Then, ATTO 465 NHS ester dissolved in DMF (1mg/mL) was added. The final anti-body:fluorochome ratio was 100 µg antibody : 10µg ATTO 465 NHS. The mixture was incubated overnight at 4°C in complete darkness. Finally, the conjugate was filtrated from uncoupled reagents. A column with Sephadex G25 Medium (12 x 1 cm) was used. Flow rate was 0.2 mL/min and fractions were 2 mL each. Elution was performed with Solution A. Fractions were analyzed at 280 nm and 453 nm wavelength for protein and ATTO 465, respectively.

Preparation of solutions for analysis of leukocytes and stem cells by new image cytometer "EasyCounterWBC"

The total leukocyte concentration was determined. Dye solution (0.1mg/mL Sofia Green and 1% Triton X-100) was added to 50µL sample. The sample was mixed and 8 µL of it was placed in a chip and the count of leukocytes was determined.

Cell suspensions of leukocytes and stem cells were prepared. To 50 µL isolated leukocytes in 10 mM PBS, pH 7.4 were added 2 µL anti-CD 45 antibody–ATTO 465 conjugate (5µg/mL). The sample was mixed and incubated at 37°C for 20 min in a shaker. After the incubation, 8 µL of it was placed in a chip and the count of leukocytes was determined in a minute. To 50 µL of stem cell suspension in BSS and 0.2% EDTA were added 2 µL anti-CD 34 antibody–FITC conjugate (5µg/mL). The sample was analyzed in a similar way.

RESULTS AND DISCUSSION

FITC-conjugation with CD 34 antibody

Fluorescein isothiocyanate (FITC) is conjugated to protein molecules (such as antibodies) through its isothiocyanate group (Fig. 1).

The conjugating mixture had antibody-fluorescent dye conjugate, free antibody and unconjugated dye. The mixture was filtrated with Sephadex G25 Medium for size-exclusion chro-

matography.

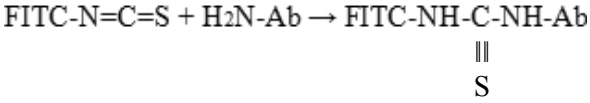

Fig. 1. Reaction between fluorescein 5(6)-isothiocyanate (FITC) and antibody.

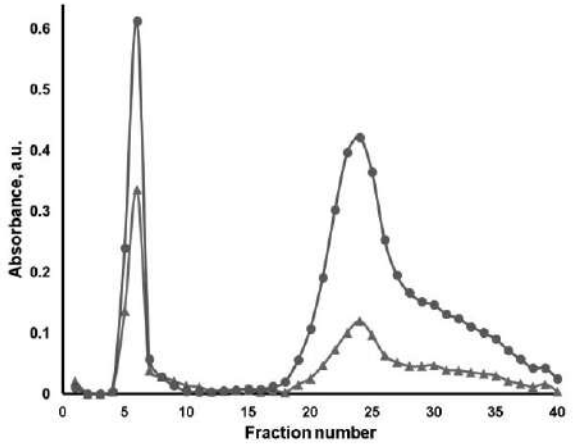

Fig. 2. Sephadex G25 gel filtration of anti-CD34 antibody – FITC conjugate absorbance at 280 nm and 495 nm.

The conjugate had the highest molecular weight in the mixture and exited the column first. Flow rate was 0.5 mL/min. Anti-CD 34 antibody–FITC conjugate was in fractions 6 (Fig. 2). Fluorescent dye: protein ratio (F/P) is in optimal values (3–10). This ratio was found to be preferable due to obtained signal-to-noise results (not shown). In this case, the conjugate provided high enough fluorescent signal and negligible background.

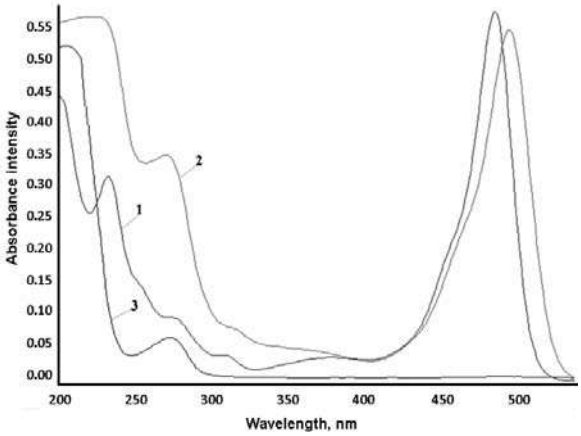

Fig. 3. UV-Vis spectrophotometric assay of free FITC (1), anti-CD34 antibody-FITC conjugate (2) and uncoupled anti-CD34 antibody (3).

The UV-Vis spectra of conjugate fraction 6, free FITC and unbound anti-CD34 antibody were compared and presented in Figure 3. Anti-CD34 antibody had a characteristic peak at 273 nm. That maxima is also presented in the obtained conjugate. Furthermore, FITC absorbance maximum at 492 nm was slightly shifted to 498 nm in anti-CD34 antibody conjugate spectra. Both maxima proved the antibody and fluorochrome existence in the conjugate fraction 6.

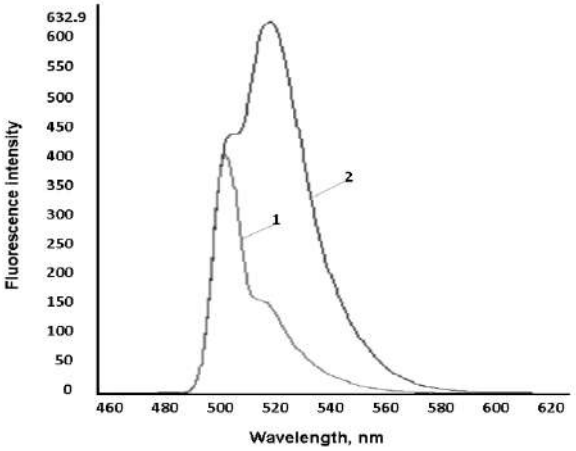

Fig. 4. Fluorescence spectrophotometric assay of free FITC (1) and anti-CD34 antibody-FITC conjugate (2).

Figure 4 shows fluorescence spectrophotometric assays of the obtained conjugate anti-CD34 antibody–FITC. The analysis was performed with Fluorescent Spectrophotometer Perkin Elmer LS45. The characteristic maxima at 518 nm for free FITC was observed also at anti-CD34 antibody - FITC conjugate, too and showed the successful binding between the antibody and the fluorescent dye.

ATTO 465-conjugation with CD45 antibody

ATTO 465 products, produced by ATTO-TEC GmbH (Germany), offer a large variety of high-quality dyes for labelling amino and thiol groups. NHS-esters readily react with amine-modified oligonucleotides or amino groups of proteins, i.e. the ε- amino groups of lysines or the amine terminus, forming a chemically stable amide bond between the dye and the protein (Fig. 5).

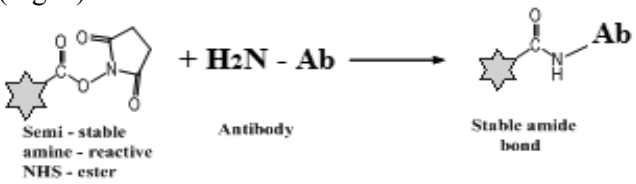

Fig. 5. Reaction between ATTO 465 and the antibody.

Anti-CD 45 antibody – ATTO 465 conjugate was prepared to visualize the antibody- CD 45^{+} cell capturing. The conjugating mixture has antibody-fluorescent dye conjugate, free antibody and unconjugated dye. The mixture was filtrated with Sephadex G25 Medium for size-exclusion chromatography. The absorbance of the fractions was measured at 280 nm (for antibody) and 453 nm (for ATTO465).

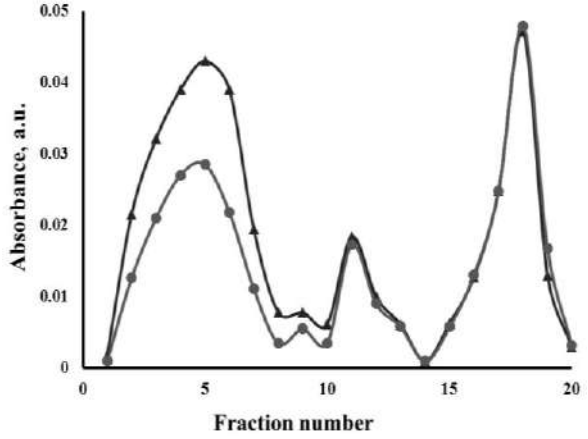

Fig. 6 Sephadex G25 gel filtration of anti-CD45 antibody – ATTO 465 conjugate, absorbance at 280 nm (▲) and at 453 nm (●)

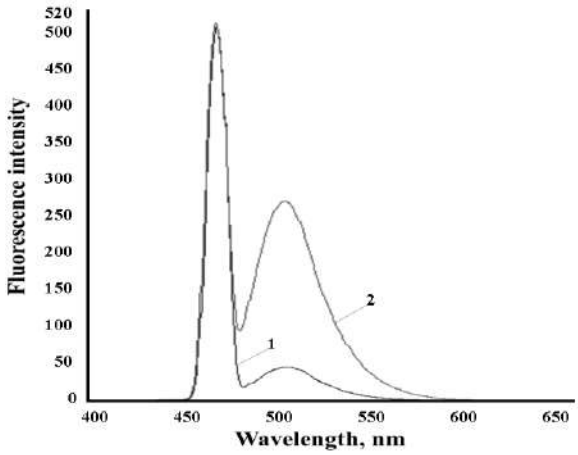

Fig. 7. Fluorescence spectrophotometric assay of free ATTO 465 (1) and anti-CD45 antibody-ATTO 465 conjugate (2**).**

The obtained chromatogram is shown in Figure 6. Anti-CD45 antibody–ATTO 465 w as in fraction 5. Figure 7 shows fluorescence spectrophotometric analysis of fraction 5 and free fluorescent dye (ATTO 465). The analysis was performed with Fluorescent Spectrophotometer Perkin Elmer LS45.The free ATTO 465 had peak at 508 nm and CD45 antibody - ATTO 465 conjugate has peak at 508 nm, too. This result proves the antibody-dye coupling.

Leukocyte isolation from human peripheral blood

Human blood leukocytes from healthy patients were isolated and p roved microscopically through standard Giemsa-Eosin staining (Figure 8).

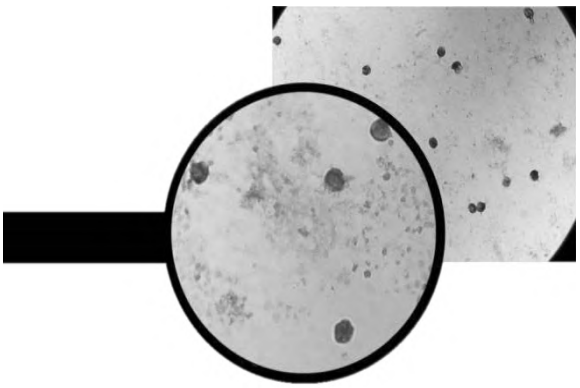

Fig. 8. Giemsa-Eosin staining of white blood cells.

The total leukocyte concentration was determined by an image cytometer ''Easy Counter WBC'' and the cell concentration was 35 x 10^{6} cells/mL (Figure 9).

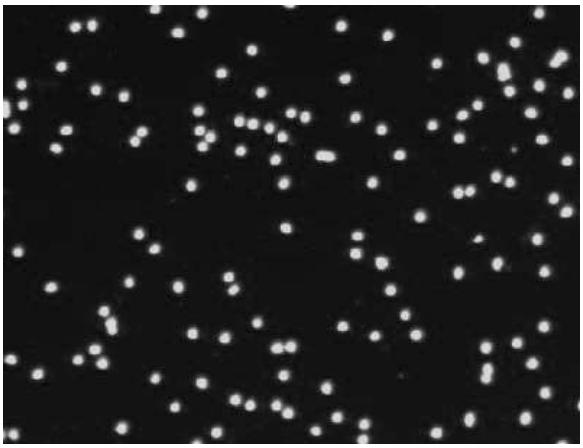

Fig. 9. Determination of leukocyte concentration using DNA stain Sofia Green

Two cell suspensions of leukocytes and stem cells were prepared. The resulting conjugates (anti-CD34 antibody - FITC and anti-CD45 antibody - ATTO465) were added to the samples. The suspensions were incubated for 20 min and cell counts were ''Easy Counter WBC" (Figure 10 and Figure 11). The leukocyte count

was 34 x 10^6 cells/mL and the stem cell count was 1.25 x 10^6 cell/mL.

Fig. 10. Fluorescent image of leukocyte cells stained with anti-CD45 antibody–ATTO465 using "EasyCounterWBC"

Fig. 11. Fluorescent image of stem cells stained with anti-CD34 antibody–FITC using "EasyCounterWBC"

CONCLUSIONS

Two fluorescent conjugates anti-CD34 antibody - FITC and anti-CD45 antibody - ATTO465 were obtained.

Human blood leukocytes were isolated and proven.

The total number of mature and immature cells was determined with the obtained conjugates (anti-CD34 antibody - FITC and anti-CD45 antibody - ATTO465).

The developed method for leukocytes and stem cells determining by labelled antibodies – anti-CD 34 antibody - FITC and anti-CD45 antibody – ATTO 465 is direct, accurate and fast .

REFERENCES

1. Caldwell C-W, Patterson W-P. Relationship between CD45 antigen expression and putative stages of differentiation in B-cell malignancies. *Am J Hematol* 1991, 36, 111–115.

2. Babusˇikova´ O, Glasova´ M, Stasˇ´akova´ J, Kusenda J, Kon´ıkova´ E. Quantitative immunocytofluorometry: new parameters for the definition of leukemia cells. *Neoplasma* 1997, 44,348–355.

3. Lavabre-Bertrand T, Duperray C, Brunet C, et al. Quantification of CD24 and CD45 antigens in parallel allows a precise determination of B-cell maturation stages: relevance for the study of B-cell neoplasias. *Leukemia* 1994, 8, 402–408.

4. Caldwell C-W, Patterson W-P. Relationship between T200 antigen expression and stages of B-cell differentiation in resurgent hyperplasia of bone marrow. *Blood* 1987, 70, 1165–1172.

5. Shah V-O, Civin C-I, Loken M-R. Flow cytometric analysis of human bone marrow IV. Differential quantitative expression of T-200 common leukocyte antigen during normal hemopoiesis. *J Immunol* 1988, 140, 1861–1867.

6. Ashfaq UI Hassan, Ghulam Hassan, Zahida Rassol. Role of Stem Cells in Treatment of Neurological Disorder. International Journal of Health Sciences, Qassim University, Vol.3, №2,(Jualy 2009/Jamada II 1430H)

7. Dyson JED. Fluorescent dyes for studying cell death. *App Fluores Technol* 1990, 2, 1–9.

8. Juneja S, Lukeis R, Tan L, Cooper I, Szelag G, Parkin JD, Ironside P, Garson OM. Cytogenetic analysis of 147 cases of non-Hodgkin lymphoma: Non-random chromosomal abnormalities and histological correlations. *Br J Haematol* 1990, 76, 231–237.

9. Zelenin AV, Poletaev AI, Stepanova NG, Barksky VE, Kolesnikov VA, Nikitin SM, Zhuze AL, Gnutchev NV. 7-amino-actinomycin D as a specific fluorophore for DNA content analysis by laser flow cytometry. *Cytometry* 1984, 5, 348–354.

10. Darzynkiewicz Z, Bruno S, Del Bino G, Gorczyca W, Hotz MA, Lassota P, Traganos F. Features of apoptotic cells measured by flow cytometry. *Cytometry* 1992, 13, 795–808.

11. Harrison CJ. The lymphomas and chronic lymphoid leukaemias. In: Rooney DE, editor. Human Cytogenetics: Malignancy and Acquired Abnormalities, 3rd ed. Oxford: Oxford University Press, 2001.

12. Philpott N, Turner A, Scopes J, Westby M, Marsh J, Gordon-Smith E, Dalgleish A, Gibson F. The use of 7-amino actinomycin D in identifying apoptosis: Simplicity of use and broad spectrum of application compared with other techniques. *Blood* 1996, 87, 2244–2251.

13. Schmid I, Ferbas J, Uittenbogaart CH, Giorgi JV. Flow cytometric analysis of live cell

proliferation and phenotype in populations with low viability. *Cytometry* 1999, 35, 64–74.

14. Schmid I, Krall WJ, Uittenbogaart CH, Braun J, Giorgi JV. Dead cell discrimination with 7-amino-actinomcin D in combination with dual color immunofluorescence in single laser flow cytometry. *Cytometry* 1992, 13, 204–208.

15. Schmid I, Uittenbogaart CH, Giorgi JV. Sensitive method for measuring apoptosis and cell surface phenotype in human thymocytes by flow cytometry. *Cytometry* 1994, 15, 12–20.

16. Schlenke P, Frohn C, Klu¨ter H, Saballus M, Hammers HJ, Zajac SR, Kirchner H. Evaluation of a flow cytometric method for simultaneous leukocyte phenotyping and quantification by fluorescent microspheres. *Cytometry* 1998, 33, 310–317.

17. Zlatina Becheva, Katya Gabrovska & Tzonka Godjevargova. Immunofluorescence microscope assay of neutrophils and somatic cells in bovine milk. Food and Agricultural Immunology, 28:6, 1196-1210, 28 May 2017

18. Becheva, Z., K. Gabrovska and Y. Ivanov, Enhancement of immunoassay fluorescence and detection sensitivity to neutrophils by using antibodies multiple labeled with dye/DNA conjugate, *Annual Assen Zlatarov University, Burgas*, XLVI (2017) p. 31.

ANNUAL OF ASSEN ZLATAROV UNIVERSITY, BURGAS
BULGARIA, 2018, v. XLVII (1)

PREPARATION OF FUNCTIONALIZED MAGNETIC NANOPARTICLES

Milka Atanasova, Yavor Ivanov, Luka Godjevargov, Tzonka Godjevargova
E-mail: *godjevargova@yahoo.com*

ABSTRACT

Magnetic nanoparticles (MNPs) have gained a lot of attention in biomedical and industrial applications due to their biocompatibility, easy surface modification, high surface area, large surface-to-volume ratio and easy separation under external magnetic fields. In this work magnetic nanoparticles were prepared using thermal co-precipitation of Fe^{2+} and Fe^{3+} in aqueous solution. The influence of pH, and stirring rate was observed. The stirring rate was varied from 1300 to 1500 rpm and pH was varied from 13 to 14. The mean size of the particles was determined by transmission electron microscopy (TEM) analysis. The selected kinds of particles were functionalized using three different modifying agents: (3-aminopropyl) triethoxysilane (APTES); tetraethyl orthosilicate (TEOS) and APTES; sodium oleate and chitosan. Amino groups after functionalization were determined by colorimetric method using Traut's and Ellman's reagents. The modifications of nanoparticles were proved by Fourier-transform infrared spectroscopy and by differential scanning calorymetry analysis. The mean size of modified MNPs was determined by TEM analysis. Bovine serum albumin was immobilized on the surface of the functionalized MNPs. The protein immobilization capacity of the MNPs was evaluated, as the concentration of bovine serum albumin was measured before and after immobilization by the Bradford method. MNPs functionalized with APTES turned out to be the most appropriate carrier for protein immobilization. APTES-functionalized MNPs showed a high degree of homodispersity, high protein immobilization capacity and possibility to perform an assay in pseudo-homogeneous mode.

Key words: *magnetic nanoparticles, synthesis, modification, characterization, immobilization, protein*

INTRODUCTION

Nanomaterials have shown tremendous potentials to impact the broad field of biological sensing. Nanomaterials of extremely small sizes and appropriate surface modifications allow intimate interaction with target biomolecules [1]. The higher dispersion of nanoparticles permits the reactions between the selective reagent (antibody, enzyme) immobilized on the carriers and the analyte to be carried out in a pseudo-homogenous solution. Magnetic nanoparticles (MNPs) are manifested as an ideal medium for the immobilization of selective reagents because of the possibility to achieve effective separation by applying a magnetic field. MNPs have a number of advantages for the immobilization of bioagents compared to conventional solid supports: easy manipulation, low-pressure drop, high mass transfer rate, good fluid–solid contact, and capabilities for automation and miniaturization [2 – 4]. The collection of MNPs by a permanent magnet allows the easy separation of the bound and free fraction of the tracer. The choice of separation procedure is important to enhance the sensitivity in heterogeneous assays. The high specific surface of the MNPs allows rapid immobilization of the selective bioreagents and implementation of rapid assay. The magnetic particles provide a high binding capacity of the specific proteins and good homogeneity and this makes them ideal solid support for different tests [5].

In the present work, the synthesis of five kinds of MNPs and three kinds of functionalized nanoparticles was studied. The choice of MNPs with certain optimal size and optimal functionalization was made, necessary for performing an assay in pseudo-homogeneous mode. The degree of protein immobilization onto the modified MNPs was determined.

EXPERIMENTAL

Material

The reagents of analytic grade ($FeCl_3 \cdot 6H_2O$, $FeCl_2 \cdot 4H_2O$, NH_4OH) were purchased from Sigma Aldrich, Germany. Bovine serum albumin (BSA), (3-aminopropyl) triethoxysilane

(APTES), tetraethyl orthosilicate (TEOS), oleic acid (OA), chitosan, sodium citrate, glutaraldehyde, Bradford reagent, methanol were ordered from Sigma Aldrich, Germany. Water was purified with ELGA PURELAB Option.

Synthesis of MNPs

The synthesis of the MNPs was performed on a Syrris Globe system, UK, as described in the literature [6], [7]. Firstly, $FeCl_3 \cdot 6H_2O$ and $FeCl_2 \cdot 4H_2O$ with molar proportion of 1:2 were dissolved in deionized water. The mixture was flushed with nitrogen and stirred at different stirring rate 1300-1500 rpm. The pH of the mixture was maintained alkaline at pH from 13 to 14 by the addition of 25% NH_4OH solution. The temperature was increased to 90°C for 30 min. The MNP suspension (final volume?) was allowed to stir for 30 min at 90°C followed by adding 50 mL 0.3 M $C_6H_7O_7Na$. The particles were washed with deionized water and collected with a magnet. The supernatant was removed and the MNPs were redispersed in deionized water. The procedure was repeated at least five times to wash excess ammonia from the suspension. The aqueous MNP suspension was stored between 0°C and 4°C.

Modification of MNPs with APTES

Functionalization of the MNPs with APTES was carried out as described in the literature [8]. 100 mL of C_2H_5OH were flushed with nitrogen for 30 min in a Syrris Globe system and stirred at 600 rpm. The stirring rate was increased to 1000 rpm and 1 mL deionized water and 0.05 g MNPs were added to the solution. The suspension was mixed for 30 min. Then, 20 mL of APTES were added to the suspension and left for incubation at 7 h with orbital agitation at 1000 rpm. After the incubation period, the suspension was centrifuged and the supernatant was discarded. Then, 4x50 mL C_2H_5OH and 2x1 mL 10 mM phosphate buffer (PB) solution (pH 7.4) were added to the MNPs for washing.

Modification of MNPs with TEOS and APTES

Functionalization of the MNPs with TEOS and APTES was carried out by the method described by Wang et al. [9]. MNPs (30 mg) were suspended in 1-propanol (90 mL) by sonification for 30 min at room temperature. Then, 200 µL NH_4OH, 3 mL deionized water and 200 µL TEOS were added to the above solution, and the mixture was stirred at 1500 rpm for 10 h. After that, 100 µL APTES were added to the mixture. The mixture was stirred at room temperature for 10 h and then centrifuged to separate the precipitate. The resulting black precipitate was washed four times with deionized water and dried.

Modification of MNPs with chitosan

The chitosan-coated MNPs were prepared by a method described by Shete et al. [10]. MNPs (108 mg) was dispersed in 10 mL methanol by ultrasonication. Then, 10 mg OA were added to it slowly with continuous stirring at 80°C. At this temperature, the whole amount of methanol gets evaporated. The particles were washed with deionized water 3 times, collected by forceful application of acetone on it and dried at room temperature till acetone gets evaporated. Then, OA-MNPs were used for the coating procedure. The particles were dispersed in 10 ml of 1% chitosan solution in 2% acetic acid. The mixture was ultrasonicated for 30 min. After ultrasonication, the chitosan-coated MNPs were washed with deionized water 3 times to remove excess chitosan, separated and dried at 50°C.

Characterization methods of initial and modified MNPs

The *Fourier-transform infrared* (FTIR) spectra of nanoparticles were recorded on a Fourier transformation infrared spectrophotometer Tenzor 27-Bruker, Germany, with the KBr technique in the range of 400–4000 cm^{-1}. The size and morphology of nanoparticles were characterized using transmission electron microscopy (TEM) (JEM-1400 PLUS, USA). Before loaded in the instrument, the functionalized nanoparticles were dispersed in methanol and dropped on copper grid. Thermo gravimetric analysis (TGA) and differential scanning calorimetry (DSC) characteristics were measured using TGA-50 (SHIMADZU, Japan) from 25°C to 1000°C under N_2 atmosphere with heating rate of 20°C/min.

Immobilization of protein onto modified nanoparticles

MNPs (5 mg) were suspended in 1 mL glutardialdehyde solution (5 % w/v in 50 mM PB, pH 8) and incubated for 2 h at room temperature with orbital agitation. The nanoparticles were washed once with 50 mM PB, pH 8 and five more times with 10 mM PB, pH 7.4. Then the nanoparticles were resuspended in 0.5 mL 10 mM PB, pH 7.4, containing 1 mg/mL BSA and incubated at 4°C for 2 h. After that the nanoparticles were collected with a magnet and the residual BSA in the supernatant was measured by the method of Bradford [11]. The immobilized protein concentration was calculated as the difference between the initial protein concentration and the residual concentration after immobiliza-

tion. The immobilized protein was expressed as μg protein per mg MNPs.

RESULTS AND DISCUSSION

Preparation of MNPs

H

The highlights of the proposed study are the synthesis of MNPs with a high degree of dispersion, the optimal functionalization of the nanoparticles and finding an optimal immobilization degree of protein onto them. The higher dispersion of MNPs permits the reactions between the selective proteins immobilized on the carriers and the analytes to be carried out in pseudo-homogenous solution. This fact reduces the reaction time to 15 min without breaking the analytical result. The acceleration of the mass exchange processes in a pseudo-homogenous system results in achieving a greater sensitivity of the assay. Immobilization of proteins on the surface of the MNPs increases their stability in the aqueous-organic medium, thereby minimizing the degree of sample dilution. The proposed pseudo-homogeneous approach can be applied for detection of a wide range of compounds.

The MNPs were prepared using thermal co-precipitation of Fe^{2+} and Fe^{3+} in aqueous solution. The influence of pH and stirring rate was observed. Three pH values and three different stirring rates were varied. Six samples were prepared according to their synthesis conditions (Table 1).

Table 1. The influence of pH and stirring rate on MNP synthesis

Stirring rate, rpm	*pH*	*Average size*, nm
1300	13.7	19.2
1400	13.7	12.3
1500	13.7	6.6
1500	13.5	10.2
1500	13.3	15.3

The average size of the six types of magnetic nanoparticles was determined by TEM analysis. It was found out that the MNPs with the smallest average size (~6.64 nm) were obtained at the highest pH and highest stirring rate. It was found out that optimal conditions for the preparation of nanoparticles with small size, about 6 nm, were at stirring rate of 1500 rpm and pH of 13.7.

Modification of MNPs

Three different modifications of MNPs obtained at optimal conditions were carried out by the methods described in Experimental:

1) Modification of MNPs with APTES;
2) Modification of MNPs with TEOS and APTES;
3) Modification of MNPs with OA and chitosan.

Characterization of unmodified and modified MNPs

The morphology and distribution of the obtained MNPs at optimal conditions (stirring rate of 1500 rpm and pH of 13.7) were further characterized using TEM, as shown in Fig. 1.1. The unmodified MNPs show homogeneously spherical shape with diameter about 6-7 nm. The modified MNPs (Fig. 1.2, 1.3 and 1.4) show good dispersion capability in deionized water, which should be due to the fact that the high surface energy and dipolar attraction of the MNPs greatly reduced after modification by functional agents. The mean size of unmodified MNPs is 6.64 nm, modified with APTES – 8.18 nm, with TEOS and APTES – 11.4 nm, with OA and chitosan – 8.31 nm. The modified MNPs with TEOS and APTES (Fig. 1.3) have higher average size, because the particles are coated with two layers.

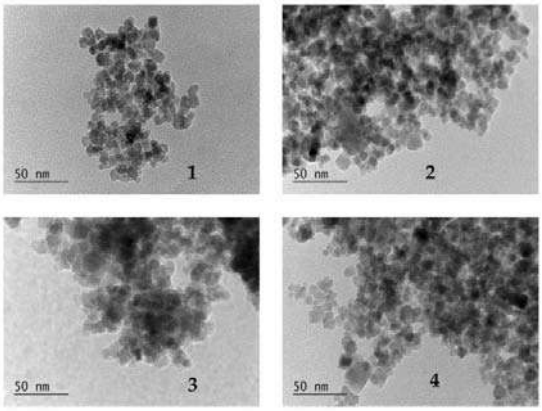

Fig. 1. TEM analysis (JEM-1400 PLUS, USA) of unmodified MNPs (1), modified with APTES (2), with TEOS and APTES (3), with chitosan (4)

The functionalization of MNPs was proved by FTIR analysis (Fig. 2). Evidence of the formation of MNPs is the strong absorption bands at 585 cm^{-1} for all four spectra, corresponding to the Fe–O vibration from the magnetite phase. The adsorption of the APTES polymer (spectra 2) onto the particle surface can be confirmed by the bands at 1113, 1048 and 989 cm^{-1} due to Si-

O-H and Si-O-Si bonds. The OH groups present in the APTES and chitosan polymer (spectra 2 and 4) are clearly seen at 3400 cm^{-1}. The two broad bands at 3417 and 1625 cm^{-1} are due to valence junction of the N-H bond and the free amino groups of APTES and chitosan.

The FTIR spectra of MNP-TEOS-APTES (spectra 3) have the strong absorption bands at 1094, 804, and 471 cm^{-1}, corresponding to the stretching and deformation vibrations of SiO_2 reflecting the coating of silica on the magnetite surface. Successful aminopropyl functionalization of the silica layer on Fe_3O_4-SiO_2 was also evidenced by the absorption at 1572 and 1498 cm^{-1}, attributed to the stretching and bending vibrations of amino groups. The absorption peaks in the region 2800–3025 cm^{-1} were associated with the stretching vibration of methylene groups of Fe_3O_4-SiO_2-NH_2. The results verified the formation of a silica shell on the Fe_3O_4 surface and the amino-functionalization of the silica shell by APTES.

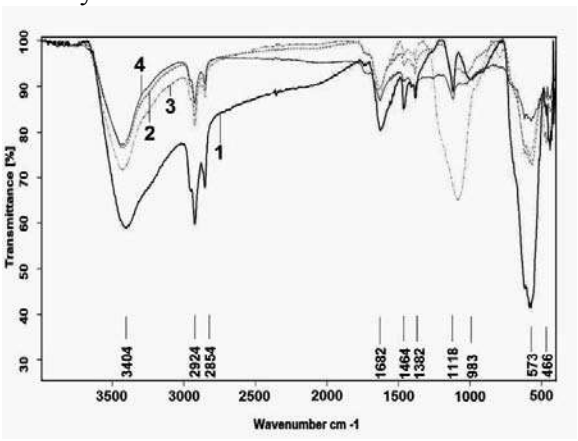

Fig. 2. FTIR analysis of MNPs: unmodified (1), modified with APTES (2), with TEOS and APTES (3), with chitosan (4)

The coating of MNPs was proved by DSC (Fig. 3). For naked Fe_3O_4 no significant peak appeared in the thermo gravimetric analysis /differential thermal analysis (TGA/DTA) curve 1. The TGA/DTA curves of modified MNPs with APTES (2), with TEOS + APTES (3) and with chitosan (4) in the range from 30°C to 300°C lost weight from 8 to 20%. This might be the loss of residual water in the samples. On the other hand, for Fe_3O_4 nanoparticles coated with polymers below 300°C, the weight loss of all the nanocomposites particles was due to the removal of absorbed physical and chemical water. When the temperature was raised to over 300°C, the weight loss was significant because the polymer was degraded: APTES 6.89%, TEOS and APTES 4.73%, and chitosan 6.18%. The results proved modification of MNPs.

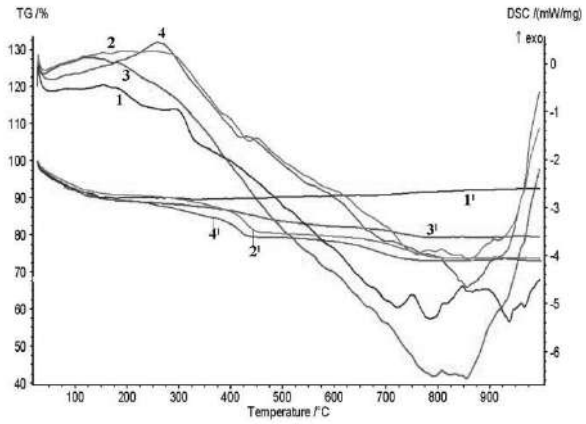

Fig. 3. DSC of unmodified MNPs (1), modified with APTES (2), with TEOS and APTES (3), with chitosan (4).

Immobilization of BSA

The immobilization of BSA on modified MNPs was carried by glutaraldehyde. The base characteristics of modified MNPs and BSA immobilized MNPs were determined (Table 2).

Table 2. The characteristics of modified MNPs and BSA immobilization degree

Modified MNP_S	*Surface Charge*, mV	*Amount of amino-groups*, mgeq/g MNPs	*Bound protein*, μg/mg MNPs	*Degree of BSA immobilization*, %
naked	-43.0	-	-	-
with APTES	+13.6	0.028	24.5	28.50
with TEOS-APTES	+23.8	0.016	13.4	14.90
with chitosan	+31.8	0.024	21.0	23.50

All the modified MNPs have positive charges. These results correlated very well with amount of amino groups on the surface of MNPs. The initial MNPs have negative charge because they were treated at the end with sodium citrate. The modified MNPs with APTES have the highest positive charge, corresponding to the highest amount of amino groups. The protein immobilization capacity of different modified MNPs was evaluated by determination of amount of bound proteins and protein immobilization degree (Table 2). It was evident that the modified MNPs with APTES have the highest BSA immobilization degree.

CONCLUSION

Magnetic nanoparticles functionalized with APTES turned out to be the most appropriate carrier for protein immobilization. APTES-functionalized magnetic nanoparticles showed the highest degree of homodispersity and protein immobilization capacity, a good rate of magnetic separation and permitted the reactions between the selective proteins immobilized on the carriers and the analytes to be carried out in a pseudo-homogenous solution.

ACKNOWLEDGMENT

This research was supported by the National Scientific Fund of Bulgaria, Project DN 17/03, 2017.

REFERENCES

1. Hou S., A. Zhang, and M. Su. *Nanomaterials (*Basel),. **6,** (2016), p. 58.
2. Solé S., A. Merkoçi, and S. Alegret. *Trends in Analytical Chemistry,*. **20**, (2001), p. 102.
3. Rad A. Y., H. Yavuz, M. Kocakulak, and A. Denuzli. *Macromolecular Bioscience,*. **3**, (2003), p. 471.
4. Zhao X. and S. Shippy. *Anal. Chem,*. **76**, (2004), p. 1871.
5. Koh I. and L. Josephson. *Sensors*,. **9**, (2009), p. 8130.
6. Kim D. K., Y. Zhan, W. Voit, K. V. Rao, and M. Muhammed. *J. Magn. Magn. Mater*,. **225**, (2001), p. 30.
7. Chang Y. and D. Chen. *J. Colloid. Interface Sci,*. **283**, (2005), p. 446.
8. Cao H., J. He, L. Deng, and X. Gao. *Appl. Surface Sci*,. **255**, (2009), p. 7974.
9. Wang J., S. Zheng, Y. Shao, J. Liu, Z. Xu, and D. Zhu. *J. Colloid. Interface Sci*,. **349**, (2010), p. 293.
10. Shete P.B., R.M.Patil, B.M.Tiwale, and S.H.Pawar. *J. Magn. Magn. Mater,*. **377**, (2015), p. 406.
11. Bradford M. *Anal. Biochem*,. **72**, (1976), p. 248.

ANNUAL OF ASSEN ZLATAROV UNIVERSITY, BURGAS
BULGARIA, 2018, v. XLVII (1)

STUDY OF TOTAL MICROBIAL COUNT IN RAW MILK

Galina Grigorova
E-mail: galinakirova@abv.bg

ABSTRACT

Microbiological tests were performed on raw cow, sheep, buffalo and goat milk for presence of total microbial count in milk. Calculations were made of the total count of microorganisms in the different types of raw milk intended for downstream processing and production of dairy products. The tests were made in April, May and June. The resultant data demonstrated satisfactory results for the tested samples. In order to enable assessment of the quality of work, the same methods were applied in parallel for testing suitability based on pre-established criteria as organized by the accredited provider and inter-laboratory comparisons were performed. It has been proved that the assessment of work was satisfactory.

Key words: *total microbial count, cow milk, sheep milk, buffalo milk, goat milk, suitability testing*

INTRODUCTION

Microorganisms are part of the biosphere of the Earth together with plants and animals. These are the organisms that can be found at the beginning and the end of the nutritional chain and life in general is dependent on them [1].

According to the definition of BDS, milk is a complex biological fluid obtained from the udder of dairy animals and is used after day seven of birth of a young animal. Milk has a complex composition that makes it complete and indispensable food [1]. Milk is the product that has low degree of natural protection and degrades easily. Heat can transform it; multiple microorganisms can develop in milk and cause various subsequent changes. Qualitatively and quantitatively the composition of the microflora of fresh raw milk is greatly diverse. Lactic microflora depends of the animal's health condition and cleanliness of skin and udder during milking, milking devices, personal hygiene of the milking operator, and the hygiene of the milking premises; and the water used to wash the vessels. The predominant composition is made up of lactic acid bacteria, staphylococci, streptococci, micrococci, coliforms, and spore-forming bacteria. Among all, there are microorganisms that can cause various degradation phenomena in milk. Storage temperature is of utmost importance and it can suppress the development of certain microorganisms and can favor the development of others. In a temperature range of 20 to 37 ^{0}C, mainly mesophilic milk microflora develops, which makes the milk sour, and stimulates the coagulation of milk. These are mainly streptococci, though development of enterobacteria can also occur and these are resistant to temperature changes. In the range of 5 to 15 ^{0}C, psychotrophic microflora develops: various Gram-negative bacteria, among them many impolitic and proteolytic species, which can slowly though definitely degrade milk quality. Changes of microbial content of milk with time are determined on the basis of the initial insemination of milk, cooling mode and duration of storage prior processing. Each phase of milk contains a specific group of microorganisms [1, 2]. There is a relation between the age of the animal and the microbial count in aseptic milk. Cows of lactation number one and two would give milk with a lower microbial count compared to cows of the third lactation. A significant difference can be observed in the microbial count in different milk spouts. It is highest in the initial spouts. Copeland and Olson have found 5,896 bacteria in 1ml in the first milk spouts, 557 cells/ml in the mid spouts and 465 cells/ml in the last spouts. In the case of aseptic milking, predominant are the types of the species *Staphyloccus* and species *Micrococcus*, followed by the types of the species *Staphylococcus* and species *Corynebacterium*. Types of the species *Lactobacillus* are not detected. G. Klefer has isolated 124 strains of coccidial bacteria and 45 strains of the species *Corynebacterium* from aseptic cow milk. Out of the coccidian bacteria, 13 strains belong to the species *Micrococcus and* 111 strains to the species *Staphyloccus*. Out of the isolated 111 strains of staphylococci, 106 strains are coagulase-

negative *Staphyloccus epidermides* and 5 strains are coagulase-positive *Staphyloccus aureus* [2].

Considering the research made by certain authors [5, 6], namely that milk quality depends on the content of microorganisms in it, this study has traced the fluctuations of the total microbial count in raw milk produced in the spring season. Monitoring of microbiological parameters of food is the basic aspect to ensure food safety. In order to assess the quality of work, the same methods were applied in participation in testing of suitability based on pre-established criteria, as organized by the accredited provider, and an intra-laboratory comparison was made.

EXPERIMENTAL

Materials and methods:

Materials

The diluent used was peptone salt solution (Maximum Recovery Diluent), made by Fluka-Germany and Skim Milk PCA. The subject of this study are samples of raw milk taken from dairy manufacturing facilities in Burgas district. The total microbial count (TMC) in raw milk was tested as per BDS EN ISO 4833:2013. Sample preparation for microbiological testing was performed according to the requirements of BDS ISO 7218: 2002 / A_1:2002 - [7] and BDS EN ISO 4833:2013 - [8].

Sampling procedure

The accuracy of the microbiological study of milk depends primarily on adequate sampling. Sampling for a microbiological study requires observance of the following conditions: The sample shall reflect the actual composition of microflora in the product; sampling shall be made via a sterile method; no changes shall occur in the sample microflora before sample testing. Sample storage temperature shall be under control [3].

Determination of total microbial count

Under sterile conditions, from a well-homogenized sample, withdraw 1 ml of milk and transfer this quantity into 9 ml diluent (peptone saline solution). Make two more dilutions to achieve 10^{-3}. Transfer the 1 ml quantity diluted at 10^{-3} of the test sample into a sterile Petri dish. Repeat this procedure with an identical quantity of test sample in a second dish. Pour approx. 15-18 ml of molten and cooled (down to 44 - 47^{0}C) nutrient media (PCA) on the inoculate. Using circular movements, agitate and mix the nutrient media and the inoculate, then place the dishes on a horizontal surface and let the agar cure. Cultivate the dishes bottom up in a thermostat at a temperature of 30^{0}C for 72 h. Upon expiry of the thermostat time, read the results [7, 8]. Read out the count of the aerobes and the facultative anaerobic microorganisms; read only dishes that contain more than 15 and less than 300 colonies (Fig. 1).

Fig. 1. Shaped colonies of aerobes and facultative anaerobic microorganisms

Calculate as per the following formula:

$$N_E = \frac{\Sigma a}{V(n_1 + 0{,}1n_2).d},$$

where N_E - average count of mesophilic microorganisms in the test sample, (CfU) in 1 ml; Σa – sum of colonies counted in the two Petri dishes; n_1 - number of dishes for dilution step one; n_2 – number of dishes for dilution step two;

V - inoculate volume in ml, in each Petri dish; *d* - dilution factor; CfU – Colony forming Units.

Suitability testing

In order to prove the precision of the results using this method, we participated in a testing arrangement for suitability under a program for microbiological analysis of a dairy matrix for the parameter Total Microbial Count in the period May - June 2018.

RESULTS AND DISCUSSION

Many authors refer to various factors for insemination of milk with microorganisms. In the opinion of Yotov et al. [5], sources of milk pollution can be diverse. The most important of these are the udder and the skin of the milking animal, animal bedding, milking facilities and milking systems, work wear of milking operators, fodder, water, etc. Additional burden due to microbial insemination of milk has adverse effects on its processing and quality of finished dairy products. According to Münch et al. [4], the presence of saprophytic microorganisms in raw milk indicates the level of hygiene during the production phase, cleanliness of the milking system, storage and transport conditions.

The microbial count predetermines the production of high quality, durable dairy products. Temperature is a factor that also has its effect on bacterial growth in raw milk. The test samples were promptly cooled down to 4°C and testing was completed within 6 hours from sampling.

Good hygiene practices in production, adequate transportation and storage of milk and mandatory pasteurization can significantly minimize any hazard of milk inoculation with diseases such as tuberculosis, brucellosis and typhoid fever [1]. Cow milk is considered good in terms of microbial count; it contains a maximum of 100 000 bacteria per 1 ml., while according to the requirements of EC Regulation 853, for all other types of milk such as goat, sheep, TMC must not exceed 1 500 000 CFU/ml.

Data obtained from the test samples of raw milk have been demonstrated in the two tables. Table 1 shows the average value of TMC and Table 2 shows the minimum and the maximum value of the total microbial count of the subject test samples. Mandatory norms for total microbial insemination of milk are specified in Regulation (EC) 853/2004 and Regulation No.2/2017, where for raw milk the total microbial count must not exceed 100 000 CFU/ml.

Table 1. Average value of total microbial count in raw milk

Milk type	Average TMC, CFU/ml
Cow milk	85 300
Goat milk	1 179 000
Sheep milk	1 009 000
Buffalo milk	1 132 000

Table 2. Total microbial count in raw milk

Milk type	Minimum TMC, CFU/ml	Maximum TMC, CFU/ml	Parameter allowable range
Cow milk	78 000	91 000	≤ 100 000 CFU/ml
Goat milk	990 000	1 300 000	≤ 1 500 000 CFU/ml
Sheep milk	640 000	1 400 000	≤ 1 500 000 CFU/ml
Buffalo milk	720 000	1 300 000	≤ 1 500 000 CFU/ml

In the spring season, i.e. April, May, in the absence of high temperatures with their indirect effect on the microbiological condition of raw milk, the total microbial count varies within the allowable range. Microbiological analysis of goat and buffalo milk demonstrates repeatability of results and this indicates constancy and stability during the production step. The lowest values obtained, $7{,}2.10^5$ CFU/ml with buffalo milk and $9{,}9.10^5$ CFU/ml with goat milk, demonstrate satisfactory results. With microbiological analysis of goat and buffalo milk, the most frequently repeated result has been $1{,}2.10^6$ CFU/ml. Raw sheep milk has demonstrated the lowest value of this parameter, $6{,}4.10^5$ CFU/ml, and this is presumably attributable to the specific conditions of sheep breeding and milking. The most frequently repeated result for sheep milk has been $8{,}9.10^5$ CFU/ml, while with cow milk it has been $8{,}2.10^4$ CFU/ml.

From the results thus obtained, findings demonstrate a satisfactory microbial insemination of the test samples of the milk types studied, and this has provided evidence of good sanitary

and hygiene condition of dairy production and adequate application of milk refrigeration processing. The higher level of total microbial count in the case of goat, sheep and buffalo milk compared to cow milk, is attributable to the specific conditions of breeding and milking of the animals.

We participated in an arrangement for suitability testing under a program for microbiological analysis of a dairy matrix in reference to the parameter Total Microbial Count (TMC) during the period May-June 2018. The dairy matrix was based on skimmed milk powder. The total number of cells determined in the dairy matrix was 16,363 CFU/g, as shown in Table 3. Determination was made of the randomization criterion Z.

Table 3. Results from the report for participation in the PT.

Analyte	Method	Result	Units	Z score
Total aerobic mesophilic count	MPCA PP 30	16,363	cfu/g	-0,67

The results as per the Z criterion have formed the assessment obtained from the participation in the inter-laboratory comparison.

The results have been assessed at three levels:

$|Z| < 2,0$ - "satisfactory" presentation; no alarm generated.

$2,0 < |Z| < 3,0$ - the assessment demonstrates "suspicious presentation" and a warning alarm is generated.

$|Z| \geq 3,0$ - the assessment demonstrates "unsatisfactory presentation" and an action alarm is generated.

Table 3 demonstrates that the value obtained for Z is equal to - 0,67. Therefore, the assessment is satisfactory and the resultant value for the Z criterion indicates the reliability of the results for a total number of microbial cells.

REFERENCES

1. Antonova-Nikolova S., L. Yocheva., I. Ivanova „Food microbiology" University Publishing House Sv. Kliment Ohridski, Sofiya, 2015.
2. Chomakov Hr., "Microbiology of Milk and Milk Products", Sofiya, 1978, pp 113-115.
3. Dimov N., Iv. Georgiev, S. Velev, Hr. Chomakov, "Control of Milk and Milk Products".
4. Ordinance № 2/23.02.2017 the specific requirements for the production, collection, transport and processing of raw cow's milk.
5. Yotov Yo., Animal health and hygiene requirements for milk production, Zemizdat, 1979.
6. Myunh, Microbiology product animal products, 1985.
7. BDS ISO 7218: 2007/A1:2013 Microbiology. Basic rules for microbiological tests.
8. BDS EN ISO 4833-1: 2013" Microbiology of food and feed. Horizontal method of enumeration of microorganisms. Colony counting technique at 30^0C.
9. BDS EN ISO/IEC 17043:2010, Conformity assessment. General requirements for PT.

ANNUAL OF ASSEN ZLATAROV UNIVERSITY, BURGAS
BULGARIA, 2018, v. XLVII (1)

STUDY OF THE VIABILITY OF BAKER'S YEAST AND OPTIMAL DEVELOPMENT CONDITIONS

Galina Yordanova, Maria Brinkova, Dobromir Yordanov, Ruska Nenkova
E-mail: burdelova@abv.bg

ABSTRACT

The quality of yeast Saccharomyces cerevisiae is determined by many parameters, including their viability and lifting power. In this connection, the viability of the yeast may be examined and compared by a standard method and by a fluorescence counter produced by different manufacturers. Additionally, we measured and compared the lifting force of the yeast at different concentrations and different fermentation temperatures of the dough. This work helps to solve problems related to ensuring the quality of the yeast and bread respectively.

Key words: *viability, leavening force, baker's yeast*

INTRODUCTION

Questions about food quality and its impact on human health have been particularly relevant in recent years. The quality of yeast directly affects the quality of bread. The development of methods for the analysis of baker's yeast qualities will allow of very good control of its viability. Pressed yeast is produced on the basis of molasses to which other nutrients needed for yeast food or as per technological requirements are added: ammonium sulphate, phosphates, sunflower oil, barley malt, etc. The main microflora is *Saccharomyces cerevisiae*. In addition to it, some wild yeasts inevitably also appear in yeast production. *Saccharomyces cerevisiae* yeast has an optimal breeding temperature of 15 °C, and 35 °C for fermentation. Their optimal pH is 5.0-6.0 [1].

The main requirement for baker's yeast is that it has a good lifting power, i.e. it can decompose sugars to provide the necessary carbon dioxide and aromatics to ensure the volume and pleasant smell of the finished products [2].

The quality of yeast *Saccharomyces cerevisiae* is determined by many parameters, including storage stability, osmolarity, freeze-thaw resistance, dry yeast rehydration resistance and colour. In view of the basic role of baker's yeast in the dough, the fermentative capacity (i.e. the specific production rate of yeast carbon dioxide when introduced into the dough) is a particularly important parameter [3]. In the case of use of degraded or insufficient yeast, the fermentation processes do not proceed properly and their rate is lower, therefore, it takes a longer time for the dough to reach readiness for further processing or this is not attained at all. The ready-to-use products of low quality yeast are of low volume and porosity, spilled form, raw medium, and often have cracks on the surface. Our goal is to develop methods for determining the properties of baker's yeast. Therefore, we have studied and compared the viability of cells of different yeast species by a standard counting method, and by a rapid method of counting through a fluorescence counter.

MATERIALS AND METHODS

Materials:

The following were used to make the dough: flour type 500, potable water from the water supply network, yeast and sunflower oil. The dough was prepared by the single-phase method. From the raw materials specified in the recipe for the respective sample, dough is mixed, left to ferment at the appropriate temperature, and its uplift is monitored.

Methods:

Determination of the number of cells by the Toma chamber method and the cell counting of methylene blue staining [4].

Cell number determination by a rapid method using a fluorescence counter.

The lift force was determined by the method of doubling the dough for a set time [5].

RESULTS AND DISCUSSION

The comparison of the quality of different types of yeast was based on the number of microorganisms, while at the same time their viability was determined.

Table 1 shows the number of yeast cells counted by the standard method and the fluorescence counter method. The results show that there is no significant difference between the values obtained by the two methods, i. the efficiency of both methods is high ($\Delta < U\Delta$) for the defined range of the yeast samples tested [6-7].

Table 1. Results for the number of yeast cells in the different yeast species, counted by the standardized method and the fluorescence counter

Yeast type	***Standard method,*** *(result ± u).10^7*	***A method with a fluorescence counter,*** *(result ± u).10^7*	***Efficiency*** $\Delta.10^7$	$U_\Delta.10^7$
1.	990±244	845±195	145	625
2.	1040±260	1846±443	806	1027
3.	870±218	695±160	175	540
4.	955±240	1183±272	228	725
5.	3515±880	4162±980	647	2634
6.	1834±460	2674±642	840	1580
7.	1305±320	1225±280	80	850

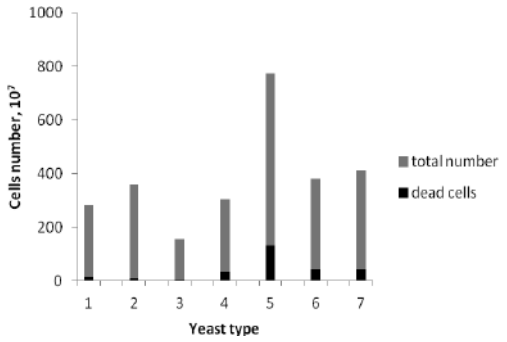

Fig. 1. Comparison of total and dead cells counted by a standard counting method

Figure 1 shows the difference between the total number of yeasts and the dead cells reported by the standard methylene blue method. The fewest cells were found in yeast No. 3, and the most in yeast No. 5, live and dead cells, respectively. Based on these data, cell viability was calculated as a percentage (Fig. 2) and it was observed that yeasts No. 1, No. 2 and No. 3 had the highest viability compared to the others.

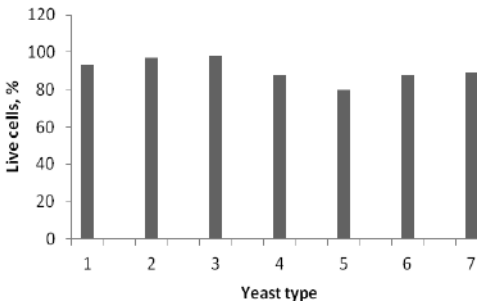

Fig. 2. Viability calculated using a standard counting method

In the counting of yeast cells, similar results were reported by the fluorescence counter (Fig. 3 and 4) for total and dead cells, respectively. With this method, yeast No. 5 had the most live and dead cells, yeast No. 3 again had the fewest cells. Here, the most viable were yeast cells No. 1, No. 2, and No. 3, which had fewer dead cells than the rest.

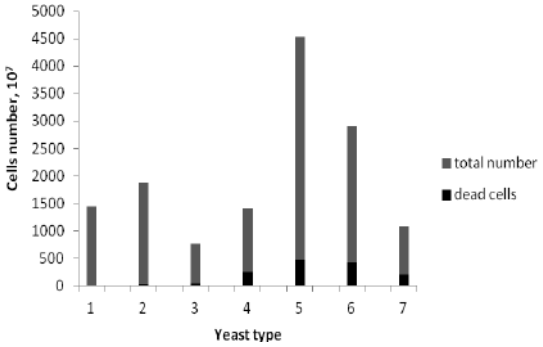

Fig.3 . Comparison of total cell number and dead count by fluorescence counter

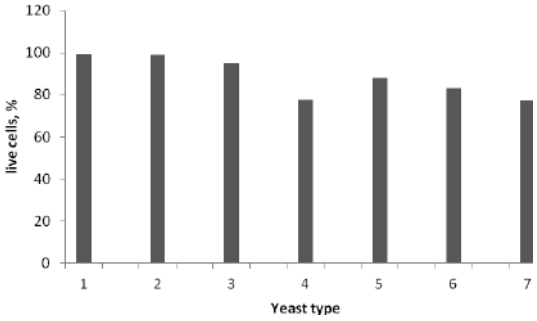

Fig. 4. Viability calculated based on data from the fluorescence counter

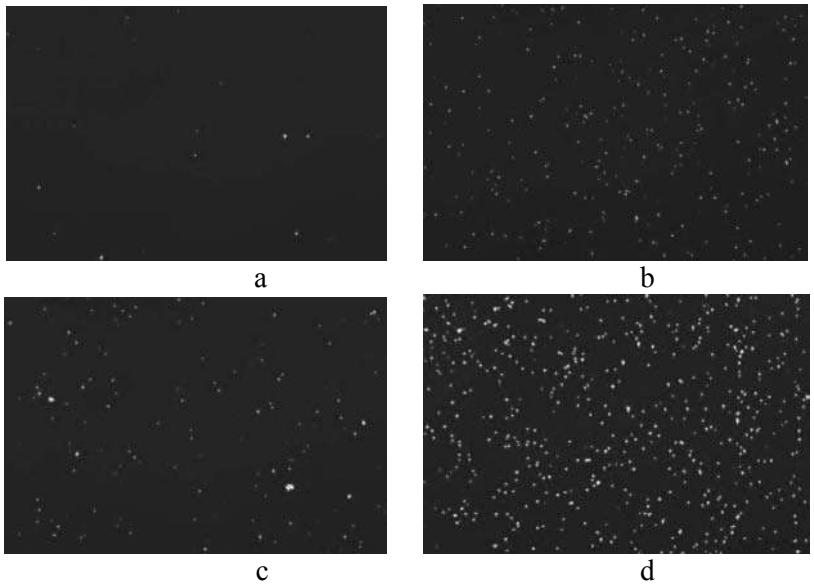

Fig. 5. Pictures from the fluorescence counter: a) dead cells in yeast No. 2; b) total number of *Saccharomyces cerevisiae* cells in yeast No. 2; c) dead cells in yeast No. 7; d) total number of cells in yeast No. 7;

The data are also confirmed by the electronic pictures shown in Fig. 5. In yeast No. 2, a negligible amount of dead cells was observed (Fig. 5a) and in yeast No. 5 there was a significantly higher amount of dead cells (Fig. 5c).

Fig. 6. Determination of swelling speed (lift force)

As a next step, the shear strength of the yeast species was compared at different concentrations of yeast at different temperatures (Figure 6).

From Table. 2 it can be seen that 5 and 6 grams of yeast produce the closest and even decreasing results in the rise time.

Our next experiments were made with 5 grams of yeast, but at different elevation temperatures (Table 3):

As the temperature increased, the dough lifting time was reduced. The nearest results were obtained at optimal yeast development temperature of 35 °C.

The shortest rise time was observed in yeast No. 5, which had the largest number of cells, total and dead. The time for yeasts No.1, 2 and 3 was the longest, with the fewest dead cells and higher viability.

Table 2. Time for growth at different yeast concentrations

	Yeast type						
	1	2	3	4	5	6	7
Quantity, g	*Uptime, min*						
1	151	112	106	85	107	143	73
2	84	88	91	71	52	70	74
3	64	61	105	59	56	72	43
4	53	39	51	45	20	33	26
5	45	46	48	31	32	36	32
6	38	35	39	27	26	28	27
7	33	32	35	20	20	34	24
8	28	30	31	18	22	21	19
9	26	26	31	18	19	20	17
10	26	25	28	19	20	18	16

Table 3. Time to raise yeast species at different temperatures

	Yeast type						
	1	2	3	4	5	6	7
Temperature, ^0C	*Uptime, min*						
10	196	194	266	111	107	145	136
25	71	66	75	40	41	46	35
30	48	46	55	28	30	37	34
35	45	46	48	31	32	36	32
45	36	34	39	22	20	26	22

CONCLUSIONS

1. Data on the number of yeast cells counted by the standard method and the fluorescence counter method show that there is no significant difference between the values obtained by the two methods: the efficiency of both methods is high.

2. Yeasts No. 1, 2 and 3 have the highest viability, respectively. They also have the smallest number of dead cells as determined by both cell counting methods.

3. As the temperature increases, the dough lifting time is reduced.

4. The results obtained confirm that the optimum temperature for yeast development is 35°C.

REFERENCES

1. Vangelov, A. Tehnologia na hlyaba i testenite izdeliya. Sofia, Zemizdat, 1989.

2. Pim Van Hoek, Johannes P. Van Dijken, and Jack T. Pronk. Effect of Specific Growth Rate on Fermentative Capacity of Baker's Yeast. Appl Environ Microbiol. 1998 Nov; 64(11): 4226–4233.

3. Benitez B, Gasent-Ramirez J M, Castrejon F, Codon A C. Development of new strains for the food industry. Biotechnol Prog. 1996; 12:149–163.

4. Gunetti et al. Validation of analytical methods in GMP: the disposable Fast Read 102W device, an alternative practical approach for cell counting. Journal of Translational Medicine 2012, 10:112.

5. Werner-Washburne, M., E. L. Braun, G. C. Johnston, and R. A. Singer. 1993. Stationary phase in *Saccharomyces cerevisiae*. Microbiol. Rev. 57:383–401.

6. Application Note 1. 2010. Comparison of a measurement result with the certifies value. European reference materials.

7. Yordanov, D. New trends in quality management in laboratories testing crude oil, fuels and lubricants. Industrial technologies, V. II(1), 2015, p. 33-38.

ANNUAL OF ASSEN ZLATAROV UNIVERSITY, BURGAS
BULGARIA, 2018, v. XLVII (1)

INVESTIGATION OF POLYMERIC MATERIALS BY MEANS OF ELECTRO-ACOUSTIC METHODS

Radostin Kasarov
E-mail: diagnostika.kasarov@abv.bg

ABSTRACT

Eight types of optical polymeric materials have been examined by two basic non-destructive techniques. Ultrasonic and eddy current measurements have been accomplished. Attenuation coefficients and paths of sound waves in the materials have been determined by means of the pulse-echo multireflection technique. Comparison of the acoustic properties of the investigated polymers and the standard polymethil methacrylate test sample at 15MHz frequency has been carried out. The obtained results are used to qualify homogeneity and isotropy of studied materials. The results of the applied eddy current technique show sufficiently distinct and well reproducible differences in samples of the same thickness, which may be a criterion for characterizing the electrical insulating properties of the examined plastics.

Key words: *pulse-echo method, ultrasonic attenuation coefficient, eddy current technique, optical polymers*

INTRODUCTION

Nowadays, polymers are widely used in all areas of industry, science, medicine, domestic consumption, etc. In many applications, they are preferable to traditional materials mainly because of their low cost and weight. Excellent electrical and thermal insulation properties of plastics, high abrasion and corrosion resistance, good transparency in optical applications are an essential issue for their usage, too [1].

In this paper, several types of thermoplastic optical polymers have been investigated applying non-destructive ultrasonic and eddy current testing techniques. Velocity and attenuation of ultrasonic waves are the most important parameters for material characterization [2, 3]. The obtained values and the frequency dependence of these two quantities are related to composition and structure of the medium as well as to the different mechanism of interaction of sound waves with substance particles. The ultrasonic study of a material provides information about elastic constants, structural inhomogenities, mechanical and thermal properties under different conditions, etc. [3].

We have determined the velocities of the longitudinal ultrasound waves propagating through the optical polymeric materials and elastic moduli have been determined [4]. The measurements of thin walled plastic samples were carried out at frequencies of 2.25 MHz, 5.0 MHz and 10.0 MHz [5]. In this report, investigations at 15MHz are accomplished to obtain additional information on acoustic properties of polymers.

The principle of eddy current technique is based on the interaction between a magnetic field and test material. Thickness of non-metallic coatings on metals can be determined simply from the effect of lift-off on impedance. This method can be used for measuring thickness and structure investigation of thin walled non-conductive materials. Eddy current experiments have been applied for qualitative characterization of the studied polymers.

EXPERIMENT

Several types of transparent polymeric materials have been studied: acrylic, styrene acrylonitrile (SAN), low-molecular weight S-low Styrene, cellulose and some trade-marks as Optorez 1330, Zeonex E48R and Bayer. Samples were prepared as plane-parallel plates with thickness varying from 2.00 mm to 5.57 mm.

Ultrasonic investigations of the studied polymers have been carried out by means of Krautkramer flaw detector USM 35XS. A pulse-echo contact ultrasonic method was applied and a 15 MHz CLF4 transducer with delay line was used as both transmitter and receiver of the ultrasonic signal. The transducer is aligned on the Krautkramer test specimen, made of polymethyl methacrylate (PMMA), and the instrument is

adjusted to obtain a maximal number of back echoes, clearly observed on the horizontal time axis (x) at the display. The fixed time interval is set the same during the measurements of all studied polymers. Attenuation in dB of longitudinal ultrasound waves in the samples was determined at level of signal amplitude of 80% of the full screen height.

Additional experiments based on the eddy-current method have been performed. Plastic samples were positioned between a steel plate and the differential probe of the apparatus. The signal on the display of the device depended on the thickness and structure of the sample. The first factor can be minimized by selecting polymeric samples with almost equal thicknesses. In our experiment, the PMMA test specimen was compared to the Zeonex and Optorez materials.

RESULTS AND DISCUSSION

In Table 1 the number of back echoes and the sound path length L in the studied polymers are presented. The total attenuation coefficient α is estimated by the well-known equation:

$$\alpha = \frac{1}{L} \lg \frac{A_0}{A_L}, \qquad (1)$$

where A_0 and A_L are the signal amplitudes at $x = 0$ and $x = L$, respectively. The results and thickness of the samples are included in the table.

In the case of plastics, the energy decrease of the ultrasonic wave is due mainly to absorption. It is related to the structure and homogeneity of the material and depends on the wave frequency. The obtained results are compared to the Krautkramer test PMMA sample. This polymer is typically used as a delay line in ultrasonic non-destructive testing and its acoustic properties are well investigated and guaranteed by the producer. The test specimen gives many clearly defined reflected signals in the defined time interval and consequently has low acoustic resistance.

Table 2 shows the required increase in sensitivity in dB, compensating the damping of ultrasound waves for multiple passes of the distance in the studied polymeric samples. The number of rows corresponds to the number of registered echoes in each material. The lower the required increase in sensitivity, the lower the acoustic resistance of the polymer is. As seen, at lowest damping the best results are obtained for the Optorez and SAN samples as well as for the Krautkramer test specimen. It is interesting to note that the acrylic polymer produced by the American Eastman Chemical Company (ECC) has much higher damping than the test specimen which is acrylic, too. However, the thicknesses of the two specimens are rather different. The thicker the sample the stronger absorption is observed and fewer back echoes are registered. The difference in the results for both acrylic specimens may be due also to the production conditions such as degree of polymerization, processing temperature, moulding injection rates and pressure, cooling time, etc. as well as to the used additives as plasticisers, mould release agents and brand peculiarities. As a result acoustic properties of different types of a given polymer may vary significantly.

Table 1. Sound path lengths and attenuation coefficients of polymeric materials

Optical polymer	d, mm	Number of echoes	L, mm	α, dB/mm
PMMA (test sample)	2.00	12	48.00	2.06
SAN	2.77	11	60.94	1.69
Optorez 1330	2.01	9	36.18	2.45
S-low styrene	3.09	7	43.26	2.33
Zeonex	2.07	6	24.84	4.02
Bayer	2.51	6	30.12	3.35
Cellulose	4.65	4	37.20	2.67
Acrylic	5.57	3	33.42	2.93

Attenuation of the wave signal at corresponding back echoes is visualised in Fig.1. Along the abscissa axis the number of echoes is given for each material while damping is indicated at the ordinate axis. As can be seen, the studied poly-

Table 2. Adjusting the sensitivity in dB for different types of polymers in respect to the registered back pulse echoes

Compensating increase in sensitivity, dB							
PMMA	SAN	Optorez 1330	S-low styrene	Zeonex E48R	Bayer	Cellulose	Acrylic
22.5	24	21	39	40	45	57.5	60.5
39	41.5	39	59.5	61.5	64.5	74.5	81.5
47.5	53	47.5	69.5	73	74.5	87.5	98
55.5	61.5	55	78.5	81.5	84.5	99.5	
62.5	69.5	63	87.5	90.5	93.5		
69.5	76.5	69.5	94.5	100	101		
75	81.5	77.5	101				
81	88	84					
85.5	92.5	89					
92	98						
95	103						
99							

mers can be divided into three groups. Test PMMA specimen, SAN and Optorez 1330 samples show similar acoustic characteristics and form the first group. The numbers of registered back wall echoes in these materials are more than 6 and attenuation coefficients are with small values bellow 2.5 dB/mm (Table 1). The results slight decrease of the amplitude of the reflected signals is observed.

Among the studied polymers, the SAN material has the lowest values of α (Table 1). The thickness of the sample is about 1.4 times greater in comparison to the other two plastics in the group and therefore, the decrease of wave energy

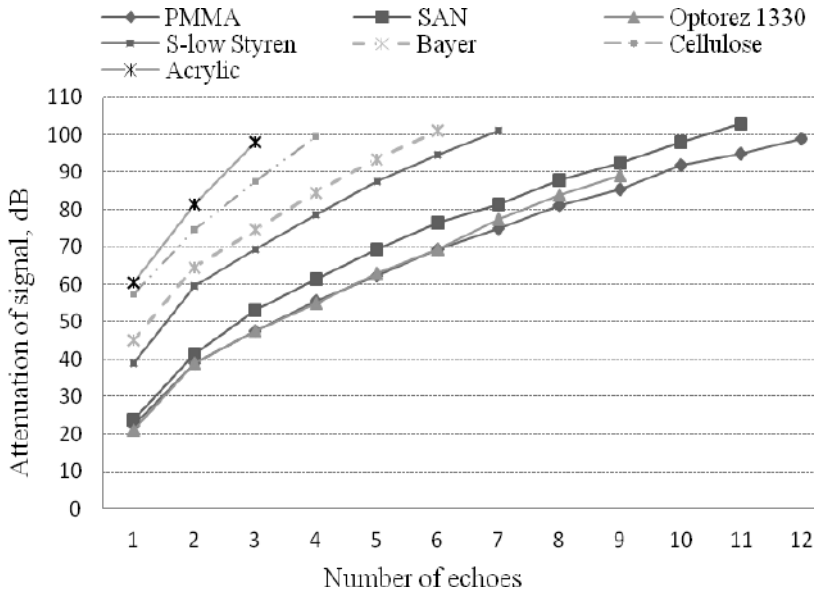

Fig. 1. Signal attenuation in dependence of the number of registered back echoes

for Optorez almost coincide with those of the test sample for the first six reflected signals and the ultrasound path length is up to 24 mm and then a at the opposite surfaces is smaller. The large number of back echoes, even at frequency of 15 MHz, indicates the negligible relaxation time of the medum in comparison to the durability of the

wave propagation which means that the polymer remains practically in equilibrium state. The results for SAN and Optorez samples reveal high acoustic homogeneity of their structure.

The second group in Fig. 1 consists of the Zeonex E48R, Bayer and S-low styrene samples. For the first two polymers the attenuation coefficients are 4.02 dB/mm and 3.35 dB/mm at 6 registered echoes, respectively. The results show that absorption in these materials is high with initial attenuation of the signal over 38 dB (Table 2). The S-low styrene can be also assigned to this group with 7 echoes in the sample but smaller value of α.

The acrylic and cellulose polymers of ECC are with considerably low attenuation coefficients and form the third group. The samples are much thicker in comparison to the other specimens and, therefore, the number of echoes is restricted and lower energy losses due to reflection at opposite surfaces occur. The energy decrease is determined mainly by the absorption in media with high acoustic resistance.

The results of the research conducted with the eddy current method showed that we can confidently distinguish the samples with a different structure. The data obtained for the Optorez sample unambiguously shows a 3% increase in signal amplitude in respect to the null position of the indicator on the screen. The results are obtained with the optimal adjustment mode: phase angle 355 ^{o}, sensitivity of 27 dB and frequency 1kHz. With the same parameters for the Zeonex sample we get a 10% higher amplitude than that of the test sample of Krautkramer.

Observations during the eddy current experiment show minimal but sufficiently distinct and well reproducible differences in samples of the same thickness, which may be a criterion for characterizing the electrical insulating properties of the investigated polymeric materials.

CONCLUSIONS

The conducted experiments show that the applied non-destructive testing methods can serve as a comparison between the different polymeric materials in terms of structure and homogeneity, as well as for quality control of samples of a certain shape through the so-called "Express-analysis" without disturbing their integrity. The co-application of these methods with optical and mechanical measurements ensure a better study and correct selection of polymeric materials in respect to their applications in various optical, electro-optical and acousto-optical devices.

REFERENCES

1. Lampman, S. (Ed.) *Characterization and Failure Analysis of Plastics, ASM International, Materials Park, OH, 2003, p. 11.*
2. Pandey, D. K. and S. Pandey. *Ultrasonics: A Technique of Material Characterization,* In *Acoustic Waves*, *Sciyo Publishers, Sciyo, Croatia, 2010, pp. 397-430.*
3. Chen, C. H. *Ultrasonic and Advanced Methods for Nondestructive Testing and Material Characterization*, *World Scientific Pub Co Inc, 2007, p. 3.*
4. Kasarova, S. and R. Kasarov. Ultrasonic investigation of optical polymers, *Proceedings of National Conference "Acoustic 2007"*, *vol. 9*, 2007, pp. 74-79 (in Bulgarian).
5. Kasarova, S., N. Sultanova and R. Kasarov. Investigation on thin-walled optical polymer samples by means of pulse-echo method, *Scientific Proccedings*, *vol. 1(121)*, NDT days 2011 and 26th International Conference "Defectoscopy'11, 2011, pp. 56-58 (in Bulgarian).

ANNUAL OF ASSEN ZLATAROV UNIVERSITY, BURGAS
BULGARIA, 2018, v. XLVII (1)

SOLAR POWERED THERMOELECTRIC COOLING SYSTEM

Ivaylo Belovski, Vasil Ivanov
E-mail: ivbel@abv.bg

ABSTRACT

Thermoelectric cooling is becoming more and more popular nowadays due to the incessant improvement of the thermoelectric properties of the materials used for manufacturing Peltier modules. The main advantage of this technology is the absolute environmental cleanliness by the operation of the transformers while the main disadvantage is considered to be the high amount of power required to achieve the desired effect. The present paper presents the realization of a project involving thermoelectric refrigerator powered by a solar system consisting of photovoltaic panels, controller and rechargeable batteries. Thus, making a proper choice of each individual component of the solar system, continuous 24/7 power supply is ensured for the thermoelectric refrigerator and problem with the power consumption is solved.

Key words: *thermoelectric cooling, Peltier module, solar power*

INTRODUCTION

In recent years, thermoelectric technics has been developing very fast. This is stipulated by the increased interest in small-size thermoelectric devices that are harmless to the environment, noiseless, safe, reliable and have a long service life. All these requirements are met by devices using semiconductor modules with a principle of operation based on the effect of Peltier. [1].

The unconditional advantages determine also the wide use of thermoelectric modules. They are used in space and military industries, medicine, electronics, biology and many other branches of science, technology and modern life [2 – 4].

The thermoelectric converters of energy are elements which directly convert the temperature difference into electric energy or electric energy into temperature difference. They can be classified into three basic groups:

- thermoelectric generators;
- thermoelectric refrigerators;
- thermoelectric heaters.

The main unit in the thermoelectric converter is the thermo element [5, 6]. The thermo element is defined as a converter of thermoelectric energy containing minimum number of components within which an effect necessary for its operation occurs. The most widely used thermo element is the one based on the longitudinal spin Seebeck effect or Peltier, simply called a thermocouple. Its simplified schematic is shown in Fig.1.

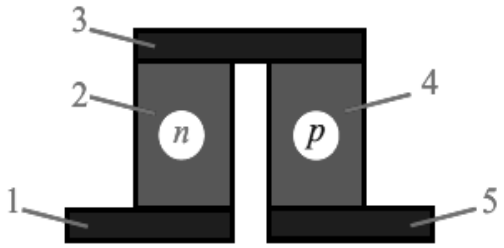

Fig. 1. Thermo element
1, 3, 5 – metal plates; 2 – semiconductor n – type; 4 – semiconductor p – type.

The thermo elements are connected in series electrically and in parallel with respect to heat to obtain thermoelectric modules (TEM). They are the active component of the devices and systems where thermoelectric conversion of energy takes place [7].

The aim of the present paper is to present the realization of a thermoelectric cooling system (TCS) powered by a classic solar system: photovoltaic panels, controller and rechargeable batteries.

PRESENTATION

The block diagram of TCS is shown in Fig. 2. It consists of the following units:

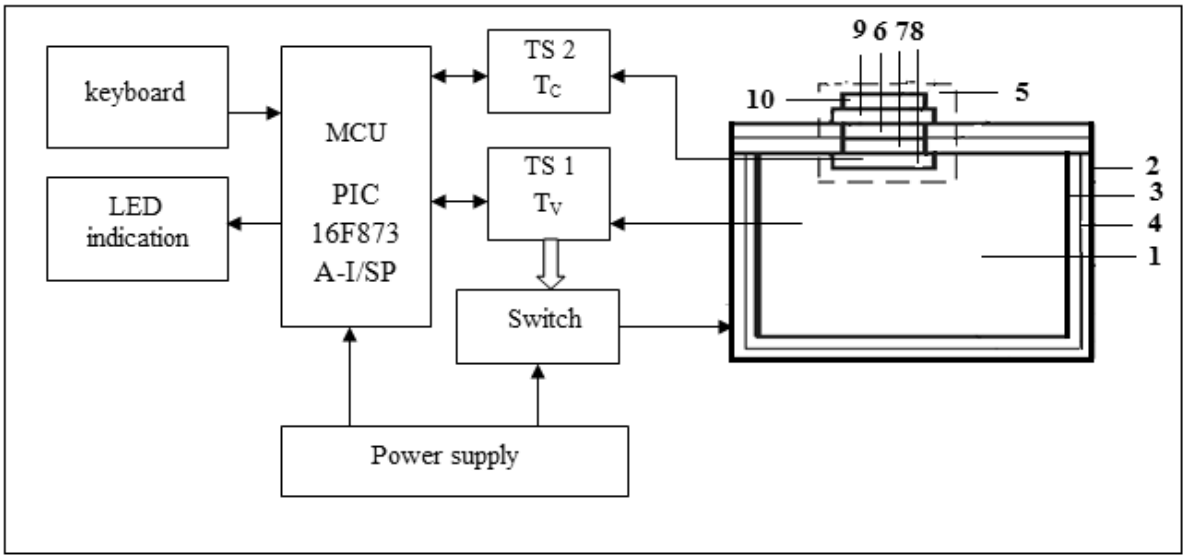

Fig. 2. Block diagram of the thermoelectric cooling system

- Thermally insulated chamber - 1;
- Thermoelectric pump (TEP) based on Peltier modules - 5;
- Two-state thermoregulatory realized using microcontroller PIC 16F873A-I/SP – MCU;
- Temperature sensors monitoring the temperature in the chamber – TS 1 and the temperature in the cold heat sink – TS 2;
- Switch – to switch on/off the thermoelectric module;
- Keyboard;
- LED indicators;
- Power Supply.

The thermally insulated chamber was a vessel of 50 l volume built with double walls 2 and 3 between which thermo insulation layer 4 was placed.

A thermoelectric pump 5 was mounted on the lid of the thermally insulated chamber. TEP consisted of two Peltier modules 6, heat conductor 7, heat sink for absorption 8 and dissipation 9 of the heat power generated and fan 10 for effective cooling of the hot side of the TEM.

The TEP design includes heat-conducting paste with high coefficient of heat conduction – k = 6 W/m.K. It was spread between the heat sink and the ceramic plates of the thermoelectric module.

The parameters of the Peltier modules used are shown in Table 1.

Table 1. Catalog data of Peltier modules

Type	U_{max} (V)	I_{max}, (A)	ΔT_{max} (°C)	Q_{max}, (W)	R (Ω)
PM-40x40-89	15.2	10.5	66	85	1.8

The two-state thermoregulatory was realized on the basis of microcontroller PIC 16F873A-I/SP. The desired temperature is set in the main cycle of the program and the two-state algorithm for the temperature is realized.

The desired temperature and the number of cycles in timer 0 are kept in the EEPROM of the microcontroller even after the power supply is switched off. IC TCN75AVUA was used as temperature sensor in TCS. It has digital output and provides 12-bit values in the range: (– 40 ÷ 125) °C at resolution from 0.5 to 0.0625 °C. The precision in the temperature interval (20 ÷ 40) °C is less than 0.2 °C.

The output is two-wired, according to protocol I2C. The maximal clock frequency is 400 κHz and the minimal period of sampling at resolution of 0.0625 °C is 240 ms.

The indication is dynamic. It was realized with four LED 7 segment digital indicators showing the temperature rounded to 0.01 °C. After setting the desired temperature, the display shows the current temperature and, simultaneously, it is recorded in the EEPROM of the microcontroller. A possibility to visualize the temperature of the cold heat sink T_c was also provided (the regime is selected by the operator).

The thermoelectric pump is powered by a regulated power supply unit which supplies voltage U = 0 – 12V and current I = 0 - 20A. The microcontroller and the temperature sensors are powered with an adapter providing voltage U = 5V. A DC-DC convertor was connected directly to the rechargeable batteries of the solar system – Fig. 3.

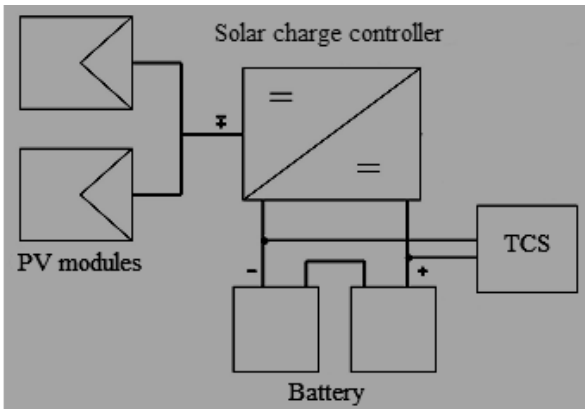

Fig. 3. Block diagram for the Solar Powered System

The block diagram of the photovoltaic solar system is shown in Fig. 3. It consists of the following units:

- Photovoltaic panels 2 pcs .– type *WINAICO WST-275P6* with maximum power P_{max} = 275W, maximum power voltage U_{max} = 31,3V and maximum power current I_{max} = 8,8A (Fig. 4);
- Solar charge controller type *SCC 3kW* with Intelligent Maximum Power Point Tracking (MPPT) technology. Maximum charging current – up to 60A (Fig. 5);
- Battery 2 pcs. type *BANNER ENERGY BULL* 230Ah/12V.

The thermoelectric modules work at optimal voltage and current so that they could produce maximum cooling ability of the thermally insulated chamber. The conversion characteristic T_V = f*(I)* showing the dependence of the temperature in the chamber T_V on the current I , passing through TEP is presented in Fig. 6.

The analysis of the plot in Fig. 6 indicated that the temperature in the volume T_V significantly increases at current supply higher than 4A.

Fig. 4. PV modules

Fig. 5. Solar charge controller

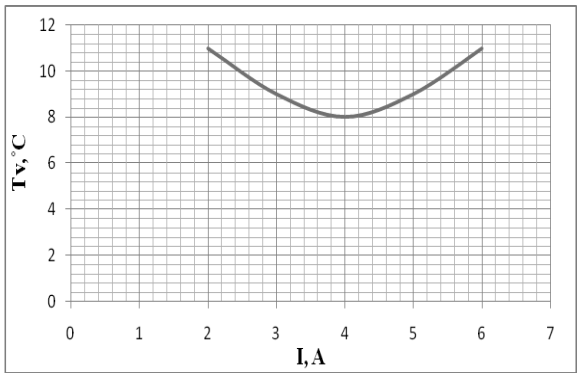

Fig. 6. Conversion characteristic $T_V = f(I)$

CONCLUSION

A thermoelectric cooling system powered only by solar power was designed and manufactured. The conversion characteristics of Peltier TEM were analyzed and the optimal direct current regime of operation was selected. In the thermally insulated chamber, temperature of 8-10 ºC was reached and kept constant.

The solar photovoltaic system was so designed and equipped as to ensure the required power supply and consumption of the thermoelectric cooler. This solar system can be used for other constant and direct current consumers but, in the second case, a suitable inverter should be added to the system.

ACNOWLEDGMENT

The authors are grateful for the support provided by the project "Design and implementation of a thermoelectric cooler powered by a photovoltaic system," funded by the Scientific Research Sector, Prof. Assen Zlatarov University, (No. НИХ-402/2017).

REFERENCES

1. Lineykin S., S. Ben-Yaakov, *Modeling and analysis of thermoelectric modules*, IEEE Trans. Ind. Appl. 43 (2), March/April 2007.
2. Putra N., et al., *The characterization of a cascade thermoelectric cooler in a cryosurgery device*, Cryogenics 50, 759-764, 2010.
3. G. Min, D.M. Rowe, *Experimental evaluation of prototype thermoelectric domestic refrigerators*, Appl. Energy 83, 133-152, 2006.
4. Zhou Y., Jianlin Yu, Design *optimization of thermoelectric cooling systems for applications in electronic devices*, Int. J. Refrig. 35,1139-1144, 2012
5. Fraisse G., M. Lazard, C. Goupil, J.Y. Serrat, *Study of a thermoelement's behavior through a modeling based on electrical analogy*, Int. J. Heat Mass Transf. 53, 3503-3512, 2010.
6. Yazawa K., Ali Shakouri, *Optimization of power and efficiency of thermoelectric devices with asymmetric thermal contacts*, J. Appl. Phys. 111, 024509, 2012.
7. Wang X., Jianlin Yu, Ming Ma, *Optimization of heat sink configuration for thermoelectric cooling system based on entropy generation analysis*, Int. J. Heat Mass Transf. 63, 361-365, 2013.

ANNUAL OF ASSEN ZLATAROV UNIVERSITY, BURGAS
BULGARIA, 2018, v. XLVII (I)

GENERALIZED NET MODEL OF THE PROCESS OF CLASSIFICATION

Veselina Bureva[1], Krassimir Atanassov[1,2], Anthony Shannon[3], Todor Petkov[1], Stanimir Surchev[1]

[1] Laboratory of Intelligent Systems, "Prof. Dr. Asen Zlatarov" University
1 "Prof. Yakimov" Blvd., Burgas 8010, Bulgaria
[2] Department of Bioinformatics and Mathematical Modelling
Institute of Biophysics and Biomedical Engineering
Bulgarian Academy of Sciences
"Acad. G. Bonchev" Str., Block 105, Sofia 1113, Bulgaria
[3] Faculty of Engineering & Information Technology, University of Technology
Sydney, NSW 2007, Australia

E-mail: *vbureva@btu.bg*

ABSTRACT

A generalized net model (GN) of the process of classification is constructed. The proposed model presents the classification task with some improvements for optimizing. The transitions of the generalized net model can be substituted with subnets describing the selected processes in detail. The constructed GN is used for monitoring the possibility of the datasets classifying.
Keywords: *classification, generalized net, data mining, knowledge discovery, machine learning*

INTRODUCTION

The intelligent instruments for data mining include methods for preprocessing the datasets, data analyzing and visualizing the received outcomes. The frequently used techniques for knowledge discovery are classification analysis, cluster analysis, and association rules discovery [1, 6, 13]. Classification analysis is used for obtaining important and relevant information about data. The classification process predicts the label or class for a given unlabeled point. The step of learning is made by training set. It helps us to construct a classification model from the input data. The received model can be specified by the step of validation. The result of classification can be tested by the testing set. In this step it can predict the future class for new unlabeled data. The process of classification is presented in Fig. 1. The classification methods include techniques such as a decision tree, Bayesian networks, support vector machine (SVM), and neural networks [10, 11, 14]. In the current paper the process of classification will be observed and a generalized net model will be constructed. The model can be extended using hierarchical operation of the theory of the generalized nets.

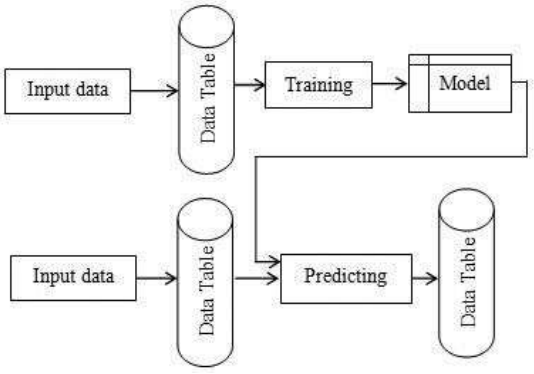

Fig. 1 The process of classification

GENERALIZED NET MODEL OF THE PROCESS OF CLASSIFICATION

The concept of generalized nets is introduced in [3, 4, 5]. The methods and algorithms for knowledge discovery which are modelled by generalized nets are presented in [2, 7-12, 15, 16]. The Generalized Net model of the process of classification contains 9 transitions and 34 places (Fig. 2). The set of transitions A has the following form:

$$A = \{Z_1, Z_2, Z_3, Z_4, Z_5, Z_6, Z_7, Z_8, Z_9\},$$

where the transitions describe the processes:

- Z_1- "there is a database";

- Z_2- "preprocessing the input data";
- Z_3 - "the input data is separated on training, validation and testing sets ";
- Z_4 - "there are criteria for classification";
- Z_5 - "there are methods for classification";
- Z_6 - "there are algorithms for classification";
- Z_7 - "there is a process of classification";
- Z_8 - "validating the output classifier";
- Z_9 - "testing the output classifier".

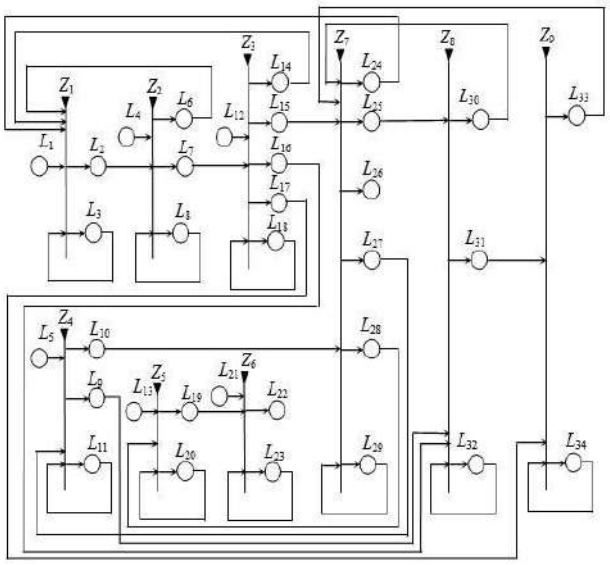

Fig. 2 Generalized net model of the process of classification

Initially the generalized net has the following tokens:

In place L_3 there is one α_2-token. It will be in its own place during all the time of GN functioning. It has the following characteristic: "*database*". The α_2-token in place L_3 generates a new α_3-token at certain time moments which will move to place L_2 with a characteristic: "*selected data for preprocessing*".

In place L_8 there is one α_4-token. It will be in its own place during all the time of GN functioning. It has the following characteristic: "*preprocessing methods*". The α_4-token in place L_8 generates newα_5- and α_6- tokens at certain time moments which can move to the places L_6 and L_7 with characteristics: "*preprocessed data*" in place L_6 and "*new data*" in place L_7.

In place L_{20} there is one η_2-token. It will be in its own place during all the time of GN functioning. It has the following characteristic: "*methods for classification*". The η_2-token in place L_{20} generates a new η_3-token at certain time moments which can move to place L_{19} with a characteristic: "*selected method for classification*".

In place L_{23} there is one λ_2-token. It will be in its own place during all the time of GN functioning. It has the following characteristic: "*algorithms for selected classification methods*". The λ_2-token in place L_{23} generates a new λ_3-token at certain time moments with a characteristic: "*selected algorithm for classification method*" which will move to place L_{22} .

α_1-token enters the net via place L_1 with initial characteristics: "*new data*". The transition Z_1 has the form:

$$Z_1 = \langle\{L_{24}, L_{14}, L_6, L_1, L_3\}, \{L_2, L_3\}, R_1, \vee(L_{24}, L_{14}, L_6, L_1, L_3)\rangle,$$

where

R_1 =

	L_2	L_3
L_{24}	*false*	*true*
L_{14}	*false*	*true*
L_6	*false*	*true*
L_1	*false*	*true*
L_3	$W_{3,2}$	$W_{3,3}$

and:

- $W_{3,2}$ ="There are selected data";
- $W_{3,3}= \neg W_{2,3}$.

The α_{13}-,α_8-,α_5- and α_1- tokens, entering in place L_3 from places L_{24}, L_{14}, L_6, L_1 don't obtain new characteristics. The α_3-token enters in place L_2 with characteristic: „*selected data for preprocessing*“.

The β_1-token that enters the net via place L_4 has initial characteristic: "*preprocessing method*". The transition Z_2 has the form:

$$Z_2 = \langle\{L_4, L_2, L_8\}, \{L_6, L_7, L_8\}, R_2, \vee(\wedge(L_4, L_2), L_8)\rangle,$$

where

R_2 =

	L_6	L_7	L_8
L_4	*false*	*false*	*true*
L_2	*false*	*falsee*	*true*
L_8	$W_{8,6}$	$W_{8,7}$	$W_{8,8}$

and:

- $W_{8,6}$ ="it's necessary to select new data ";
- $W_{8,7}$ ="There are preprocessed data for partitioning";
- $W_{8,8}= \neg (W_{8,6} \wedge W_{8,7})$.

The β_1- and α_3-tokens, entering in place L_8 from places L_4, L_2 don't obtain new characteristics. The token in place L_8 generates two new α_5- and α_6- tokens that enter in places L_6 and L_7 with characteristics: „*data*“ in place L_6 and „*preprocessed data for partitioning* “ in place L_7.

The γ_1-token that enters the net via place L_{12} has initial characteristic: "*criteria for partitioning*". The transition Z_3 has the form:

$$Z_3 = \langle \{L_{12}, L_7, L_{18}\}, \{L_{14}, L_{15}, L_{16}, L_{17}, L_{18}\}, R_3, \vee(\wedge(L_{12}, L_7), L_{18}) \rangle,$$

where

R_3 =

	L_{14}	L_{15}	L_{16}	L_{17}	L_{18}
L_{12}	*false*	*false*	*false*	*false*	*true*
L_7	*false*	*false*	*false*	*false*	*true*
L_{18}	$W_{18,14}$	$W_{18,15}$	$W_{18,16}$	$W_{18,17}$	$W_{18,18}$

and:

- $W_{18,14}$ ="it's necessary to select new data ";
- $W_{18,15}$ ="There is training set for classification";
- $W_{18,16}$ ="There is validation set for validation the received model";
- $W_{18,17}$ ="There is testing set for testing the received model ";
- $_{18,18}= \neg (W_{18,14} \wedge W_{18,15} \wedge W_{18,16} \wedge W_{18,17})$.

The γ_1- and α_6- tokens, entering in place L_{18} from places L_{12}, L_7 don't obtain new characteristics. The token in place L_{18} generates new α_8-, α_9-,α_{10}- *and* α_{11}- tokens that enter in places L_{14}, L_{15}, L_{16} and L_{17} with characteristics: „*data* " in place L_{14}, „*training set for classification*" in place L_{15}, „*validation set*" in place L_{16} and „*testing set*" in place L_{17}.

The δ_1-token enters the net via place L_5 and has initial characteristic: "*criteria for classification (and validation the classified model)*". The transition Z_4 has the form:

$$Z_4 = \langle \{L_5, L_{27}, L_{11}\}, \{L_9, L_{10}, L_{11}\}, R_4, \vee(L_5, L_{27}, L_{11}) \rangle,$$

where

R_4 =

	L_9	L_{10}	L_{11}
L_5	*false*	*false*	*true*
L_{27}	*false*	*false*	*true*
L_{11}	$W_{11,9}$	$W_{11,10}$	$W_{11,11}$

and:

- $W_{11,9}$ =" There are selected criteria for validation ";
- $W_{11,10}$ ="There are selected criteria for classification";
- $W_{11,11}= \neg (W_{11,9} \wedge W_{11,10})$.

The δ_1- and α_{16}- tokens, entering in place L_{11} from places L_5, L_{27} don't obtain new characteristics. The δ_2-token in place L_{11} generates new δ_3- and δ_4- tokens that enter in places L_9, L_{10} with characteristics: „*selected criteria for validation*" in place L_9, „*selected criteria for classification*" in place L_{10}.

The η_1-token enters the net via place L_{13} and has initial characteristic: "*methods for classification*". The transition Z_5 has the form:

$$Z_5 = \langle \{L_{13}, L_{28}, L_{20}\}, \{L_{19}, L_{20}\}, R_5, \vee(L_{13}, L_{28}, L_{20}) \rangle,$$

where

R_5 =

	L_{19}	L_{20}
L_{13}	*false*	*true*
L_{28}	*false*	*true*
L_{20}	$W_{20,19}$	$W_{20,20}$

and:

- $W_{20,19}$ ="There is selected method (technique) for classification";
- $W_{20,20}= \neg W_{20,19}$.

The η_1- and α_{17}- tokens, entering in place L_{20} from places L_{13}, L_{28} don't obtain new characteristics. The token in place L_{20} generates one new η_3-token that enter in places L_{19} with characteristic: „*selected method for classification*".

The λ_1-token enters the net via place L_{21} and has initial characteristic: "algorithms for classification". The transition Z_6 has the form:

$$Z_6 = \langle \{L_{21}, L_{19}, L_{23}\}, \{L_{22}, L_{23}\}, R_6, \vee(\wedge(L_{21}, L_{19}), L_{23}) \rangle,$$

where

R_6 =

	L_{22}	L_{23}
L_{21}	*false*	*true*
L_{19}	*false*	*true*
L_{23}	$W_{23,22}$	$W_{23,23}$

and:

- $W_{23,22}$ ="There is selected algorithm for classification method (technique)";
- $W_{23,23}= \neg W_{22,22}$.

The λ_1- and η_3- tokens, entering in place L_{23} from places L_{21}, L_{19} don't obtain new characteristics. The token in place L_{23} generates one new λ_3-token, that enters in places L_{22} with characteristic: „*selected algorithm for classification method*". The transition Z_7 has the form:

$Z_7 = \langle \{L_{30}, L_{33}, L_{15}, L_{10}, L_{22}, L_{29}\}, \{L_{24}, L_{25}, L_{26}, L_{27}, L_{28}, L_{29}\}, R_7, \vee(\wedge(L_{15}, L_{10}, L_{22}), L_{30}, L_{33}, L_{29}) \rangle$, where

R_7 =

	L_{24}	L_{25}	L_{26}	L_{27}	L_{28}	L_{29}
L_{30}	*false*	*false*	*false*	*false*	*false*	*true*
L_{33}	*false*	*false*	*false*	*false*	*false*	*true*
L_{15}	*false*	*false*	*false*	*false*	*false*	*true*
L_{10}	*false*	*false*	*false*	*false*	*false*	*true*
L_{22}	*false*	*false*	*false*	*false*	*false*	*true*
L_{29}	$W_{29,24}$	$W_{29,25}$	$W_{29,26}$	$W_{29,27}$	$W_{29,28}$	$W_{29,29}$

- $W_{29,24}$ ="It is necessary new dataset to be chosen";

- $W_{29,25}$ ="there is a constructed classification model for validation";
- $W_{29,26}$ ="there is a constructed classification model";
- $W_{29,27}$ ="It is necessary new criteria to be chosen ";
- $W_{29,28}$ ="It is necessary new method for classification to be chosen ";
- $W_{29,29}= \neg(W_{29,24} \wedge W_{29,25} \wedge W_{29,26} \wedge W_{29,27} \wedge W_{29,28})$.

The α_{19}-, α_{22}-, α_9-,δ_4- and λ_3- tokens, entering in place L_{29} from places L_{30}, L_{33}, L_{15}, L_{10}, L_{22} don't obtain new characteristics. The token in place L_{29} generates new α_{13}-,α_{14}- and α_{15}- tokens, that enter in places L_{24}, L_{25}, L_{26} with the following characteristics: „*data*“ in place L_{24}, „*constructed classification model for validation*“ in place L_{25}, „*constructed classification model*“ in place L_{26}. The tokens, entering in place L_{27} and L_{28} don't obtain new characteristics.

The transition Z_8 has the form:

$$Z_8 = \langle \{L_{25}, L_9, L_{16}, L_{32}\}, \{L_{30}, L_{31}, L_{32}\}, R_8, \vee(\wedge(L_{25}, L_9, L_{16}), L_{32})\rangle,$$

where

R_8 =

	L_{30}	L_{31}	L_{32}
L_{25}	*false*	*false*	*true*
L_9	*false*	*false*	*true*
L_{16}	*false*	*false*	*true*
L_{32}	$W_{32,30}$	$W_{32,31}$	$W_{32,32}$

and:

- $W_{32,30}$="there is a validated classification model";
- $W_{32,31}$ =" there is a validated classification model for testing";
- $W_{32,32}= \neg (W_{32,30} \wedge W_{32,31})$.

The α_{14}-,δ_3-,α_{10}- and tokens, entering in place L_{32} from places L_{25}, L_9, L_{16}, don't obtain new characteristics. The token in place L_{32} generates newα_{19}- and α_{20}- tokens, that enter in places L_{30}, L_{31} with the following characteristics: „*validated classification model*“ in place L_{30} and „*validated classification model for testing*“ in place L_{31}.

The transition Z_9 has the form:

$$Z_9 = \langle \{L_{31}, L_{17}, L_{34}\}, \{L_{33}, L_{34}\}, R_9, \vee(L_{31}, L_{17}, L_{34})\rangle,$$

where

R_9 =

	L_{33}	L_{34}
L_{31}	*false*	*true*
L_{17}	*false*	*true*
L_{34}	$W_{34,33}$	$W_{34,34}$

and:

- $W_{34,33}$ ="there is a tested classification model";
- $W_{34,34}= \neg W_{34,33}$.

The α_{20}- and α_{11}- tokens, entering in place L_{34} from places L_{31}, L_{17} don't obtain new characteristics. The token in place L_{34} generates one new α_{22}- token, that enters in place L_{33} with the characteristic: „*tested classification model*“.

CONCLUSION

The constructed Generated net model can be used for description and simulation of the classification analysis. The transitions of the net can be replaced by subnets that describe the subprocesses in detail. In future research, the presented generalized net model of the process of classification will be modified by extending its transitions.

ACKNOWLEDGEMENT

This work is partially supported by the project of Asen Zlatarov University under Ref. No. NIH-418/2018 "Intelligent instruments for knowledge discovering and processing" and Bulgarian National Science Fund, Grant Ref. No. DN-02-10/2016 "New Instruments for Knowledge Discovery from Data, and their Modelling".

REFERENCES

1. Aggarwal C., Data Mining: The Textbook, Springer, 2015.
2. Atanassov K.: Generalized Nets as a Tool for the Modelling of Data Mining Processes, IN: *Innovative Issues in Intelligent Systems, Vol. 623 of the series Studies in Computational Intelligence*, 161-215 (2016).
3. Atanassov, K. Generalized Nets. World Scientific, Singapore, 1991.
4. Atanassov, K. On Generalized Nets Theory. Prof. M. Drinov Academic Publishing House, Sofia, 2007.
5. Atanassov K., E. Sotirova, Generalized Nets, Prof. Marin Drinov Academic Publishing House, 2017 (in bulgarian).
6. Bramer M., Principles of Data Mining, Springer, 2013, ISBN: 978-1-4471-4883-8.
7. Bureva V., E. Sotirova, Generalized Net Of The Process Of Association Rules Discovery By Eclat Algorithm Using Weather Databases, *14-Th Int. Workshop On Generalized Nets*, 2013,1-10.

8. Bureva V., E. Sotirova, K. Atanassov, Hierarchical generalized net model of the process of selecting a method for clustering, *15th Int. Workshop on Generalized Nets*, 2014, p. 39–48.
9. Bureva V., E.Sotirova, K. Atanassov, Hierarchical generalized net model of the process of clustering, *Issues in Intuitionistic Fuzzy Sets and Generalized Nets*, Warsaw School of Information Technology, Vol.1, 2014, p.73-80.
10. Bureva V., M. Puleva, E.Sotirova, Generalized Net Of The Process Of Support Vector Machines Classifier Construction, Annual of the Informatics Section, Union of Scientists in Bulgaria, Vol. 7, 2014.
11. Bureva V., P. Chountas, K. Atanassov. A Generalized Net Model Of The Process Of Decision Tree Construction. Proc. Of 13th Workshop On Generalized Nets, London, 29 October 2012,1-7.
12. Bureva V., S. Popov, E. Sotirova, B. Miteva, Generalized net of the process of hierarchical cluster analysis, Annual of Assen Zlatarov University, Burgas, Bulgaria, 2017, v. XLVI.
13. Sotirov S., Opportunities for application of the intercriteria analysis method to neural network preprocessing procedures, 2 and International IFS Conference, Mersin, Turkey, 14–18 Oct. 2015 Notes on Intuitionistic Fuzzy Sets., Vol. 21, 2015, No. 4, 143–152.
14. Sotirova E., Classification of the students' intuitionistic fuzzy estimations by a 3-dimensional self organizing map, Seventh International Workshop on IFSs, Banská Bystrica, Slovakia, 27 Sept. 2011 NIFS 17 (2011), 4, 39–44.
15. Sotirova, E., D. Orozova, Generalized Net Model Of The Phases Of The Data Mining Process, Developments In Fuzzy Sets, Intuitionistic Fuzzy Sets, Generalized Nets And Related Topics. Vol. II: Applications, Warsaw, Poland, 2010, 247–260.
16. Zoteva D., Krawczak M., Generalized Nets as a Tool for the Modelling of Data Mining Processes. A Survey, Issues in IFSs and GNs, Vol. 13, 2017, 1–60.

ANNUAL OF ASSEN ZLATAROV UNIVERSITY, BURGAS
BULGARIA, 2018, v. XLVII (I)

INTERCRITERIA ANALYSIS OF THE GYROSCOPE DRIFT

Todor Kostadinov
E-mail: kostadinov_todor@btu.bg

ABSTRACT

This work presents an application of the intercriteria analysis approach over the readings obtained by an integrated sensor. Due to bias instabilities in the gyroscope data an angular error occurs, which causes an instability and displacement in the readings of the accelerometer unit and thus displacement in the direction readings. The aim of the present work is to establish a correlation in the gyroscope drift in order to facilitate the filtration of noise that causes displacement. The approach is performed over experimental data gathered by a combined sensor.

Key words: *gyroscope drift, gyroscope bias, intercriteria analysis, white noise*

INTRODUCTION

Since the beginning of ground and air transportation navigation and positioning are of the greatest importance. In order to keep certain trajectory, direction and orientation, especially in case no reference point is available, it is necessary to exclude deviation in the course. This is performed by using the gyroscope principle [1]. This principle is also applicable in the field of optical stabilization, motion sense and navigation [2]. The gyroscope effect is implemented in the Micro Electro Mechanical System (MEMS) suitable for embedded systems and micro devices [1, 2]. Due to temperature fluctuations and presence of noise, it is difficult to maintain stability. An analysis approach and compensation method for the gyroscope drift has been proposed in [3]. Adaptive temporal noise modelling technique to compensate the gyroscope bias is suggested in [4]. Due to the noise nature and multitude of factors that influence the gyroscope bias, it is difficult to devise a technique for its full compensation. Noise filtration using kalman filter [6] is an option. Its application is usually related to increased computational burden of the system that may affect the response time. The Intercriteria analysis (ICA) approach [5] proposed in this work is an approach that facilitates the decision-making process by providing the correlation of certain criteria for a set of objects. By using the data measured by the sensor in different speed and direction of movement on the whole coordinate system axis, it is possible to obtain the pattern of the noise and thus improve the sensor accuracy. The data sampling from the sensor in a variety of cases is performed in section one, section two deals with the data analysis and section three presents the obtained results.

DATA SAMPLING APPROACH

The sensor, an object of analysis, is manufactured by Pololu under the model altimu-10 v5, a sensor of combined type: gyroscope, accelerometer, compass, and altimeter. The unit consists of the following modules: LSM6DS33 that represents a 3-axis gyroscope and accelerometer, LIS3MDL 3-axis magnetometer, and LPS25H digital barometer. The modules combined together form an inertial measurement unit (IMU). To interface the sensor unit with a microcontroller unit (MCU) an IIC interface is used. The software on the MCU performs the processing of the sampled data which is then transferred to a personal computer (PC) for further visualisation, processing and decision making by applying the ICA with respect to the reduced computational capabilities of the MCU. The structure of the data sampling system is presented in Fig. 1.

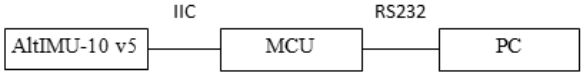

Fig. 1. Structure of a data sampling system

The data output is formatted as a vector containing three elements: roll, yaw and pitch angle for one measurement. The sample rate of the sensor is one hundred milliseconds. The data is then visualised in terms of the angle of roll that stands for the angle of rotation of the *x* axis, angle of yaw which is the angle of rotation of the *y* axis and angle of pitch – the turning angle of *z* axis. In order to state the gyroscope bias a visual

representation of the data sampled during idle state of the sensor in four different positions is performed. In the first position the *x* axis of the sensor is oriented collineary to the ground, *y* axis is oriented transversally to the *x* axis and the *z* axis is pointing up – a left oriented coordinate system, stated as reference. The deviation of roll, pitch and yaw angles is presented in Fig. 2. The second measurement of gyroscope bias is with a sensor rotated at 90 degrees on axis *x* as shown in Fig. 3 and the third measurement is performed with the sensor rotated at 90 degrees on axis *y* - Fig. 4.

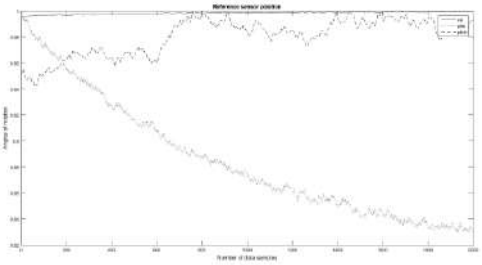

Fig. 2. Bias during idle state of the sensor in reference position

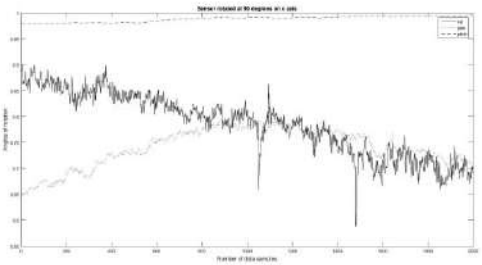

Fig. 3. Bias during idle state and sensor *y*-*z* plane rotated at 90 degrees

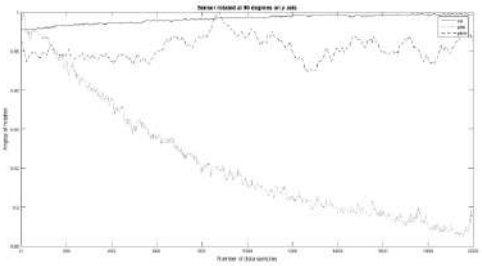

Fig. 4. Bias during idle state and sensor *x*-*z* plane rotated at 90 degrees

The last data present the gyroscope noise during rotation of the *z* plane at 90 degrees as presented in Fig. 5:

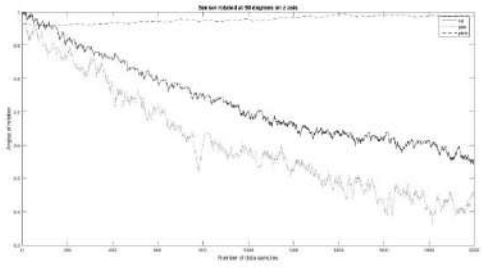

Fig. 5. Bias during idle state and sensor *x*-*y* plane rotated at 90 degrees

As can be seen in Figs. 2 – 5, the gyroscope drift can be regarded as an additive white noise to the data sampled at four different positions of the sensor. The four data sets differ according to the position of the sensor which makes the filtration process even more difficult.

DATA ANALYSIS APPROACH

The method, called intercriteria analysis, applies the concepts of intuitionistic fuzzy sets and index matrices over an array of data that consist of objects and criteria. It is introduced in [5]. To discover the relationships and examine the correlations between the values of an image of opportunity, the InterCriteria Decision Making method (ICDM) is used.

The objects can be estimated over several criteria. The number of the criteria can be reduced by taking into account the correlations of each pair of criteria presented in the form of intuitionistic fuzzy pairs of values. The intuitionistic fuzzy pairs of values are the intuitionistic fuzzy evaluations in the interval [0,1]. The relations can be established between any two groups of indicators C_w and C_t.

Let us have a number of C_q group of indicators, q= 1, …, n, and a number of O_p universities, p= 1, …, m. So we use the following sets: a set of indicators C_q=$\{C_1,\ldots, C_n\}$ and a set of universities O_p = $\{O_1,\ldots, O_m\}$.

An index matrix M that contains two sets of indices, one for rows and another for columns is evaluated for each processed image. For every p, q ($1 \le p \le m$, $1 \le q \le n$), O_p in an evaluated object, C_q is an evaluation criterion, and a_{O_p,C_q} is the evaluation of the p-th object against the q-th criterion, defined as a real number or another object that is comparable according to relation R with all the rest of the elements of the index matrix M.

$$M = \begin{array}{c|cccccccc} & C_1 & \dots & C_k & \dots & C_l & \dots & C_n \\ \hline O_1 & a_{O_1,C_1} & \dots & a_{O_1,C_k} & \dots & a_{O_1,C_l} & \dots & a_{O_1,C_n} \\ \dots & \dots & \dots & \dots & \dots & \dots & \dots & \dots \\ O_i & a_{O_i,C_1} & \dots & a_{O_i,C_k} & \dots & a_{O_i,C_l} & \dots & a_{O_i,C_n} \\ \dots & \dots & \dots & \dots & \dots & \dots & \dots & \dots \\ O_j & a_{O_j,C_1} & \dots & a_{O_j,C_k} & \dots & a_{O_j,C_l} & \dots & a_{O_j,C_n} \\ \dots & \dots & \dots & \dots & \dots & \dots & \dots & \dots \\ O_m & a_{O_m,C_1} & & a_{O_m,C_k} & & a_{O_m,C_l} & \dots & a_{O_m,C_n} \end{array}.$$

From the requirement for comparability above, it follows that for each i, j, k, l the relation $R(a_{O_i,C_k}, a_{O_j,C_k})$ holds. The relation R has dual relation $\bar{R}$, which is true in the case when relation R is false, and vice versa.

The approach aims to discover correlation in the noise added to the sensor readings. For that purpose the data that consist noise measured in idle state along with the data sampled during the movement of the sensor in all coordinate axis is used as a criterion. The values sampled on even intervals for each criterion is used for objects.

The ICA approach is applied over more than 5,000 objects and the following criteria:

- 1 – Idle in reference position
- 2 – Idle for x axis rotation
- 3 – Idle for y axis rotation
- 4 – Idle for z axis rotation
- 5 – Movement on x axis
- 6 – Movement on y axis
- 7 – Movement on z axis
- 8 – Random movement

The ICA has been performed over the sampled data to determine the degrees of correlation between the criteria, depending on the user's choice of μ and ν. We call these correlations between the criteria: 'positive consonance', 'negative consonance' or 'dissonance' as presented in Fig. 6

Fig. 6. Scale of the type of the correlations between the criteria

The values of interest are between 0 and 0.15 and 0.85 and 1 which stands for negative consonance and positive consonance.

RESULTS

In order to find a pattern it is required to compare the gyroscope bias for the cases of sensor in idle state, moving on a single axis and randomly moving on all axis for every one of the parameters – roll, yaw and pitch. This is performed in the Figs. 7 – 9. The following correlation between criteria for the angle of roll occurs (Fig. 7): positive consonance is observed for criteria 1-2, 1-3, 1-5, 2-3, 2-5,3-5, 4-6, 4-7, negative consonance is discovered among criteria 1-4, 1-6, 1-7, 2-4, 2-6, 2-7, 3-4, 3-6, 3-7, 4-5. The correlations for the angle of yaw (Fig. 8) are as follows: positive consonances for criteria 1-3, 1-4, 1-5, 3-4,3-5, and negative for criteria 1-3, 1-4, 1-5, 3-4, 3-5, 4 -5. Last for the pitch angle in Fig. 9 the positive consonances are 3-6,3-7, 6-7 and the negative ones are 1-5, 3-6, 3-7.

ρ	1	2	3	4	5	6	7	8
1	1	0.813253	0.880495	0.214914	0.754898	0.091569	0.120822	0.408216
2	0.813253	1	0.819234	0.239265	0.717908	0.159872	0.205996	0.422347
3	0.880495	0.819234	1	0.169166	0.759737	0.059098	0.131888	0.417062
4	0.214914	0.239265	0.169166	1	0.265693	0.820423	0.745888	0.572567
5	0.754898	0.717908	0.759737	0.265693	1	0.207824	0.170251	0.389373
6	0.091569	0.159872	0.059098	0.820423	0.207824	1	0.87897	0.589405
7	0.120822	0.205996	0.131888	0.745888	0.170251	0.87897	1	0.607409
8	0.408216	0.422347	0.417062	0.572567	0.389373	0.589405	0.607409	1

σ	1	2	3	4	5	6	7	8
1	0	0.109445	0.052623	0.698076	0.169812	0.853445	0.822762	0.535002
2	0.109445	0	0.131976	0.690954	0.226236	0.808886	0.76111	0.544343
3	0.052623	0.131976	0	0.770818	0.194379	0.919234	0.84495	0.559297
4	0.698076	0.690954	0.770818	0	0.667242	0.135561	0.208615	0.381541
5	0.169812	0.226236	0.194379	0.667242	0	0.763697	0.799713	0.580271
6	0.853445	0.808886	0.919234	0.135561	0.763697	0	0.117812	0.407026
7	0.822762	0.76111	0.84495	0.208615	0.799713	0.117812	0	0.38713
8	0.535002	0.544343	0.559297	0.381541	0.580271	0.407026	0.38713	0

Fig. 7. Correlation between criteria for the angle of roll

ρ	1	2	3	4	5	6	7	8
1	1	0.622132	0.970483	0.807689	0.947465	0.695617	0.327473	0.438052
2	0.622132	1	0.622571	0.610747	0.611824	0.43576	0.382667	0.399681
3	0.970483	0.622571	1	0.805573	0.951265	0.700559	0.334092	0.44317
4	0.807689	0.610747	0.805573	1	0.79319	0.636758	0.293996	0.450403
5	0.947465	0.611824	0.951265	0.79319	1	0.697134	0.329261	0.441054
6	0.695617	0.43576	0.700559	0.636758	0.697134	1	0.361357	0.488743
7	0.327473	0.382667	0.334092	0.293996	0.329261	0.361357	1	0.485549
8	0.438052	0.399681	0.44317	0.450403	0.441054	0.488743	0.485549	1

σ	1	2	3	4	5	6	7	8
1	0	0.307832	0.008008	0.136327	0.028487	0.281725	0.647808	0.541581
2	0.307832	0	0.31319	0.296447	0.323633	0.503242	0.555106	0.541932
3	0.008008	0.31319	0	0.145102	0.030675	0.284639	0.649557	0.544782
4	0.136327	0.296447	0.145102	0	0.156926	0.316854	0.658275	0.505916
5	0.028487	0.323633	0.030675	0.156926	0	0.28784	0.654675	0.54701
6	0.281725	0.503242	0.284639	0.316854	0.28784	0	0.62689	0.504096
7	0.647808	0.555106	0.649557	0.658275	0.654675	0.62689	0	0.506395
8	0.541581	0.541932	0.544782	0.505916	0.54701	0.504096	0.506395	0

Fig. 8. Correlation between criteria for the angle of yaw

ρ	1	2	3	4	5	6	7	8
1	1	0.18796	0.157238	0.294459	0.732966	0.228942	0.259265	0.54788
2	0.18796	1	0.670611	0.614371	0.337749	0.631641	0.601413	0.519122
3	0.157238	0.670611	1	0.561693	0.209888	0.750842	0.77596	0.430435
4	0.294459	0.614371	0.561693	1	0.491066	0.49592	0.472279	0.468974
5	0.732966	0.337749	0.209888	0.491066	1	0.071968	0.102251	0.602315
6	0.228942	0.631641	0.750842	0.49592	0.071968	1	0.839944	0.376942
7	0.259265	0.601413	0.77596	0.472279	0.102251	0.839944	1	0.407489
8	0.54788	0.519122	0.430435	0.468974	0.602315	0.376942	0.407489	1

σ	1	2	3	4	5	6	7	8
1	0	0.737485	0.7981	0.653198	0.231872	0.738858	0.706475	0.420471
2	0.737485	0	0.265549	0.314379	0.60804	0.31818	0.346635	0.431345
3	0.7981	0.265549	0	0.397621	0.767593	0.23085	0.203369	0.552208
4	0.653198	0.314379	0.397621	0	0.478834	0.477884	0.499337	0.505525
5	0.231872	0.60804	0.767593	0.478834	0	0.920679	0.88816	0.391313
6	0.738858	0.31818	0.23085	0.477884	0.920679	0	0.154707	0.621485
7	0.706475	0.346635	0.203369	0.499337	0.88816	0.154707	0	0.588128
8	0.420471	0.431345	0.552208	0.505525	0.391313	0.621485	0.588128	0

Fig. 9. Correlation between criteria for the angle of pitch

Visual representation of the correlating criteria is depicted in Figs 10 – 12, where all of the criteria are placed in the intuitionistic triangle. It represents the degree of membership, non-membership or uncertainty of the correlating pairs.

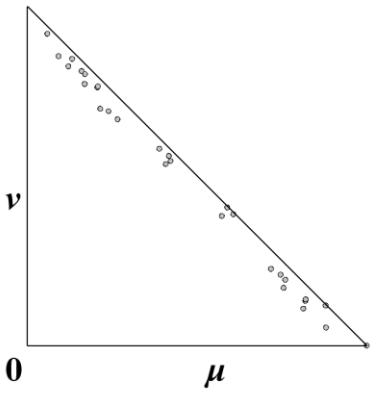

Fig. 10. Intuitionistic triangle of the criteria for the angle of roll

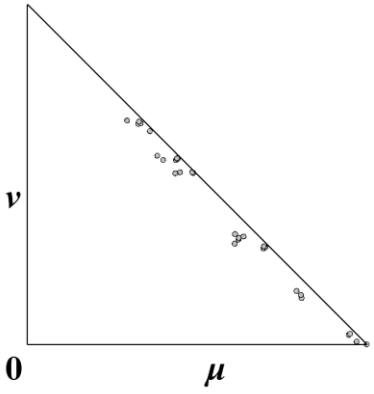

Fig. 11. Intuitionistic triangle of the criteria for the angle of yaw

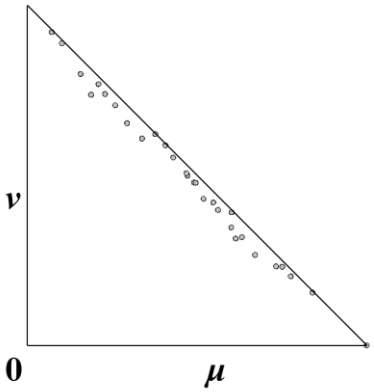

Fig. 12. Intuitionistic triangle of the criteria for the angle of pitch

As can be observed from the figures above, the criteria with the highest level of correlation are the idle reference position – 1, idle for *y* and *z* rotation – 2 and 3, movement on *x* and movement on *z* axis – 5 and 7.

Criterion 8 – random sensor movement data does not correlate with the other criteria. This means that the gyroscope noise can be predicted when the sensor is idle or it is moving in one direction, but not in any other case for the current data set. It is obvious when the ICA is applied over all data sets, including roll, yaw and pitch data (Fig. 13).

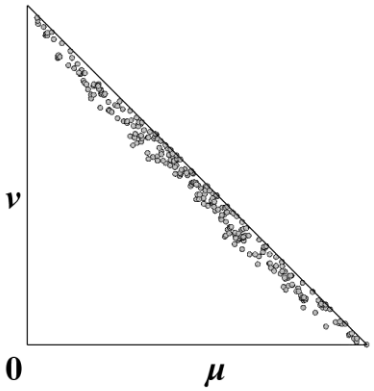

Fig. 13. Intuitionistic triangle for all criteria

As seen in Fig. 13, there is a high level of uncertainty (most of the correlating criteria are in the middle of the hypotenuse) and too few are located in the areas of high consonance (at both ends of the hypotenuse) and thus a noise pattern is difficult to be extracted.

CONCLUSION

An analysis of the gyroscope drift expressed as a bias in the direction of movement caused by the presence of an additive white noise to the sensor data has been performed. The analysis in section two included a novel approach in multi criteria decision making called the intercriteria analysis (ICA). The purpose is the establishment of correlation between the data sampled by the gyroscope: gyroscope in idle position, rotation and movement on single coordinate axis and random movement. As a result, an uncertainty between the criteria under analysis has been established. This could be explained with the small number of criteria taken as well as the insufficient number of objects and thus no noise pattern can be extracted from the data in order to facilitate the process of noise filtration.

An object of future work is the repetition of the proposed analysis procedure over a large set of data including several sensors of different type as well as data sampled in different conditions.

REFERENCES

1. Piyabongkarn, D., Rajamani, R., Greminger, M., "The development of a MEMS gyroscope for absolute angle measurement", IEEE Transactions on Control Systems Technology, Vol. 13 , Issue: 2, pp 185 – 195, 28 February 2005
2. Barbour, N., Schmidt, G., "Inertial sensor technology trends", IEEE Sensors Journal, Volume: 1 , Issue: 4, pp 332 – 339, Dec 2001
3. Diao, Z., Quan, H., Lan, L., Han, Y., "Analysis and compensation of MEMS gyroscope drift", 2013 Seventh International Conference on Sensing Technology (ICST), Wellington, New Zealand, 3-5 Dec. 2013, ISBN: 978-1-4673-5222-2
4. Priydarshi, Jaiswal, R., Nair, R., Yarlagadda, N., Senapati, A., Mulage, P., "Adaptive gyroscope drift compensation based on temporal noise modelling", 2016 International Conference on Microelectronics, Computing and Communications (MicroCom), Durgapur, India, 23-25 Jan. 2016, ISBN: 978-1-4673-6621-2
5. Atanassov, K., D. Mavrov, V. Atanassova. Intercriteria Decision Making: A New Approach for Multicriteria Decision Making, Based on Index Matrices and Intuitionistic Fuzzy Sets. Issues in Intuitionistic Fuzzy Sets and Generalized Nets, Vol. 11, 2014, 1–8.
6. Sabatini, A.M., "Quaternion-based extended Kalman filter for determining orientation by inertial and magnetic sensing", IEEE Transactions on Biomedical Engineering (Volume: 53 , Issue: 7 , July 2006), p.p. 1346 – 1356,

ANNUAL OF ASSEN ZLATAROV UNIVERSITY, BURGAS
BULGARIA, 2018, v. XLVII (1)

STUDY OF THE EFFECT OF TURBINE BLADE PITCH ANGLE ON FLOW HYDRODYNAMICS

Dimitar Rusev
E-mail: dr_rusev@mail.bg

ABSTRACT

In engineering practice, both graphical and analytical methods are used to build the profile of subsonic turbine blades. In the present work, a method employing three dimensional simulations of the hydrodynamics of flow of the coolant through the working and guiding wheels of the turbine is suggested for optimization of turbine blade shape.

The method suggested makes it possible to build a complete picture of the hydrodynamic conditions of operation of the turbine in the design phase and take measures to optimize the shape and angle of the blades, the velocity triangle for relevant extent and avoid areas of turbulence flow which greatly downgrades turbine efficiency.

Key words: *turbines, turbine vanes, hydrodynamics*

INTRODUCTION

At present, the conversion of heat energy to electric one can be classified as an insufficiently effective process. Therefore, new technological solutions as well as new approaches to the organization of this process should be looked for. The existing ORC (Organic Rankine Cycle) installations use turbines with non-aqueous heat carrier. The expansion of the fluid within them is adiabatic, due to which their efficiency coefficient is usually in the range from 5% to 17% in the best case. This expansion method does not provide the necessary results and it is a precondition for building large-size and inefficient installations.

New solutions have been suggested in the literature [1] for organization of the expansion of the heat carrier to increase process efficiency. However, this approach involves the use of turbines working with Freon in a closed cycle.

Another solution in the efforts to increase the coefficient of efficiency of the installations is to find an optimal design of turbine blades (Fig. 1), which takes into account the thermodynamic properties of the heat carrier [2], flow hydrodynamics and the working angles of the velocity triangle, and conforming with certain conditions: size, rounds per minute, power generated and high efficiency of the turbine. To fulfil all these requirements and ensure the necessary working speed of the flow, often blades with small cross-sections are used. This sharply reduces their surface area and operating efficiency.

On the other hand, the methods used for dimensioning and constructive design of the turbines [3-6] use many experimentally determined coefficients and diagrams. They have been derived under various working conditions and their application results in certain deviations.

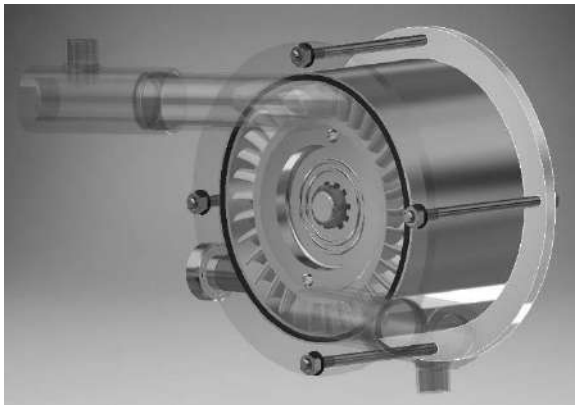

Fig. 1. Turbine design

To solve this problem, it is necessary to optimize the shape of the channels and blades for a particular design. This can be done by simulation modelling of the process of expansion and the hydrodynamics of the particular turbine which allows to obtain correction coefficients and use them to improve the calculations and increase turbine efficiency as a whole. Furthermore, the development of a correct mathematical model of the turbine working under action of dynamic forces might improve its reliability [6].

FORMULATION OF THE PROBLEM

At given initial parameters of the heat carrier and working conditions: consumption, temperature, dynamic viscosity and pressure, it is necessary to determine the absolute velocity of the flow at outlet nozzle and at the inlet of the first stage of the turbine.

To determine this velocity, the nozzle dimensioning methods of de Laval [7] were used (Fig. 2).

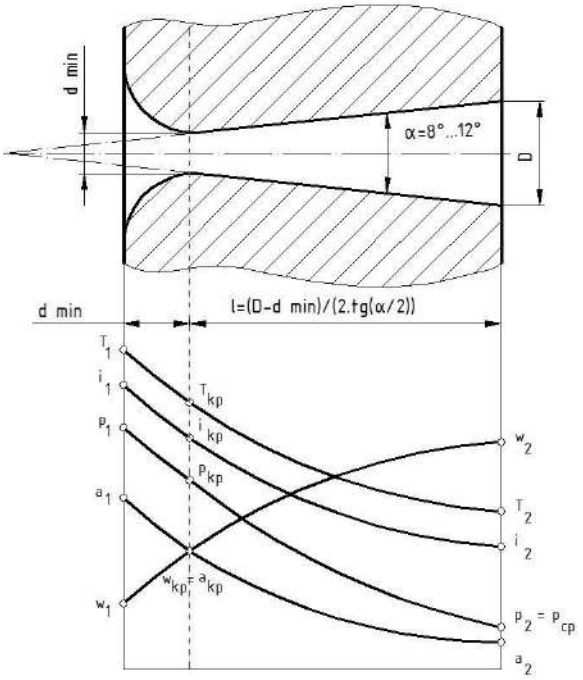

Fig. 2. Dimensioning of the nozzle

Using computer modelling and investigating the three dimensional models of the nozzle, results were obtained for the distribution and magnitude of the velocities and pressures. Fig.3 shows their distribution along the nozzle unit. Using these data, an analysis of the performance can be made and take constructive measures to optimize the length and angle of the diffuser and the critical dimensions of the nozzle.

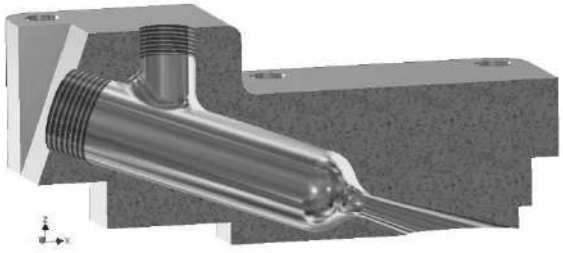

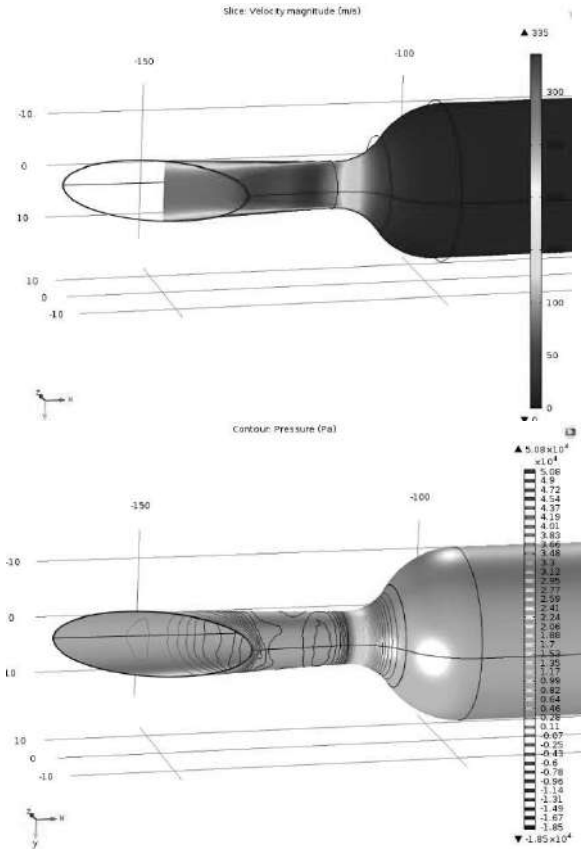

Fig. 3. Distribution of the flow velocity and pressure at nozzle outlet

The numeric results obtained for the flow velocity at nozzle outlet at heat carrier debit (Freon R-507a) 0.122 kg/s and pressure at the inlet 1.5 MPa were up to 260 m/s. These results were almost the same as the ones calculated theoretically according to the dependence [7]:

$$w_2 = \sqrt{\frac{2.k.p_1.\rho_1}{k-1}.\left[1-\left(\frac{p_2}{p_1}\right)^{\frac{k-1}{k}}\right]}, \text{ m/s} \qquad (1)$$

where: k - is the coefficient of adiabaticity determined by dependences (2) and (3):

$$\frac{T_2}{T_1} = \left(\frac{\rho_1}{\rho_2}\right)^{k-1} \qquad (2)$$

$$k = 1 + \frac{lu\left(\frac{T_2}{T_1}\right)}{lu\left(\frac{\rho_1}{\rho_2}\right)} \qquad (3)$$

p_1 - vapor pressure at nozzle inlet, MPa;

p_2 - vapor pressure at nozzle outlet, MPa;

ρ_1 - relative volume of the vapor at nozzle inlet, m^3/kg;

T_1 - vapor temperature at nozzle inlet, ^0C;

T_2- vapor temperature at nozzle outlet, ^0C.

Knowing the velocities at the outlet of the nozzle unit and using computer modelling and investigation of three dimensional models, the flow around the blades can be simulated and the velocity and hydrodynamics of the flow at the inlet of the first stage of the turbine analyzed. Besides, it should be taken into account that a certain number of blades work with one nozzle so the flow and its kinetic energy are distributed among several channels. The flow distribution and the specifics of the hydrodynamics in the channels of the first working wheel are illustrated in Fig. 4.

On the basis of these results, decisions are taken for optimization of the blades shape and the front and rear angles. This leads to optimization of the velocity triangle (Fig. 5) for the particular design at the given parameters.

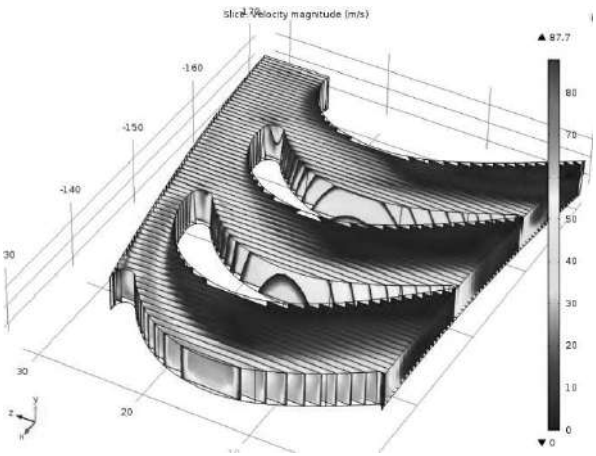

Fig. 4. Distribution of the flow velocities at the inlet of the first stage of the turbine.

As can be seen from Fig. 4, there was good flow around without vortex zones and it optimally converts the kinetic energy of the flow to mechanical work.

Blade height was determined by the dependence [4]:

$$l = \frac{G.\nu}{\pi.d.\varepsilon.c_1.\sin\alpha_1} \qquad (4)$$

where: G - heat carrier consumption, kg/s;
ν - dynamic viscosity of the heat carrier under the selected conditions of operation, Pa. s;
d - average diameter of the blade, m;
ε - degree of partiality;
c_1 - velocity of the fluid flow, m/s;
α_1 - inlet angle of the flow.

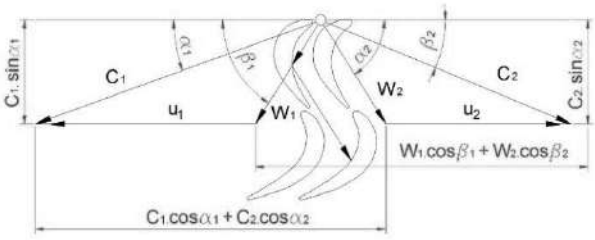

Fig. 5. Velocity triangle

The tangential force generated by the vapor stream attacking the blades is determined using dependence (5) [4]. The magnitude and direction of this force is determined by the configuration of the velocity triangle (Fig. 5).

$$P_U = G(w_1.\cos\beta_1 + w_2.\cos\beta_2) \qquad (5)$$

where: w_1 is the relative inlet velocity at the working blade, m/s, and w_2 - relative outlet velocity of the working blade, m/s.

The latter are determined by the equations:

$$w_1 = c_1.\frac{\sin\alpha_1}{\sin\beta_1},\ \text{m/s} \qquad (6)$$

$$w_2 = \psi.c_1,\ \text{m/s} \qquad (7)$$

where: α_1 - angle of the vapor stream with respect to the working wheel; $\alpha_1 = 10° \div 25°$;
β_1 – inlet angle of the working blade; β_2 – outlet angle of the working blade;
ψ – velocity coefficient of the working blade (from 0.6 to 0.95) which is determined from the graphical dependence and is a function of the sum $\beta_1 + \beta_2$.

The angle β_1 is calculated by the dependence:

$$\beta_1 = \text{arctg}\left(c_1.\frac{\sin\alpha_1}{c_1.\sin\alpha_1 - u}\right) = \text{arctg}\left(\frac{\sin\alpha_1}{\cos\alpha_1 - \frac{u}{c_1}}\right) \qquad (8)$$

Where the absolute outlet velocity of the blade is

$$c_{2л} = \frac{w_2.\sin\beta_2}{\sin\alpha_2},\ \text{m/s}, \qquad (9)$$

and α_2 is calculated by the equation

$$\text{tg}\alpha_2 = \frac{\sin\beta_2}{\cos\beta_2 - \frac{u}{w_2}} \qquad (10)$$

The studies and simulations made on the basis of the mathematical model suggested showed that a criterion for optimal hydrodynamics of the working and guiding wheels in the individual sections of the turbine is the rotation angle at blade rear. This angle shapes the cross section of

the channels in the zones of outflow from the blade (Fig. 6).

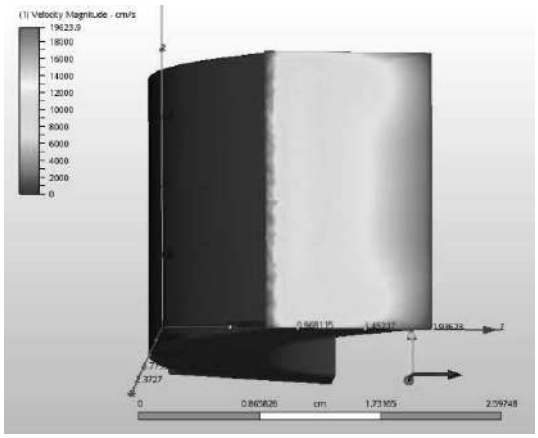

Blade with vertical rear wall

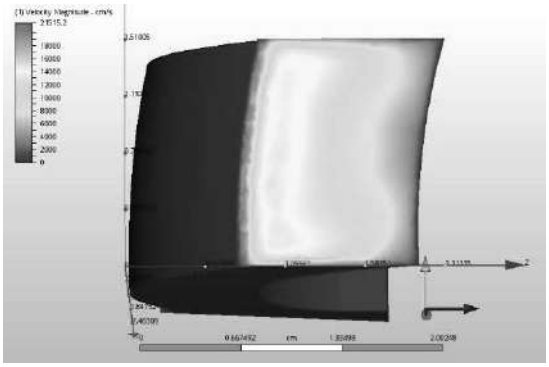

Blade with rear wall at 10° angle

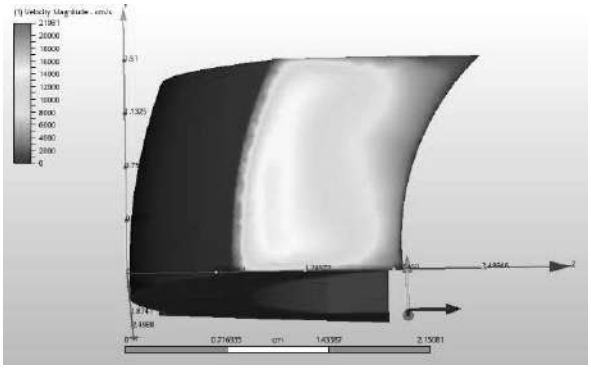

Blade with rear wall at 15° angle

Fig. 6. Influence of the slope at blade rear on the hydrodynamics of the flow

Analyzing the results illustrated in Fig. 6, it can be concluded that the flow distribution concentrates at blade base with the increase of the rotation angle of the blade at equivalent initial conditions. This results in flow densification and increase of the tangential force generated by the vapor stream acting on the working blades (5). A result of the increased tangential force is the increase of the flow velocity (Fig. 6), velocity of wheel rotation and, hence, turbine power. Therefore, under equivalent conditions, greater power is generated and the coefficient of efficiency of the whole turbine increases.

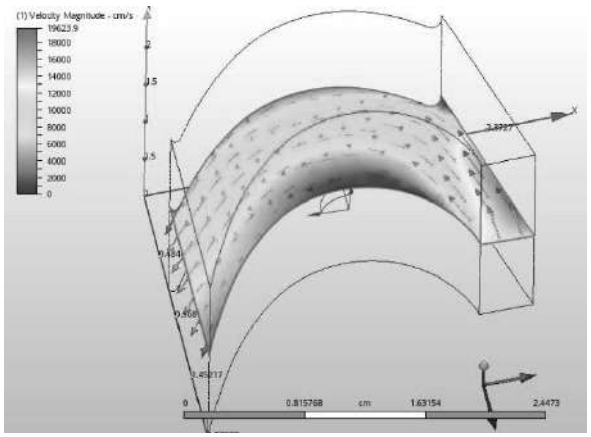

Blade with vertical rear wall

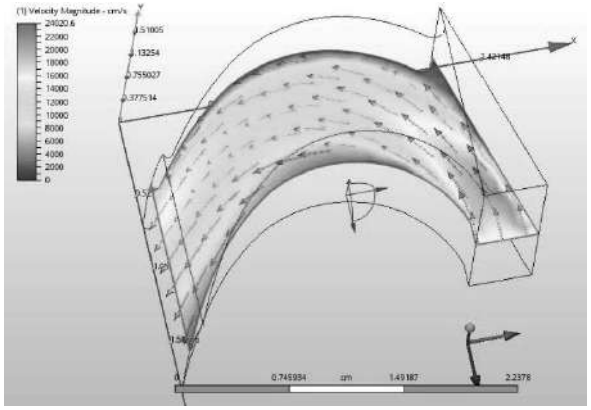

Blade with rear wall at 10°

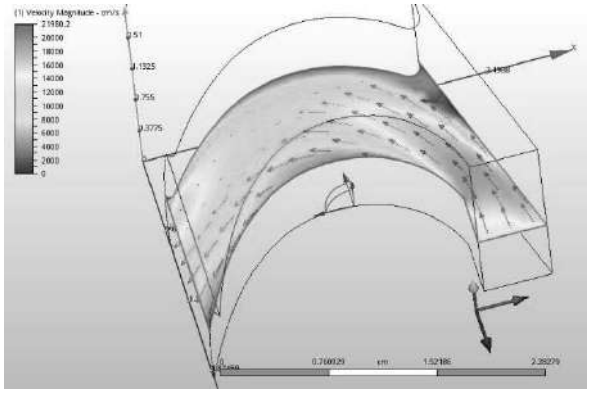

Blade with rear wall at 15°

Fig. 7. Influence of the angle at blade rear on the velocity of the outgoing flow

The optimization of the rotation angle of the blade should be carried out for particular blade design and using simulation modelling. Since the distribution and behavior of the flow depends on many external factors (temperature, physico-chemical properties of the heat carrier, design features of the blade itself and the nozzle, etc.), development of general mathematical dependence is encumbered.

The second factor determining the power obtained is the tangential velocity of the heat carrier flow out of the blade. To determine this velocity, the velocity triangle (Fig. 5) and eq. (7) were used.

Fig. 7 shows the effect of the blade rotation angle on the velocity of the outflowing carrier. It can be seen from the figure that the values of the outgoing flow velocity increase with the increase of the rotation angle of the rear wall of the blade at equivalent initial conditions.

The main problem of the technology suggested for optimization of the turbine blade design is that a blade with quite a complex form is obtained which is hard to manufacture by the traditional methods.

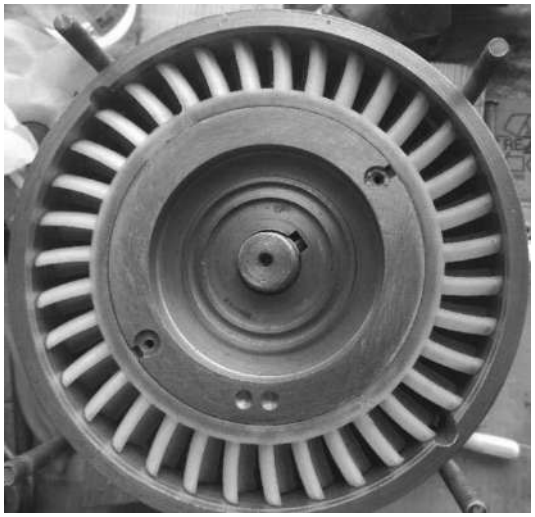

Fig. 8. Working wheel of turbine for ORC installations manufactured with 3D printing technology from reinforced thermoplastic material

An original approach for solving this problem is to replace the metal working wheels of the turbine with wheels manufactured from hard thermoplastic materials. In combination with the 3D printing technology and the possibilities it provides for bulk reinforcement of printed part with carbon fibers glass plastic fibers [8, 9], it allows the production of turbine blades of complex shape (Fig. 8) comparatively rapidly, at low cost and without using instrumental equipment, mechanical processing and casting.

Taking into account the fact the Freon turbines in ORC installations operate at comparatively low pressures and temperatures, this provides a number of advantages for turbine manufacturing from both design and technological points of view.

A disadvantage of the plastics is that, in some cases, they do not ensure sufficient strength under certain regimes of operation of the turbine and the blades suffer erosion or breaking. Another problem is the wear resistance of the blade and its front rounding. It takes the “attack” of the working fluid the velocity of which may reach 200-300 m/s depending on the working regime of the nozzle.

To solve these problems, it is sometimes necessary to deposit a surface coating.

The technologies for deposition of surface coatings onto polymeric substrate are described in [10-16].

Combining 3D printing of hard thermoplastic reinforced plastics and deposition of a metal coating, one can design and manufacture highly efficient blades with shapes conforming to flow hydrodynamics and reducing to a minimum the loses from parasite vortices rapidly and at a comparatively low cost. This would result in a significant increase of turbine efficiency. The initial experiments in this direction have given promising results.

RESULTS AND DISCUSSION

The analysis of the two factors described in the present paper show that to draw maximum power from the turbine, the determining factor is the flow velocity in the channels of the working wheels (Fig. 2) at certain thermodynamic characteristics of the heat carrier. This velocity directly depends on the slope at blade rear and has an immediate effect on the efficiency of the turbine as a whole.

Using computer modelling and investigating three dimensional models of various types of blades and channels, certain results and correction coefficients were obtained. They were used for constructive design and optimization of the channel shapes and the shapes of the blades of the guiding and working wheels of the turbine. Using the results obtained, a turbine was designed and manufactured (Fig. 1) with power of 15 kW, working with Freon R-507a at pressure

of the heat carrier at the inlet 1.5 MPa and debit of 0.122 kg/s.

The comparison of the results obtained by calculation with the experimental data registered during turbine operation showed good agreement. This is a proof that the approach suggested for dimensioning and constructive design can be used for design of non-standard equipment.

A solution was also suggested to replace the metal working wheels of turbine working in ORC installations with ones manufactured from thermoplastic reinforced material with metal coating deposited on them. This results in a significant increase of turbine efficiency. The initial experiments in this direction have given very good results.

REFERENCES

1. Mitev, D. T., D. R. Rusev, *Technological Thermodynamics,* Rota pecht, Burgas, 2013, p. 305.
2. Koshkin, V., T. Mihaylova, *The thermodynamic theory of the expiration of gases and vapors,* Moscow Aviation Institute, Moscow, 1983, p.51.
3. Genbach, A., A. Kibarin, T. Hodanova, *Steam and gas turbines,* Thermal engineering, Almaty: AIES, 2008, p.58.
4. Emin, O., V. Karasev, Yu. Rzhavin, *Selection of parameters and gas-dynamic calculation of axial compressors and turbines GTE,* Moscow Aviation Institute, Moscow, 2004, p.124.
5. Balabanovich, V., N. Panteley, *Turbine power plants,* Belarusian National Technical University, Minsk, 2005, p.106.
6. Rusev, D., M. Dyulgerova, *Structural design of turbine blades for working with extension to a negative entropy*, „Mechanics of Machines“, Varna, 2014.
7. Kadminskiy, V., *Engineering thermodynamics and heat transfer,* Marshrut, Moscow, 2005, c.223.
8. https://all3dp.com/arcam-cocr-process-ebm-technology/
9. http://www.maketechnics.com/3d-printeri
10. Milusheva P., Vacuum deposition of aluminium coatings onto various grades of polymers and determination of the adhesion stress, Sci. Session with int. particip. “Technics, technology and education 2008”, Yambol, July 3, 2008, Col.reports, p.70.
11. Milusheva P., Metal coatings on polymeric materials, PhD thesis, 2016.
12. Milusheva P., T. Uzunov, N. Ivanov, Research on the surface characteristics of *Ti* and *Fe-Cr-Ni* alloy thin films on polymeric substratum, Journal of the Balkan Tribological Association Vol. 16, No 4, 564–569 (2010).
13. Milusheva P., Determination of the mechanical properties of metal layers deposited onto crystalline polystyrene, Part 1. Preparation of metal layers. Proc. Nat. conf BULTRIB’2011 Oct 28, 2011, Sofia, Tribological journal BULTRIB, v.II, No 2 (02), 100-104, (2012).
14. Milusheva P., Study on the wear resistance of metal layers deposited onto polymeric materials, Nat.Mil.Univ. “Vasil Levski”, Univ. Sci. conf. 2016, Oct. 20-21, 2016, Veliko Tarnovo 2016.
15. Milusheva P., Determination of the mechnical properties of metal layers deposited onto crystalline polystyrene, Part 2. Study on the mechanical properties of metal layers, Proc. Nat. conf BULTRIB’2011 Oct 28, 2012, p.105.
16. Milusheva P., Deposition and study of titanium coating on polymer substates, Journal of the Balkan Tribological Association Vol. 24, No 2, 250–261 (2018).

ANNUAL OF ASSEN ZLATAROV UNIVERSITY, BURGAS
BULGARIA, 2018, v. XLVII (1)

MODIFICATION OF THE SURFACE LAYER OF A BLADE FOR FREON OPERATED TURBINE

Dimitar Rusev
E-mail: dr_rusev@mail.bg

ABSTRACT

The object of the study is the improvement of the wear resistance and strength properties of a turbine blade made from thermoplastic. A technology is suggested for modification of the blade surface layer by impregnation with wear-resistant coating of aluminium oxide. An analysis is made of the difficulties arising from using the traditional methods and a new approach is suggested in this direction. The essence of the method is that the coating is deposited using fluidized bed. Aluminium oxide particles are fluidized. The bed is heated to temperatures at which, after immersing the blade in the bed, the thermoplastic surface partially melts and the aluminium oxide particles penetrate the molten zone. The molten material wraps the particles of the reinforcing phase and binds them in a dense structure when the temperature is decreased.

The depth of the surface melting and the thickness of the coating formed are determined by the bed temperature and the period of time the blade stays within the bed.

The location and size of the aluminium oxide coating on the blade surface as well as the boundary between the wear resistant layer and polyamide bulk are determined by microscopic analyses.

Key words: *fluidized bed, wear-resistant coating, aluminium oxide*

INTRODUCTION

3D printing technology is at the basis of many new production technologies. The use of 3D printing with hard thermoplastics and the opportunities it provides for bulk reinforcement of the printed article with carbon fibers of plastic glass fibers [1, 2] allows the manufacture of turbine blades of complex shape (Fig. 1) cheaply and at a comparatively high speed without the need for production equipment or further mechanical treatment of the cast.

Furthermore, the materials used are wear-resistant, withstand mechanical stress and have a high modulus of elasticity by bending (6.2 GPa) at average deformation at break (8-10%) [3].

The turbines using Freon as a working fluid in ORC facilities operate at a comparatively low pressure and temperature, which provides the possibility to replace the metal blades of the working rotors with hard thermoplastic materials. This has a number of advantages of constructive and technological nature in the manufacturing of a turbine. The modification of turbine blades makes it possible to optimize flow hydrodynamics to the highest level and improve turbine efficiency.

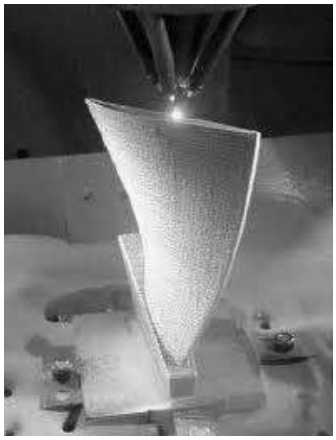

Fig. 1. 3D printing technology

The blades are usually processed by metal cutting machines (Fig. 2), which is a rather expensive process: it takes too much machine time to manufacture the necessary instruments, complex and expensive digital cutters should be used and, nevertheless, it does not always allow cutting a complex shape blade.

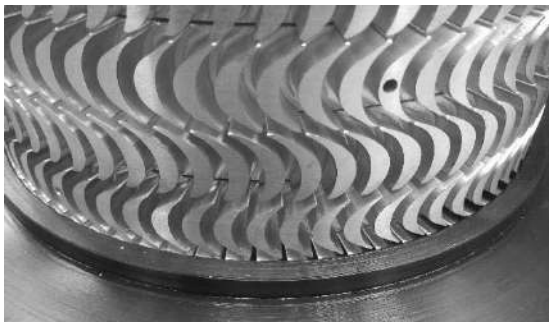

Fig. 2. Blade cutting technology

A disadvantage of the 3D printing technology is that the plastics with which it works in some cases do not ensure proper strength of the blade and, under certain regimes of operation, the blades erode or break (Fig. 3). Another important problem is also the wear-resistance of the blade edge and its rounding [4] as it takes the attack of the working fluid the velocity of which can reach 200-300 m/s depending on the regime of operation.

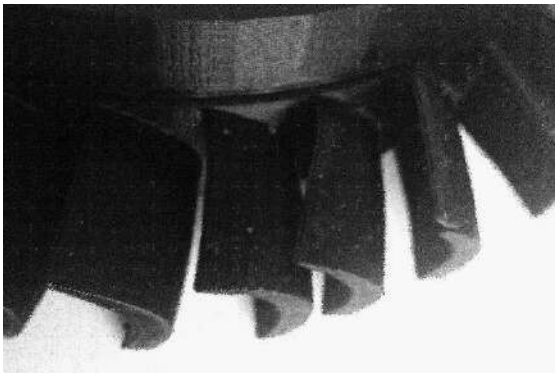

Fig. 3. Breaking of a blade

In some cases it is necessary to deposit surface coating to solve these problems.

The technologies for deposition of metal coating onto polymeric substrate have been studied and described in [3, 5 ,6 ,13]. However, the use of these technologies makes the blades rather expensive and in some cases the coating breaks (Fig. 4). This happens due to the process of deposition which is accompanied by heating the substrate to a certain temperature. After taking the part with deposited coating out of the vacuum chamber and letting it cool to room temperature, stresses arise between the polymeric substrate and the metal coating. They are generated by the different coefficients of heat expansions of the polymer and the coating. In some cases these stresses become stronger than the strength of the adhesion, which results in bursting or disjoining of the coating [7-10].

Fig. 4. Breaking of the coating

One of the promising solutions to this problem is the modification of the surface layer of the blade by impregnation with aluminium oxide particles using the fluidized bed technology.

The aim of the present work is to study the possibility for modification of the surface layer of a part made from the polymeric material *POLIPOM® POM* by impregnation with aluminium oxide particles in fluidized bed.

FORMULATION OF THE PROBLEM

The experiments were carried out using *POLIPOM®POM (*polyacetal) [11]. This is a plastic prepared by polymerization of formaldehydes. The material has a comparatively high strength and mechanical hardness without additional reinforcement due to the highly crystalline structure of the oxygen and the methylene groups. It is resistant to alkali, hot water, the most widely used solvents, petroleum products and mineral oils. This material [11] is known for its good mechanical properties: tensile break by DIN 53415 in the range of 70 N/mm^2, elasticity modulus DIN 53457 31000, maximal working temperature DIN53461 up to 124 $^{\circ}C$ and excellent wear resistance, low flammability and stability under radiation, and chemical resistance.

The modification of the surface layer was carried out in fluidized bed [12] with aluminium oxide Al_2O_3. This is the most widely spread aluminium oxide, identified as aluminium (III) oxide, with density of 3.96 g/cm^3, melting temperature 2050 °C, boiling temperature above 3000 °C, insoluble in water (Fig. 5). It can exist in

several crystalline phases but at high temperature it transforms back to its most stable hexagonal α-phase called corundum or α-aluminium oxide. This phase is thermodynamically stable, with high purity, resistant to acids and bases and has low heat release. The high hardness (hardness 9.0 Mohs of pure corundum), excellent insulation properties, refractive period and good insulation properties make Al_2O_3 the preferred material for production of abrasives, components in cutting instruments (alloyed with Cr, Fe, Ti) and refractory materials.

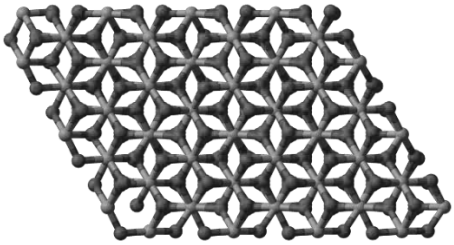

Fig. 5. Structure of Al_2O_3

The Al_2O_3 used for the present experiments (Fig. 6) had disperse particle composition from 50 to 50 to 250 μm which were to be impregnated into the partially molten surface layer of the material.

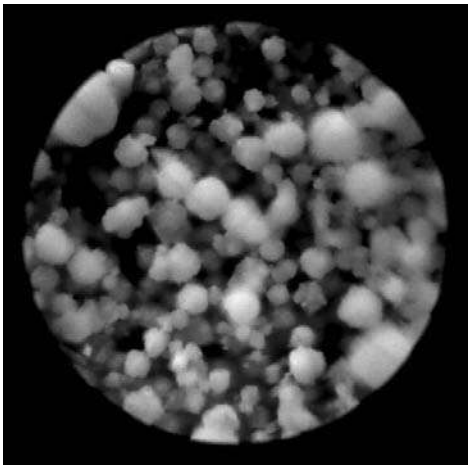

Fig. 6. Disperse composition of Al_2O_3

Fig. 7. Turbine blades of polyacetal before treatment

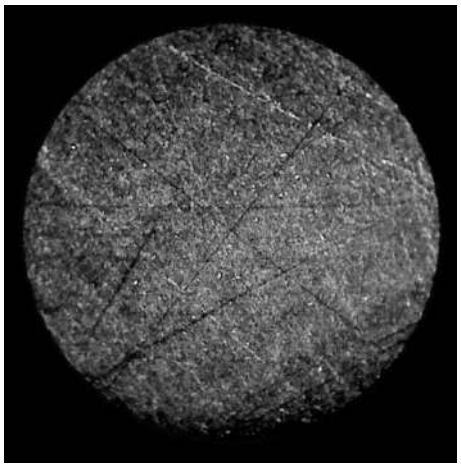

Fig. 8. Microstructure of ***POLIPOM®POM*** before treatment (x60)

To obtain the wear-resistant coating, fluidized bed with aluminium oxide particles was used. The hydrodynamics and the conditions for fluidizing the particles have been described in detail in the literature [2]. The bed was heated to the working temperature and the blade was immersed into it. By setting the bed temperature and period of treatment of the blade, one can achieve conditions under which the aluminium oxide particles penetrate the molten zone. The molten material wraps the reinforcing phase and, when the temperature decreases, it binds them in a dense structure (Fig. 9 and Fig. 10).

The bed temperature was determined by taking into account the physical characteristics of the polymer treated and selecting a temperature from 10 to 50 °C above the melting temperature of the material. The detailed study on the selection of this temperature is the topic of another paper.

To determine the thickness of the coating and the period of treatment in the bed, the equation expressing the quantity of heat necessary for full melting of the blade can be used:

$$Q = G.c.(t_2 - t_1),\ \text{J} \qquad (1)$$

where: G - mass of the sample, kg;

c - specific heat capacity of the material, J/(kg.^{0}C);

t_1 - temperature of the sample, ^{0}C;

t_2 - temperature of the bed, ^{0}C.

Transforming (1) as a function of blade geometry, temperature conditions and assuming the sample stays in the bed for 1 s, the depth of the molten layer can be calculated at a given power of the heater from the dependence:

$$h = \frac{4Q_K}{\pi d^2 c(t_2 - t_1)} \quad (2)$$

where: h is the thickness of the molten layer, m; Q_K - energy put into the bed (heater power), W; d - diameter of the sample, m.

Fig. 9. Turbine blades from *POLIPOM®POM* after modification of the surface layer

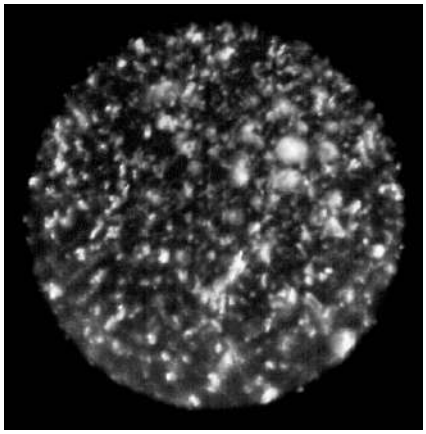

Fig. 10 Microstructure of *POLIPOM®POM* with deposited coating of Al_2O_3 (x60)

Fig. 10 shows the microstructure of the sample with deposited coating of aluminium oxide. The Al_2O_3 particles penetrate the molten surface and form a surface layer which spreads into the bulk of the polymer structure (Fig. 10) to form a surface coating with the properties of Al_2O_3.

Observing a transverse cut (Fig. 11), the depth to which the aluminium oxide particles have penetrated can be determined – it was about 500 μm on average, under the conditions of coating selected. The depth can be regulated in narrow intervals by varying the bed temperature and period of treatment of the part in the bed (dependence 2).

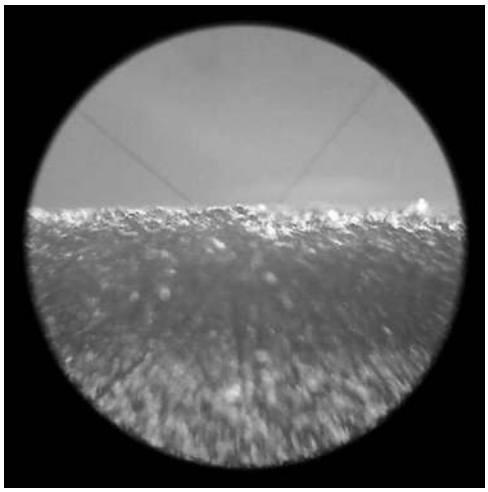

Fig. 11. Transverse cut of the surface (x60)

RESULTS AND DISCUSSION

A new technology for deposition of wear-resistant coating of aluminium oxide onto the polymer structure *POLIPOM®POM* which employs fluidized bed of aluminium oxide particles heated to temperature higher than the melting temperature of the polymer was suggested.

The depth of penetration of the aluminium oxide particles at a certain temperature, sample geometry and heater power was studied.

A dependence was derived, which provides means to regulate the penetration depth in a narrow interval by varying the bed temperature and duration of the treatment.

The suggested method solves the problems related to the strength and wear resistance of the polymer *POLIPOM®POM* and its use for the manufacture of blades for turbines operating with Freon by 3D printing.

The blades with deposited coating were tested with a turbine of 16 kW power operating with Freon R-507a, under inlet heat carrier pressure 1.5 MPa and debit of 0.122 kg/s.

REFERENCES

1. https://all3dp.com/arcam-cocr-process-ebm-technology/
2. http://www.maketechnics.com/3d-printeri
3. Milusheva P., Determination of the mechnicalproperties ofmetal layers deposited onto crystalline polystyrene, Part 2. Study on the

mechanical properties of metal layers, Proc. Nat.conf BULTRIB'2011 Oct 28, 2012, p.105.
4. Genbach, A., A. Kibarin и T. Hodanova, *Steam and gas turbines,* Thermalengineering, Almaty: AIES, 2008, p.58.
5. Milusheva P., T. Uzunov, N. Ivanov, Research on the surface characteristics of *Ti* and *Fe-Cr-Ni* alloy thin films on polymeric substratum, Journal of the Balkan Tribological Association Vol. 16, No 4, 564–569 (2010).
6. Milusheva P., Determination of the mechanical properties of metal layers deposited onto crystalline polystyrene, Part 1. Preparation of metal layers. Proc. Nat.conf BULTRIB'2011 Oct 28, 2011, Sofia, Tribological journal BULTRIB, v.II, No 2 (02), 100-104, (2012).
7. Milusheva P., Study on the wear resistance of metal layers deposited onto polymeric materials, Nat.Mil.Univ. "Vasil Levski", Univ. Sci. conf. 2016, Oct. 20-21, 2016, Veliko Tarnovo 2016.
8. Parashkevov D., P. Milusheva, Chemical Composition and Morphology of Thin Deposition Method, Journal of Materials, Science and Technology, vol.18, 2010, №1.
9. Milusheva P., Vacuum deposition of aluminium coatings onto various grades of polymers and determination of the adhesion stress, Sci. Session with int. particip. "Technics, technology and education 2008", Yambol, July 3, 2008, Col.reports, p.70.
10. Milusheva P., Metal coatings on polymeric materials, PhD thesis, 2016.
11. http://www.omniaplastica.ru/pa6_akulon.html
12. Rusev D.R., Method for technological calculation and constructive design of fluidized bed units, Annual of Univ. "Prof. Dr.Asen Zlatarov", v.XXXIV, No 1, 2005, pp. 115-120.
13. Milusheva P., Deposition and study of titanium coating on polymer substates, Journal of the Balkan Tribological Association Vol. 24, No 2, 250–261 (2018).

ANNUAL OF ASSEN ZLATAROV UNIVERSITY, BURGAS
BULGARIA, 2018, v. XLVII (1)

$PM_{2.5}$ - SELECTION OF SAMPLING POINTS ON THE TERRITORY OF BURGAS MUNICIPALITY

Stela Naydenova, Lenia Gonsalvesh
E-mail: *steltion@gmail.com*

ABSTRACT

The levels of $PM_{2.5}$, which are among the most dangerous pollutants to human health and ecosystems, are not directly measured in any of the National Environmental Monitoring System of Ambient Air stations in the Municipality of Burgas. Only inventory data, which are based on estimation of the emissions of airborne pollutants, i.e. $PM_{2.5}$, and calculated using the quantities of fuels, emission factors and pollutants dispersion over the city by mathematical models, are available as information. However, these data give the expected emissions of pollutants and respectively the actual concentration of the $PM_{2.5}$ and the PAH contained therein can be only known by sampling and analysis according to standardized methods with the necessary equipment. The purpose of the study is to determine the areas on the territory of the Municipality of Burgas with inflated concentrations of $PM_{2.5}$ and to select sampling points for $PM_{2.5}$, representative for the different types of pollution sources, i.e. domestic heating, automobile traffic and industry.

Key words: *$PM_{2.5}$, air pollution, sources of $PM_{2.5}$, urban air, sampling points*

INTRODUCTION

Air quality is an important requirement for a healthy environment as it has a direct and indirect impact on all its components. In this respect, air pollution with fine particulate matter (PM) in recent years has become a subject of growing interest and concern for the public, the research sector and the institutions responsible for environmental protection. Epidemiological studies support this concern and show that exposure to PM with aerodynamic diameter below 10μm (PM_{10}) and especially with aerodynamic diameter below 2.5μm ($PM_{2.5}$) leads to increased incidence of lung cancer and mortality under the effects of cardiovascular system problems [1, 2]. The main hypothesis is that the toxicity of PM depends not only on their size but also on their composition, and compounds that can cause or increase PM toxicity are aldehydes, ketones, benzene, dioxins, polycyclic aromatic hydrocarbons (PAHs) alkylated PAHs and their nitro (nitro-PAB) and oxidized (quinones) derivatives [2, 3]. In addition, PM can serve as a "vehicle" for the transportation of all these harmful substances over long distances depending on the weather conditions.

Efforts to improve the atmospheric air quality will lead to the protection of human health, living nature, water and soil, as well as the prevention of hazards and damages to society. The protection of the cleanness of the ambient air is based on the principles of sustainable development and is carried out under the terms and conditions of the Clean Air Act [4]. As a member state of the European Union, Bulgaria has fully synchronized its national legislation in this area with the European directives. Respectively, the general condition of the atmospheric air can be assessed using the indicators considered in Art. 4 of the Clean Air Act [4]. The average annual and maximum one-off allowable concentrations of pollutants, the permissible number of excee-dances of the average daily or hourly limit values for the limit values and the respective thresholds are set out in Regulations 11 and 12. Bulgarian legislation establishes the limit value for *benzo[a]pyrene* in the ambient air according to Ordinance No. 11 of 14.05.2007 (State Gazette, issue 42 of 29.05.2007) with an average annual limit value of 1 ng/m^3. The content of PM in the atmospheric air in settlements is regulated by Ordinance No. 12 (SG, No. 58/2010), which specifies: i) Fine particulate matter standards PM_{10} - daily average value for protection of human health - 50 $\mu g/m^3$; average annual human health protection standard - 40 $\mu g/m^3$; (ii) Fine

particulate matter $PM_{2.5}$ - annual average for the protection of human health - 25 μg/m^3 [5, 6].

The $PM_{2.5}$ levels, which are very dangerous for human health and ecosystems, are not measured in the atmospheric air monitoring stations available on the territory of the Municipality of Burgas. Among the chemical compounds that are classified as volatiles, only benzene, whose level systematically exceeds the average annual rate, is measured and traced. The levels of PAHs, dioxins, furans, toluene, etc. are not monitored. This determines the need to assess the quality of ambient air with respect to these specific pollutants.

The purpose of the present study is to determine the areas on the territory of the Municipality of Burgas with inflated concentrations of $PM_{2.5}$. In general, the town is affected by the release of pollutants from different types of sources. The determination of the atmospheric air quality in such a large area cannot be achieved using instruments to measure the concentrations of all different types of pollutants directly. Up to now, concentrations of $PM_{2.5}$ are not directly measured in any of the National Environmental Monitoring System of Ambient Air Stations in Burgas. Therefore, our survey is based on inventory data and the estimation of the emissions of airborne pollutants (calculated using the quantities of fuels and emission factors) and their dispersion over the city through mathematical models for atmospheric dispersion of pollutants [7]. Based on that survey, sampling points for $PM_{2.5}$, representative for the different types of pollution sources in the Municipality of Burgas, i.e. domestic heating, car traffic and the industry, will be selected. As a next step, the $PM_{2.5}$ concentration and their composition in the Municipality of Burgas will be assessed in order to evaluate the ambient air quality with regards to specific pollutants, in particular $PM_{2.5}$ and PAH content in $PM_{2.5}$.

EXPOSITION

Burgas is the largest city in south-eastern Bulgaria and it is an administrative center both of the Municipality of Burgas and Burgas region with a population of more than 200,000 people. It is designated as a Functional Urban Area, according to the classification of European cities and is an important industrial, transport and tourist center. The main structuring sectors are the chemical, petroleum, wood, food, shipbuilding, electrical and electronics industries as well as machine building and metalworking. Two large industrial zones are situated in the territory of the city of Burgas, where the main industrial production and transport activities are concentrated. These are the industrial zones "North" and "South". The production site of "LUKOIL Neftochim Burgas" AD is located 2 km northwest of Dolno Ezerovo village.

According to Order No RD-969/21.12.2013 of the Minister of Environment and Water, the Municipality of Burgas is included in the Southeast Region Code for assessment and management of atmospheric air with code BG0006 and is classified as a territorial unit exceeding the norms for the following indicators: sulfur dioxide, fine particulate matter, i.e. PM_{10} and $PM_{2.5}$, and ozone. The main recognized sources of emissions are domestic heating through wood and coal combustion, automobile traffic, industry, in particular the largest oil refinery in the country "LUKOIL Neftochim Burgas" AD, and the construction and repair activities [8, 9].

For the region of Burgas, the national environmental monitoring system observes the air quality in a continuous mode at four points: the AMS “Dolno Ezerovo” (BG0044A), AMS "Meden Rudnik" (BG0056A), DOAS OPSIS (BG0063A) and Mobile Station. The levels of $PM_{2.5}$, which are among the most dangerous pollutants to human health and ecosystems, are not measured in the atmospheric air monitoring stations on the territory of the municipality. Therefore, for the purpose of our study, an overview of the sources of pollution with $PM_{2.5}$ within the Municipality of Burgas was made. As mentioned above, three groups of sources have been identified: domestic heating (all residential areas and settlements in the Municipality of Burgas), automobile traffic (as linear sources from the national road network, primary street network, parts of streets, crossroads and entry/exit of highways) and industry (21 companies and industrial plants with one or more stacks which independently emit $PM_{2.5}$ in the atmosphere) [10,11]. Table 1 provides a summary of the annual aggregate emissions of $PM_{2.5}$ for Burgas Municipality.

1. Domestic heating

In order to assess the annual emissions of harmful substances from domestic heating in urban areas it is necessary to have data on the annual fuel consumption by types (wood, coal, briquettes, oil, gas, etc.), as well as their percentage distribution by residential areas and respec-

tive emission factors. According to data from the Territorial Statistical Office, Burgas and the National Statistical Institute, the total number of households in the smaller neighborhood of the Burgas districts is about 15,455, and only 5% of them use electricity for heating, while the remaining 95% use wood and coal [11]. However, the share of consumption of fuel and electricity for heating purposes by the households for the whole town is different as can be seen from Fig.1. The data presented in Fig. 1 allow us to trace the trend in the choice of different types of fuels by the population of Burgas and indirectly judge the emissions of harmful substances generated due to domestic heating, by the use of emission factors.

Table 1. Summary of the annual aggregate emissions of $PM_{2.5}$, t/y [11].

Sources	$PM_{2.5}$
1. Domestic heating	1358.7
2. Automobile traffic	687.60
3. Industry	688.17
Total	**2734.47**

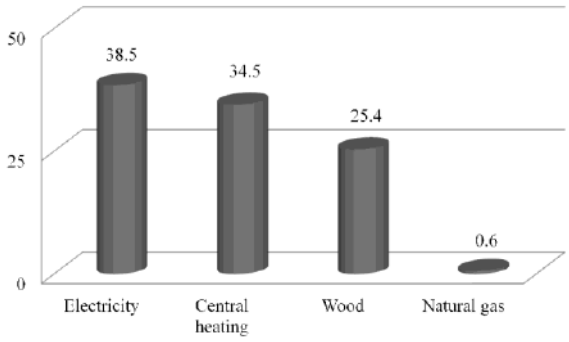

Fig. 1. Percentage distribution of different sources used for domestic heating for 2010, % [10,11].

According to available data in 2014, 43.5% of the households in Burgas and 95% of the households in the other settlements of the municipality use solid fuels for heating, which determines the annual solid fuel consumption of 170,110 tons. The highest consumption of solid fuels is seen in the Central Town unit, i.e. Vazrazhdane (35,599 t/y), and Meden Rudnik (34,081 t/y). In Fig. 2, the annual emissions of $PM_{2.5}$ due to domestic heating are presented.

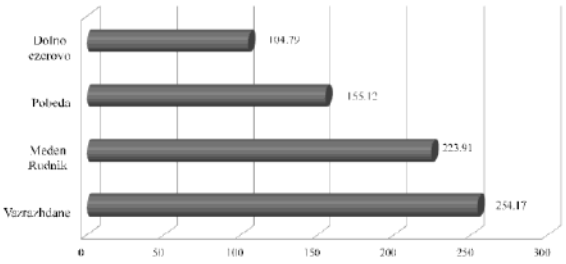

Fig. 2. Annual emissions of $PM_{2.5}$ from domestic heating for 2014, t/y [11].

Analysis of the data published in the Program for Improvement of the Ambient Air Quality in Burgas Municipality for the period 2016 – 2020 [11] shows that the highest expected concentrations with respect to $PM_{2.5}$ will be in the areas of the complexes Vazrazhdane, Meden rudnik, Slaveykov, Pobeda and Dolno Ezerovo village. However, the material balance approach cannot provide a single answer for the quantitative and qualitative content of PAHs in $PM_{2.5}$ as different types of wood, coal of different rank and deposits, and other combustible materials are burnt in the furnaces.

2. Automobile traffic

The impact of road transport on air quality in the Municipality of Burgas is essential because it is the most dynamically developing source of emissions. Due to the incomplete combustion of the heavy components in the fuel, soot is formed and discharged into the atmosphere through the exhaust system of vehicles. Diesel fuel combustion in many cases leads to generation of soot, while gasoline engines do not have such type of emissions.

Reported $PM_{2.5}$ emissions [11] from automobile traffic are estimated considering 59 independent line sources (street or part of it) with a total length of about 121.97 km defined in three main groups: high traffic (over 10,000 vehicles/24h), medium traffic (5,000–10,000 vehicles/24h) and low traffic (below 5,000 vehicles/24h). The highest pollution is observed in Stefan Stambolov and Struga Boulevards. The annual $PM_{2.5}$ emissions from the transport scheme of Burgas Municipality for 2014 are estimated at 168.93 t/y. The seasonal distribution of $PM_{2.5}$ emissions from automobile traffic in Burgas Municipality is presented in Fig. 3.

The assessment of air pollution with $PM_{2.5}$ and the PAH contained therein depends not only on exhaust emissions from the vehicles but also on the processes of mechanical pulping and suspension of particulate matter from the roadway.

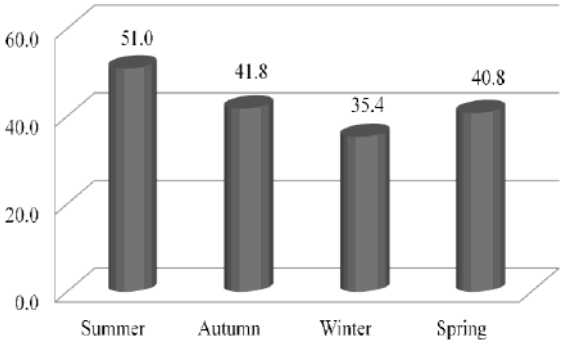

Fig. 3. Seasonal emissions of $PM_{2.5}$ from the transport system of Burgas Municipality for 2014, t/y [11].

3. Industrial sources

The industry of Burgas Municipality comprises 21 companies on the territory of which one or several emission sources of $PM_{2,5}$ can be present. Most of these industrial sites are concentrated in the North and South industrial zones of Burgas. However, the largest industrial sources of $PM_{2.5}$, i.e. LUKOIL Neftochim Burgas AD and LUKOIL Thermal Power Plant operated by Lukoil Energy and Gas Bulgaria EOOD, are located on the territory of the Municipality of Kameno, but also affect the pollution of Burgas. In some cases, the industrial plants are the sources of pollution, while in other cases the different aspiration systems or production processes are associated with the emission of pollutants into the ambient air. The annual $PM_{2.5}$ emissions from the five largest organized industrial sources on the territory of Burgas Municipality for 2014 are presented in Fig.4.

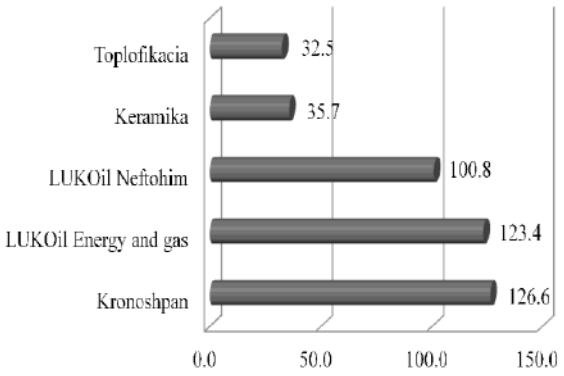

Fig. 4. Main industrial sources of $PM_{2.5}$ emissions for 2014, t/y [11].

Annual $PM_{2.5}$ emissions from non-organized sources are estimated at 0.984 t/y, from mining and processing of underground materials at 10.8 t/y and from aviation transport at 5.42 t/y [11].

DISCUSSION AND CONCLUSIONS

The analysis of the data presented in the Program for Improvement of the Ambient Air Quality in the Municipality of Bourgas for the period 2016-2020 [11] shows that domestic heating is the major source of $PM_{2.5}$ emissions, emitting 67.6% of the whole amount, the share of transport is about 8.8%, while as a result of industrial processes about 23.6% $PM_{2.5}$ are emitted. However, the presented data give the expected emissions of pollutants. They can be considered as a guideline when selecting sampling points. The actual concentration of $PM_{2.5}$ and PAH contained therein can be known only by sampling and analysis, according to standardized methods with the necessary equipment.

The survey of aforementioned data shows that the highest $PM_{2.5}$ contaminations are expected at the following points in the city: Central Town and the area of the complexes (neighborhoods) Vazrazhdane, Meden Rudnik, Pobeda, Slaveikov and Dolno Ezerovo village. Accordingly, the selection of $PM_{2.5}$ sampling points within these areas is highly reasonable. Nevertheless, the specific sampling site selection is based on a multifactorial criterion analysis that includes a combination of several factors:

1. The impact of main sources of pollution - location, current status of installations, load, etc.

2. The influence of the non-organized sources of pollution - open slopes and loading/unloading sites.

3. The influence of the topography of the area and the presence of buildings preventing vertical mixing of atmospheric layers, as well as the presence of large water areas leading to increased air humidity and to the formation of photochemical smog.

4. The influence of meteorological factors – mainly the presence of wind (secondary dispersion of dust particles) and the intensity of solar radiation (photochemical processes of atmospheric chemistry leading to secondary pollution). During rain, the atmosphere is purified, which is not a suitable time for sampling. The organization of sampling for $PM_{2.5}$ should be consistent not only with the main sources of emissions, but also with seasonal variations and weather conditions.

In relation to all above, the following sampling points are selected as appropriate:

- Hristo Botev St, which agglomerates the central part of the town and Vazrazhdane - $PM_{2.5}$

contamination in this area is related to domestic heating (during the winter) and increased automobile traffic during the summer;

- Zahari Stoyanov Blvd, which agglomerates the village and the neighborhood of Meden Rudnik - $PM_{2.5}$ contamination is mainly related to domestic heating (during the winter) and automobile traffic as this boulevard is part of the Republican Road Network;
- Industrialna St, which passes through the neighborhoods of Acatsiite and Pobeda, and is influenced by emissions from domestic heating, road traffic, the South industrial zone and, last but not least, by emissions from the loading and unloading of bulk cargo at the Port of Burgas;
- Yanko Komitov St, which separates Slaveikov neighborhood from the North industrial zone. The emissions in the area are influenced by domestic heating, road traffic and nearby enterprises. The influence on $PM_{2.5}$ emissions from Kronospan production company and road traffic is expected to be higher;
- Zahari Zograf St in Dolno Ezerovo village, where an influence on $PM_{2.5}$ pollution from domestic heating during the winter, from LUKOIL Neftochim and to a much lesser extent from road traffic is expected.

Additionally, sampling days will be chosen according to the weather conditions.

REFERENCES

1. R. Pozzi, B. De Berardis, L. Paoletti, C. Guastadisegni, *Winter urban air particles from Rome (Italy): Effects on the monocytic–macrophagic RAW* 264.7 cell line, Environmental Research, 99 (2005) 344-354.

2. O.R. Abou Chakra, M. Joyeux, E. Nerrière, M.-P. Strub, D. Zmirou-Navier, *Genotoxicity of organic extracts of urban airborne particulate matter: An assessment within a personal exposure study*, Chemosphere, 66 (2007) 1375-1381.

3. A.G. Santos, A.C.D. Regis, G.O. da Rocha, M.d.A. Bezerra, R.M. de Jesus, J.B. de Andrade, *A simple, comprehensive, and miniaturized solvent extraction method for determination of particulate-phase polycyclic aromatic compounds in air*, Journal of Chromatography A, 1435 (2016) 6-17.

4. *Clean Air Act*, Ministry of Environment and Water and Ministry of Health, last amended State Gazette, 12, 3 February, (2017).

5. Regulation No 11 of 14 May 2007 on *Arsenic, Cadmium, Nickel and Polycyclic Aromatic Hydrocarbons in Atmospheric Air*, Prom. SG. No. 42 of May 29, 2007.

6. Ordinance No. 12 of July 15, 2010, for the *norms for sulfur dioxide, nitrogen dioxide, fine particulate matter, lead, benzene, carbon monoxide and ozone in the atmosphere* in force from 30.07.2010 issued by The Ministry of Environment and Waters and the Ministry of Public Health. SG. No.58 of 30 July 2010

7. *Unified methodology for inventory of emissions of harmful substances in air* (Order № RD-165 / 20.02.2013 of MOEW).

8. Kutsarov, R., Ivanova, D, *An evaluation of the intensity changes of the road transport in town Burgas under the information of the stations for monitoring the air pollution*, Scientific publications Volume II, The twelfth International Symposium, Ecology 2003.

9. Nikolaeva, Z., S. Naidenova, D. Ivanova *Investigation on the Dependence of Atmospheric Transparency on Concentration of Particulate Matter PM_{10}.* International Journal of Scientific Engineering and Applied Science, 3 (5), pp. 109-114, May 2017.

10. *Sustainable Energy Development Strategy of Bourgas Municipality 2011 – 2020*.

11. *Program for improvement of the quality of the ambient air in Burgas Municipality for the period 2016 – 2020*.

ANNUAL OF ASSEN ZLATAROV UNIVERSITY, BURGAS
BULGARIA, 2018, v. XLVII (I)

STUDY OF THE EFFECT OF IMPLEMENTING AN INTERACTIVE FORM OF EDUCATION IN THE DISCIPLINE "TECHNICAL SAFETY AND DISASTER PROTECTION"

Sabina Nedkova, Plamena Atanasova
E-mail: sabina_nedkova@abv.bg

ABSTRACT

Interactive education as an educational approach focused on the personal involvement of every student in the educational process is quite important nowadays when the principle „Learning through doing" has been proven as effective and successful. This type of education is even more important when teaching complex subjects, such as „Technical safety and disaster protection", where the ability of the student to apply his or her subjective experience and knowledge in working on the worst case scenarios and planning prevention and evacuation measures is of great importance. The dialogue regime of studying this case helps the student to understand the importance of the matter, where the decision-making time is limited but crucial.

Key words: *interactive learning, technical safety and disaster protection*

INTRODUCTION

The following study is based on the application of the interactive methods of education and assessment in the subject „Technical safety and disaster protection" for students in the Faculty of Technological Sciences and Faculty of Natural Sciences in Prof. Dr Asen Zlatarov University. The following study has been organized among a total number of 67 students.

The effectiveness of learning depends on many factors, one of which is the learner's engagement in education and learning-related actions. Traditionally, education practice is based on the premise that knowledge is something that can be passed on to the trainee by the trainer. Passive reading and writing with traditional content is accepted as a norm. Theoretically, education focused on the "participant" is encouraged. This is the so-called interactive, hands-on, learner-centered, outcome-based learning [1].

Educational strategies are based on the work of the teacher and on the methodological tasks and balance of impacts [2].

EXPERIMENT

The main idea of the study is to assess the effect of the interactive way of teaching a subject, which includes both lots of new and specific information (dangerous chemical substances, flammable gases, radioactive sources. etc.) and, at the same time, important data, which should be used in the time of incident or crisis. These two characteristics make the subject „Technical safety and disaster protection" quite complicated for both teaching and learning.

According to the Law for Disaster Protection 16 (1), the study of disaster protection and first aid is obligatory. Its main focus are disasters as a significant disturbance to the normal functioning of society caused by natural phenomena and/or by human activity and resulting in negative consequences for the life or health of the population, property, economy and environment, the prevention, capture and overcoming of which exceeds the capacity of the system for serving the usual activities of protecting the public [3].

The subject requires interactive involvement of the students in the educational process, and not only teaching it, but creating the right motivation for a subject so specific and different from the rest in the university (Table 1).

Table 1. Students' opinion about the differences between the traditional and the interactive way of teaching the subject "Technical safety and disaster protection"

Teaching through speaking	Teaching through doing
The focus is on the discipline itself	The focus is on the personality of the student and the personality of the teacher
Teaching through listening	Teaching through doing
Passive learning	Active learning
One way connection teacher-student	Two-way connection teacher-student
No connection student-student in the group	Connection between students in the group

RESULTS AND DISCUSSION

The students were asked to point out the differences between traditional education (teaching through speaking) and interactive education (teaching through doing). The results are listed in Table 1. The students are more open to the interactive way of studying; they find the principle of focusing on the personality instead of on the discipline more efficient and successful.

The results obtained confirm the principles and forms of effective learning listed in the learning pyramid (Fig. 1).

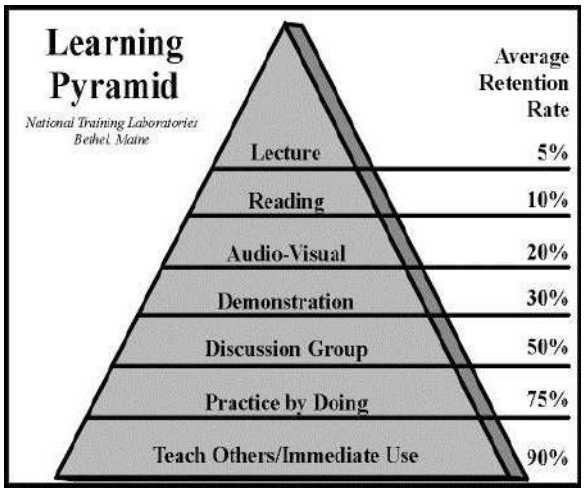

Fig. 1. Learning pyramid

The subject matter of „Technical safety and disaster protection" is very specific. Despite its complexity and importance and the serious consequences that any action might have in the area, students like it and study it willingly [4, 5].

The main principle in studying "Technical safety and disaster protection" is the active involvement of the student, because of which the interactive way of teaching is quite useful (Fig. 2).

Fig. 2. Technical safety and disaster protection studying principle

The specific knowledge, which should be obtained in „Technical safety and disaster protection" is knowledge about the:

- risks associated with specific activities;
- major technological risks: fire, radioactive, chemical;
-major environmental risks: floods, earth-quakes, storms, landslides;
- main biological risks;
- health risks;
- planning;
- control.

The specific skills which should be acquired in the subject are the skills for:

- making decisions;
- communication;
- observation forecasts;
- analysis of the situation;
- evaluation;
- planning;
- control;
- first aid knowledge;
- action in case of fires, industrial accidents, etc;
- protection in case of floods, earthquakes;
-.working with individual protective equipment.

CASE STUDIES

The interactive methods used in the lectures and practical exercises in the discipline are vari-

ous. Their main aim is to obtain practical knowledge and skills related to the discipline.

CASE 1: IDENTIFYING RISKS AND DANGER

Identifying risks and danger is a very important part of the discipline, because it is related to the application of the information about the eventual risk sources and their actual effect and after effect. The students are divided into two groups: the first one are the plant designers who should design the technological system, having in mind the process which should be led inside, the basic substances, the middle and the final products, the chemical reactions which can happen as well as their management. The "designers" try to think of the accident in advance and incorporate prevention in the design and development of the equipment. The second group are the „technological experts", these are students who play the role of the experts who should check the system and its reliability by questioning the designers' ideas and development. This way of identifying risk and dangers is quite useful, because the students should be well acquainted with lots of related information: process, main idea of the technological system, chemical compounds, etc. The game has a competitive element, which makes studying a game.

CASE 2: FAULT TREE ANALYSES

The method of fault tree analyses is used in the process of analysis and assessment of risk and danger. The students are divided in groups of experts and each group should build a logical scheme about the sequence of events, from basic, through intermediate to major event, a major accident. The groups should choose the scope of the events correctly and connect them with the right ports, having in mind their relation and the context of the whole system. After each group presents their project, we start a discussion and then every student can assess the work of their colleagues. This exercise is very useful, because the discussion give an opportunity to all the students, even the ones who are not very talkative and active, to take part in the lesson.

CASE 3: WORST CASE SCENARIOS

This exercise plans the events which can lead to an accident. The worst case scenario is part of the assessment of risks and dangers and it is related to the fault tree analyses. Each student has to build his own scenario about the worst case of the events resulting from a major accident. Here the students have to apply all their experience and suggest real actions to prevent the events from happening - the so called barriers.

CASE 4: COMPUTER-BASED TOOLS

Purposefully developed test-based assessment materials for the discipline that provide a wide variety of questions and answers are used. This gives the opportunity to play each of them at random and the results to be visualized both textually and graphically. The answers of each student individually and all of them together can be processed to generate summary results. Besides an objective assessment of their knowledge, this also enables the student to make decisions in an interactive environment.

CONCLUSIONS

The present study gave us opportunity to prove that in disciplines such as "Technical safety and disaster protection" there is not only the need to transfer knowledge to students, but to turn this knowledge into skills. Actually, this principle could be applied to all disciplines taught nowadays in universities, because of the main idea of education, to be applicable and useful in real life, where not the knowledge of certain data but how to use it, when planning and organizing actions when needed, is really important. Accordingly, there are three main principles that we can formulate:

1. Knowledge and skills must be distributed in the specific directions: focused on the roots of the problems;

2. Knowledge and skills should respond to events - there are many cases of accidents and fatal events that, though unimaginable, can happen, such as the Grenfell Tower fire on June 2017 in North Kensington, West London, which caused 74 deaths, 70 injured and 223 people escaped, the Fukushima Nuclear disaster in March 2011, etc.

They prove that knowledge in "Technical safety and disaster protection" should be focused on prevention and thinking of the possible actions which can lead to a crisis before, and not after the accident.

The skills needed to manage an accident are related to planning, prediction and analysis of the situation, making decisions and implementing

them, etc. All these skills are provoked by the interactive way of teaching;

3. Knowledge and skills in eliminating the consequences.

REFERENCES

1. Ivanov, I., Yubileyna nauchna konferentsiya s mezhdunarodno uchastie 50 godini DIPKU Varna na tema: „Obrazovanie i kvalifikaciya na peragogicheskite kadri-razvitie i proektsii prez XXI vek“, 2005

2. Terzieva, S. Savremenni obrazovatelni strategii. Orientatsii na prepodavaneto v inzhenernotehnologichnite spetsialnosti, izdatelstvo na Himikotehnologichen i metalurgichen universitet, Sofia, 2003

3. Zakon za zashtita pri bedstviya, izm. i dop. DV., br. 97 ot 05.12. 2017г.

4. Atanasova, Pl., Nedkova S., Pipeva P., Survey on the opinion of students in university „Prof. Dr Asen Zlatarov”, Bourgas on the education on „Technical safety”, Union of scientists-Stara Zagora, volume V, number 4, Technical studies, Science and Technologies p. 74-78, 2015.

5. Atanasova, Pl., Nedkova S., Prouchvane gotovnostta za reagirane na mladite hora pri vaznikvane na prirodni bedstviya I kritichni situacii, Akademichno spisanie “Industrialni tehnologii”, tom V (1), str. 113 - 116, 2018.

ANNUAL OF ASSEN ZLATAROV UNIVERSITY, BURGAS
BULGARIA, 2018, v. XLVII (1)

EXPERIMENTAL STUDY OF THE WORK OF THROTTLE TEMPERATURE FLOW COMPENSATOR FOR FLOW RATE

Rumen Yankov, Vasil Bobev
E-mail: r.yankov_@abv.bg; v_bobev@yahoo.com

ABSTRACT

The present paper offers the *authors' experimental solution to the problem when the temperature of the work body (fluid) rises. This solution compensates the volume losses in volumetric hydraulic machines and control devices. It presents the principle diagram of the product and the obtained results for different temperature and pressure values in analytical and graphical form.*

Key words: *temperature compensator; throttle; volume losses*

INTRODUCTION

As is known, the change in the working fluid temperature has a significant effect on the amount of volume losses in the volume hydraulic machines and control devices. This, in turn, degrades the characteristics of the respective hydraulic drive systems. By using systems to stabilize the temperature of the working fluid, this effect can be fully or partially compensated. Another way is to incorporate an original hydraulic device to compensate for the change in volume losses.

EXPERIMENT

In [1] are presented the results of the pressure influence study in a flowing hydraulic chamber. Based on these, the authors developed a flow temperature compensator.

Dependence $p_к(t)$ of the flow chamber was experimentally studied in the temperature range 26-58° C and a des irable pressure fall $p_1 - p_2 = 0{,}2\ [MPa]$, with the working fluid (MHL) used.

Under these conditions, in the indicated temperature range dependence $p_к(t)$ is almost linear with a constant gradient:

$$\left|\frac{dp_k}{dt}\right| = 8{,}3\left[\frac{kPa}{℃}\right]. \qquad (1)$$

Figure 1 shows t he diagram of a hydraulic throttle temperature compensator developed by the authors. Its task is to increase the flow to the hydro system with a value corresponding to the increase in volume losses due to the increase in the temperature of the working fluid.

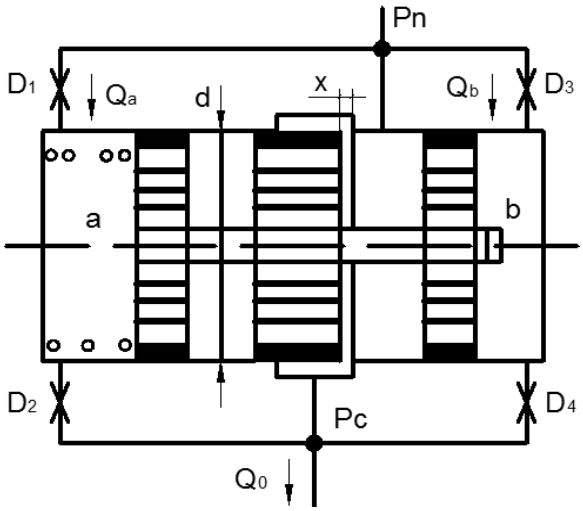

Fig. 1 Compensator scheme

The flow chambers (a) and (b), which are shown on figure 1, are formed on both sides of the plunger. A turbine throttle D_1 is mounted at the inlet of the chamber (a), and a laminar choke D_2 at the output. A pressure spring is mounted in the chamber (a). In non-working position, the spring holds the plunger to the right, which corresponds to zero displacement (x = 0) and minimum flow rate of the flowing fluid. In this connection scheme with temperature rise, the pressure p_a in chamber (a) decreases, and that in chamber (b), p_b, increases. This may cause the plunger to move to the left, respectively to increase the flow rate of the liquid.

Let at $t = t_0$ pressures p_a and p_b be equal to:

$$p_a = p_b = \frac{p_п + p_c}{2}\Big|_{t=t_0}, \quad (2)$$

which can be achieved by the corresponding sizing of the throttle.

Here, $p_п$ is the pressure at the entrance; p_c is the output pressure. For example, when raising the temperature by $\Delta t = 5°C$, the resultant force of both pressures p_a and p_b on the plunger front is equal to the spring force from the pre-compression (x_0) of the spring:

$$(p_b - p_a)\frac{\pi D^2}{4} = c.x_0|_{t=t_0+\Delta t}. \quad (3)$$

RESULTS AND DISCUSSION

Basic dependencies

For each temperature value greater than $t_0 + \Delta t$, the plunger is in an equilibrium position corresponding to the further contraction (x) of the spring. The balance of forces, without regard to friction, is:

$$(p_b - p_a)\frac{\pi D^2}{4} = c.(x_0 + x), \quad (4)$$

where:

c is spring constant;

x is moving the plunger from the right end position to the left.

Using the pins for p_a and p_b from [1] and replaced in (4), for x is obtained:

$$x = \left[p_п - p_c + A^2 - A\sqrt{4(p_п - p_c) + A^2}\right]\frac{\pi d^2}{4c} - x_0 \quad (5)$$

which is dependent on the species $x = x[A(t)]$.

Pre-compression is determined by (5), where parameter **A** has a value corresponding to $t = t_0 + \Delta t$.

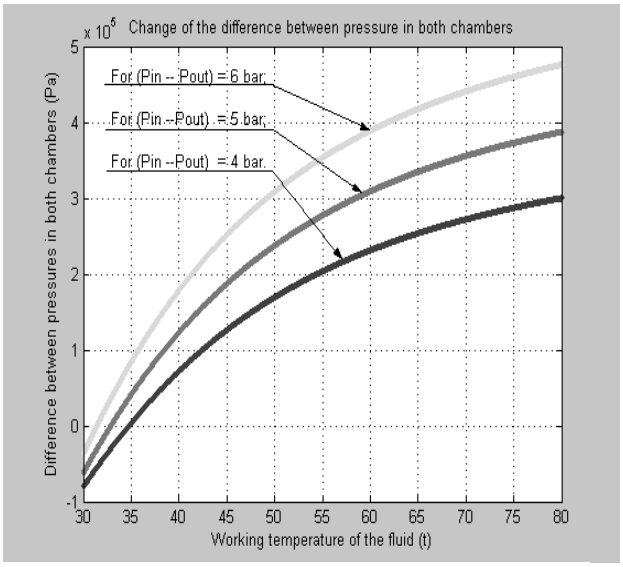

Fig. 2

Fig. 2 shows the graphical dependence (5) for the temperature range of 26-58 °C.

The flow rate Q_0 of the fluid flowing through the compensator is a sum of the flow rates going through the two flow chambers and through the throttle hole with a width x and diameter d:

$$Q_0 = Q_a + Q_b + Q_{th}. \quad (6)$$

It is accepted that $Q_a = Q_b$ for each temperature value.

The debit Q_{th} is determined by the dependence:

$$Q_{th} = \eta\pi dx\sqrt{\frac{2}{\rho}(p_п - p_c)} = \eta f_{th}\sqrt{\frac{2}{\rho}(p_п - p_c)} \quad (7)$$

where $f_{th} = \pi dx$ is the area of the throttle hole.

Constructive feature

The flow Q_0 is represented as the sum of the volumetric flow rate and the Q_{work} compensator:

$$Q_0 = \Delta Q_{lost} + Q_{work}. \quad (8)$$

The volume of volumetric losses in the hydro motor ΔQ_{lost} depends on the temperature, post-epithelial

$$\Delta Q_{lost} = \Delta Q_{lost}(t).$$

The flow rate Q_{work} is required to achieve the requested speed of the operating tool of the driven machine.

From (6), (7) and (8) the dependence of the compressor throttle area as a function of the temperature:

$$f_{th} = \frac{Q_{work} + Q_{lost}(t) - 2Q_a(t)}{\eta\sqrt{\frac{2}{\rho}(p_п - p_c)}} \quad (9)$$

The joint solution of (5) and (9), which usually happens in a graph-analytical way, makes it possible to construct the structural characteristic of the compensator in question, which has the form:

$$f_{th} = f(x). \quad (10)$$

The obtained dependencies show that in order to obtain unambiguous flow correction as a function of temperature only, it is imperative to observe the condition of constant difference between the input and output pressures $p_п - p_c = const.$ This can be don e when the compensating compensator is combined with a reduction valve or a pressure valve with indirect action according to the known circuit solutions.

CONCLUSION

The presented results can be used to create a methodology for the design and dimensioning of a throttling compensator for a particular system.

This schema and given dependencies enable the creation of an item with a reverse slope of the flow rate debit feature.

REFERENCES

1. Yankov, R.V. The chamber passage as fluid's temperature function, University "Prof. Dr. Assen Zlatarov" 2010, Vol. 4, T. 6, pp.187-189. **(article)**

Assen Zlatarov University
ANNUAL, VOL. XLVII, BOOK 1, 2018
TECHNICAL AND NATURAL SCIENCES

Design and layout:
Libra Scorp Publisher
www.meridian27.com

Edition of:
Assen Zlatarov University
www.btu.bg

ISSN 2603-3968

BURGAS, 2018

ISSN 2603-3968